Cluster Superlattices on Hexagonal Boron Nitride and Graphene/Ir(111) and Their Embedding with Carbon

I n a u g u r a l - D i s s e r t a t i o n

zur

Erlangung des Doktorgrades

der Mathematisch-Naturwissenschaftlichen Fakultät

der Universität zu Köln

vorgelegt von

Moritz Will

aus Bergisch Gladbach

Köln 2020

Abstract

Cluster and nanoparticle research is at the forefront of nanotechnology owing to the exceptional physicochemical properties of individual nanoparticles which greatly differ from their bulk counterparts. The preparation of similar sized and well ordered clusters is a challenging task. A remarkable method to fabricate dense, two-dimensional arrays of clusters with a narrow size distribution is ultra-high vacuum growth on surface templates. Such templated cluster superlattices have been successful as model systems for heterogeneous catalysis, magnetism, optics, and electronics, as they allow the study of cluster properties with conventional surface science techniques. Their periodic arrangement allows the application of both local probes and integrating methods.

Wide-spread application of supported cluster superlattices is inherently hampered by their tendency to degrade under reaction conditions, *i.e.* atmospheric pressure and/or temperatures of a few hundred degrees Celsius. Under these circumstances, they lose their advantageous periodic arrangement, narrow size distribution and homogeneous environment, and in some cases even the cluster structure may be altered or destroyed. One way of approaching this issue is to curb the decay of cluster superlattices, another is the exploration of new substrates for templated cluster growth that provide enhanced stability.

Single-layer hexagonal boron nitride on Ir(1 1 1) is a new template for the growth of highly stable cluster superlattices. We demonstrate, that it enables the synthesis of highly ordered Ir, Pt, Au, and C cluster superlattices. Characterization with scanning tunneling microscopy reveals high superlattice densities and an unparalleled thermal stability. The results are corroborated by x-ray photoemission spectroscopy and density functional theory calculations, which unravel the binding mechanism of the clusters to the substrate. Furthermore, we explore carbon embedding of cluster superlattices in ultra-high vacuum as a method to suppress sintering of cluster superlattices. Carbon embedding is also an integral step in the formation of a novel free-standing material containing a cluster superlattice sandwiched between a two-dimensional material and a thin matrix of amorphous carbon. The thesis comprises three manuscripts in their entirety, a comprehensive overview of the relevant scientific background, and a detailed discussion of each chapter together with an outlook.

In the first manuscript, we introduce a monolayer of hexagonal boron nitride on Ir(1 1 1) as a template for the growth of periodic arrays of clusters. We demonstrate the templating capabilities for Ir, Au and C clusters. In an exemplary case study on Ir clusters, we examine the

cluster binding site and epitaxial growth, and compare scanning tunneling microscopy results to *ab initio* density functional theory calculations. Ir clusters grow epitaxially in the valley regions of the moiré. By varying the Ir deposition, the average cluster size of the arrays can be tuned. Moreover, we find that the thermal stability of the cluster superlattices on h-BN/Ir(1 1 1) is exceptional and exceeds all other known substrates for templated growth. The excellent stability is explained by selective rehybridization of the h-BN underneath the clusters with bond formation between B and Ir cluster atoms.

In the second experimental chapter, we expand the range of cluster materials forming superlattices on hexagonal boron nitride on Ir(1 1 1) to Pt. We elucidate the growth and structure of the Pt clusters by means of x-ray photoemission spectroscopy and scanning tunneling microscopy. The XPS results provide direct evidence of the binding mechanism by rehybridization and confirms the calculated results obtained for Ir clusters on hexagonal boron nitride on Ir(1 1 1). We analyze the thermal stability of Pt clusters and observe cluster superlattice degradation *via* Smoluchowski ripening and intercalation below the h-BN above 650 K. Notably, one- and three-layer clusters are favored during growth of Pt clusters on hexagonal boron nitride on Ir(1 1 1). Moreover, mild heating to 730 K induces a shape transformation from one- to three-layer clusters for the case of an average cluster size of 63 atoms, indicating two-layer Pt clusters to be metastable. Scanning tunneling spectroscopy reveals the electronic decoupling of the Pt clusters from the substrate, which gives rise to Coulomb blockade effects.

Third, we demonstrate the embedding of Ir cluster superlattices on graphene on Ir(1 1 1) with elemental carbon. Embedded clusters have a dramatically increased thermal stability against coalescence compared to bare clusters, as evidenced by scanning tunneling microscopy. Moreover, in controlled cluster pick-up experiments with the tip of the scanning tunneling microscope, we show the improved mechanical stability of embedded clusters. We demonstrate that the deposited carbon adheres first to the clusters, leading to conformal embedding without impeding the structural perfectness of the cluster superlattice. Scanning tunneling spectroscopy reveals that the only path left for cluster degradation is *via* intercalation below the Gr layer at temperatures above 850 K. This embedding method constitutes a crucial step in the fabrication of a novel material, consisting of a cluster superlattice sandwiched between a 2D material and an embedding matrix of carbon.

The scientific appendix provides additional data on the interaction of further materials with graphene and hexagonal boron nitride on Ir(1 1 1). We explore low temperature deposition as a method to create perfect arrays of Au and Fe clusters on hexagonal boron nitride on Ir(1 1 1). Furthermore, we investigate Mo, Ta, Nb, Dy, and Tm deposition on graphene and hexagonal boron nitride on Ir(1 1 1) in view of cluster superlattice formation. The interaction of CO with Pt clusters on hexagonal boron nitride on Ir(1 1 1) is studied *in operando* by scanning tunneling microscopy. Shape transformations and sintering of Pt clusters are found to occur upon CO adsorption.

Deutsche Kurzzusammenfassung
(German Abstract)

Forschung an Cluster und Nanoteilchen gehört gegenwärtig zu den Eckpfeilern der Nanotechnologie. Diesen Umstand verdanken sie ihren außergewöhnlichen physikochemischen Eigenschaften, die sich oft fundamental von denen des gleichen Materials im Kristall unterscheiden. Dabei ist das Wachstum von ähnlich großen und wohlgeordneten geträgerten Clustern oft eine Herausforderung. Eine bemerkenswerte Methode für die Präparation zweidimensionaler Clustergitter mit einer schmalen Größenverteilung ist das Wachstum auf Oberflächentemplaten im Ultrahochvakuum. Solche Cluster-Übergitter stellen erfolgreiche Modell-Systeme für heterogene Katalyse, Magnetismus, optische Anwendungen sowie Nanoelektronik dar, da sie durch ihre regelmäßige Anordnung sowohl Charakterisierungen mit lokalen Sonden als auch integrierenden Methoden erlauben.

Ein weitverbreiteter Einsatz solcher Cluster-Übergitter wirkt ein besonderer Prozess entgegen: Unter Reaktionsbedingungen wie Atmosphärendruck und Temperaturen von einigen hundert Grad Celsius, wie sie für viele Anwendungen beispielsweise in der Katalyse auftreten, werden die Clustergitter zersetzt. Sie verlieren ihre herausragenden Eigenschaften, wie ihre periodische Anordnung über große Distanzen, ihre schmale Größenverteilung, ihre wohldefinierte Umgebung und verändern ihre Struktur. Ansätze zur Bewältigung dieses Problems sind daher z. B. das Eindämmen der Zersetzungsmechanismen oder die Suche nach neuartigen Substraten, die eine erhöhten Stabilität ermöglichen.

Ein neues Templat für die Synthese von Cluster-Übergittern ist eine Monolage hexagonalen Bornitrids auf der Ir(1 1 1)-Oberfläche. Wir demonstrieren in dieser Arbeit die Bildung von hochgeordneten Cluster-Übergittern von Ir, Pt, Au und C auf diesem Substrat. Charakterisierungen mit Hilfe von Rastertunnelmikroskopie offenbaren die enorme Dichte der Cluster sowie ihre beispiellose thermische Stabilität. Die Ergebnisse werden durch Röntgen-Photoelektronenspektroskopie und Dichtefunktionaltheorierechnungen ergänzt, durch die wir den Bindungsmechanismus der Cluster zum Substrat verstehen können. Darüber hinaus führen wir die Einbettung mit elementarem Kohlenstoff im Ultrahochvakuum als Methode zur Unterdrückung von Clustergitter-Reifung ein. Dieser Einbettungsschritt ist des Weiteren ein essentieller Bestandteil in der Herstellung einer neuartigen "Cluster-Übergittermembran", in der ein Clustergitter zwischen einer Lage Graphen und einer ultradünnen Matrix aus amorphem Kohlenstoff eingeschlossen ist. Diese Dissertation beinhaltet drei Manuskripte in ihrer Gesamtheit, eine umfassende Einleitung

in den wissenschaftlich relevanten Hintergrund sowie eine detaillierte Diskussion eines jeden experimentellen Kapitels.

Im ersten Manuskript führen wir ein neuartiges Substrat für das Wachstum periodischer Clusterstrukturen ein: Eine Monolage hexagonales Bornitrid auf Ir(1 1 1). Wir demonstrieren die Cluster-Übergitterbildung von Ir, Au und C Clustern auf dieser Unterlage und führen eine Fallstudie an Hand von Ir Clustern durch, in der wir den Adsorptionsplatz bestimmen und das epitaktische Wachstum zeigen. Der Vergleich zwischen den experimentellen Daten und *ab initio* Dichtefunktionaltheorie erlaubt es uns den Bindungsmechanismus der Ir-Cluster nachzuvollziehen. Wir zeigen, dass die Cluster präferiert im "Valley"-Platz wachsen und wir durch Variation der Depositionsmenge die mittlere Clustergröße beeinflussen können. Überdies erforschen wir die unübertroffene thermische Stabilität der Ir-Cluster und erklären selbige durch selektive Rehybridisierung der Monolage hexagolen Bornitrids unterhalb der Cluster, in der die B-Atome durch sp^3-Bindungen an die Clusteratome binden.

Im zweiten experimentellen Kapitel erweitern wir den Umfang an Materialien, die hexagonales Bornitrid auf Ir(1 1 1) zu Cluster-Übergittern templiert, um Pt. Wir erläutern Wachstum und Struktur der Pt-Cluster mit Hilfe von Röntgen-Photoelektronenspektroskopie und Rastertunnelmikroskopie. Die experimentellen Resultate sind direkter Beweis des sp^3-Bindungsmechanismus und bestätigen die Dichtefunktionaltheorierechnungen des vorigen Kapitels. Wir analysieren die thermische Stabilität der Pt-Cluster und beobachten dabei Zerfall des Clustergitters durch Smoluchowski-Reifung sowie Interkalation unter die h-BN-Lage oberhalb von 650 K. Eine besondere Eigenschaft der Pt-Cluster ist die bevorzugte Bildung von ein- und dreilagigen Clustern und das fast vollständige Fehlen von zweilagigen Clustern bei jeder Bedeckung. Ausheilen der Cluster auf 730 K bewirkt außerdem eine Umwandlung der Clusterstrukturen von ein- zu dreilagigen Clustern für den Fall einer durchschnittlichen Clustergröße von 63 Atomen. Rastertunnelspektroskopie erlaubt uns den entkoppelnden Charakter des Substrates aufzudecken, den wir an Hand von Coulomb-Blockade-Effekten beweisen.

Das dritte Manuskript beschreibt die Einbettung von Ir-Cluster-Übergittern auf Graphen auf Ir(1 1 1) mit elementarem Kohlenstoff. Eingebettete Cluster offenbaren eine dramatisch erhöhte thermische Stabilität und sind nahezu vollständig resistent gegenüber Koaleszenz und Reifung. Diesen Sachverhalt belegen wir mit Rastertunnelmikroskopie-Messungen. Kontrolliertes Aufsammeln der Cluster mit der Spitze des Mikroskops lässt uns außerdem Rückschlüsse über die erhöhte mechanische Stabilität der eingebetteten Cluster treffen. Wir zeigen weiterhin, dass der deponierte Kohlenstoff zuerst an die Metallcluster anhaftet, ohne die Struktur des Übergitters zu verändern, die Einbettung also "konform" ist. Rastertunnelspektroskopie zeigt, dass der letzte verbleibende Zerfallsmechanismus der Cluster Interkalation unter die Graphenlage ist und bei Temperaturen oberhalb von 850 K stattfindet. Die hier aufgezeigte Methode der Einbettung mit amorphem Kohlenstoff ist außerdem ein wichtiger Schritt in der Herstellung eines neuen

zweidimensionalen Materials, welches aus einem Clusterübergitter besteht, das zwischen einer Lage eines 2D-Materials und einer einbettenden Schicht eingekapselt ist.

Im wissenschaftlichen Anhang befinden sich zusätzliche Messdaten zur Interaktion verschiedenster Materialien mit Graphen und hexagonalem Bornitrid auf Ir(1 1 1). Zuerst erläutern wir Deposition bei niedrigen Temperaturen als eine Methode zur Herstellung hochgeordneter Fe und Au Clustergittern. Überdies untersuchen wir Deposition von Mo, Ta, Nb, Dy und Tm auf Graphen und hexagonalem Bornitrid auf Ir(1 1 1) als mögliche Kandidation für die Bildung von Cluster-Übergittern. Die Wechselwirkung von CO mit Pt-Clustern auf hexagonalem Bornitrid auf Ir(1 1 1) wird im letzten Kapitel in Form von *in operando* Experimenten mit dem Rastertunnelmikroskop analysiert. CO bewirkt bei den Pt-Clustern eine Veränderung der Morphologie sowie Cluster-Reifung.

Frequently used Acronyms and Abbreviations

2D	-	two-dimensional
a-C	-	amorphous carbon
ARPES	-	angle-resolved photoemission spectroscopy
AFM	-	atomic force microscopy
CVD	-	chemical vapor deposition
DFT	-	density functional theory
(P)DOS	-	(projected) density of states
Gr	-	graphene
h-BN	-	hexagonal boron nitride
HOMO	-	highest occupied molecular orbital
LEED	-	low-energy electron diffraction
LUMO	-	lowest unoccupied molecular orbital
MBE	-	molecular beam epitaxy
ML	-	monolayer
PMMA	-	polymethyl methacrylate
SEM	-	scanning electron microscopy
STM	-	scanning tunneling microscopy
STS	-	scanning tunneling spectroscopy
(HR)TEM	-	high resolution transmission electron microscopy
TPD	-	temperature-programmed desorption
TPR	-	temperature-programmed reaction
UHV	-	ultra-high vacuum
XAS	-	x-ray absorption spectroscopy
XMCD	-	x-ray magnetic circular dichroism
(HR)XPS	-	(high resolution) x-ray photoelectron spectroscropy

Contents

PART I

Introduction and Background

CHAPTER 1

Overview

L IKE many other physical phenomena, nanoparticles have been utilized, yet unperceived by mankind for a considerably longer period of time than they have been described. When you marvel at the breathtaking windows in medieval Christian churches and cathedrals, plasmon resonances of colloidal silver and gold clusters woven into the glass are the origin of their lustrous colors. The singular *Lycurgus Cup* made by Roman artisans in the 4th century is made of dichroic glass. Apart from the fact that it is perceived as an exceptionally fine display of glass-cutting craftsmanship, it showcases another magnificent property when exposed to light: Due to gold colloids in the glass, the cup may change colors from green to a deep ruby red, depending on whether the light is reflected from or transmitted through it. [1] The gold particles are only few tens of nanometers in size and it is doubtful, that they were intentionally processed, or even noticed by their makers. Similarly, very small quantities of carbon nanoparticles like fullerenes have been inevitably created in the soot of combustion processes for millennia without mankind knowing about them. Only since the advent of condensed matter physics in the 20th century have researchers wondered what happens if you make a solid really, really small.

A cluster is an entity of just a few to a few ten thousand atoms. It bridges the gap between an atom and a (crystalline) solid. While both of those were being decently understood in the 1970s, the question arose how the elemental properties of atoms eventually sum up to form a bulk solid. Clearly, a bi-atomic gold cluster behaves more like a molecule rather than a crystal, but how about one containing a hundred, or a few thousand atoms?

In response to this, researchers began to figure out that small particles of a material behaved fundamentally differently. Collective phenomena like ferroelectricity and ferromagnetism were scrutinized and unique effects such as superparamagnetism were reported. The finding of the cluster magic numbers led to the description of superatoms and was eventually followed by the discovery of the C_{60} 'Buckyballs'. [2] Owing to their smallness, clusters present a playground for a multitude of quantum size effects, making them attractive for theoreticians and experimentalists alike. As a consequence of the wealth of exciting cluster phenomena, a new field of research emerged in the 1980s.

Cluster science is flourishing still today. This is mainly thanks to the ever increasing need of nanoparticles as catalysts in industrial chemistry. The *Acmite Market Intelligence* states,

that 'global demand on catalysts was valued US\$33.5 billion in 2014 and will witness robust growth in the next years'; [3] a significant part of those demands are covered by nanoparticles and clusters. Because most of a cluster's atoms are situated on its surface, cluster science lies at the boundary of chemistry and physics. Nowadays, metal clusters offer intriguing possibilities not only as catalysts, but also for magnetic storage miniaturization, [4,5] in photochemistry, [6] optics, [7–9] electronic device fabrication, [10] and even in biology and medicine, [11] *e.g.* as nanosensors. [12] Characterization of their physicochemical properties on the nanoscale, as well as finding elaborate preparation techniques are formidable tasks that will keep fundamental scientists employed for at least a few more decades.

Almost regardless of the application, it is mandatory to bring the clusters onto a suitable substrate. While some intrinsic properties can be studied in free cluster beams or in liquid phase colloids, clusters are of most use when they are supported. Over the decades, it turned out that there are some requirements on the substrate. Ideally, the dispersion[1] of particles on the support is high in order to maximize the response to external stimuli, be it the conversion rate of a chemical reaction, the magnetic storage density, or simply the signal of a spectroscopic measurement. Meanwhile, the clusters need to be stably bound to the support, because mobility will inevitably reduce the nanoparticle dispersion by agglomeration, and consequently destroy their distri-

Figure 1.1: A periodic array of $Ir_{\overline{39}}$ clusters on h-BN/Ir(1 1 1), measured with a scanning tunneling microscope. Image size is (75 nm× 75 nm).

bution. Agglomeration of clusters is called 'sintering' and is generally undesirable. In heterogeneous catalysis, unwanted cluster-substrate interactions by adsorbant spillover are additionally unpleasant, because they can drastically alter the outcome of the chemical reaction. Finally, shape and size of clusters affect the turnover rates of catalyzed reactions, the cluster electronic structure, and many other properties. An ideal cluster substrate is therefore inert, with a strong enough interaction to prevent sintering, but weak enough to preserve the chemistry of the clusters. Moreover, similar (identical) cluster shapes and sizes are to be preferred over random arrangements because they facilitate the understanding of the system and increase the measurement signal.

Substrates which offer many of these qualities are so-called templates. A template is able to organize deposited species in a periodic fashion without further external manipulation. This

---

[1]Dispersion in supported cluster terms generally means the cluster density on the substrate.

happens due to an intrinsic variation of the potential energy an arriving cluster (or atom) experiences when it arrives on the surface of the template. When the parameters are chosen just right, templated growth is able to produce beautiful two-dimensional cluster arrays spanning over an entire sample, where every cluster is equidistant and almost identically sized. An example is provided in Figure 1.1, showcasing the astounding ability of a monolayer of hexagonal boron nitride on Ir(1 1 1) to produce highly ordered Ir cluster assemblies, as measured with the STM. Apart from the aesthetic joy it brings to investigate such systems, their clean and fast production, as well as their structural perfection make them superior to many other cluster preparation techniques. They offer an unparalleled combination of cluster density and size control to the researcher. Consequently, cluster arrays have been studied as model system for heterogeneous catalysis and for fundamental research in nanomagnetism. [13]

An inherent disadvantage of supported cluster superlattices[2] is their degradation under high temperature and high pressure conditions, where most conventional catalysts operate. Exposure to a few hundred degrees Celsius, or simply bringing the cluster superlattice out of the clean UHV environment leads to sintering and oxidation of the clusters. Wide-spread use of such systems is substantially hampered mainly owing to this reason. [14]

In simple terms, this thesis is dedicated to explore supported cluster superlattices, and to design a pathway to bring them closer to 'real world' applications. We aim at tackling the *sintering problem*, that is the degradation of the cluster lattice by cluster agglomeration. Our approach is twofold: First, we explore and characterize a new template, hexagonal boron nitride on Ir(1 1 1). As we will see, it provides excellent templating capabilities and unparalleled cluster stability. Second, we introduce the idea of a *cluster superlattice membrane* – a new, free-standing 2D material, consisting of a cluster superlattice embedded into a matrix of amorphous carbon. Therefore, we investigate the first crucial step in the formation of a cluster superlattice membrane: conformal embedding of cluster superlattices with amorphous carbon. We find first of all a dramatic increase in the thermal stability of C-embedded clusters. Moreover, we prove that elemental C *conforms* to the clusters, *i.e.* it covers the cluster superlattice without deteriorating its structural perfectness.

We utilize a combination of several UHV-based techniques for our studies. Our main tool is scanning tunneling microscopy, which is a versatile tool to probe the spatial and electronic structure of conductive samples, well suited for the characterization of cluster superlattices. It operates by raster-scanning a metallic tip across the sample at a very small distance of a few Å. At this distance, a small but measurable tunneling current flows, which is proportional to the distance between tip and sample. As the tip scans over the sample, the tunneling current produces an image of the sample topography. Moreover, one is able to probe the local electronic density of states, *e.g.* by measuring $I(V)$ characteristics at a given sample location. This

---

[2]A superlattice is here the term for a periodic arrangement of clusters. In general, superlattices are (periodically repeating) heterostructures of thin films. Due to lattice mismatch between the layers, a moiré superstructure may emerge, which in turn may act as a template for cluster growth on top – hence the term cluster superlattice.

altogether allows us to image the sample morphology and access the electronic structure of cluster superlattices with and without carbon embedding.

Two inherent disadvantages of STM imaging are the lack of chemical contrast and the extreme surface sensitivity, as we can only ever 'see' the very topmost atoms. This poses a problem once the clusters are embedded with carbon – we are blind as to what happens to the metal underneath the carbon matrix. Therefore, we complement the STM measurements with synchrotron-based x-ray photoemission spectroscopy, whereby we extract and analyze photoelectrons created by x-rays. XPS is able to resolve the full electronic structure of the sample from the Fermi level to the deep-lying states. With XPS, changes in the binding configuration of an atomic species can be measured as shifts of the core level electrons. This allows us to monitor for example the binding of the substrate to the clusters, the gradual degradation of superlattices upon annealing, or the adsorption of gases. Moreover, we support our findings with density functional theory calculations. DFT is able to provide both structural models as well as the electronic structure of the samples, complementing the experimental techniques.

———————————

This thesis is organized as follows: part I provides an overview on the fundamentals relevant for the work and simultaneously serves as a motivation for the experimental work. We introduce the reader to the topic of cluster science in chapter 2, discuss key properties and applications, and overview important preparation methods. In particular, template-assisted growth of cluster superlattices is extensively reviewed in section 2.3 due to its increased relevance. In chapter 3, we introduce the prevalent routes of cluster degradation and their significance for cluster super-lattices. We present methods to circumvent cluster degradation from the literature, as well as our own concept of tackling this problem: the fabrication of a cluster superlattice membrane.

The experimental results are included in part II. It consists of two peer-reviewed papers (chapters 4 and 6) and one manuscript in preliminary stage (chapter 5). Chapters 4 and 5 are dedicated to monolayer hexagonal boron nitride on Ir(111) as a template for cluster superlattice growth. We employ STM, XPS and DFT to describe the templating capabilities of h-BN/Ir(1 1 1), the thermal stability of Ir and Pt clusters, and their binding mechanism. Chapter 6 deals with the conformal embedding of Ir clusters on Gr/Ir(1 1 1) with molecular carbon. We unravel the embedding mechanism and demonstrate the increased thermal stability of embedded Ir clusters.

Finally, conclusions and retrospective discussion on the experimental results are comprised in part III of the thesis. It contains additional scientific advances during the time of the completion of this thesis and puts our results into the context of the field. Furthermore, we outline prospects for future research following from our work.

CHAPTER 2

Supported Metal Clusters

This chapter deals with the topic of metal clusters on substrates. It serves as a motivation for the research conducted in part II of this thesis. We begin with a general overview of their physicochemical properties and give examples on break-through studies. In the second part, we lay out some important preparation methods, as well as their goals and weaknesses. We pay special attention to cluster superlattice growth on template supports, as it is the method of choice for the experiments of this work.

WHILE the first studies of metal clusters in the 1970s were carried out in free beam experiments, researchers were already aware, that in order to utilize the exciting properties of clusters, it would be mandatory to bring them onto a substrate. In fact, preparing heterogeneous catalysts by washing a soluble metal compound onto a carrier material (the support) and then reducing and calcining it, was well-known already before the 70s. [15] Such a support had to have two qualities: it needed to have a high surface area in order to maximize catalyst dispersion and it had to stabilize the clusters to reduce agglomeration. Back then however, the term cluster was seldom used – the authors preferred 'crystallite' or 'metal particle'. *Atomic dispersion*, that is distributing the metal evenly in mono-atomic form, was the ultimate goal in catalyst fabrication, but even when authors claimed to have achieved this, it could hardly be verified with the available characterization methods. [15] Many inherent features of nanoparticles, even basic ones like their structure, were often unknown to the community. Consequently, acquiring the true rate of catalytic conversion for a given chemical reaction, the turnover rate, was challenging. Once methods to measure the size of small clusters, such as high resolution electron microscopy and scanning probe microscopy became available, many lingering questions could be resolved, while new ones surfaced.

Today, with powerful techniques at hand, cluster properties can be thoroughly explored. Plenty of progress has been made in controlled cluster synthesis on a variety of substrates, ranging from oxide thin films over single crystals to single-layer 2D materials. With the rise of nanotechnology at the turn of the millenium, the interest in clusters only grew. Nowadays, a zoo of cluster materials is available and research on supported metal clusters is an active field at this time and age.

2.1 General Properties
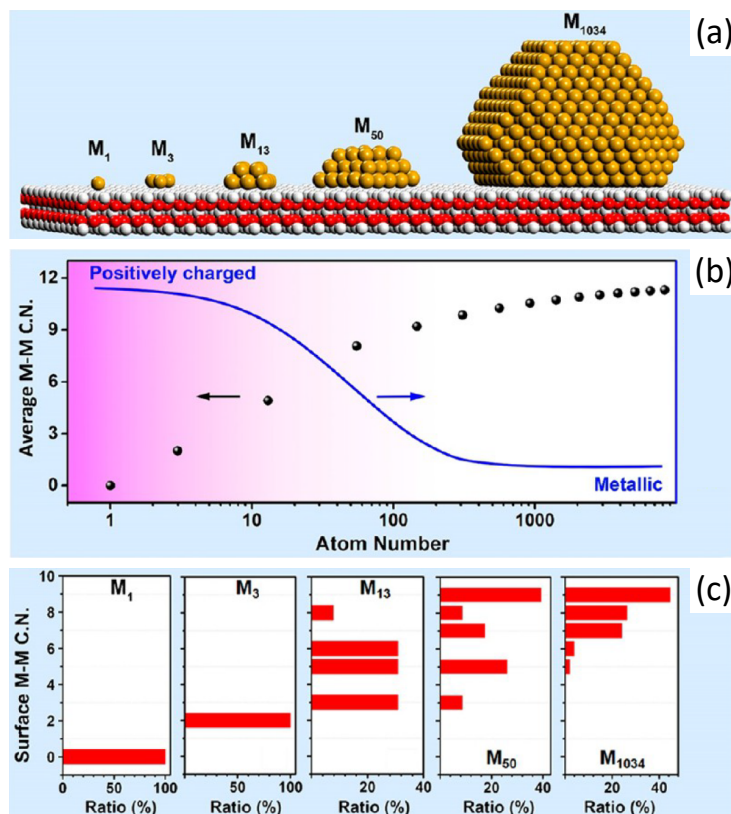
Figure 2.1: (a) Exemplary models of five different metal clusters on a support with an assumed fcc structure. M_n denotes the cluster size with n the amount of atoms and M the element. (b) Average metal-metal coordination number as a function of cluster size in atoms. The blue line represents the general trend of the cluster charge when deposited on a support. The substrate was assumed to accept charge. (c) Metal-metal coordination number of the surface atoms in the clusters depicted in (a). Adapted from ref. 16.

As has been alluded before, the unique aspect of clusters is their small size. With this comes a very important aspect: within a cluster, many, sometimes most of its atoms lie on the surface. Because there is an endless combination of cluster materials, shapes, sizes and substrates, we will consider first a very basic example presented in Figure 2.1a. Arranging an fcc metal on an arbitrary substrate gives an idea on the geometric structure of a real supported cluster and allows to determine the coordination number by simply counting the metal-metal bonds of an individual atom. For a cluster of >1000 atoms, the average number approaches the bulk limit of 12 (see Figure 2.1b), while smaller clusters have a significantly reduced coordination number, *e.g.* 7.4 for a 50-atom cluster and 4.9 in a 13-atom cluster. This goes along with a drastic change in the surface atom coordination number, depicted in Figure 2.1c. For a two-layered 13-atom cluster, most of its constituents are surface atoms with a coordination number between 3 and 6. The population shifts towards higher coordinated atoms when the cluster size is increased: for

a 1034-atom cluster it ranges predominantly from 7 to 9. This illustrates the transition from a severely undercoordinated nanocluster to a nanoparticle with close-packed facets. Meanwhile, the fraction of atoms at the surface is remarkably high. It can be calculated that for a free, spherical cluster containing 1000 atoms in total, one fourth are surface atoms [17, 18] and this number is noticeably higher for smaller clusters.

The surface provides sites for gas adsorption and catalytic conversion. The size-dependent catalytic activity of clusters has been proven quite early [15] and was confirmed in many experiments thereafter. [19–26] However, not only the size of a cluster is crucial for the determination of its properties but also its morphology. [27] Depending on the substrate, cluster material and the growth conditions, the cluster structure varies heavily not only from the bulk equilibrium shape but also from cluster to cluster (for a detailed overview on this topic, the reader is forwarded to the article by C. Henry [28]). Naturally, the amount of kinks and steps in a cluster influences adsorption geometries and local electron densities, thus affecting its physicochemical properties. [29] Structure determination is therefore critical to ensure fruitful modeling of supported metal clusters. [30] To this end, a combination of surface science techniques has been successfully applied. However, even in modern days precise structure determination of clusters remains a challenge. [31]

Historically, it posed a problem to theoretically describe small clusters in the transition regime between molecule-like and bulk-like. A landmark finding was made in 1984 in the group of Knight, who experimented with a beam of Na clusters produced by supersonic expansion into vacuum. [32] Mass spectrometric analysis revealed the emergence of abundance peaks at specific cluster sizes of $N = 8,20,40$ and so forth. These peaks were attributed to 'magic numbers' of valence electrons, in analogy to atomic nuclei in nuclear physics. A successful approach was provided by the jellium model [33, 34] which describes a cluster as a positively charged sphere filled with electrons. This spherical potential reproduces the observed peaks very well, precisely at the numbers where the amount of valence electrons fills a shell. Apart from these electronic magic numbers, cluster structures with a maximal number of nearest-neighbor bonds are the most stable. When clusters are brought to a surface, the interfacial interaction heavily influences their structure and dynamics. [35] Nevertheless, also for supported clusters, structural and electronic magic numbers are observed, albeit at different cluster sizes than in the free beam. [36, 37] Magic sizes have been reported *e.g.* for Ga clusters on the (7×7) reconstructed Si(1 1 1) surface. [38–40] Moreover, it is misleading to assume one fixed cluster structure for a given cluster size. For non-magic clusters, many morphologies may be local energy minima and the thermal energy suffices to induce incessant restructuring. With fast measurement techniques, one is able to resolve these structural changes. Size-selected Pd clusters deposited onto an inert h-BN/Rh(1 1 1) surface exhibit dynamics on a timescale much faster than 16 Hz at 150 K. [41] Later in section A.2 of this work, we will see that Pt clusters on h-BN/Ir(1 1 1) are subject of re-organization as well.
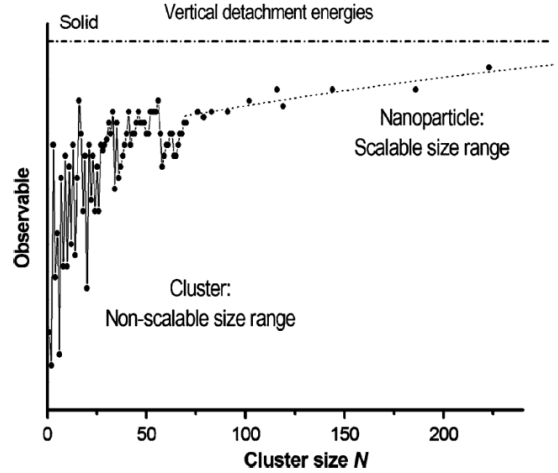
Electronic Structure
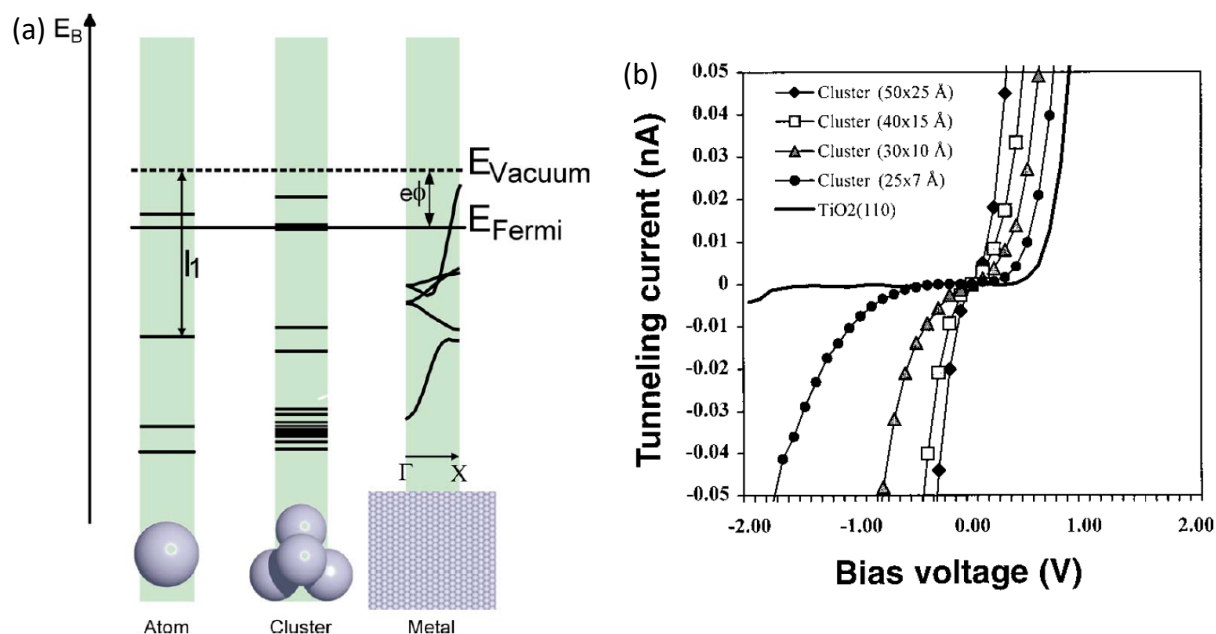
Figure 2.2: (a) Diagram representing the transition in electronic structure from a single atom to a bulk metal. E_B on the ordinate denotes the binding energy; I_1 is the first ionization energy; $e\phi$ is the work function; Γ and X are symmetry points in the Brillouin zone. Adapted from ref. 42. (b) I(V) curves acquired with STS on Au clusters on $TiO_2(1\,1\,0)-(1\times1)$ and of the bare $TiO_2(1\,1\,0)-(1\times1)$ surface. Adapted from ref. 23.

In order to understand the intriguing properties of clusters, it is useful to consider the electronic structure of such a particle. H.-J. Freund stated in his recommended review on oxide-supported clusters, that '[..]generally speaking, we would like to know the geometric structure of the entire deposited particle–substrate complex, and in addition the distribution of electrons within the system'. [42] While the substrate certainly plays a crucial role in modulating the electronic system (as does the structure of the cluster), we will only consider a simplified picture of a free cluster, illustrated in Figure 2.2a. Consider first the electrons of a single atom which can be represented by electronic shells located at the position of the atom. Once we bring multiple atoms together, the electrons begin to overlap and quantum mechanics leads to a splitting of the electronic shells into molecular levels. Once many atoms agglomerate periodically, we end up with a bulk solid, whose crystal lattice induces the formation of energy bands. Because clusters are a state between an isolated atom and a crystal, their electronic structure resembles more that of a molecule. In analogy to molecular orbitals, clusters possess cluster orbitals with a distinct energy gap between their lowest unoccupied and highest occupied states which is dependent on the amount of electrons, hence the amount of atoms in the cluster. Increasing the cluster size means we approach the bulk solid case depicted on the right hand side of Figure 2.2a. The gap vanishes and the cluster becomes metallic. This energy gap can be directly measured with local

probes, as shown in Figure 2.2b. Here, Au clusters were grown on a $TiO_2(1\,1\,0)$ substrate and $I(V)$ curves as a function of cluster size were taken with an STM. Clearly visible is the plateau of zero current around zero bias voltage for all clusters, characteristic for an electronic gap. The size of this STS gap depends on the inverse cluster size, as we would expect from the previous considerations.

Notably, the changes in the electronic structure are highly irregular for very small clusters. In the 90s, Taylor *et al.* conducted ultraviolet photoemission spectroscopy (UPS) on free Au clusters and obtained, among other quantities, the vertical detachment energy (*i.e.* the energy to remove one electron from the cluster, equivalent to the bulk work function) which is directly correlated to the internal electronic structure. [44] The results are depicted in Figure 2.3. Two regimes can be unambiguously identified. Firstly, the scalable regime, where the cluster vertical detachment energy obeys a simple power law until it reaches the bulk value. Second, below a certain cluster size the non-scalable regime, where the quantum size effects within the cluster

Figure 2.3: Work function of free Au_N^- clusters. Adapted from ref. 43 with data from ref. 44.

dominate its physical and chemical properties. For many metals, this fluent transition lies in the range around 100 atoms, but it is heavily dependent on the material and, when the clusters are supported, also on the substrate. [42, 45–47] For this reason, systematic investigations of size effects in the non-scalable regime prove to be challenging. A review about the electronic structure of metal clusters and its implications can be found in ref. 48.

Optics

Apart from being challenging to study, the size-dependency of many properties of clusters may also offer the prospect to tailor cluster properties by controlling their size. Prominent examples come from nano-optics [49], where metal clusters are utilized to great avail. [9] Especially noble metal clusters in the scalable size regime above a few hundred atoms exhibit plasmons, *i.e.* collective excitations of the charge density. Moreover, the plasmon resonance frequency and line shape is strongly dependent on particle size and shape. [50] Introducing anisotropies such as non-spherical particle shapes gives rise to splitting of plasmon bands into multiple modes. [51] Significant advances in particle preparation and characterization have enabled researchers to tune the optical response of the clusters, making them attractive for applications in (bio-)sensing [10, 42, 52, 53] and as nano-scale plasmonic waveguides. [7, 54]

Coulomb Blockade

Another intriguing prospect is the use of clus-
ters for nano-scale devices. [56] A concept in-
tensively studied in the 1990s is the single-
electron transistor (SET). A SET consists of
a metallic nanodot sandwiched between two
insulating resistances and contacted by a gate
electrode (see Figure 2.4a). [57] The nanodot
may be a small island, a nanoparticle, a clus-
ter, and even a single molecule. [58] With large
enough resistances, one reaches the case of
a double-barrier tunneling junction and the
electronic transport is governed by tunnel-
ing. In the absence of background charge, one
needs to overcome the classical charging en-
ergy E_C in order to induce transport, given
by

$$E_C = \frac{Q^2}{2C_\Sigma} \tag{2.1}$$

Figure 2.4: (a) Schematic circuit diagram of a sin-
gle electron transistor. The nano-dot is visualized
as a golden sphere and is capacitively contacted by
source, drain, and gate. (b) Conductance of an
Al-Al$_2$O$_3$ SET as a function of gate voltage, mea-
sured at 30 mK. Coulomb oscillations are shown for
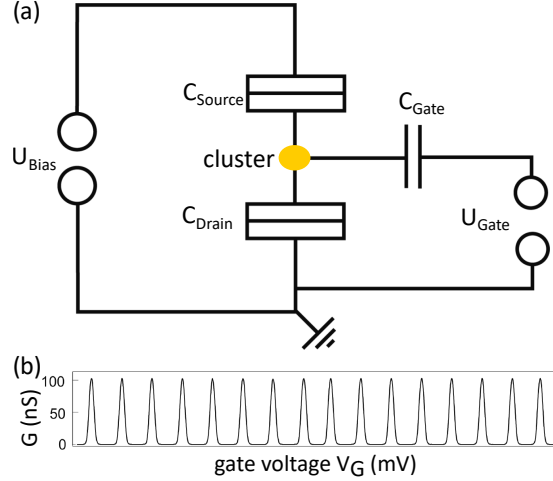$U_B = 10\ \mu$V. Adapted from ref. 55.

where $C_\Sigma = C_S + C_D$ is the self-capacitance of the cluster and $Q = ne$ is an integer value of the
electron charge e. There is thus an initial energy difference $e^2/(2C_\Sigma)$ that needs to be overcome
to change the total amount of electrons n on the cluster by one. This charging energy acts
as an energy barrier for electron transport. Just like in a standard field-effect transistor, the
current flow in a SET can be controlled by tuning the gate voltage U_G and the bias voltage U_B.
For $|U_B| < e/C_\Sigma$, one observes periodic conductance peaks as a function of U_G, the so-called
Coulomb oscillations (compare Figure 2.4b for an Al/Al$_2$O$_3$ SET created by lithography). [59]
The peaks occur precisely, when the following condition is fulfilled: [60]

$$e\alpha U_G(n) = \frac{(n - \frac{1}{2})e^2}{C} \tag{2.2}$$

with $\alpha = C_G/C_\Sigma$. In the absence of external charge, this gives $U_G(n) = (e/C_G)(n + \frac{1}{2})$ with a
spacing given by

$$\Delta U_G = \frac{e^2/C_\Sigma}{e\alpha} = \frac{e}{C_G} \tag{2.3}$$

For all other values of U_G, no current flows between source and drain because the energy to
charge the island cannot be overcome. This effect is the so-called Coulomb blockade. At finite

temperatures, a necessary requirement to observe Coulomb blockade is that the charging energy E_C is larger than the thermal energy $k_B T$, so that electrons cannot pass through the cluster by thermal excitation. The island capacitance scales with the inverse radius $1/r$ which means that the charging energy increases when the island shrinks. In order to observe and make use of the Coulomb blockade, sufficiently small islands and low temperatures need to be reached. [61, 62]
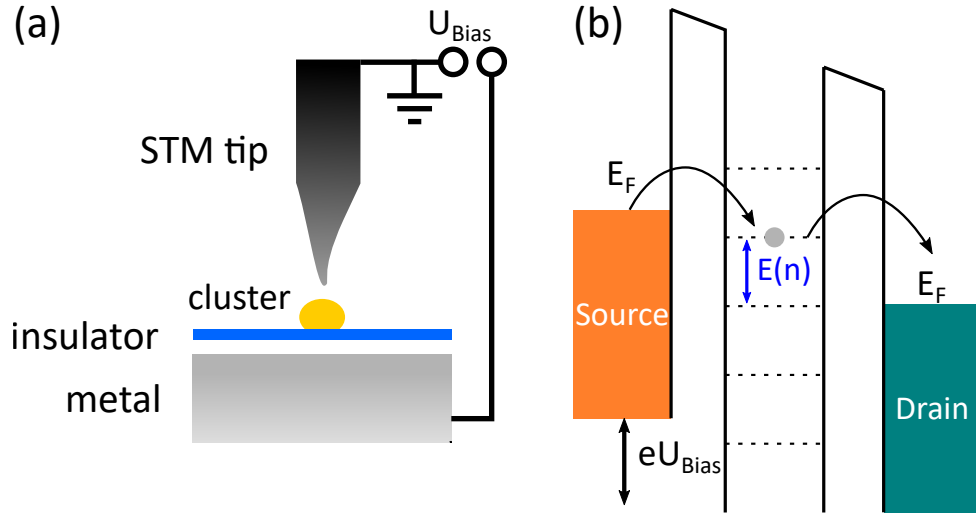
Figure 2.5: (a) Schematic of a Coulomb blockade experiment with an STM. A metallic nanodot resting on a thin insulating sheet is contacted by the STM tip with an applied bias voltage U_{Bias}. (b) Schematic drawing of the single-electron tunneling process through a cluster with adjacent tunneling barriers. The Fermi energies of source and drain electrodes are depicted in orange and blue, respectively. The electronic levels $E(n)$ on the dot are indicated by dashed lines, see text.

In addition to the Coulomb blockade and the Coulomb oscillations, the double barrier tunneling junction causes another effect: the Coulomb staircase. A typical method to probe Coulomb blockade and Coulomb staircase effects in small clusters is the STM, illustrated in Figure 2.5a. The two tunneling junctions emerge between tip and cluster, and between cluster and metal substrate. Typically, cluster and substrate are separated by a thin insulating film or by ligand molecules. In this setup, no gate voltage is applied. The residual charge on the cluster is therefore unknown. The spatial resolution of the STM allows one to measure the local electronic structure of individual clusters by approaching the STM tip above it and measuring $I(V)$ curves. A schematic drawing of tunneling through the cluster is shown in Figure 2.5b. The Fermi level of the source (in this case the sample) can be tuned by U_{Bias} and controls the tunneling current and direction. As we have seen, the electronic levels on the cluster $E(n)$ are quantized by units of e^2/C and therefore appear as steps in the $I(V)$ curves, where the n-th step corresponds to tunneling by n electrons through the island at a time. In the example depicted in Figure 2.5b, one level is available for tunneling. Increasing the bias eventually enables tunneling through more states when eU_{Bias} surpasses the necessary energy $E(n = 2,3,..)$. This phenomenon is the Coulomb staircase. [63]

The Coulomb blockade is related to the quantization of charge by units of e. The theoretical aspects of the Coulomb blockade were studied in depth by several authors. [61, 62, 64–66] In a real quantum dot, such as a small cluster or a single molecule, the electronic level spacing is not necessarily regularly spaced. As we have seen, the electronic structure of a metallic cluster can be quite complicated and depends on structure and size, leading to an internal level spacing ΔE. It was shown by Beenakker, that for $e^2/C > \Delta E$ the charging energy regulates the observed spacing. Furthermore, the level spacing, peak amplitude and line shape were theoretically described. [65] Coulomb blockade was observed on ligand-stabilized clusters [67–70], semiconductor nano-wires, [71–73], embedded islands, [74, 75] cluster arrays, [76] free clusters, [31, 77–79] and single C_{60} molecules [80] (for a recent review on the topic, we refer to the article by Thijssen [81]). Regularly spaced colloids have been used to build a SET operating at room temperature, promising for the reduction of power consumption and device miniaturization. [82]

Heterogeneous Catalysis

Perhaps the most prominent use of supported metal clusters is found in the field of heterogeneous catalysis – we have alluded before the enormous economic potential which has been constantly growing in recent history. [3] Heterogeneous catalysis is a surface chemical process which can be generally described as a lowering of the kinetic barrier of a chemical reaction in the presence of a catalyst which is often a transition metal. [83] Due to their substantial surface-to-bulk ratio, the catalytic activity per volume and per time increases when the same amount of material is dispersed in the form of clusters when compared to a bulk. [84, 85] Historically, catalysis has been studied mostly in two ways. [86–88] In applied catalysis, a catalyst (usually clusters on a porous support) is prepared and measured under harsh reaction conditions to obtain and optimize turnover frequencies and chemical selectivity of a specific reaction. Due to the complexity of these systems, their characterization and understanding is challenging. A more recent approach stemming from the surface science community is the use of model catalysts which can be precisely characterized and lead to a knowledge-driven approach. These may be single crystal surfaces or supported metal clusters, which we will focus on here. [89]

On a first note, the amount of review articles and book chapters on the topic is remarkable – we refer to references $42, 84, 86, 87, 91, 92$ for early reviews of general properties on supported clusters in catalysis, to references $14, 16, 93–95$ for progress during the last decade and to $96, 97$ for reviews focusing solely on mass selected clusters. Within the community, two main methods of fundamental studies on cluster catalysis have been established. (1) Soft-landing of a beam of mass-selected clusters onto an inert substrate, and (2) (templated) growth on a substrate either in UHV or by chemical deposition. [86] The outstanding advantage of method (1) is the precise control of the individual clusters. It allows the structure sensitive determination of catalytic processes and enables direct comparison between theory and experiment. [98, 99] This way, the CO oxidation over Pt clusters [100] or the cyclotrimerization of acetylene over Pd clusters [101]
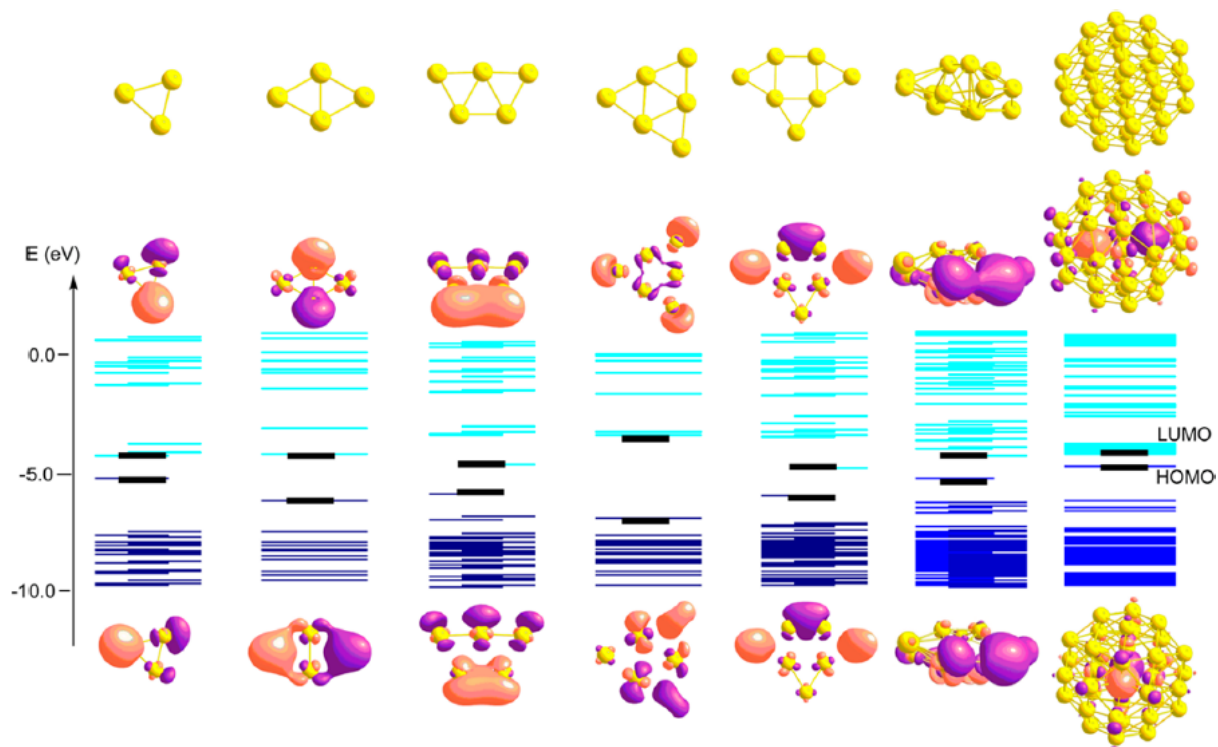
Figure 2.6: Calculated electronic structures of differently sized, free Au clusters. From top to bottom: optimized structure, calculated isosurfaces of the LUMO, molecular orbital structure of occupied and unoccupied states and isosurface of the HOMO. From left to right: Au_3, Au_4, Au_5, Au_6, Au_7, Au_{13}, and Au_{38}. Adapted from ref. 90.

could be investigated with atomic precision. It provides an excellent tool to study the non-scalable regime where size effects have a substantial influence on the surface chemistry. [30, 102] Method (2) on the other hand generally yields a much higher density of nanoparticles, closer to an industrial catalyst. [22, 86, 88] UHV preparation methods allow a clean preparation and *in situ* investigation of catalytic reactions with averaging techniques. [14, 88]

We have already seen, that the precise cluster shape and environment greatly affect its electronic structure. Thus, size, [103, 104] shape, [28, 90, 105] and support effects [42, 106] play an enormous role in the study of supported model catalysts. An example is given in Figure 2.6 for Au clusters which have been a hot topic ever since the surprising activity of very small Au clusters for CO oxidation was demonstrated. [23, 29, 31, 107–110] It presents DFT calculations conducted on free Au_3-Au_{38} clusters showing the relaxed free structure models, the electronic orbitals and their spatial extent. [90] Au clusters are special in that they are preferentially flat for a cluster size of 7 atoms or less. For those sizes, the calculated isosurfaces of HOMO and LUMO protrude substantially from the cluster which makes them accessible to gas adsorbates. Larger clusters however grow in three dimensions [111] and surface coordination increases. By that, the frontier orbital composition changes and thereby the interaction with molecules. From

this model, it becomes clear that cluster size and structure play vital roles in their chemical selectivity and activity. [90]

Magnetism

On a final note, we want to address the study of cluster magnetism. Besides the obvious interest of fundamental research on magnetism in the domain of quantum effects, magnetic clusters were historically promising to increase the bit density in magnetic hard disks [112,113] (for reviews on the topic, we refer to refs. 4,48). Early studies with clusters in the free beam revealed magnetism in Stern-Gerlach type experiments for non-magnetic elements such as Rh, [114–116] V, [117] Pd, [118] and Mn, [119–121] which displayed considerable size effects. Small particles of bulk ferromagnets exhibit superparamagnetic behavior with a drastically increased magnetic moment. [122] For particles on a support, additionally the cluster-substrate interaction needs to be taken into consideration. [123] Magnetic clusters need to be uniaxial and the distribution of their magnetic moments and magnetic anisotropy energies should preferably be small. That is why for magnetic storage, ordered lattices of clusters are preferred over random arrangements, [124] which could be realized on reconstructed metal surfaces, [124] strain relief patterns, [125], moiré patterns, [126–128], or embedded in polymer matrices. [129] Regular arrangement of clusters additionally enable the investigation with averaging techniques such as XAS or magneto-optical Kerr effect. A notable finding was the observation of magnetic hysteresis in Dy single atoms on Gr/Ir(1 1 1). [128] The same authors also studied the magnetic response of Nd, Tb, Ho, and Er atoms on Gr/Ir(1 1 1). [130] Considerable attention was also attracted by nanoparticles of FePt in the $L1_0$ phase because of their enormous uniaxial magnetocrystalline anisotropy [113, 131] and the potential for magnetic recording or as permanent magnets. [132, 133] Sun *et al.* were the first to synthesize ordered superlattices of such clusters with wet chemical methods [13] and to measure their crystallinity. [134] Their magnetism was confirmed in following studies. [135,136] Because the formation of the $L1_0$ phase requires a sensitive Fe/Pt composition of about 50/50 and annealing to around 500 °C, [137] they are often embedded in a matrix to prevent coalescence. [135, 138–140] However, magnetically aligned arrays of FePt nanoparticles in the $L1_0$ phase have not yet been synthesized.

2.2 Preparation Methods

In the following section, we will review possible routes to produce metal clusters on a substrate. As each individual application has different challenges and needs, a multitude of pathways for sample preparation have been explored.

Wet-Chemistry Methods

Historically, the synthesis of nanoparticles in solution and their subsequent deposition onto a solid substrate was the first method to produce supported nanoparticles. Conventional catalysts were and are still fabricated this way. This practically happens by deposition of a metal in solution onto a porous, inert support, *e.g.* by precipitation. The process is then followed by drying, calcination, and reduction. [16, 84, 141] For transition metal clusters, there are plenty of precursors such as metal carbonyls, salts or organic metal complexes. [142, 143] Common supports are refractory oxides (such as SiO_2, Al_2O_3, TiO_2), zeolites, and amorphous carbon. [141] All of these offer chemical inertness, porosity, and thermal stability. A common trade-off is the weak interaction between precursors and supports, leading to aggregation after activation of the catalyst by ligand removal. The resulting zero-valent metal clusters often have a random distribution of sizes and shapes, and are non-uniformly dispersed. This makes them not only hard to characterize but also usually leads to a low chemical selectivity. [144, 145] However, methods such as strong electrostatic adsorption have led to highly dispersed clusters, [146] and progress in precursor chemistry allows synthesis of atomically precise nanoparticles. [147–149] The lack of control about the cluster-support system is a downside of many wet-chemical methods. On the other hand, it produces large quantities of supported metal clusters and is highly scalable.

Self-Assembly

Self-assembly is a process, where colloids or other particles arrange themselves into regular structures. While this technically includes the mundane crystallization of solids, we focus here on the self-assembly of clusters into superlattices. For reviews on the subject, we refer to citations 14, 150–154. The general process begins with a colloid or cluster species in solution. Those can be particles of a diameter between $1 - 1000$ nm and may be metals, semiconductors or dielectrics, depending on the application. [153] The clusters in solution are protected by suitable ligand molecules. Self-assembly may be driven by the evaporation or destabilization of the solvent when deposited on solids, [155, 156] but can also happen at liquid-liquid or liquid-gas interfaces. [157, 158] External stimuli such as magnetic or flow fields have been applied successfully to induce self-assembly. [152, 159] By controlling the cluster concentration, ligands, solvent, temperature, and other parameters, one is able to obtain superlattices in one, two and three dimensions. [160–162]

In many examples, self-assembled monolayers of ligands are utilized to control the formation of the network, *e.g.* the well-known example of alkylthiolates for metal clusters such as Au. [163] The functional groups of the ligands can then be tuned to enable cross-linking of the network once it is placed on a substrate. These links serve as stabilizing entities but may also be used as electronic coupling, for example for Coulomb blockade devices. [76, 164] Self-assembled superlattices have been proposed for single-electron transistors and have attracted interest in nano-optics and electronics, [8, 165] as well as catalysis. [166] Semiconductor and metal

nanoparticles in a multitude of shapes and sizes can be prepared in solution and assembled into regular structures, offering a playground for plasmonics. [167, 168] The obtained superlattices are highly regular over several μm^2, and can be produced in a variable size range from 2-100 nm. [151] However, very small clusters of one to a few hundred atoms cannot be assembled so far. Additionally, the attached ligands reduce the catalytic activity of the clusters. [14]

Lithography

Electron-beam lithography is used to create arrays of nanoparticles for nano-optical, [169, 170] nano-electronic, [171] or catalytic [172, 173] applications. It is considered to be a time-consuming and expensive technique but allows the control about size and shape of the particles as well as the geometric arrangement of the array. [8] A standard procedure is to deposit a resist (such as the polymer PMMA) on a substrate, which is chemically altered by the electron beam. This allows removal of the resist where it was exposed to the beam, producing holes where clusters can be adsorbed. The resist can then be chemically dissolved. [92] Within the resolution of the method, any arbitrary structure can be created, which has allowed the study of two isolated paired clusters [174] or the influence of particle spacing in a periodic arrangement on plasmon resonances. [175, 176] Lithography was also envisioned as a route to produce model catalysts. [177] However, the minimum particle sizes created by electron-beam lithography are in the range of tens of nm. [178] Moreover, it is possible to combine self-assembly and lithography to produce well-ordered arrays of clusters. In a process called nanosphere lithography, nanosphere masks are assembled on a surface prior to deposition of metal from the gas phase. [179, 180] Removal of the nanospheres then yields a superlattice of metal clusters. Arrays created by nanosphere lithography have been used *e.g.* for plasmonics and nano-optics. [181, 182]

Cluster Softlanding

Softlanding of size-selected metal clusters onto a substrate is a technique which has emerged at the end of the previous century. The dream to prepare atomically precise model systems for catalytic studies became reality when UHV-compatible cluster sources with a size range of a few to more than 10000 atoms were developed. The procedure typically involves three steps: (i) cluster production by a cluster source, (ii) mass selection, and (iii) controlled deposition onto the desired substrate. An overview about the method is provided in the review articles of references 96, 97, 183, 184. Step (i) is usually performed by evaporating the desired metal. This may happen *e.g.* in a furnace or by local heating with a pulsed laser. An inert carrier gas is used to seed the produced clusters, which is subsequently expanded through a nozzle into UHV. The resulting supersonic expansion cools down the clusters and leads to a narrow kinetic energy distribution. [33] Step (ii) usually involves a time-of-flight or quadrupole mass spectrometer. Mass selection is carried out in the gas phase prior to deposition. This step is necessary because the cluster source produces a wide range of different cluster sizes. Finally, in step (iii) the mass-

selected clusters are deposited onto a substrate. Since the whole purpose of the method is to produce monodisperse clusters on a surface, fragmentation and implantation have to be avoided. Therefore, the kinetic energy of the clusters needs to be $E_{kin} < 1$ eV/atom. [185]

Common substrates used for softlanded clusters are oxides or other inert materials such as Gr or h-BN. [186–188] The atomic control of the cluster size allowed researchers to understand catalytic reactions at the smallest scale, leading to catch-phrases such as 'every atom counts'. [100] Precise modeling with DFT can be compared directly to the experiment. [99, 189] Notable progress was made in the field of low temperature catalysis on Au clusters, where crucial size and charging effects on the CO oxidation turnover were revealed. [102, 190, 191] However, when clusters agglomerate, *e.g.* by Smoluchowski or Ostwald ripening (see chapter 3), the selectivity of the process is lost. Thus, the density of the deposited clusters and their mobility on the surface need to be sufficiently low. Nevertheless, combined TPD/TPR studies with local probes such as STM or TEM have been proven successful for the study of size-selected clusters. [184]

Molecular Beam Growth

Another preparation method based on gas phase deposition is cluster growth in UHV by the use of molecular beams. Molecular beam epitaxy (MBE) was extensively studied for the growth of thin films. [22] In contrast to softlanding of size-selected clusters, the assembly of supported metal clusters from deposited adatoms on a (single crystal) surface suffers from its statistical nature. Thermally activated motion of arriving adatoms on a surface inherits a Brownian character and the growth of clusters on the surface is described by the laws of nucleation. The statistics and therefore the size distribution of the clusters are controlled by deposition flux and sample temperature. In order to tailor cluster size and arrangement, one needs to introduce some sort of anisotropy in the substrate. [125] Early works were performed with epitaxial growth on metal surfaces, *e.g.* on the $(1\,1\,0)$ surfaces of fcc metals. Deposition of Cu on Pd$(1\,1\,0)$ yielded chains of metal atoms in the troughs in $\langle 1\,\bar{1}\,0 \rangle$-directions. [192]

A different form of substrate are dislocation networks and moiré patterns. A prominent example of the former is the Au$(1\,1\,1)$ $22 \times \sqrt{3}$ herringbone reconstruction. It emerges as a consequence of isotropic strain relief in the topmost Au layers. Ni deposition on Au$(1\,1\,1)$ leads to cluster formation in a periodic pattern, with clusters sitting at the elbows of the reconstruction. [193] On unreconstructed surfaces, one can induce dislocation networks by growing strained thin films on top of single crystals. Fe clusters could be grown in a hexagonal array on a (13×13) reconstructed Cu bilayer on Pt$(1\,1\,1)$. [194] On a similar note, vicinal Au$(7\,8\,8)$ have been utilized to grow regularly spaced Co clusters on them. [124] Using a substrate with a periodic modulation of the potential energy to create regular cluster arrays is called templated cluster growth and we will explore this method in detail in the upcoming section 2.3.

On a final note, because of the strong metal-metal interaction of the clusters with these substrates and the presence of the highly reactive metal surface, such systems are unfeasible

for catalytic studies. Thus, MBE has been applied to grow metal clusters on oxide supports as well. [42, 186] An example is the nucleation of Pd clusters on MgO(1 0 0), which, under the right growth conditions, leads to a dense arrangement of particles. [195] The MBE growth of Au clusters on TiO$_2$(1 1 0) has been studied in quite some detail during the 'gold rush'. [38, 109] For a recent perspective on clusters supported on thin oxide films we refer to article 196.

2.3 Templated Growth of Cluster Superlattices

We have seen in the previous section that the ideal cluster support hosts clusters of identical size, shape, and chemical environment in a periodic array. The support is preferably inert and interacts weakly with the clusters so that their properties can be effectively studied. In order to act as a template, it needs to fulfill certain requirements: some sites on the surface need to act as traps, anchoring arriving adsorbants. At the same time, the adsorbants need to be able to arrive at these sites by diffusion. Thus, a periodic modulation of the potential energy landscape needs to be present on the surface. This can be realized for example by the topology, by a regular difference in chemical composition, or by the presence of periodic defects. [197] The flux of deposition and the sample temperature then serve as levers to control the size distribution of the obtained clusters. It is centered around an average cluster size s_{av} or $\bar{s}$. Furthermore, cluster sizes are commonly denoted as M$_{\bar{s}}$ (M is the cluster element and $\bar{s} = s_{av}$ the average cluster size in atoms). The density of clusters is often given as the cluster number density n, which is the number of clusters divided by the amount of available adsorption sites. The size distribution of cluster sizes s is generally close to a Poisson distribution, described by the formula Poi$_{\bar{s}}(s) = \frac{s_{av}}{s!}e^{-s}$. It assumes that there is a constant flux of atoms onto the sample and that atoms do not diffuse into neighboring cells, leading to growth of exactly one cluster per unit cell. [198, 199]

The alumina double layer on Ni$_3$Al(1 1 1) was found to produce highly ordered metal cluster superlattices after straightforward atomic vapor deposition [200] and fueled the research in the community. With the emergence of graphene in the 2000s, a lot of effort was dedicated to studying the properties and growth of 2D materials. The graphene moiré on metal single crystal surfaces such as Ir(1 1 1), Rh(1 1 1) and Ru(0 0 0 1) provides a periodic modulation in the potential energy [201] which, as we will see, can be used as a template to form highly ordered cluster superlattices. Templated growth is another way to bridge the 'materials gap' of catalysis – the gap between a well understood single crystal and a complicated system that is a commercial catalyst. It produces highly dispersed samples, close to a real world catalyst, which can be analyzed with surface science methods. [88] While it does not provide the atomic precision of cluster deposition by softlanding, it poses fewer experimental demands to the researcher, is less time consuming than electron lithography, and offers a high degree of cleanliness as it takes place under UHV conditions. We will introduce a few substrates which can be used for templated

cluster growth in the following. In addition, the inclined reader is referred to the excellent reviews by Becker, Henry, and others. [14, 88, 197, 202, 203]

2.3.1 Al$_2$O$_3$/Ni$_3$Al(111)
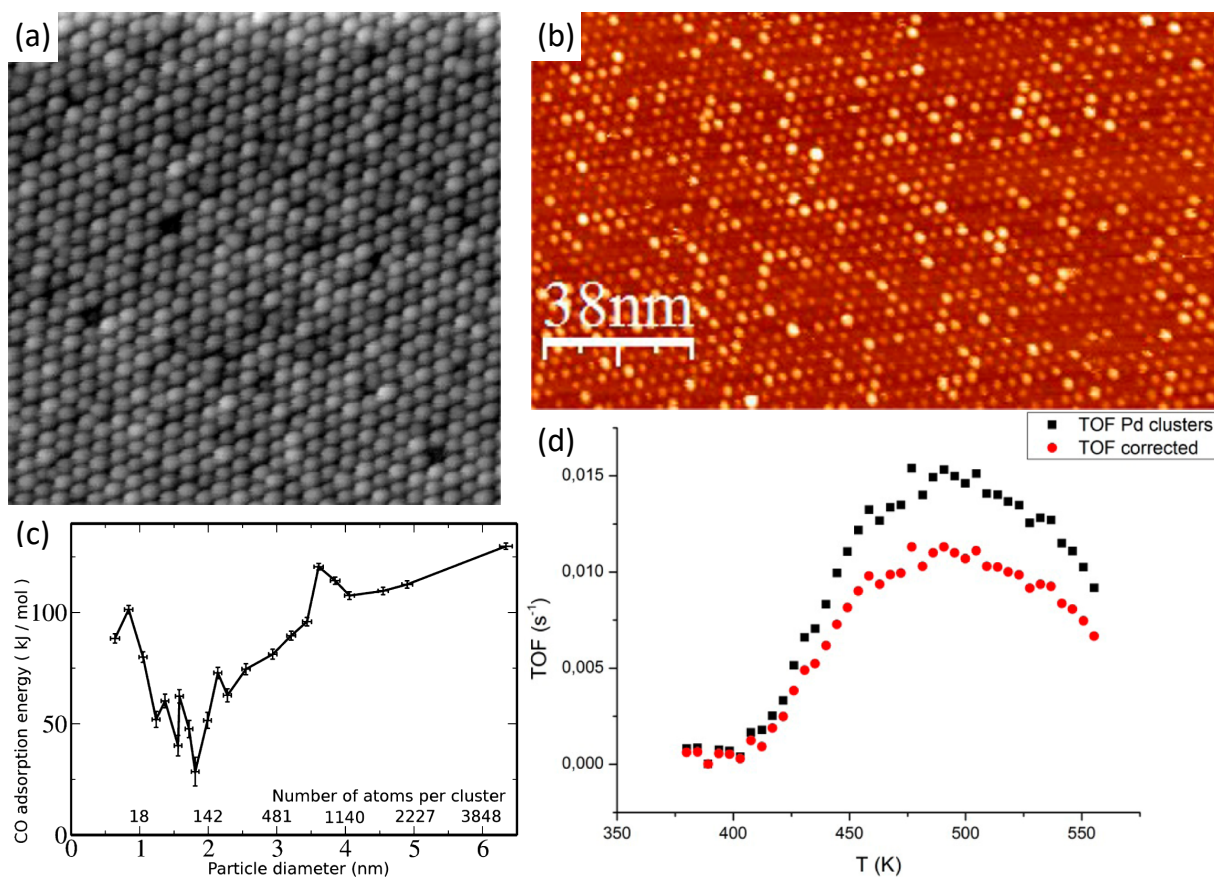
Figure 2.7: (a) Pd cluster superlattice with $n \approx 1$ on Al$_2$O$_3$/Ni$_3$Al(1 1 1). Image size is 108 nm× 108nm, adapted from ref. 204. (b) Pd$_{\overline{35}}$ cluster superlattice on Al$_2$O$_3$/Ni$_3$Al(1 1 1) after deposition of $\theta = 0.15$ ML Pd at 300 K and subsequent annealing at 470 K. Adapted from ref. 205. (c) CO adsorption energy as a function of cluster size measured on Pd cluster superlattices on Al$_2$O$_3$/Ni$_3$Al(1 1 1). Adapted from ref. 206. (d) Turnover frequency (TOF) for CO oxidation over Pd$_{\overline{181}}$ clusters on Al$_2$O$_3$/Ni$_3$Al(1 1 1) as a function of substrate temperature for $p_{CO} = 6.8 \times 10^{-8}$ mbar and $p_{O_2} = 5 \times 10^{-8}$ mbar (black squares). Red dots are the same data corrected for reverse spillover. Adapted from ref. 205.

Ultrathin films of Al$_2$O$_3$ on NiAl(1 1 0) were among the first intensively studied supports for clusters, but do not act as templates for cluster arrays. [42, 207] Al$_2$O$_3$ layers on Ni$_3$Al(1 1 1) however are inherently nanostructured and were first shown in 2001 to form highly ordered superlattices of Ag, Au, Cu, Mn and V clusters. [200, 208] The superlattices are prepared by high-temperature oxidation of the clean Ni$_3$Al(1 1 1) surface and subsequent metal deposition. Two coexisting alumina superstructures are observed in STM, commonly called 'dot' (4.5 nm

periodicity) and 'network' (2.6 nm periodicity) structure. [209–211] Depending on the cluster material, nucleation of the clusters may take place in one or the other structural node. [212] For example, Ag deposited at 300 K preferentially grows on the dot structure, while Mn nucleates on the nodes of the network structure. Mild annealing at 600 K is sufficient to move the clusters to the more stable site, which is the dot node. [200] The range of cluster materials templated by $Al_2O_3/Ni_3Al(1\,1\,1)$ was later extended to Co, [213] Fe, [213–215] Pd, [204–206, 216, 217] and recently Pt. [218] However, good ordering and a cluster number density close to $n = 1$ was only achieved for Pd, and V clusters, which is explained by the high cohesive energy of these metals. [14] An example is given in Figures 2.7a and b, which display STM topographs of Pd cluster superlattices on $Al_2O_3/Ni_3Al(1\,1\,1)$. Seeding was applied to create bimetallic arrays, for example of AuPd [219, 220] clusters. Subsequentely deposited Au atoms bind stronger to the Pd seeds, which significantly increases n. Pd-seeded Ni and Co clusters were further oxidized to form oxide clusters, which are a relatively new class of cluster materials. [221, 222] In addition, individual Pd atoms trapped in the corner holes of the oxide were reported to act as nucleation sites of Fe and Co clusters, significantly improving their order. [223]

An important characteristic of a cluster superlattice in view of applications is its stability under reaction conditions, *i.e.* high temperature and ambient pressure. Therefore, UHV heating experiments have been established to monitor the degradation of the clusters *in situ*. For Pd, V and Mn clusters, the lattice is perfectly stable until 600 K. [14] On the other hand, Fe arrays have generally worse ordering and less filling ($n \ll 1$), and are stable only up to 350 K. [214]

Cluster arrays on $Al_2O_3/Ni_3Al(1\,1\,1)$ have been used to study inherent cluster properties. An example is the study of CO adsorption on Pd clusters as a function of average cluster size by Sitja *et al.* [206], which beautifully validates supported cluster arrays as functioning model catalysts. As depicted in Figure 2.7c, even with the distribution of cluster sizes produced by the templated cluster growth, one is able to distinguish between the scalable and non-scalable regimes of cluster sizes. The CO adsorption energy asymptotically trends towards the bulk value of 138.2 kJ/mol [224] for clusters with $s_{av} > 150$ atoms. Smaller clusters exhibit substantial variations in the CO adsorption energies, consistent with mass-selected clusters. [206] Furthermore, the turnover of CO into CO_2 in the presence of oxygen has been investigated (see Figure 2.7d), confirming that such Pd cluster arrays are catalytically active for CO oxidation. [205] The reverse spillover effect, which is the (often unwanted) diffusion of compounds from the substrate to the clusters, [225] could be investigated for CO molecules. The true turnover frequency of CO oxidation over Pd cluster arrays is given as the red dots in Figure 2.7d, while the uncorrected values are the black squares. XAS and XMCD measurements of cluster superlattices of Fe and Co on $Al_2O_3/Ni_3Al(1\,1\,1)$ have revealed no exchange or dipolar coupling between clusters and Ni_3Al substrate, indicating the strong electronic decoupling of the thin alumina film. [213] In addition, the magnetic anisotropy energies and magnetization curves could be obtained.

2.3.2 Graphene Moirés
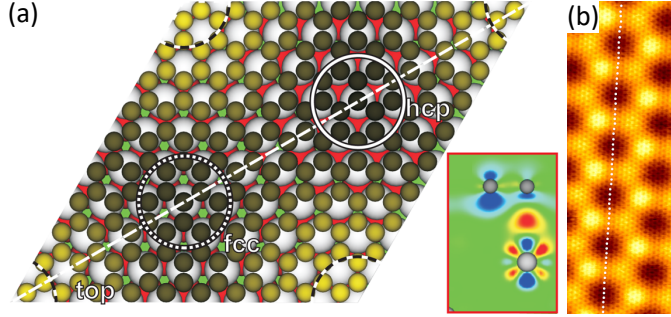
Figure 2.8: (a) Relaxed DFT unit cell of the Gr/Ir($1\,1\,1$) moiré. High-symmetry regions are marked by circles. The color scale indicates the height of C atoms relative to the Ir($1\,1\,1$) plane from 3.2 Å (dark) to 3.65 Å (yellow). The inset shows a side view charge density difference plot of a single Gr unit cell in the hcp region. The color scale reaches from $-0.0138\frac{e}{Å^3}$ (blue) to $0.018\frac{e}{Å^3}$ (red). Adapted from ref. 226 (b) STM topograph of Gr/Ir($1\,\bar{1}\,1$)with the top regions imaged as dark contrast. The atomic lattice is visible. Image size (154 Å × 54 Å). Adapted from ref. 227

Graphene, being a single sheet of graphite, is the most prominent example of the family of 2D materials. Its interesting physics are well-known. [228–230] Already in the year 1992, 'single layer graphite' films were obtained *via* the chemical decomposition of ethene on a hot Pt($1\,1\,1$) surface. [231] Due to the lattice mismatch of Gr and Pt($1\,1\,1$), a moiré superstructure emerges. The relatively weak interaction of Gr and Pt($1\,1\,1$) gives rise to the growth of many rotated Gr domains which were observed with STM. With the advent of graphene and other 2D materials in 2004,

graphene growth on metal single crystals was extensively studied.[1] Nowadays, Gr can be grown in high quality on Ni($1\,1\,1$), Pt($1\,1\,1$), Ir($1\,1\,1$), Cu($1\,1\,1$), Rh($1\,1\,1$), Ru($0\,0\,0\,1$), and SiC($0\,0\,0\,1$) (for a comprehensive review see ref. 201). On some of these surfaces, especially Ir($1\,1\,1$), Rh($1\,1\,1$), and Ru($0\,0\,0\,1$), the Gr exhibits moirés with lattice constants of 2-3 nm, depending on the specific Gr-substrate lattice mismatch. Moreover, the mismatch also induces a chemical modulation on the Gr, because the configuration of the C atoms with respect to the substrate continuously changes within one moiré unit cell. This chemical modulation gives rise to a corrugation in the Gr. [227] These superstructures possess a natural undulation in the potential energy landscape for adsorbed species. [226] The nature and strength of this undulation, the corrugation and the electronic structure of the Gr depends on the metal on which it is placed. [234]

In 2006 the potential of Gr/metal moirés for cluster growth was discovered. [198] Graphene and Ir(111) form an incommensurate superstructure with a lattice periodicity of 25.3 Å, where (10.32 × 10.32) Gr unit cells rest on (9.32 × 9.32) Ir surface atoms. [227] A top view of a commensurate approximation of the moiré unit cell, calculated by DFT, is shown in Figure 2.8a. Gr binds stronger to Ir(111) in the fcc and hcp regions, where a C atom lies directly on top of an Ir atom. The charge density difference plot visualizes the bonds between Ir and C atoms in the hcp region. The moiré as it appears in STM is additionally given in Figure 2.8b. Both

---

[1]It is noteworthy, that in the 1980s a relatively unknown group in St. Petersburg have grown graphene on many substrates, were aware of its structure and even intercalated it by metal deposition in UHV [232,233] – it is likely that they grew cluster superlattices as well without ever noticing.

the long range moiré periodicity and the atomic lattice are visible. Notably, at these imaging conditions, the top regions appear as low-lying.

Room temperature deposition of Ir on Gr/Ir(1 1 1) led to a cluster superlattice with $n = 1$ for $Ir_{\overline{5}}$ up to $Ir_{\overline{130}}$ clusters, controlled by the coverage θ. The superlattice periodicity is given by the moiré. For $\theta \geq 1.5$ ML, cluster coalescence occurs which reduces the cluster number density n. The calculated unit cell of an Ir_4 cluster placed in the hcp site of Gr/Ir(1 1 1) is illustrated in Figure 2.9a. The four Ir cluster atoms rest directly on top of C atoms, and the Gr sheet buckles, as visible in the side view. The hcp site is energetically favorable over the fcc and top sites according to DFT. Indeed, as visible from the STM topograph in Figure 2.9b, the top sites, do not pin clusters. [198] Moreover, the DFT calculations revealed sp^3 hybridization of Gr underneath the Ir clusters as the anchoring mechanism. [235] This is only efficiently possible, when a C atom rests directly on top of an Ir surface atom, which explains the nonexistence of clusters in the top region and the poor ordering of clusters in rotated domains. [236] The hcp site was unambiguously identified as the preferred cluster adsorption site, in line with the DFT results. [198]

In a following study, the range of cluster materials which could be efficiently templated was expanded to Pt, W, and Re. [237] Examples are shown in Figures 2.10a-c, where cluster superlattices of $Ir_{\overline{17}}$, $Pt_{\overline{28}}$, and $W_{\overline{33}}$ are depicted. Seeding with Ir enabled bimetallic AuIr, FeIr, and CoIr clusters, [127] but pure Au and Fe are only very poorly templated by Gr/Ir(1 1 1) ($n < 0.5$ for room temperature deposition). [237] The authors also studied the thermal stability of clusters, which is highest – up to 700 K – for Pt and Ir clusters. Deposition at low temperatures reduces the thermal diffusion of adatoms and increases the cluster number density towards unity. For example, deposition at 80-110 K yielded well ordered Sm clusters (see Figure 2.10). [238] It was later demonstrated that careful tuning of the substrate temperature during deposition enables the growth of ordered Dy and Sm single atoms, which, in the case of Dy, act as single atom magnets. [128, 239]

The exceptional ordering of cluster superlattices on Gr/Ir(1 1 1) enables their study with integrating techniques. This was impressively demonstrated by Franz *et al.* by means of surface x-ray diffraction and x-ray standing waves for Ir and Pt cluster superlattices. [240, 241] Average lattice parameter, compressive strain, and reversible structure transformation upon CO adsorption and desorption could be obtained. This finding motivated Billinge to compare cluster superlattices on Gr/Ir(1 1 1) to 'nanoparticles served up on a tray'. [242] In addition, CO adsorption and reaction was studied extensively for Ir and Pt cluster superlattices. It was reported that very small $Pt_{\overline{<10}}$ clusters coalesce upon CO dosing, while larger ones are found to change their morphology. [243, 244] The binding of CO to Pt clusters was investigated with STM, photoelectron spectroscopy, *ab initio* simulations, and infrared reflection-absorption spectroscopy. [244, 245] Moreover, CO oxidation was observed on Pt cluster arrays on Gr/Ir(1 1 1), but not on Au. [246] Combined XPS and DFT studies allowed the understanding of cluster
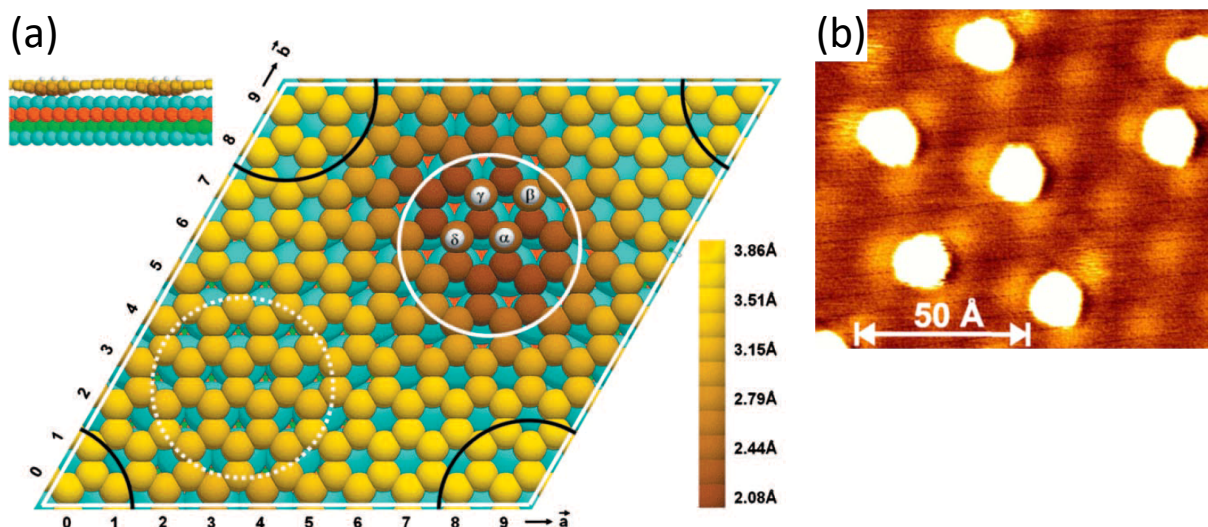
Figure 2.9: (a) Relaxed DFT unit cell showing top view (main image) and side view (small inset) of an Ir_4 cluster in the hcp region of the Gr/Ir(1 1 1) moiré. The Gr atoms are color coded from brown to yellow, indicating the relative height to the first Ir(1 1 1) surface plane. Ir cluster atoms are depicted in silver, first layer Ir surface atoms in cyan. Adapted from ref. 235. (b) STM topograph of 0.02 ML Ir deposition at 350 K on Gr/Ir(1 1 1), showing the cluster adsorption site. Top regions are imaged as bright in apparent height. Adapted from ref. 198.

structure and XPS core level shifts for Pt [247] and Rh [248] clusters. Moreover, the periodic arrangement of the clusters allows one to precisely address it with local probes. Manipulation of the clusters was performed under controlled conditions by Martínez and co-workers to produce nanometer-sized structures by 'nano-lithography'. [249]
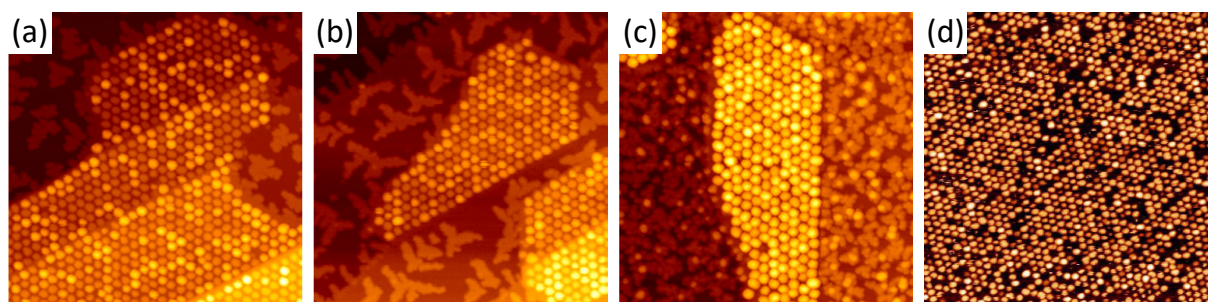
Figure 2.10: STM studies of various cluster superlattices on Gr/Ir(1 1 1). (a) $Ir_{\overline{17}}$ clusters, (b) $Pt_{\overline{22}}$ clusters, (c) $W_{\overline{38}}$ clusters grown at 300 K. Image sizes in all cases (70 nm×70 nm). Adapted from ref. 237. (d) Deposition of 0.08 ML Sm at 110 K. Image size (90 nm×90 nm). Adapted from ref. 238.

Other Gr moirés have also been shown to template cluster superlattices. Donner *et al.* demonstrated ordered Pt cluster arrays on Gr/Ru(0 0 0 1) with $n = 1$ at a deposition temperature of 145 K. [250] Notably, due to the stronger Gr-substrate interaction, Gr/Ru(0 0 0 1) is significantly more corrugated (1-1.2 Å [234, 251–253]) than Gr/Ir(1 1 1). Naively, one could expect the larger

corrugation to result in better ordering of cluster lattices, due to the larger diffusion barrier. However, combined theoretical and experimental studies revealed that cluster adsorption does not induce pinning of the Gr to the Ru surface, because the Gr is already substantially hybridizing with the Ru surface without a cluster. [254, 255] Consequently, the clusters are only weakly bonded. No or only poor ordering was reported for Au, [256–258], Co, [258, 259], Rh, [258] Ru, [260, 261] and Pd deposition [254, 258] at room temperature. It should be noted that it is possible to grow clusters of ceria (CeO_2) [262, 263] and titania (TiO_2) [264] on Gr/Ru(0 0 0 1), but not in an ordered lattice.

A similar case as for the strongly interacting Gr/Ru(0 0 0 1) can be made for Gr/Rh(1 1 1), which features a corrugation of ≈ 1 Å [265, 266]. Pd, [267] Pt, [268] and Ni [269] deposition have not yielded highly ordered cluster superlattices. Nevertheless, clusters on Gr/Rh(1 1 1) have been actively studied with regards to catalytic activity in the group of Papp. [88] For example, the temperature dependent CO adsorption on Pd clusters was studied with temperature-programmed XPS. [270] The authors determined the CO adsorption sites and reported similar behavior to stepped Pd single crystals. As important chemical reactions in heterogeneous catalysis, SO_2 and CO adsorption and oxidation were investigated on Pt and bimetallic PdPt clusters on Gr/Rh(1 1 1). [268, 271–273]

2.3.3 Hexagonal Boron Nitride Moirés

Hexagonal boron nitride is probably the second most known representative of the 2D materials. It is isoelectronic and isostructural to its analog Gr, but consists of B and N atoms. Because of the electronegativity difference of the two elements, the electron density is located at the nitrogen sites which induces the opening of a wide band gap of ≈ 6 eV. [274] Similar methods to Gr synthesis on single crystals have been reported for h-BN, *e.g.* by the dehydrogenation of borazine ($B_3N_3H_6$) and ammonia borane (BH_3NH_3) over Cu(1 1 1), [275, 276] Pt(1 1 1), [277] Ni(1 1 1), [278, 279] Ir(1 1 1), [280, 281] Rh(1 1 1), [282] and Ru(0 0 0 1). [283] Just like its analog Gr, it forms moiré patterns with a varying degree of corrugation dependent on the interaction between the sheet and the single crystal surface. [234, 284] These superstructures provide excellent templates and substrates for molecules and clusters. A comprehensive overview of h-BN/metal growth, structure and templating effects can be found in ref. 285.

Templating growth on h-BN moirés has been less extensively studied than on Gr. The first report with a high degree of ordering is found in 2008 on Co clusters on h-BN/Rh(1 1 1), depicted in Figure 2.11a. [79, 286] Cycles of low-temperature adsorption of a Xe buffer layer, Co deposition, and heating to remove the Xe resulted in the formation of a cluster superlattice with $n = 0.7$ after several cycles. Co clusters are found to adsorb in the low-lying pore regions of the moiré. This complex technique is employed because Co deposition on bare h-BN/Rh(1 1 1) does not result in ordered cluster lattices. Ag, Mn, and Ni clusters have been grown by metal deposition
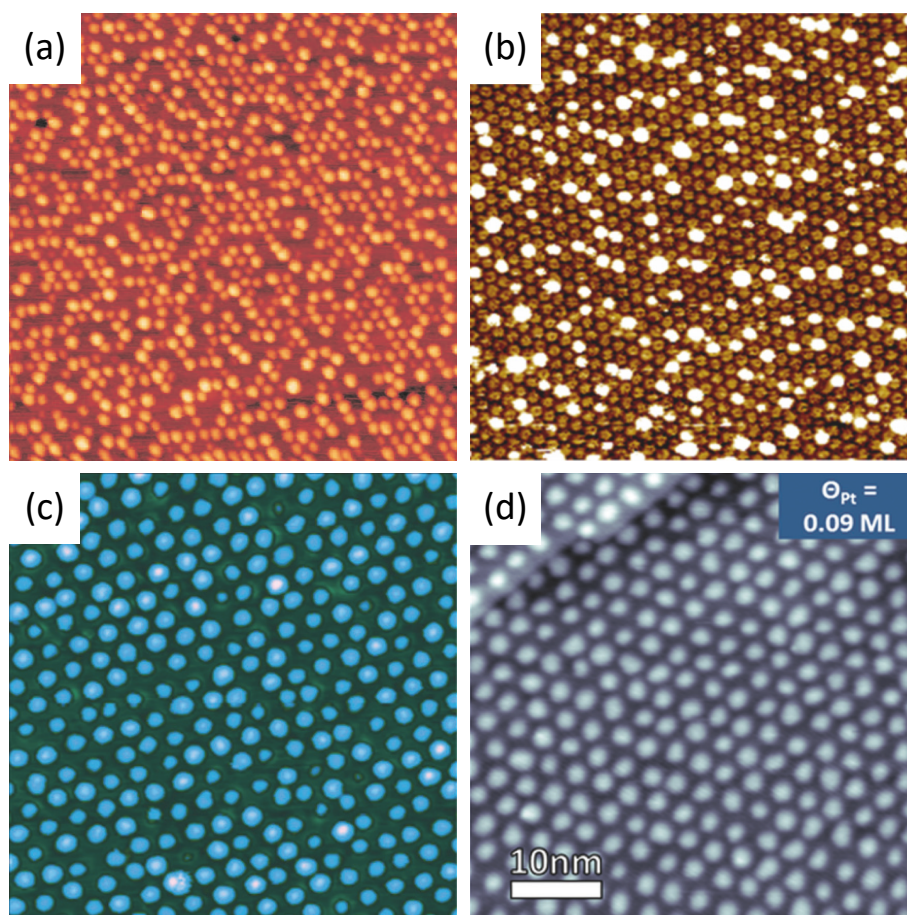
Figure 2.11: STM studies of various cluster superlattices on h-BN/Rh(1 1 1). (a) Co clusters on h-BN/Rh(1 1 1), grown by three cycles of buffer-layer assisted growth (see text). Image size (100 nm×100 nm). Adapted from ref. 286. (b) 0.16 ML Au deposited at 300 K on h-BN/Rh(1 1 1). The moiré pore regions appear as bumps instead of depressions at the given tunneling conditions. Image size (100 nm×100 nm). Adapted from ref. 287. (c) 0.3 ML Ir deposited at 300 K on h-BN/Rh(1 1 1). Image size (50 nm×50 nm). Adapted from ref. 288. (d) $Pt_{\overline{12}}$ grown at 295 K on h-BN/Rh(1 1 1). Image size (50 nm×50 nm). Adapted from ref. 289.

on h-BN/Rh(1 1 1) but showed no regular organization. [287, 290, 291] The interaction of h-BN/Rh(1 1 1) with Au, Pt, Ag, Pd, Cu, and Ni was investigated by means of DFT calculations. It was found that all metals receive negative charge from the substrate and adsorb on the B sites of the pore region. [287] The highest degree of binding was predicted for Au and Pt, which is in line with STM measurements. Au deposition on h-BN/Rh(1 1 1) was specifically studied using DFT, XPS, and STM in several groups, but the cluster arrangement, dispersion, and uniformity is poor (compare Figure 2.11b). [292–295] The same holds true for Au clusters on h-BN/Ru(0 0 0 1). [296] CO adsorption was studied theoretically and experimentally on Au/h-BN/Rh(1 1 1). [297] The authors demonstrated that the CO adsorption strength is heavily influenced by particle size and morphology.

The best result in terms of filling and regularity was achieved after the publication of manuscript

1 [298] of this thesis by Martínez-Galera and co-workers. Ir deposition on h-BN/Rh(1 1 1) yielded a highly ordered cluster superlattice with $n = 1$ for $\theta = 0.3 - 1.8$ ML. [288] This is exemplified for 0.3 ML Ir deposition in Figure 2.11c. The Ir clusters are stable upon annealing to 570 K, and coalesce at higher temperatures. Especially at lower coverages and thus cluster sizes, the clusters bind to several different sites of the pore region of h-BN/Rh(1 1 1), which decreases the degree of ordering. When more atoms are deposited, the overall order approaches a perfect hexagonal lattice. Another example was demonstrated a while later, when Düll *et al.* reported highly ordered cluster superlattices by Pt deposition on h-BN/Rh(1 1 1) (compare Figure 2.11d). [289] Their approach included a deposition gradient on the sample, which was achieved simply by positioning the evaporator laterally displaced with respect to the sample. This method allowed the simultaneous study of many different Pt coverages on a single sample by means of STM and XPS. Pt$_{\overline{12}}$ clusters on h-BN/Rh(1 1 1) are found to be stable to annealing at 400 K.

CHAPTER 3

The Sintering Problem

In this chapter we discuss the principal mechanisms responsible for the degradation of supported clusters. We first give a detailed explanation on four relevant decay mechanisms and then discuss possible prevention measures. Finally, we motivate the research of part II by introducing the concept of a cluster superlattice membrane.

TWO-DIMENSIONAL cluster arrays grown on templates have been established over the last decades as model catalyst systems. In chapter 2 we have introduced the most prominent templates for supported cluster arrays and gave several examples of studies conducted on these systems. The inherent advantages of cluster superlattices are their regularity and uniformity, which persists on a very large scale. The periodic arrangement allows comprehensive investigations of the clusters' physicochemical properties. A crucial problem which hinders wide-spread use of cluster superlattices is degradation of the quality of the superlattice under reaction or ambient conditions. These conditions are typically elevated temperatures (exceeding the growth temperature), and/or increased gas pressure (including exposure to air), as cluster superlattices are typically grown under clean UHV conditions. Moreover, chemical reactions involving certain precursors can irreversibly degrade the cluster superlattices. For example, a common occurrence after reactions involving hydrocarbons are strongly bound carbon compounds which remain on the clusters and block their active sites. Likewise, background gas (which does not participate in any desired catalytic reaction) can readily adsorb on the clusters, hence impairing their catalytic efficiency.

In industrial catalysts, there are additional pathways for catalyst deactivation and degradation. [299] These may include poisoning with reaction contaminants, dusting with fly ash, or even mechanical abrasion. In this chapter however, we focus on the main mechanisms for the decay of cluster superlattices, namely: (1) sintering, (2) intercalation, (3) poisoning, and (4) oxidation. All of these changes are inevitable, but many of them are quite slow (especially under UHV conditions). In addition, most decay mechanisms are irreversible. Thus, more effort has been put into prevention rather than recovery.

3.1 Mechanisms of Cluster Superlattice Degradation

Sintering

Sintering is the loss of surface area of a catalyst by migration-induced particle agglomeration. In non-catalytic terms, it means reduction of the cluster number density of a cluster superlattice, for example by agglomeration of individual entities. It is the prevalent degradation mechanism of cluster superlattices and inherently irreversible, thus crucial to circumvent. Two main modes of cluster sintering have been advanced:

The principal agglomeration mechanism is Smoluchowski ripening, *i.e.* coalescence of two clusters by diffusion of the entire cluster entity. [300] Coalescence is thereby induced by the surface free energy gain when two metal clusters, which come into close vicinity, merge. Because Smoluchowski ripening is consequential to surface diffusion, the key aspect here is the interaction between support and cluster. The cluster size, as well as the cluster material and support have an influence thereon. In most cases, Smoluchowski ripening is thermally driven and has been observed *in situ* with electron and scanning probe microscopy. [31, 237, 301] It was theoretically described by Granqvist and Buhrman for supported clusters. [302]

In reality, the binding strength of an individual cluster to the substrate depends on its exact structure and size. Smaller particles tend be more mobile than larger ones, which leads to an asymmetrical particle size distribution, slanted towards larger particle sizes. [302] In addition, the increased mobility of small clusters leads to a higher sintering probability compared to larger ones. Consequently, the particle size distribution has a sharp cutoff at a critical cluster size and the cluster number density decreases once Smoluchowski ripening sets in. Individual coalescence events of small clusters happen on a time scale much faster than the diffusion. Thus, Smoluchowski ripening is usually rate-limited by diffusion for model catalyst systems. [303]

The other important cluster ripening mechanism is Ostwald ripening, that is shrinkage of smaller clusters at the expense of larger ones by single-atom detachment and diffusion. [304] Ostwald ripening becomes more likely when the detachment energy is small compared to the diffusion activation energy of a cluster. The process is a consequence of two things: the chemical potential difference between the surface atoms of small and large clusters, and the curvature dependence of the effective vapor pressure due to the Gibbs-Thomson effect. Small particles have a larger effective vapor pressure than bigger ones, which leads to a flow of material from small to large particles. Ostwald ripening is described by the Lifshitz-Slyozov-Wagner theory, which produces a particle size distribution with a tail towards small cluster sizes. [305–308] The cluster number density does not immediately decrease at the onset of Ostwald ripening, because even though small clusters shrink, they do not immediately disappear. The occurrence of Ostwald ripening has been reported in both TEM and STM studies. [187, 309–311]

In the catalysis community there is an ongoing debate on which of the two mechanisms is applicable to any given system. [94, 299, 311] To disentangle the two mechanisms, size- and

support-dependent studies were carried out on oxide-supported metal clusters. [312, 313] It is not uncommon, that the two mechanisms transition from one into the other, [314] or occur at the same time. [299] An example is provided in the work of Datye *et al.*, who investigated Pd clusters on a Al_2O_3 support with TEM. [301] They specifically tuned the sintering conditions so that Smoluchowski or Ostwald ripening would preferentially occur and observed the particles *in situ*. They concluded that for oxide-supported catalysts, the size distribution does not unambiguously allow the deduction of the ripening mode.

On the other hand, mass-selected supported clusters provide an excellent framework to study sintering on a given support. This was systematically done for example for Pt clusters on SiO_2 and Si_3N_4 [188]. The authors were able to show that size selection with an accuracy down to the single atom effectively suppresses Ostwald ripening when identically sized Pt_{68} clusters are deposited on a substrate. For bimodal Pt_{22} and Pt_{68} clusters, significant Ostwald ripening is observed. Size-selected Pd clusters deposited on $Gr/Rh(1\,1\,1)$, $Gr/Ru(0\,0\,0\,1)$, $h\text{-}BN/Rh(1\,1\,1)$, and bare $Rh(1\,1\,1)$ allowed the disentangling of Ostwald and Smoluchowski ripening by means of STM and DFT. [187] It was found, that on bare and h-BN-covered $Rh(1\,1\,1)$, clusters exclusively sinter by Ostwald ripening, while for the Gr-covered substrates, Smoluchowski ripening was prevalent up to 600 K. This is related to the differences in cluster-substrate adsorption strength.

Cluster superlattices on Gr and h-BN moirés have been extensively studied with regards to thermally induced sintering. Smoluchowski ripening has been identified as the predominant mechanism for cluster superlattice degradation at temperatures up to as high as 700 K, for example for Ir cluster superlattices on $Gr/Ir(1\,1\,1)$. [237] The clusters fluctuate around their equilibrium position in the moiré unit cell. In order for a cluster to diffuse into the neighboring moiré unit cell, it needs to overcome an activation barrier E_a. The activation barrier depends on the potential energy landscape of the substrate and, for the examplary case of $Gr/Ir(1\,1\,1)$ lies in the order of 0.5 eV. Assuming a single diffusion parameter for the entire superlattice, the temperature T gives an interaction frequency $\nu(T) = \nu_0 e^{-E_a/(k_B T)}$, where ν_0 is an attempt frequency of cluster fluctuations and $k_B T$ is the thermal energy. With this basic model, the authors were able to qualitatively reproduce the evolution of the Ir, Pt, and W cluster number density with temperature. Thermally-induced cluster coalescence has also been observed for Au clusters on $h\text{-}BN/Rh(1\,1\,1)$, [297] and Pd clusters on $Gr/Rh(1\,1\,1)$. [267]

In UHV, Ostwald ripening is exclusively a thermally activated process. Smoluchowski ripening however can also be induced by other factors. Gerber *et al.* studied the interaction of CO with $Pt_{\bar{5}}$-$Pt_{\overline{39}}$ cluster superlattices supported on $Gr/Ir(1\,1\,1)$ with STM, XPS and DFT. [243] They observed considerable CO-induced cluster coalescence at room temperature only for average cluster sizes smaller than ten atoms. The critical CO dose was determined as 1.1 L. Above this threshold, $Pt_{\bar{5}}$ clusters become mobile and merge with other clusters upon encounter. This finding becomes perspicuous when one considers the DFT results. CO adsorption on Pt cluster edge atoms leads to a reversal of the cluster-induced rehybridization of the underlying Gr, thus

weakening the cluster-substrate interaction. [244] For small clusters this effect is strong and induces mobility. For larger clusters however, some CO-free Pt atoms remain hybridized to the Gr and mobility is suppressed. Interestingly, no Smoluchowski ripening was observed for H_2 and O_2 dosing, which is explained by the different adsorption behavior of these compounds. [246]

The particle-substrate interaction and the potential energy landscape of the surface are key for the activation of ripening processes. When the interaction is too small, even large clusters may diffuse and coalesce, which reduces the cluster number density. A method to arbitrarily alter the strength of this interaction was demonstrated by intercalation of the Gr/Ir(1 1 1) interface with oxygen. O_2 readily intercalates at slightly elevated temperatures around 400 K to the Gr/Ir(1 1 1) interface, through edges or surface defects. [315] The intercalated oxygen forms a p(2 × 1)-O structure, which binds to the Ir surface atoms and interacts only weakly with the Gr. Consequently, the Gr-Ir(1 1 1) bonds are weakened and the Gr is decoupled from the Ir surface. [316] This entails suppression of Gr hybridization with adsorbed clusters, and leads to consequential coalescence *via* Smoluchowski ripening. Moreover, metal deposition on O-intercalated Gr does not yield a cluster lattice for the same reason. In similar fashion, CO and H_2 intercalation below Gr/Ir(1 1 1) inhibits formation of a cluster superlattice and induces Smoluchowski ripening. [317, 318]

We want to emphasize here the importance of the size-dependency of Smoluchowski ripening for templated cluster growth by MBE. In order to form a perfect cluster superlattice, one needs to find a balance between diffusion and sticking of adsorbed metal atoms. For cluster-substrate combinations with too small of a potential energy barrier between two adjacent adsorption sites, single atoms and even small clusters might diffuse and coalesce before more atoms arrive to form a nucleation seed. This reduces the total cluster number density as is the case *e.g.* for substrates like Gr/Rh(1 1 1) and h-BN/Ru(0 0 0 1). Even for the substrate with the best order and highest density of clusters, Gr/Ir(1 1 1), the mobility of monomers leads to ripening and therefore a cluster number density below unity for very small coverages. [198]

Intercalation

Intercalation is a degradation mechanism specific for cluster superlattices grown on Gr or h-BN moirés. Clusters may penetrate through the 2D material layer and bind to the metal single crystal surface underneath. Due to the cohesive energy of metals, the energy gain by wetting the single crystal surface is huge. In addition, 2D materials do not feature dangling out-of-plane bonds, as they are van-der-Waals materials. In other words, metal-metal adhesion is significantly stronger than metal-2D-material adhesion. Thus, the single-crystal surface provides a huge energy minimum separated by an energy barrier, that is the 2D layer. This energy barrier is typically higher than the activation energy for cluster mobility. Accordingly, intercalation is observed at higher temperatures than the onset of sintering. Nevertheless, it may compete with

Smoluchowski ripening under certain conditions. As intercalation is irreversible, it provides the final decay mechanism of a cluster superlattice on Gr or h-BN.

Intercalation depends on the metal-substrate combination. On some templates, intercalated islands form already at low temperatures, as was observed for Mn clusters on Gr and h-BN/Rh(1 1 1) after annealing to 570 K. [290] In contrast, Pd intercalation on h-BN/Rh(1 1 1) occurs above 750 K. [267] Metal intercalation may be strongly enhanced in the presence of defects, as was reported for Co/h-BN/Rh(1 1 1). [319] Co islands in the vicinity of h-BN defect lines were reported already at room temperature. It is noteworthy, that the precise mechanism for intercalation underneath a 2D layer is not yet understood. Likely causes are defects in the sheet, which were either introduced during growth or formed at the annealing temperature.

Poisoning

Poisoning in heterogeneous catalysis refers to the degradation of the catalyst by a chemisorbed species which blocks catalytically active sites. These species may be reactants, products or impurities from the background pressure. Whether or not a compound acts as a catalyst poison is strongly dependent on the reaction and system under concern. While poisoning is usually reversible, it presents a considerable problem in industrial catalysts as it requires expensive curing cycles. [320] A well-known poisoning mechanism is coking, *i.e.* the strong chemisorption of carbon-containing species on supported metal clusters. [321] It is an unwanted by-product of hydrocarbon-involving reactions. The carbonaceous species, once dehydrogenized, adhere firmly to the metal particles used to catalyze the reaction. Deactivation of size-selected Ni and Pd clusters by ethene hydrogenation on MgO has been investigated in view of optimizing support model catalysts. [99, 322] Moreover, the reaction of ethene with Pt clusters templated on h-BN/Rh(1 1 1) have been recently investigated by means of temperature-programmed XPS. [323] Ethene is initially adsorbed on the Pt clusters at 140 K and its reaction is monitored upon annealing. Deactivation of Pt sites by strongly bound C-species is observed at 450 K.

Oxidation

A prevalent problem in the study of magnetic nanoparticles is oxidation. That is because the naturally ferromagnetic metals Fe, Co, Ni, and alloys thereof, are quite sensitive in air and readily form oxides under ambient conditions. [324] In addition, the smaller the particles are, the easier they are oxidized. [325, 326] Oxidation therefore effectively perturbs and even destroys the magnetic properties of clusters and poses a potential problem for cluster superlattices when they are brought into ambient conditions.

3.2 Preventing Cluster Degradation

Because most supported cluster degradation pathways are irreversible and essentially render the clusters unfeasible as model systems, enhancing their stability and preventing their degradation is imperative. Thus, we present here a few different routes in order to improve cluster stability.

The most obvious way of preventing cluster superlattice decay is the selection of a suitable substrate. We have elaborated in the previous section on the vital role of the cluster-substrate interaction for cluster superlattice formation. Cluster superlattices are inherently unstable because of the large surface free energy gained when clusters coalesce. Therefore, a template needs to provide the right conditions for stable cluster adsorption. We have alluded before in section 2.3.2, that strongly-corrugated substrates like $Gr/Ru(0\,0\,0\,1)$ are not necessarily better templates than weakly-corrugated ones like $Gr/Ir(1\,1\,1)$. Moreover, the thermal stability against cluster sintering on $Gr/Ru(0\,0\,0\,1)$ is worse than on $Gr/Ir(1\,1\,1)$. Notably, the cluster element has a vital influence on the degradation mechanisms: Au and Re clusters sinter and intercalate at much lower temperatures than Pt or Ir on $Gr/Ir(1\,1\,1)$. [237] With the exclusion of the work undertaken in this thesis, the highest stability for $Gr/Ir(1\,1\,1)$ was reported for Ir and Pt clusters (stable up to 400 and 450 K, respectively), [237] Ir clusters on $h\text{-}BN/Rh(1\,1\,1)$ (stable up to 570 K), [288], and V and Pd clusters on $Al_2O_3/Ni_3Al(1\,1\,1)$ (stable up to 650 and 600 K, respectively). [204,208,216] Exceptional stability was reported for Rh clusters on $Gr/Ru(0\,0\,0\,1)$, but at the cost of no periodic cluster arrangement whatsoever. [258] For all of these substrates, sintering *via* Smoluchowski ripening is the prevalent decay mechanism, while intercalation under the Gr and h-BN monolayers sets in at higher onset temperatures. On oxide supports, deliberate defect creation was also reported to improve the cluster stability. [327–330]

Apart from the substrate choice, other measures have been applied to reduce cluster degradation. In a systematic study, radical exposure and their effect on the thermal stability of $Gr/Ir(1\,1\,1)$-supported $Pt_{\overline{35}}$ clusters was investigated. [331] Exposure to radical $O_1^{\bullet}$ leads to only a marginal change of the particle size distribution upon adsorption, even after annealing at 700 K. $D_1^{\bullet}$ (radical deuterium) exposure resulted in a decrease of particle sintering as well. This increase of the cluster thermal stability is found to be caused by radical adsorption to Gr which hinders particle coalescence. For the two cases, the limits of operation are however fundamentally different. $O_1^{\bullet}$ radicals, at temperatures above 700 K, etch the Gr sheet and consequentially allow rapid intercalation of Pt clusters. $D_1^{\bullet}$ on the other hand desorbs from the surface at 700 K and thus reenacts cluster diffusion, leading to Smoluchowski ripening. We have already alluded the exceptional sintering resistance of equi-sized Pt clusters on SiO_2 and Si_3N_4, but soft-landing is not able to produce highly ordered superlattices. [188]

A route commonly applied in catalyst fabrication is embedding of supported metal clusters beneath a thin protective sheet or into an inert and resistive matrix. Atomic layer deposition of aluminum oxide layers on Pd clusters improved the sintering and coking resistance of the particles by a large extent under reaction conditions. [332] Partially embedded Pt_n ($n = 1 - 7$)

clusters on α-Al$_2$O$_3$(0 0 0 1) were found to exhibit reduced sintering and less coking during ethene hydrogenation. [333] The same was found for alumina-embedded Ni clusters in the methane dry-reforming. [334] Stabilization of Au/CeO$_2$ by porous CeO$_2$ embedding proved effective against particle agglomeration, [335] and sintering-resistant Ni clusters could be prepared inside of SiO$_2$ nanotubes. [336] Recently, Düll *et al.* demonstrated the decomposition of ethene to Gr on the surface of Pt clusters supported on h-BN/Rh(1 1 1). The resulting nanographene protects the clusters against gas adsorption. [337]

Embedding has also found wide-spread application in the protection of magnetic nanoparticles against degradation by sintering and oxidation. [325] For some cases, such as the formation of the L1$_0$ phase of FePt clusters, it is even necessary to enable the phase transition in the first place, because it prevents the clusters from sintering. The FePt particles are either separated by ligands, [13] or embedded into oxides before the crucial annealing step. [139, 338] Carbon deposition on FePt clusters on Gr/Ir(1 1 1) enabled L1$_0$ phase formation after annealing at 970 K. [140] Moreover, silica-, yttria- and carbon-coatings have been applied to magnetic clusters to successfully protect them from oxidizing and agglomerating. [339–341]

3.3 Concept of the Fabrication of a Cluster Superlattice Membrane

Many of the previously mentioned studies were conducted with a bottom-up approach: clusters were grown or deposited onto a sample and then the protective coating was applied on top, *e.g.* by atomic layer deposition or molecular beams. For templated growth this has the inherent advantage, that the structural coherency of the cluster superlattice may be conserved. In the following, we will outline an idea to eliminate the sintering problem for supported cluster superlattices entirely. By embedding a 2D cluster array into an inert matrix and then removing it from the Ir(1 1 1) crystal, we aim to form a stable, free-standing material, which is immune to sintering. This novel material is called a cluster superlattice membrane (CSLM).

The concept of CSLMs is schematically illustrated in Figure 3.1. (I) We begin with a thoroughly described cluster superlattice grown on a 2D material moiré. For simplicity we will refer to it as Gr/Ir(1 1 1) in the following. As we have elaborated in section 2.3.2, metal deposition under the right circumstances yields a highly ordered cluster superlattice. (II) In order to stabilize the metal clusters against sintering and oxidation, we embed them with a matrix of a-C. Carbon is supplied in UHV from a sublimation source and simply deposited on top of the preformed superlattice. For this step, it is crucial, that the embedding material adheres first to the clusters and does not impede the structural quality of the superlattice. Moreover, it needs to bind to the Gr so that a stable membrane is formed. We note here, that oxides might also be suitable candidates for the embedding matrix. Already in this step we essentially expect sintering to be completely suppressed because cluster mobility will be substantially limited by the
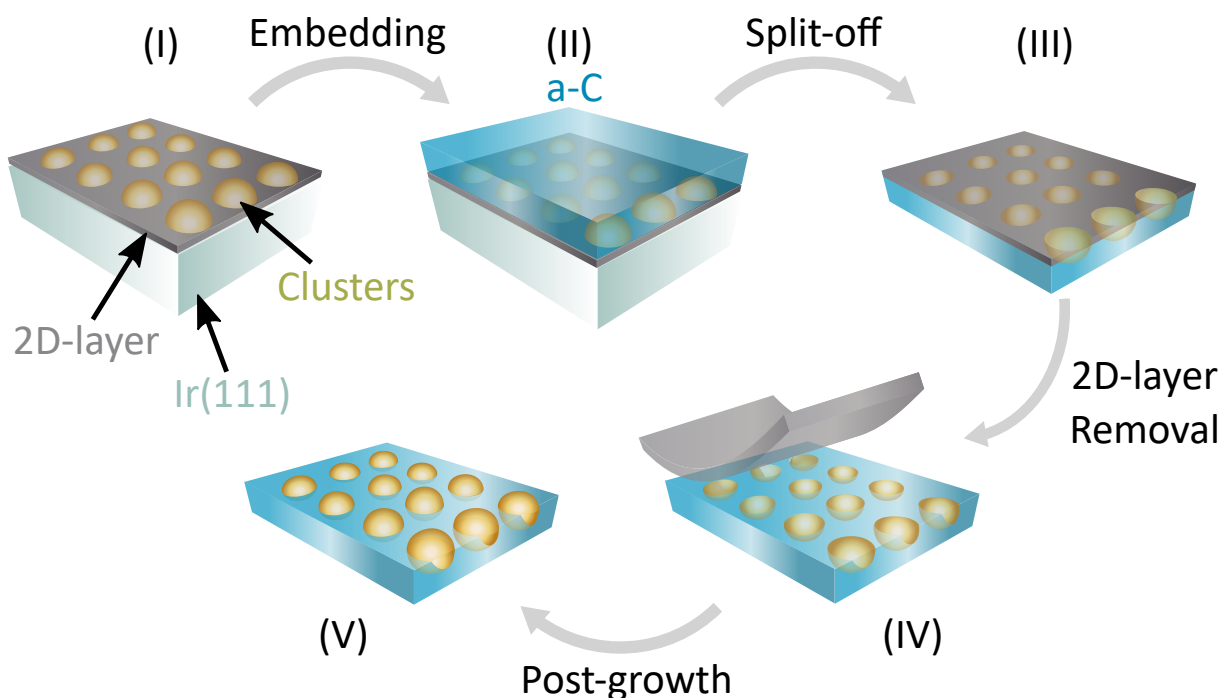
Figure 3.1: Concept for the fabrication of a cluster superlattice membrane. (I) Growth of a cluster superlattice by metal deposition onto a 2D-material/Ir(111) template in UHV; (II) Embedding of the cluster superlattice by deposition of a-C in UHV; (III) Delamination of the membrane at the interface between the 2D layer and Ir(111) with the membrane turned upside down; (IV) Optional removal of the 2D material from the membrane, exposing the clusters directly to the environment; (V) Optional post-growth of the cluster superlattice. The Ir(111) surface is depicted in silver, the 2D material layer in dark gray, the cluster superlattice in brown, and the embedding matrix in blue.

embedding. (III) Underneath the embedding material, the clusters can still escape to the metal surface below, when exposed to high temperatures. In order to prevent intercalation altogether, we split off the entire Gr/cluster/a-C membrane from the single crystal surface. Methods to transfer 2D materials away from metal single crystals onto other substrates are available in the community. [342] For example, Gr/Ir(111) was electrochemically delaminated by the so-called hydrogen bubbling method. [343] During this process, hydrogen bubbles exclusively form at the Gr/Ir(111) interface and leave the membrane intact. The delaminated membrane may then be transferred to the desired substrate. Thereafter, penetration of the cluster material through the Gr at high temperatures is highly unlikely. (IV) As a final step, the Gr side of the membrane will be removed. This way, the clusters are exposed to the environment and the material will become catalytically active. The removal of the 2D layer can be done for example by controlled oxygen etching or plasma treatment. Inside their cavities, the clusters are perfectly stabilized against sintering by Smoluchowski ripening, because of the presumably large energy cost necessary to remove the cluster from its position. (V) Optionally, post-growth with metals or molecules may be conducted on the CSLM to widen the range of applications.

The synthesis of such a membrane would eliminate the sintering problem altogether. Moreover,

inside the cavities of the matrix the clusters are perfectly protected against oxidation until the cover is removed. We want to outline and speculate on a few exciting research possibilites which would arise, if CSLMs were indeed realized.

A magnetic cluster array encapsulated between a-C and a 2D layer would enable further studies in nanomagnetism. For example, magnetic interactions could be studied as a function of cluster size and temperature without ever worrying about lattice degradation. As thermally induced sintering and intercalation have been eliminated, interesting phases such as the FePt $L1_0$ phase may be formed inside the CSLM cavities by growing a Pt-seeded and stoichiometrically correct FePt superlattice. Moreover, optical phenomena and scattering effects may be probed on the embedded clusters. A lattice of conducting particles embedded in an insulating material is interesting in view of Coulomb blockade and single-electron transistors. Electronic hopping phenomena could be studied by transport measurements on CSLMs.

Utilizing CSLMs as model catalysts in heterogenous catalysis requires to open up reactive metal sites for gas adsorption again, which makes removal of the 2D material necessary. Sintering-resistant catalysts in form of CSLMs with the 2D material cover removed are a dream scenario for model catalytic studies. Moreover, CSLMs attempt to bridge the pressure and materials gaps of catalysis – they can be easily handled under ambient conditions and serve as model systems for complex real world catalysts.

Within this context, the work program of this thesis is clear: (i) address the sintering problem of cluster superlattices either by developing and characterizing new systems or by other means, such as the formation of a CSLM. (ii) Bring cluster superlattices one step closer to applications.

PART II

Experimental Results

CHAPTER 4

Manuscript 1: A Monolayer of Hexagonal Boron Nitride on Ir(111) as a Template for Cluster Superlattices

This chapter wholly consists of the above-named manuscript and its supplement, published 19th June 2018 at ACS Nano.

The experiments were proposed by M. Will and T. Michely. All sample growth and measurements was performed at ATHENE by M. Will, with the exception of the C clusters on h-BN/Ir(1 1 1) which were measured by P. Valerius. Experimental guidance was provided by C. Herbig. STM data analysis was carried out by M. Will. DFT calculations were done by V. Caciuc and N. Atodiresei at the Forschungszentrum Jülich. The interpretation of the results was discussed in depth by M. Will, N. Atodiresei, V. Caciuc and T. Michely. All work was supervised by T. Michely.

M. Will wrote the main part of the manuscript and finalized it in close collaboration with T. Michely, with the exception of the analysis of the PDOS calculations, which were formulated by V. Caciuc and N. Atodiresei.

Some of the results shown in this Chapter can be found in the Master's theses of M. Will and P. Valerius.

ARTICLE

A Monolayer of Hexagonal Boron Nitride on Ir(111) as a Template for Cluster Superlattices

Moritz Will,*,† Nicolae Atodiresei,*,‡ Vasile Caciuc,‡ Philipp Valerius,† Charlotte Herbig,† and Thomas Michely†

†II. Physikalisches Institut, Universität zu Köln, Cologne D-50937, Germany

‡Peter Grünberg Institut (PGI-1) and Institute for Advanced Simulation (IAS-1), Forschungszentrum Jülich and JARA, Jülich D-52425, Germany

S *Supporting Information*

ABSTRACT: The moiré of a monolayer of hexagonal boron nitride on Ir(111) is found to be a template for Ir, C, and Au cluster superlattices. Using scanning tunneling microscopy, the cluster structure and epitaxial relation to the substrate, the cluster binding site, the role of defects, as well as the thermal stability of the cluster lattice are investigated. The Ir and C cluster superlattices display a high thermal stability, before they decay by intercalation and Smoluchowski ripening. *Ab initio* calculations explain the extraordinarily strong Ir cluster binding through selective sp³ rehybridization of boron nitride involving B-Ir cluster bonds and a strengthening of the nitrogen bonds to the Ir substrate in a specific, initially only chemisorbed valley area within the moiré.

KEYWORDS: *hexagonal boron nitride, Ir(111), clusters, cluster superlattice, moiré, scanning tunneling microscopy, density functional theory*
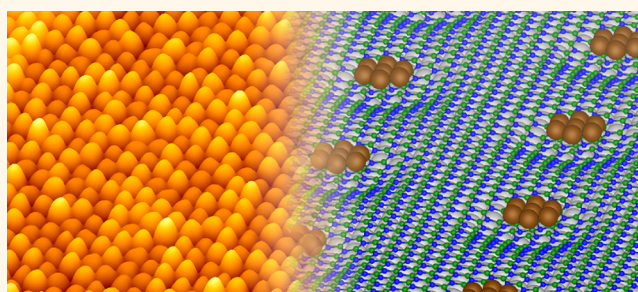
T wo-dimensional superlattices of nanoscale objects created either by self-assembly[1,2] of nanoscale building blocks or through templated growth of nanoscale clusters[3−5] establish an exciting field of research for the creation of new materials, with unique properties arising from their nanoscale constituents and interactions.

Though the methods of nanocrystal fabrication and liquid phase self-assembly advanced substantially in the recent years,[6,7] templated growth, under concern here, displays certain advantages compared to self-assembly: It enables a regular arrangement of very small clusters below nm-size even down to the single atom,[8−10] and it is superior in terms of process control as well as cleanness (templated growth usually takes place under ultrahigh vacuum conditions[8,11,12]), and thus *in situ* measurements of their properties are well suited for comparison with theoretical modeling. As templated growth keeps the clusters separate, each unit can be addressed as a single entity and independently, for example, through local probes.[13] Even more important, through the dense and regular packing of the clusters, the collective superlattice response obtained by averaging techniques displays an excellent signal-to-noise ratio and can be considered as representative information on the cluster itself, convoluted with distance-dependent interactions between the clusters, if present. To name a few examples, dedicated research with cluster

superlattices enables the determination of the magnetic moments and hysteresis of small Co clusters[14] or single Dy atoms[9] arranged on the moiré of graphene (Gr) on Ir(111), the determination of the size-dependent reactivity[15] as well as the quantification of the reverse spillover effect[16] for CO oxidation of Pd clusters on the Al₂O₃ template on Ni₃Al, or the investigation of the size dependence of adsorption induced reshaping and sintering of Pt clusters on Gr/Ir(111).[17,18] One intriguing consequence of the periodic arrangement of the equal-sized clusters is the possibility to follow the structural cluster evolution with crystallographic methods during a catalytic reaction *in operando*.[19−21]

Considering thermal stability at room temperature, a certain perfection (each lattice site occupied), and a narrow size distribution of the clusters in the superlattice as necessary conditions for its use, two templates stick out: First, the thin Al₂O₃ template on Ni₃Al which enables the growth of Pd and V cluster superlattices,[11,22] and second, Gr moirés with Ru(0001) and Ir(111), which enable the growth of Pt, W, Ir, Rh, Re, and Sm superlattices.[8,10,23−25] Using seeding

techniques, for both templates the range of materials for superlattice formation can be extended.[3,24]

In the past, strong interest evolved to use the moirés of a monolayer of the inert and insulating hexagonal boron nitride (h-BN) with noble metal surfaces as a template for cluster superlattices.[12,26−33] In terms of lattice perfection, the best results to date have been achieved for buffer layer assisted growth of Co clusters on h-BN/Rh(111). However, the cluster density n of 0.7 clusters per moiré unit cell remained well below the desired $n = 1$ situation.[12] Moreover, the method is experimentally demanding and inherently requires low-temperature cycling around the noble gas buffer layer desorption temperature.

Intense research was directed to fabrication and investigation of Au cluster arrays on h-BN resting on Ru(0001) or Rh(111)[27,28,30−32] as well as to theoretical modeling of Au adatom and Au cluster binding to h-BN,[30,33−35] which is stimulated by the impressive catalytic activity of nm-sized Au clusters for low-temperature CO oxidation.[36−38] Au clusters are in fact formed exclusively in the pore region of the h-BN/Rh(111) moiré, but they display not only a broad size distribution but also an island density n far below 1.

Despite attractive features, like the inertness of h-BN, or the charging of the Au clusters on h-BN,[35] it is fair to say that the use of the h-BN template for catalytic studies is so far hampered by the structural imperfection of the resulting cluster arrays.

Here, we go a significant step forward and demonstrate the growth of a well-developed cluster superlattice using the h-BN moiré with the noble metal substrate Ir(111). We uncover the bonding mechanism for Ir clusters to h-BN/Ir(111), investigate the relevance of defects in the template, and show that the Ir cluster superlattice on h-BN/Ir(111) is superior in thermal stability to any other templated superlattice, to the authors best knowledge. The relevance of this system is underlined by its ability to template also other materials like C or Au into superlattices.

RESULTS AND DISCUSSION

The STM topograph of Figure 1a visualizes the template effect of an h-BN monolayer grown on Ir(111) [briefly h-BN/Ir(111)]. Deposition of 0.57 ML Ir results in the formation of a hexagonal lattice of clusters with a nearest-neighbor distance of 29.1 Å, consistent with the periodicity of the incommensurate moiré superstructure with (11.7×11.7) h-BN on (10.7×10.7) Ir(111) surface unit cells.[39] A substrate step located underneath the h-BN template gives rise to a line defect in the hexagonal cluster lattice in the upper left of the topograph, while in the lower right the h-BN flake terminates, leaving bare Ir exposed. The average cluster size s_{av} is obtained by $s_{av} = \frac{A_m \theta}{n}$, where $A_m = 10.7^2 = 114.5$ represents the number of Ir surface atoms accommodated in a moiré unit cell, θ the deposited amount expressed as fraction of a monolayer (ML), and n the number of clusters per moiré unit cell (cluster number density).[8] Since $n = 1.00$ in areas undisturbed by step edges for the situation depicted in Figure 1a, we obtain $s_{av} = 65$ atoms. It is apparent from Figure 1a that there is a rather well-defined minimum average cluster height which is taken by about half of the clusters and amounts to 6.6 Å with full width at half-maximum of 0.5 Å. This height is consistent with clusters in [1 1 1]-orientation, formed by three Ir layers. The brighter clusters are interpreted to be predominantly four-
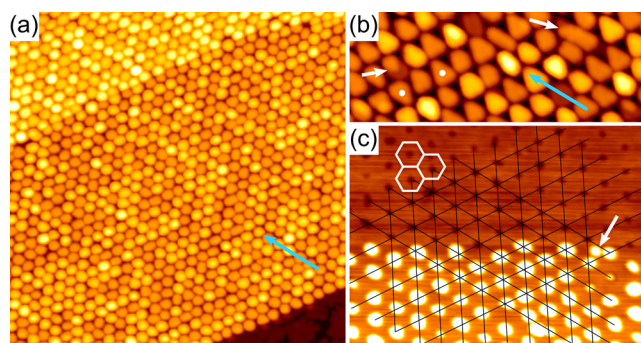

Figure 1. (a) STM topograph of h-BN/Ir(111) after deposition of 0.57 ML Ir at 250 K. Average cluster size $s_{av} = 65$ atoms. Cluster number density $n = 1.00$ islands per moiré unit cell. In the upper left, a substrate step is located underneath the h-BN template. In the lower right, bare Ir is present. (b) Topograph after deposition of 1.5 ML Ir at 350 K. $s_{av} = 175$ atoms and $n = 0.98$. Two clusters with opposing triangular envelope are marked by white dots. Two clusters each displaying two different height levels are highlighted by white arrows. (c) STM topograph after deposition of 0.05 ML Ir at 250 K and subsequent annealing to 350 K resulting in $s_{av} = 6$ atoms. In the upper half of the topograph, clusters have been removed with the STM. The grid of black lines is matched to the centers of the dark valleys in the moiré. A misaligned cluster adsorbed in the center of the triangle formed by three adjacent valleys is highlighted by a white arrow. Three Wigner−Seitz cells of the moiré are indicated by white hexagons in the upper left. Light blue arrows in (a) and (b) are in one of the $\langle 1\bar{1}0 \rangle$ substrate directions. Note that convolution with the STM tip tends to exaggerate lateral cluster sizes, most notable for small clusters. All topographs are imaged at room temperature. Topograph sizes are (a) 80 nm × 80 nm, (b) 32 nm × 12 nm, and (c) 35 nm × 26 nm. Tunneling parameters are (a) $U_{bias} = -2.75$ V and $I_t = 60$ pA, (b) $U_{bias} = -1.5$ V and $I_t = 140$ pA, and (c) $U_{bias} = -2.75$ V and $I_t = 90$ pA.

layered (average height 8.8 Å with full width at half-maximum of 0.7 Å), and few five-layered clusters are present. Figure S1 of the Supporting Information presents the cluster height distribution of Figure 1a, and Figure S2 shows additional topographs of the same experiment.

The topograph in Figure 1b taken after deposition of 1.5 ML Ir substantiates our speculation on the cluster texture. The large clusters with $s_{av} = 175$ atoms display triangular shapes (two islands with opposing triangular shapes are marked by white dots in Figure 1b) that presumably result from the energetic preference of dense-packed edges and side-facets and which are consistent with the symmetry of (111) planes. As all triangular and elongated islands display edges along the $\langle 1\bar{1}0 \rangle$ substrate directions (compare light blue arrow in Figure 1b), it is evident that the clusters fulfill the following epitaxial relations: The dense-packed cluster and Ir(111) or h-BN planes are parallel and the dense-packed cluster and Ir(111) or h-BN directions are parallel. The clusters differ by multiples of the Ir(111) monatomic step height, and single steps can be distinguished on several clusters, of which two are highlighted by white arrows in Figure 1b.

In order to determine the binding site of the clusters, we make use of the fact that clusters can be manipulated and picked-up with the STM tip. The topograph in Figure 1c represents the situation after deposition of 0.05 ML Ir resulting in small clusters with $s_{av} = 6$ atoms. In the upper part of the image, Ir clusters have been intentionally removed with the STM tip by scanning with a low tunneling resistance.
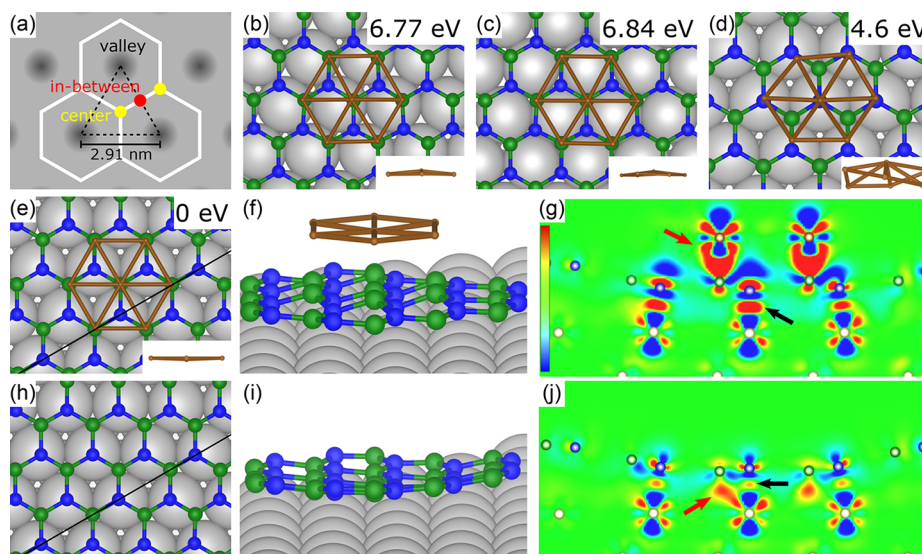
Figure 2. (a) Schematics of the h-BN/Ir(111) moiré. In the three Wigner−Seitz cells centered around the valley regions (dark gray) additionally the in-between (red dot) and the center (yellow dots) regions are indicated. (b−e) Relaxed DFT geometries of an Ir heptamer (brown balls connected by sticks) on h-BN on Ir(111) adsorbed to (b) B atoms in the in-between region, (c) B atoms in the center region, (d) N atoms in the valley region, and (e) B atoms in the valley region. In (b−e), insets display the side view of Ir clusters and numbers are system energies with respect to system energy of (e) set to zero. Color code: N atoms, blue; B atoms, green; Ir substrate atoms, gray. (f) Perspective view of (e) highlighting buckling of h-BN with B atoms approaching the Ir heptamer atoms and N atoms approaching the Ir substrate atoms. (g) Charge density difference between relaxed system represented by (e)/(f) and subsystems of Ir cluster, h-BN, and Ir substrate without changing atomic coordinates within each subsystem. Cut along black line in (e). The color scale ranges from a gain of 0.05 e/A^3 (red) to a loss of 0.05 e/A^3 (blue) in charge density. Arrows highlight the charge accumulation between Ir substrate atoms and N atoms (black arrow) as well as Ir heptamer atoms and B atoms (red arrow). (h) Valley area of h-BN/Ir(111) moiré as in (e), but without adsorbed Ir heptamer. (i) Side view of (h) highlights buckling of h-BN with low B atoms in Ir substrate hollow sites and high N atoms in Ir substrate atop sites. (j) Charge density difference between relaxed system represented by (h)/(i) and subsystems of h-BN and Ir substrate without changing atomic coordinates within subsystem. Cut along black line in (h). Color scale identical to (g). Arrows highlight charge accumulation between Ir substrate atoms and N atoms (black arrow) as well as B atoms (red arrow). Additional charge density difference cuts through pristine h-BN/Ir(111) and h-BN/Ir(111) with adsorbed 7-atom or 12-atom cluster are provided as Figure S3 in the Supporting Information.

Subsequently, the tunneling resistance was increased to avoid tip−cluster interactions, and the remaining clusters in the lower part of the topograph could be imaged together with the h-BN moiré in the upper part. The grid of black lines matched to the centers of the dark valleys in the moiré makes plain that clusters adsorb in these regions. Based on previous experimental and theoretical work analyzing the structure and STM bias dependent appearance and corrugation of h-BN on Ir(111), the valleys can be unambiguously attributed to the regions where h-BN is chemisorbed to Ir(111) with the N atoms sitting atop of Ir substrate atoms.[39,40] Also few misaligned clusters bound in the center between three valleys are visible, that is, at the regions where three Wigner−Seitz cells centered around the valleys touch (compare white hexagons in upper left part of Figure 1c).

The formation of a well developed cluster superlattice with clusters pinned to the valley regions implies that Ir adatoms deposited on h-BN/Ir(111) are mobile and either become directly trapped in the valley region or form small mobile aggregates upon encounter (dimers, trimers) that subsequently become trapped in the valley region during their random walk. In order to understand the cluster pinning, we conducted DFT calculations for cluster adsorption to the commensurate (12 × 12) hBN unit cell on (11 × 11) Ir(111) unit cell approximation of the experimental moiré supercell. As a paradigm, we investigated the binding of a planar Ir heptamer to either B atoms or N atoms in the in-between, center, and valley regions of the moiré (see Figure 2a for the definition of

the three regions). Figure 2b−e visualizes some of these DFT calculations. Variation of the cluster adsorption region with the cluster atoms atop B atoms of h-BN shows the in-between region (Figure 2b) and the center region (Figure 2c) to be similarly disfavored by almost 7 eV with respect to the valley region (Figure 2e). The similarity of the cluster binding in the in-between and center region is no surprise, as previous DFT calculations and experiments demonstrated that h-BN forms a rather flat physisorbed mesa about 3.4 to 3.7 Å above the Ir substrate, while the valley is distinct, being chemisorbed to Ir(111) with a height of about 2.2 to 2.3 Å above Ir(111).[39] Variation of the Ir cluster atom adsorption site to h-BN within the valley shows the N sites (Figure 2d) to be strongly disfavored by 4.6 eV compared to the B sites (Figure 2e). This instability is directly visible in the inset of Figure 2d, where the initially planar cluster is observed to move away from the initial N adsorption position. Likewise, after initial adsorption in hollow sites (data not shown) the entire cluster glides to the energetically preferred B sites. In conclusion, from our DFT calculations it is evident that Ir cluster binding to the valley region is energetically strongly preferred, in full agreement with our experimental findings (compare Figure 1c). Moreover, there is a strong preference for binding of Ir cluster atoms atop of B atoms in h-BN.

To understand how the Ir heptamer binds in the valley region, we now analyze the results presented in the second row of Figure 2 (2e−g) for an Ir heptamer adsorbed in the valley region of h-BN/Ir(111). In the minimum energy configuration

as shown in Figure 2e, the three N atoms and the seven B atoms underneath the heptamer display distances of 2.1 and 2.6 Å from the Ir(111) plane, respectively, and of 2.7 and 2.1 Å from the plane defined by the average z-coordinate of the heptamer atoms. The pronounced buckling of the h-BN layer underneath the Ir heptamer with the N atoms about 0.5 Å closer to the substrate plane than the B atoms is visualized through the side view of Figure 2f. It is indicative of an sp^3 hybridization of the h-BN layer. In fact, the average bond angle between B- and N atoms underneath the cluster is 111.5°, much closer to the tetrahedral angle of 109.5° characteristic for sp^3 hybridization than to the angle of 120° characteristic for sp^2 bonding. The sp^3 hybridization for B and N atoms is accompanied by bond formation in both directions normal to the average h-BN plane. The charge density difference plot in Figure 2g along the black line indicated in Figure 2e directly visualizes this bond formation: The red patch highlighted by the black arrow indicates charge accumulation between an Ir substrate and an N atom, and similarly, the extended red U-shaped area highlighted by the red arrow indicates charge accumulation between a B and an Ir heptamer atom. The locations of charge accumulation suggest that the Ir substrate atom−N atom bond forms through hybridization of the Ir d$_{z^2}$ orbital with an N p$_z$ orbital, while to the Ir heptamer atom−B atom bond all out-of-plane Ir d$_{z^2}$, d$_{xz}$, and d$_{yz}$ orbitals contribute. Also consistent with chemical bond formation are the short Ir substrate atom−N atom distance of 2.1 Å and the short B atom−Ir cluster atom distance of 2.1 Å.

Though we established that the cluster binding to the valley region is through sp^3 hybridized h-BN underneath the cluster, a clear picture of cluster binding is only achieved when we compare the geometrical and electronic structure of the h-BN valley region with the Ir heptamer adsorbed to the corresponding situation without the Ir heptamer adsorbed, as represented by the third row of Figure 2 (2h−j). In the relaxed geometry of the pristine h-BN on Ir(111) (see Figure 2h), the same three N atoms and seven B atoms as above, but without Ir heptamer adsorbed, display distances of 2.3 and 2.2 Å with respect to the Ir(111) plane, respectively. This implies that the buckling of the h-BN layer in the valley region, though less pronounced, is just opposite to the buckling when an Ir heptamer is adsorbed, that is, now the B atoms are closer to the substrate than the N atoms by about 0.1 Å, as visualized through the side view of Figure 2i and also visible in the cut of Figure 2j. Considering the same atoms as in the case of the heptamer adsorption for averaging, for the pristine h-BN on Ir(111), due to the smaller buckling amplitude the average bond angle between B and N atoms is now 119.5°, much closer to the angle of 120° characteristic for sp^2 bonding than to the angle of 109.5° characteristic for sp^3 hybridization. Thus, we have to consider the valley region as an h-BN area chemisorbed to Ir(111),[39] but predominantly sp^2 hybridized. In the charge density difference plot of Figure 2j along the line in Figure 2h, charge accumulation between Ir substrate and N atoms is visible in the valley (highlighted by the black arrow in Figure 2j), as a result of a weak hybridization between the d$_{z^2}$ orbital with the N p$_z$ orbital. However, by adsorbing the heptamer onto the h-BN layer, the N−Ir distances decrease by 0.2 Å leading to a stronger N−Ir chemical bond as also depicted by the larger charge density accumulation between these atoms (see Figure 2g). Note that for the charge density difference plots of Figure 2g,j, the same color scale has been used. Qualitatively different is the binding of the B atom for

the pristine h-BN on Ir(111) which, due to the missing Ir heptamer atom above, sits deep in the three-fold hollow site of the Ir substrate such that its p$_z$ orbital hybridizes with out-of-plane d$_{xz}$ and d$_{yz}$ states of the Ir substrate (see red arrow in Figure 2j). By adsorbing the heptamer, also the B−Ir bond distances decrease from 2.2 Å (B−Ir substrate bond) to 2.1 Å (B−Ir cluster bond), indicating the B−Ir cluster bond is stronger than the B−Ir substrate bond.

Cluster binding in the valley is selective, as this region has the proper geometry to enable a transition from a predominantly sp^2 chemisorbed state to sp^3 hybridization with the cluster adsorbed by providing Ir substrate atoms underneath N atoms and Ir heptamer atoms above the B atoms. The cluster binding is thereby not only through the Ir heptamer atom−B atom bond formation but also through the strengthening of the Ir substrate atom−N atom bonds.

The bonding mechanism suggested by the bond length analysis and the charge density difference plots is further substantiated by the analysis of the projected density of states (PDOS) calculated for clean Ir(111) and for h-BN/Ir(111) with an adsorbed Ir heptamer as depicted in Figure 3. Close to the Fermi energy E_F the PDOS of clean Ir(111) surface atoms Ir$_{surf}^{cs}$ contains contributions from the out-of-plane d$_{xz}$, d$_{yz}$ states
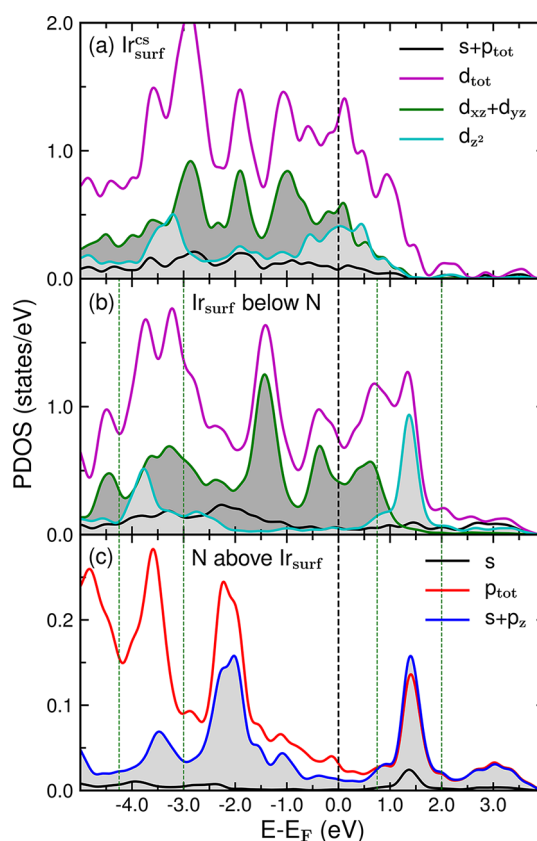
Figure 3. (a) The PDOS of a surface atom of pristine Ir(111). When a monolayer of h-BN and a 7-atom Ir cluster are adsorbed, (b) displays the PDOS of an Ir surface atom in the valley region below an N atom and (c) the PDOS of the corresponding N atom; see text. Additional PDOS plots are provided as Figure S4 in the Supporting Information. Note that in (a) and (b) the PDOS d$_{tot}$ (violet line) is the sum of out-of plane (d$_{xz}$ and d$_{yz}$: dark green line and dark gray filling; d$_{z^2}$: turquoise line and light gray filling) and in-plane (d$_{xy}$ and d$_{x^2-y^2}$: not displayed separately) states. The out-of-plane ones are relevant for bonding of the h-BN to Ir(111).

[dark green line and dark gray filling in Figure 3a], and d_{z^2} states [turquoise line and light gray filling] as well as in-plane d_{xy} and $d_{x^2-y^2}$ states (the difference of d_{tot} and the out-of-plane contributions). The out-of-plane states are relevant for bonding to h-BN. Indeed, when h-BN and an Ir heptamer are adsorbed, these out-of-plane PDOS features of an Ir(111) surface atom Ir_{surf} in the valley region shown in Figure 3b are substantially different. The Ir d_{z^2} PDOS is split away from E_F, and through hybridization of the Ir d_{z^2} orbitals with N p_z orbitals antibonding (peak around 1.4 eV, between thin vertical lines at 0.75 and 2 eV) and bonding (peak at −3.7 eV and shoulder, between thin vertical lines at −4.3 eV and −3 eV) hybrid orbitals are formed. Evidence for Ir d_{z^2} − N p_z hybridization is provided by the fact that the peak positions and weight of the N $s + p_z$ PDOS peaks in Figure 3c closely match with the ones of the Ir d_{z^2} PDOS in Figure 3b. Moreover, the weight of the Ir d_{xz} and Ir d_{yz} PDOS below E_F is considerably increased in Figure 3b as compared to Figure 3a, indicating an on-site charge rearrangement.

These features are fully consistent with the charge depletion of the d_{z^2} orbitals, the charge accumulation between Ir and N atoms through formation of Ir d_{z^2}−N p_z hybrids, and the charge accumulation in the d_{xz} and d_{yz} orbitals as visible in Figure 2g.

We note that the formation of antibonding and bonding Ir d_{z^2}−N p_z hybrid orbitals is already visible in the PDOS of Ir_{surf} when only h-BN, but no Ir cluster is adsorbed. However, the splitting between the antibonding and bonding peaks is about 0.8 eV smaller, indicating a weaker Ir surface atom−N atom bond, consistent with the smaller charge accumulation in between the two as visible in Figure 2j. This and other PDOS calculations providing an even further detailed view of bonding are provided as Figure S4 in the Supporting Information.

Our findings qualitatively agree with the picture emerging from DFT calculations for Au adatom and Au cluster bonding to h-BN/Rh(111),[33−35] but our view on h-BN bonding to Ir(111) is at variance with a repulsive interaction between N atoms atop of Ir substrate atoms as found for the adsorption of h-BN on a variety of metal surfaces, including Ir(111).[41,42] We consider the charge accumulation between the N atoms of h-BN and the Ir substrate atoms to be clear evidence for bond formation rather than repulsive interaction. The observed buckling is in our view a consequence of the extension as well as the shape of the lowest unoccupied and the highest occupied h-BN π-electronic states with a p_z character at the B and N atomic sites. Due to the larger electronegativity of N as compared to B, in the free-standing h-BN the highest occupied bonding states are mostly located at the N atoms, where they have a large extension in space (compare also Figure S5 of the Supporting Information and ref 43). This large spatial extension of the bonding π states with a p_z atomic character at the N sites enables their hybridization with the Ir d_{z^2} orbitals. At the B sites, these bonding π states exhibit a small spatial extension that allows the B atoms to dive deeply into the three-fold hollow sites of the Ir substrate. Since the lowest unoccupied π states possess a large spatial extent at B-sites (compare also Figure S5 of the Supporting Information and ref 43), a B atom being deep in the three-fold hollow concurs with an effective overlap between the out-of-plane Ir $d_{xz,yz}$ states with the lowest unoccupied π states.

We also want to briefly address the binding of misaligned clusters located in center regions already noted in Figure 1c. A population of center region adsorbed clusters is only noticeable for very small deposited amounts well below 0.1 ML. Moreover, even then their population is insignificant, if deposition is conducted at 300 K or above. Using the small coverage of 0.05 ML and a deposition temperature of 150 K, the population of center region clusters is substantial, as visible on the STM topograph in Figure 4a. Under these conditions
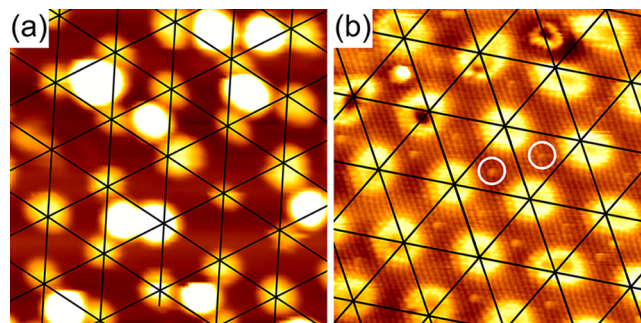

Figure 4. (a) STM topograph of h-BN/Ir(111) after deposition of 0.05 ML Ir at 150 K and annealed for 60 s at 300 K. Imaging was conducted at 150 K. Grid of thin black lines defines triangular areas between valleys. Several center regions are populated by additional clusters. (b) Atomically resolved STM topograph of pristine h-BN/Ir(111). Atomic-scale defects are visible as bright protrusions at many center regions. Two of the defects are encircled; see text. Image size in (a) is 13 nm × 13 nm and in (b) it is 12 nm × 12 nm. Tunneling parameters are (a) U_{bias} = −2.4 V and I_t = 90 pA and (b) U_{bias} = 0.48 V and I_t = 850 pA.

the partial cluster number density for the moiré cells with center region clusters amounts to n_{center} = 0.3 clusters per moiré unit cell. Another notable feature of the center region clusters at 0.05 ML coverage highlighted by the STM topograph shown in Figure 4a is their significantly larger height of around 4.4 Å as compared the valley region clusters with a height around 2.1 Å. The larger height indicates two-layer center region clusters as compared to monolayer valley adsorbed clusters.

Figure 4b displays an area of bare h-BN/Ir(111) in atomic resolution and with enhanced contrast. Note that due to modified imaging conditions compared to Figure 1c, the valleys appear here as bright protrusions with or without a center depression.[40] Apparent are several bright dots located rather precisely in the center regions, two of them are encircled in Figure 4b. Based on their point-like appearance and preparation-dependent concentration, we interpret the bright dots in Figure 4b as point defects in the h-BN layer. Their presence at a specific location (in the center region) is likely a result from the interaction of the point defect with the underlying substrate. One could for instance speculate the point defect to be a vacancy (e.g., an N vacancy) that has lowest formation energy, where the three adjacent atoms of the layer favorably bind to the substrate, as it has been found for the case of Gr on Ir(111).[44]

These point defects are assumed to provide a second, shallower adsorption energy minimum for deposited Ir atoms (and possibly also small clusters) as compared to the valley region. Being a shallower minimum, the trapping efficiency of the point defects decreases with increasing temperature earlier than the one of the valleys, making understandable why after deposition at 350 K hardly any center region cluster is observed (compare Figure S6 of the Supporting Information). Being a shallower minimum, the center region clusters are less
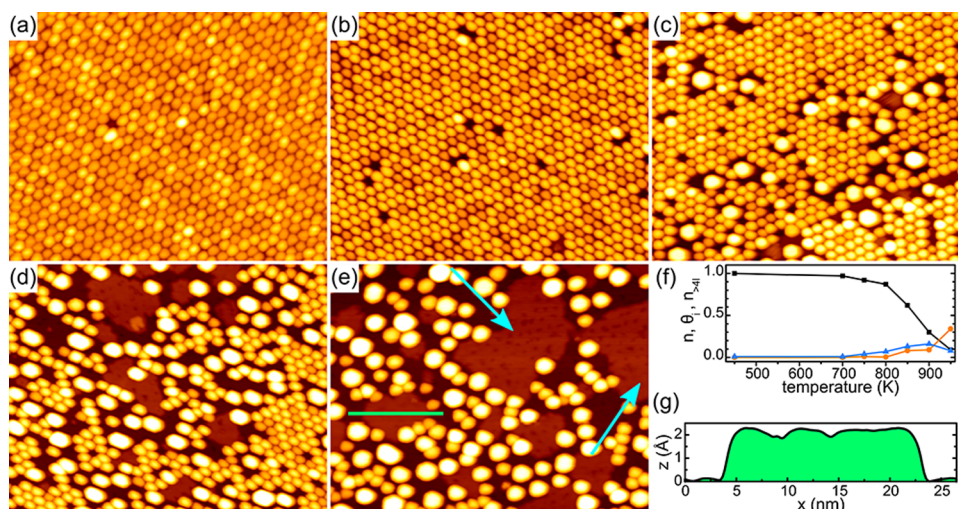
Figure 5. STM topographs of 0.57 ML Ir deposited at 350 K (a) without and (b−e) with successive annealing for 300 s at (b) 700 K, (c) 800 K, (d) 850 K, and (e) 900 K. (f) Variation of cluster number density n (black squares), partial number density $n_{>4l}$ of clusters higher than four Ir layers (blue triangles), and area fraction θ_i of intercalation islands (orange dots); see text. Lines to guide the eye. (g) Line profile along green line in (e). Size of STM topographs is 75 nm × 60 nm in (a) and 90 nm × 70 nm in the others. Tunneling parameters are (a) $U_{bias} = -2.4$ V and $I_t = 61$ pA, (b) $U_{bias} = -1.6$ V and $I_t = 100$ pA, (c) $U_{bias} = -2.7$ V and $I_t = 59$ pA, (d) $U_{bias} = -2.6$ V and $I_t = 61$ pA, and (e) $U_{bias} = -2.4$ V and $I_t = 63$ pA.

strongly bound, and upon subsequent growth merge with the growing valley region clusters, making understandable why with increasing coverage n_{center} vanishes. The point defects provide bonding only for a very small number of Ir atoms as their reactive site is point-like. Therefore, after adsorption of the first or the first few Ir atoms, these clusters turn immediately three-dimensional in order to optimize their binding. This is different from the valley region clusters which first spread out laterally, since the valleys provide more adsorption sites. In fact, even after deposition of 0.11 ML at 350 K resulting in $n_{av} = 13$ atoms, still more than 87% of the valley clusters are of only monolayer height (compare Figure S7 of the Supporting Information for this data and an entire coverage series after deposition at 350 K). Our hypothesis is also consistent with the DFT calculations which do not give any hint for a second adsorption minimum as they do not include point defects. To the contrary, the binding is weakest for the Ir heptamer in the center region (compare Figure 2c). We just note that Ir binding to the center region defects hardly affects the perfection of the cluster superlattice for room-temperature deposited amounts larger than 0.2 ML, since under these conditions center region clusters are efficiently consumed by the more stable valley region clusters during growth (compare Figure S7 of the Supporting Information).

Up to now we documented (i) the ability of h-BN/Ir(111) to rather perfectly template an Ir cluster superlattice in a temperature range between 250 and 350 K and (ii) the tunability of the average cluster size s_{av} in rather perfect superlattices between 13 atoms and 175 atoms (compare Figure 1b,c; see Figure S7 of the Supporting Information for coverage sequence). In view of potential applications in nanocatalysis and nanomagnetism two other features are of relevance: (iii) the stability of the cluster superlattice against sintering under typical catalyst operation conditions of elevated temperature and pressure and (iv) the ability of h-BN/Ir(111) to template a variety of different materials.

Figure 5 presents a sequence of STM topographs after deposition 0.57 ML Ir at 350 K, as shown in Figure 5a, and

subsequent annealing for 300 s at 700, 800, 850, and 900 K, as shown in Figure 5b−e. The lattice of three- and four-layered clusters remains very close to perfect up to 700 K (compare Figure 5b) with the cluster number density just decreasing from $n = 1.00$ clusters per moiré unit cell after growth ($s_{av} = 65$ atoms) to $n = 0.97$ after annealing to 700 K. The slight decrease of n is obviously due to a few, single cluster coalescence events which can often be recognized by a cluster of substantially larger height next to a cluster vacancy.

Gradual decay of the lattice sets in by annealing to 800 K (Figure 5c) and progresses through annealing steps at 850 and 900 K (Figure 5d,e). The decay is characterized by three features: (1) areas of unchanged cluster superlattice becoming smaller with increasing annealing temperature; (2) more and more coalesced clusters with a larger height and extension, initially at 800 K mostly surrounded by cluster lattice voids (compare Figure 5c), and finally at 900 K being the dominant type of cluster; (3) intercalation islands of monolayer height underneath the h-BN layer, which can be recognized in areas depleted of clusters as in Figure 5d,e (light blue arrows in Figure 5e highlight large intercalation islands).

Observation (1) is consistent with the absence of Ostwald ripening, which through atom detachment and reattachment processes would lead to a global broadening of the cluster size and height distributions, rather than a bimodal distribution (of unchanged and coalesced clusters), as observed here. Observation (2) implies the coalescence of clusters in consequence of thermally induced position fluctuations and subsequent encounter, that is, the cluster number density decreases by Smoluchowski ripening.[17] As a function of temperature, Figure 5f displays the decrease of n and the increase of the partial cluster number density $n_{>4l}$ of clusters with height larger than four layers, which can be considered to result from coalescence. In observation (3), intercalation is visualized by the height profile of Figure 5g drawn along the green line in Figure 5e which displays the height level of the flat area to be ≈2 Å higher than the surrounding, as expected for h-BN covering a monolayer Ir island. As a function of
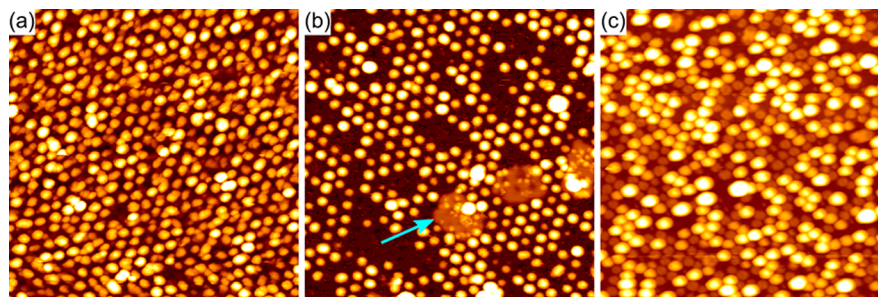
Figure 6. STM topographs after exposure of h-BN/Ir(111) to elemental vapor of (a), (b) C, and (c) Au. (a) 0.3 ML C deposited at 400 K. (b) Same as (a) but after additional annealing at 1350 K for 120 s. Light blue arrow highlights a C intercalation island. (c) 0.3 ML Au deposited at 300 K and imaged at 40 K. Image sizes are (a, b) 55 nm × 55 nm and (c) 75 nm × 75 nm. Tunneling parameters are (a) $U_{bias} = -1.3$ V and $I_t = 640$ pA, (b) $U_{bias} = -1.1$ V and $I_t = 700$ pA, and (c) $U_{bias} = -1.9$ V and $I_t = 61$ pA.

temperature, Figure 5f plots the area fraction of the intercalation islands θ_i. Apparently, intercalation sets in around 850 K, almost simultaneously with cluster coalescence. After annealing to 950 K, $\theta_i = 0.35$ ML, that is, more than half of the deposited 0.57 ML Ir initially present in clusters has been intercalated. Intercalation is driven by system energy lowering, when the cluster Ir transforms to Ir in regular crystal positions. Though the analysis of the intercalation mechanism is beyond the scope of the present work, it is obvious that it takes place very locally and the material is sucked down to the Ir substrate either through pre-existing point defects or through point defects etched during the annealing process.[45,46]

The ability of h-BN/Ir(111) to template a variety of different materials is exemplified in Figure 6. Deposition of 0.3 ML elemental C at 400 K results in the formation of an ordered C cluster superlattice with $n \approx 1$ and $s_{av} \approx 85$ (compare Figure 6a). The notable feature of C clusters on h-BN/Ir(111) is their enormous thermal stability: Even after annealing to 1350 K, a cluster superlattice is visible in most areas as shown in Figure 6b. Similar to Ir cluster superlattices (compare Figure 5), the C clusters decay by intercalation (a carbon intercalation island is highlighted by a light blue arrow in Figure 6b). In distinction to Ir cluster superlattices, cluster diffusion and coalescence appear to be hardly relevant as decay mechanism, based on the small number of larger clusters that might originate from coalescence. Due to the formation of covalent rather than metallic bonds between the carbon atoms, also the cluster binding mechanism is likely to be different from the Ir case. Formation of curved, predominantly sp^2-bonded cluster caps merged to sp^3 hybridized h-BN is a likely scenario, similar to what has been proposed for C clusters on Gr/Ir(111).[47]

As mentioned in the introduction, Au clusters are of outstanding interest for low-temperature heterogeneous catalysis, and it is therefore of evident interest to test the templating effect of h-BN/Ir(111) for Au. Figure 6c shows an STM topograph taken after exposure to 0.3 ML Au vapor at 300 K. Au forms a reasonably regular lattice with $n \approx 0.9$. Owing to the relatively low cohesion of Au to h-BN/Ir(111), clusters are easily manipulated and picked up with the STM tip even at very low tunneling currents. To avoid this, the sample has been cooled to about 40 K prior to imaging, reducing internal cluster mobility and thus tip–sample-interaction. We note that the cluster height distribution is rather inhomogeneous, as with increasing size, the cluster height switches from monolayer clusters to three-layered clusters. As a Au cluster template, h-BN/Ir(111) displays certain advantages compared

to h-BN/Rh(111), the most thoroughly investigated h-BN template:[30−33] (i) A reasonably ordered dense Au cluster array can be fabricated even by Au deposition at 300 K substrate temperature, rather than 115 K; (ii) the resulting cluster density is larger with $n = 0.9$ compared to $n = 0.7$ on h-BN/Rh(111); and (iii) last, comparing Figure 6c with Figure 5b of ref 30, the positional order of the cluster array on h-BN/Ir(111) seems to be superior. Thus, it may be rewarding to optimize Au cluster lattices on h-BN/Ir(111) for catalytic applications in future work.

Lastly, a comparison to the Gr/Ir(111) cluster template described previously[8,13,17,20,24,48,49] is in place. Both systems template epitaxial clusters, but due to the larger size of the h-BN/Ir(111) moiré, a larger maximum cluster size prior to the onset of coalescence is reached [$s_{av,max} = 175$ for Ir clusters on h-BN/Ir(111), while the limit is $s_{av,max} = 135$ for Gr/Ir(111)].[8] Both systems template through a rehybridization mechanism involving the substrate Ir. However, the initital state of the binding site is chemisorbed for h-BN/Ir(111), while it is physisorbed with a slight chemical component for Gr/Ir(111). For clusters on defect free h-BN/Ir(111), there is only a single pinning site per moiré unit cell (the valley region), while there are two distinct pinning sites for Gr/Ir(111) (the fcc and the hcp regions, compare ref 24). The unique pinning site is a conceptual advantage of the h-BN/Ir(111) systems. The stronger changes in binding due to cluster adsorption and the unique binding site both appear to make clusters adsorbed to h-BN/Ir(111) much more resistant against sintering; decay of Ir clusterlattices sets in above 700 K compared to 450 K for Gr/Ir(111).[24] Likewise, the decay of C cluster superlattices is shifted up by 350 to 1350 K on h-BN/Ir(111).[47] Lastly the two element composition of h-BN and the ionic binding component add a new chemical dimension to cluster templating. We attribute the ability to template Au cluster lattices at 300 K on h-BN/Ir(111) to this new dimension, as Au clusters are unstable on Gr/Ir(111) and can only be templated by cooling down to ≈90 K.[24]

CONCLUSIONS

To summarize, the moiré of a monolayer of h-BN on Ir(111) efficiently templates highly ordered cluster superlattices of a variety of materials with average cluster sizes of up to 175 atoms and superior stability against sintering. Under ultrahigh-vacuum conditions, Ir superlattice degradation is insignificant up to 700 K and C cluster superlattices survive up to 1350 K. As elucidated by our *ab initio* calculations, Ir clusters bind to the h-BN moiré valley by formation of strong Ir cluster atom−

B atom bonds and by reinforcing the Ir substrate atom−N atom bonds. The single pinning site in the moiré unit cell, the strong thermal stability of the adsorbed clusters, and the extra degree of freedom added by the presence of two different species in the template appear to make h-BN/Ir(111) superior to Gr/Ir(111) and to all other moiré templates known to date. Based on its excellent properties, the h-BN/Ir(111) template will enable cluster superlattice experiments with nm-sized clusters for research in nanocatalysis and nanomagnetism.

METHODS

Sample preparation, growth, and *in situ* STM imaging were carried out in an ultrahigh-vacuum system with a base pressure in the 10^{-11} mbar regime. The Ir(111) sample was cleaned by repeated cycles of 2 keV Xe^+ ion sputtering at room temperature and flash heating to 1550 K. Subsequently, h-BN islands with lateral dimension of the order of 0.5 μm covering about 80% of the substrate were grown at 1235 K by a 20 s borazine exposure ($B_3N_3H_6$) from a gas dosing tube to a pressure 1×10^{-8} mbar measured at a distant ion gauge. The gas dosing tube gives rise to a pressure enhanced at the sample location by about a factor of 80 compared to the ion gauge reading. Using LEED and STM we found well oriented h-BN islands with their dense-packed rows aligned better than 1° with respect to the Ir dense-packed rows and to display the characteristic (11.7×11.7) h-BN on (10.7×10.7) Ir(111) unit cell moiré superstructure.[39]

Ir and C were sublimated from electron-beam heated high-purity rods, while Au was evaporated from a Knudsen cell. During deposition with a typical rate of 5×10^{-3} ML/s, the pressure remained below 2×10^{-10} mbar. In all cases the deposited amount Θ of material was calibrated by determining the fractional area covered with deposit islands on the bare Ir(111) surface with STM image analysis. For Ir, the sample was additionally annealed up to 800 K in order to minimize imaging errors by transforming fractal to compact islands. For C, the sample was additionally annealed to 1470 K in order to transform the deposited C into graphene islands. The deposited amounts of Ir and Au are specified in monolayers (ML) with respect to the surface atomic density of Ir(111), while the deposited amount for C is given in ML with respect to the atomic density in Gr.

Typical parameters for STM imaging are a sample bias voltage U_{bias} in the range from −1.5 V to −4 V and a tunneling current $I_t < 100$ pA. STM data were processed with WSxM[50] and SPIP.

Our density functional theory (DFT)[51,52] calculations were carried out by employing the VASP code[53−55] with the generalized gradient approximation[56] for the pseudopotentials generated using the projector augmented wave method (PAW).[57] The (12×12) h-BN on (11×11) Ir(111) system containing 651 atoms was modeled by a slab consisting of three Ir atomic layers. To obtain the ground-state geometry of the Ir heptamer on h-BN/Ir(111), the atomic degrees of freedom of the Ir cluster, h-BN, and first Ir surface layer were relaxed for several starting configurations (see Figure 2) until the calculated Hellmann−Feynman forces were smaller than 10 meV/Å. Furthermore, these structural relaxations were performed with a plane wave basis set corresponding a cutoff kinetic energy of 500 eV and by sampling the Brillouin zone by the Γ-point. Note that as in ref 58, the van der Waals interactions (vdW), that are a key ingredient for the bonding of h-BN on Ir(111), were taken into account in our calculations by employing the nonlocal correlation energy functional vdW-DF2[59] with the exchange energy functional developed by Hamada.[60] Figure 2b−j as well as Figures S3 and S5 in the Supporting Information have been obtained by using the program VESTA.[61]

ASSOCIATED CONTENT

Ⓢ Supporting Information

The Supporting Information is available free of charge on the ACS Publications website at DOI: 10.1021/acsnano.8b02127.

Figure S1 shows the cluster height distribution for the STM image from Figure 1a, and Figure S2 shows additional STM topographs taken after deposition of 0.57 ML Ir on h-BN/Ir(111) at 250 K, and 0.34 ML Ir at 350 K. Figure S3 displays additional charge density difference cuts through pristine h-BN/Ir(111) and h-BN/Ir(111) with an adsorbed 7-atom or 12-atom cluster. Figure S4 contains additional projected density of states plots for B, N, and Ir atoms of pristine h-BN/Ir(111) and h-BN/Ir(111) with an adsorbed heptamer. Figure S5 provides plots of the highest occupied and lowest unoccupied π states of pristine h-BN. Figure S6 contains the temperature dependence of n_{center} after deposition of 0.05 ML Ir, and Figure S7 is a sequence of Ir cluster superlattice morphologies with increasing deposited amounts (PDF)

AUTHOR INFORMATION

Corresponding Authors
*E-mail: will@ph2.uni-koeln.de.
*E-mail: n.atodiresei@fz-juelich.de.

ORCID Ⓞ
Moritz Will: 0000-0003-4822-9122
Philipp Valerius: 0000-0002-2310-465X
Charlotte Herbig: 0000-0003-3106-1781

Notes
The authors declare no competing financial interest.

REFERENCES

(1) Sun, S.; Murray, C. B.; Weller, D.; Folks, L.; Moser, A. Monodisperse FePt Nanoparticles and Ferromagnetic FePt Nanocrystal Superlattices. *Science* 2000, 287, 1989−1992.

(2) Boles, M. A.; Engel, M.; Talapin, D. V. Self-Assembly of Colloidal Nanocrystals: From Intricate Structures to Functional Materials. *Chem. Rev.* 2016, 116, 11220−11289.

(3) Becker, C.; Wandelt, K. *Templates in Chemistry III*; Springer-Verlag: Berlin, 2008; pp 45−86.

(4) Henry, C. R. 2D-Arrays of Nanoparticles as Model Catalysts. *Catal. Lett.* 2015, 145, 731−749.

(5) Papp, C. From Flat Surfaces to Nanoparticles: *In Situ* Studies of the Reactivity of Model Catalysts. *Catal. Lett.* 2017, 147, 2−19.

(6) Kang, J.; Li, O. L.; Saito, N. Synthesis of Structure-Controlled Carbon Nano Spheres by Solution Plasma Process. *Carbon* 2013, 60, 292−298.

(7) Boneschanscher, M. P.; Evers, W. H.; Geuchies, J. J.; Altantzis, T.; Goris, B.; Rabouw, F. T.; Van Rossum, S. A. P.; Van Der Zant, H. S. J.; Siebbeles, L. D. A.; Van Tendeloo, G.; Swart, I.; Hilhorst, J.; Petukhov, A. V.; Bals, S.; Vanmaekelbergh, D. Long-Range Orientation and Atomic Attachment of Nanocrystals in 2D Honeycomb Superlattices. *Science* 2014, 344, 1377−1380.

(8) N'Diaye, A. T.; Bleikamp, S.; Feibelman, P. J.; Michely, T. Two-Dimensional Ir Cluster Lattice on a Graphene Moiré on Ir(111). *Phys. Rev. Lett.* 2006, 97, 215501.

(9) Baltic, R.; Pivetta, M.; Donati, F.; Wäckerlin, C.; Singha, A.; Dreiser, J.; Rusponi, S.; Brune, H. Superlattice of Single Atom Magnets on Graphene. *Nano Lett.* **2016**, *16*, 7610−7615.

(10) Mousadakos, D.; Pivetta, M.; Brune, H.; Rusponi, S. Sm Cluster Superlattice on Graphene/Ir(111). *New J. Phys.* **2017**, *19*, 123021.

(11) Degen, S.; Becker, C.; Wandelt, K. Thin Alumina Films on Ni₃Al(111): A Template for Nanostructured Pd Cluster Growth. *Faraday Discuss.* **2004**, *125*, 343−356.

(12) Zhang, J.; Sessi, V.; Michaelis, C. H.; Brihuega, I.; Honolka, J.; Kern, K.; Skomski, R.; Chen, X.; Rojas, G.; Enders, A. Ordered Layers of Co Clusters on BN Template Layers. *Phys. Rev. B: Condens. Matter Mater. Phys.* **2008**, *78*, 165430.

(13) Martínez-Galera, A. J.; Brihuega, I.; Gutiérrez-Rubio, A.; Stauber, T.; Gómez-Rodríguez, J. M. Towards Scalable Nano-Engineering of Graphene. *Sci. Rep.* **2015**, *4*, 7314.

(14) Vo-Van, C.; Schumacher, S.; Coraux, J.; Sessi, V.; Fruchart, O.; Brookes, N. B.; Ohresser, P.; Michely, T. Magnetism of Cobalt Nanoclusters on Graphene on Iridium. *Appl. Phys. Lett.* **2011**, *99*, 142504.

(15) Sitja, G.; Le Moal, S.; Marsault, M.; Hamm, G.; Leroy, F.; Henry, C. R. Transition from Molecule to Solid State: Reactivity of Supported Metal Clusters. *Nano Lett.* **2013**, *13*, 1977−1982.

(16) Sitja, G.; Henry, C. R. Molecular Beam Study of the Oxidation of Carbon Monoxide on a Regular Array of Palladium Clusters on Alumina. *J. Phys. Chem. C* **2017**, *121*, 10706−10712.

(17) Gerber, T.; Knudsen, J.; Feibelman, P. J.; Grånäs, E.; Stratmann, P.; Schulte, K.; Andersen, J. N.; Michely, T. CO-induced Smoluchowski Ripening of Pt Cluster Arrays on the Graphene/Ir(111) Moiré. *ACS Nano* **2013**, *7*, 2020−2031.

(18) Podda, N.; Corva, M.; Mohamed, F.; Feng, Z.; Dri, C.; Dvořák, F.; Matolín, V.; Comelli, G.; Peressi, M.; Vesselli, E. Experimental and Theoretical Investigation of the Restructuring Process Induced by CO at Near Ambient Pressure: Pt Nanoclusters on Graphene/Ir(111). *ACS Nano* **2017**, *11*, 1041−1053.

(19) Billinge, S. Materials Science: Nanoparticle Structures Served up on a Tray. *Nature* **2013**, *495*, 453−454.

(20) Franz, D.; Runte, S.; Busse, C.; Schumacher, S.; Gerber, T.; Michely, T.; Mantilla, M.; Kilic, V.; Zegenhagen, J.; Stierle, A. Atomic Structure and Crystalline Order of Graphene-Supported Ir Nanoparticle Lattices. *Phys. Rev. Lett.* **2013**, *110*, 065503.

(21) Franz, D.; Blanc, N.; Coraux, J.; Renaud, G.; Runte, S.; Gerber, T.; Busse, C.; Michely, T.; Feibelman, P. J.; Hejral, U.; Stierle, A. Atomic Structure of Pt Nanoclusters Supported by Graphene/Ir(111) and Reversible Transformation under CO Exposure. *Phys. Rev. B: Condens. Matter Mater. Phys.* **2016**, *93*, 045426.

(22) Becker, C.; Rosenhahn, A.; Wiltner, A.; von Bergmann, K.; Schneider, J.; Pervan, P.; Milun, M.; Kralj, M.; Wandelt, K. Al₂O₃-Films on Ni₃Al(111): a Template for Nanostructured Cluster Growth. *New J. Phys.* **2002**, *4*, 75.

(23) Donner, K.; Jakob, P. Structural Properties and Site Specific Interactions of Pt with the Graphene/Ru(0001) Moiré Overlayer. *J. Chem. Phys.* **2009**, *131*, 164701.

(24) N'Diaye, A. T.; Gerber, T.; Busse, C.; Mysliveček, J.; Coraux, J.; Michely, T. A Versatile Fabrication Method for Cluster Superlattices. *New J. Phys.* **2009**, *11*, 103045.

(25) Gerber, T. Interaction of Graphene and Templated Cluster Arrays with CO, H₂, and O₂. Ph.D. Thesis, Universität zu Köln, 2013.

(26) Auwärter, W.; Muntwiler, M.; Greber, T.; Osterwalder, J. Co on h-BN/Ni(111): from island to island-chain formation and Co intercalation. *Surf. Sci.* **2002**, *511*, 379−386.

(27) Ng, M. L.; Preobrajenski, A. B.; Vinogradov, A. S.; Mårtensson, N. Formation and Temperature Evolution of Au Nanoparticles Supported on the h-BN Nanomesh. *Surf. Sci.* **2008**, *602*, 1250−1255.

(28) Goriachko, A.; He, Y. B.; Over, H. Complex Growth of NanoAu on BN Nanomeshes Supported by Ru(0001). *J. Phys. Chem. C* **2008**, *112*, 8147−8152.

(29) Brihuega, I.; Michaelis, C. H.; Zhang, J.; Bose, S.; Sessi, V.; Honolka, J.; Schneider, M. A.; Enders, A.; Kern, K. Electronic

(30) Patterson, M. C.; Habenicht, B. F.; Kurtz, R. L.; Liu, L.; Xu, Y.; Sprunger, P. T. Formation and Stability of Dense Arrays of Au Nanoclusters on Hexagonal Boron Nitride/Rh(111). *Phys. Rev. B: Condens. Matter Mater. Phys.* **2014**, *89*, 205423.

(31) Wu, F.; Huang, D.; Yue, Y.; Liu, L. Template Growth of Au, Ni and Ni-Au Nanoclusters on Hexagonal Boron Nitride/Rh(111): A Combined STM, TPD and AES study. *RSC Adv.* **2017**, *7*, 44169−44177.

(32) McKee, W. C.; Patterson, M. C.; Huang, D.; Frick, J. R.; Kurtz, R. L.; Sprunger, P. T.; Liu, L.; Xu, Y. CO Adsorption on Au Nanoparticles Grown on Hexagonal Boron Nitride/Rh(111). *J. Phys. Chem. C* **2016**, *120*, 10909−10918.

(33) McKee, W. C.; Patterson, M. C.; Frick, J. R.; Sprunger, P. T.; Xu, Y. Adsorption of Transition Metal Adatoms on h-BN/Rh(111): Implications for Nanocluster Self-Assembly. *Catal. Today* **2017**, *280*, 220−231.

(34) Koch, H. P.; Laskowski, R.; Blaha, P.; Schwarz, K. Adsorption of Gold Atoms on the h-BN/Rh(111) Nanomesh. *Phys. Rev. B: Condens. Matter Mater. Phys.* **2011**, *84*, 245410.

(35) Koch, H. P.; Laskowski, R.; Blaha, P.; Schwarz, K. Adsorption of Small Gold Clusters on the h-BN/Rh(111) Nanomesh. *Phys. Rev. B: Condens. Matter Mater. Phys.* **2012**, *86*, 155404.

(36) Haruta, M.; Kobayashi, T.; Sano, H.; Yamada, N. Novel Gold Catalysts for the Oxidation of Carbon Monoxide at a Temperature far Below 0 °C. *Chem. Lett.* **1987**, *16*, 405−408.

(37) Valden, M.; Lai, X.; Goodman, D. W. Onset of Catalytic Activity of Gold Clusters on Titania with the Appearance of Nonmetallic Properties. *Science* **1998**, *281*, 1647−1650.

(38) Chen, M. S.; Goodman, D. W. The Structure of Catalytically Active Au on Titania. *Science* **2004**, *306*, 252−255.

(39) Farwick zum Hagen, F. H.; Zimmermann, D. M.; Silva, C. C.; Schlueter, C.; Atodiresei, N.; Jolie, W.; Martínez-Galera, A. J.; Dombrowski, D.; Schröder, U. A.; Will, M.; Lazić, P.; Caciuc, V.; Blügel, S.; Lee, T.-L.; Michely, T.; Busse, C. Structure and Growth of Hexagonal Boron Nitride on Ir(111). *ACS Nano* **2016**, *10*, 11012−11026.

(40) Schulz, F.; Drost, R.; Hämäläinen, S. K.; Demonchaux, T.; Seitsonen, A. P.; Liljeroth, P. Epitaxial Hexagonal Boron Nitride on Ir(111): A Work Function Template. *Phys. Rev. B: Condens. Matter Mater. Phys.* **2014**, *89*, 235429.

(41) Laskowski, R.; Blaha, P.; Gallauner, T.; Schwarz, K. Single-Layer Model of the Hexagonal Boron Nitride Nanomesh on the Rh(111) Surface. *Phys. Rev. Lett.* **2007**, *98*, 106802.

(42) Laskowski, R.; Blaha, P.; Schwarz, K. Bonding of Hexagonal BN to Transition Metal Surfaces: An *ab initio* Density-Functional Theory Study. *Phys. Rev. B: Condens. Matter Mater. Phys.* **2008**, *78*, 045409.

(43) Friedrich, R.; Caciuc, V.; Kiselev, N. S.; Atodiresei, N.; Blügel, S. Chemically Functionalized Magnetic Exchange Interactions of Hybrid Organic-Ferromagnetic Metal Interfaces. *Phys. Rev. B: Condens. Matter Mater. Phys.* **2015**, *91*, 115432.

(44) Standop, S.; Lehtinen, O.; Herbig, C.; Lewes-Malandrakis, G.; Craes, F.; Kotakoski, J.; Michely, T.; Krasheninnikov, A. V.; Busse, C. Ion Impacts on Graphene/Ir(111): Interface Channeling, Vacancy Funnels, and a Nanomesh. *Nano Lett.* **2013**, *13*, 1948−1955.

(45) Sicot, M.; Leicht, P.; Zusan, A.; Bouvron, S.; Zander, O.; Weser, M.; Dedkov, Y. S.; Horn, K.; Fonin, M. Size-Selected Epitaxial Nanoislands Underneath Graphene Moiré on Rh(111). *ACS Nano* **2012**, *6*, 151−158.

(46) Schumacher, S.; Huttmann, F.; Petrović, M.; Witt, C.; Förster, D. F.; Vo-Van, C.; Coraux, J.; Martínez-Galera, A. J.; Sessi, V.; Vergara, I.; Rückamp, R.; Grüninger, M.; Schleheck, N.; Meyer Zu Heringdorf, F.; Ohresser, P.; Kralj, M.; Wehling, T. O.; Michely, T. Europium Underneath Graphene on Ir(111): Intercalation Mechanism, Magnetism, and Band Structure. *Phys. Rev. B: Condens. Matter Mater. Phys.* **2014**, *90*, 235437.

(47) Herbig, C.; Knispel, T.; Simon, S.; Schröder, U. A.; Martínez-Galera, A. J.; Arman, M. A.; Teichert, C.; Knudsen, J.;

Krasheninnikov, A. V.; Michely, T. From Permeation to Cluster Arrays: Graphene on Ir(111) Exposed to Carbon Vapor. *Nano Lett.* **2017**, *17*, 3105−3112.

(48) Feibelman, P. J. Pinning of Graphene to Ir(111) by Flat Ir Dots. *Phys. Rev. B: Condens. Matter Mater. Phys.* **2008**, *77*, 165419.

(49) Knudsen, J.; Feibelman, P. J.; Gerber, T.; Grånäs, E.; Schulte, K.; Stratmann, P.; Andersen, J. N.; Michely, T. Clusters Binding to the Graphene Moiré on Ir(111): X-Ray Photoemission Compared to Density Functional Calculations. *Phys. Rev. B: Condens. Matter Mater. Phys.* **2012**, *85*, 035407.

(50) Horcas, I.; Fernández, R.; Gomez-Rodriguez, J.; Colchero, J.; Gómez-Herrero, J.; Baro, A. WSXM: a Software for Scanning Probe Microscopy and a Tool for Nanotechnology. *Rev. Sci. Instrum.* **2007**, *78*, 013705.

(51) Hohenberg, P.; Kohn, W. Inhomogeneous Electron Gas. *Phys. Rev.* **1964**, *136*, B864−B871.

(52) Kohn, W.; Sham, L. J. Self-Consistent Equations Including Exchange and Correlation Effects. *Phys. Rev.* **1965**, *140*, A1133−A1138.

(53) Kresse, G.; Hafner, J. *Ab initio* Molecular Dynamics for Liquid Metals. *Phys. Rev. B: Condens. Matter Mater. Phys.* **1993**, *47*, 558−561.

(54) Kresse, G.; Furthmüller, J. Efficient Iterative Schemes for *ab initio* Total-Energy Calculations Using a Plane-Wave Basis Set. *Phys. Rev. B: Condens. Matter Mater. Phys.* **1996**, *54*, 11169−11186.

(55) Kresse, G.; Joubert, D. From Ultrasoft Pseudopotentials to the Projector Augmented-Wave method. *Phys. Rev. B: Condens. Matter Mater. Phys.* **1999**, *59*, 1758−1775.

(56) Perdew, J. P.; Burke, K.; Ernzerhof, M. Generalized Gradient Approximation Made Simple. *Phys. Rev. Lett.* **1996**, *77*, 3865−3868.

(57) Blöchl, P. E. Projector Augmented-Wave Method. *Phys. Rev. B: Condens. Matter Mater. Phys.* **1994**, *50*, 17953−17979.

(58) Valerius, P.; Herbig, C.; Will, M.; Arman, M. A.; Knudsen, J.; Caciuc, V.; Atodiresei, N.; Michely, T. Annealing of Ion-Irradiated Hexagonal Boron Nitride on Ir(111). *Phys. Rev. B: Condens. Matter Mater. Phys.* **2017**, *96*, 235410.

(59) Lee, K.; Murray, E. D.; Kong, L.; Lundqvist, B. I.; Langreth, D. C. Higher-Accuracy van der Waals Density Functional. *Phys. Rev. B: Condens. Matter Mater. Phys.* **2010**, *82*, 081101.

(60) Hamada, I. van der Waals Density Functional Made Accurate. *Phys. Rev. B: Condens. Matter Mater. Phys.* **2014**, *89*, 121103.

(61) Momma, K.; Izumi, F. VESTA 3 for Three-Dimensional Visualization of Crystal, Volumetric and Morphology Data. *J. Appl. Crystallogr.* **2011**, *44*, 1272−1276.

4.1 Manuscript 1: Supporting Information

Supporting Information:

A Monolayer of Hexagonal Boron Nitride on Ir(111) as a Template for Cluster Superlattices

—

Supplementary information

Moritz Will,[*][†] Nicolae Atodiresei,[*][‡] Vasile Caciuc,[‡] Philipp Valerius,[†] Charlotte Herbig,[†] and Thomas Michely[†]

[†]*II. Physikalisches Institut, Universität zu Köln, Cologne, D-50937, Germany*

[‡]*Peter Grünberg Institut (PGI-1) and Institute for Advanced Simulation (IAS-1), Forschungszentrum Jülich and JARA, Jülich, D-52425, Germany*

E-mail: will@ph2.uni-koeln.de; n.atodiresei@fz-juelich.de(theory)

Phone: +49 (0)221 470-6876
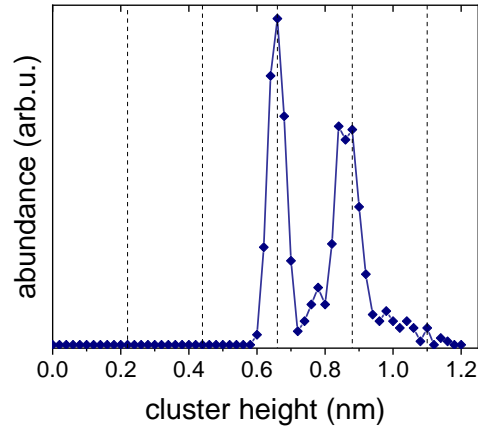
Figure S1: Cluster height distribution for the STM topograph shown in the main manuscript in Figure 1a, representing 0.57 ML Ir deposited at 250 K and imaged at 300 K. Dashed lines indicate integer multiples of the Ir(111) inter-layer distance 0.22 nm.
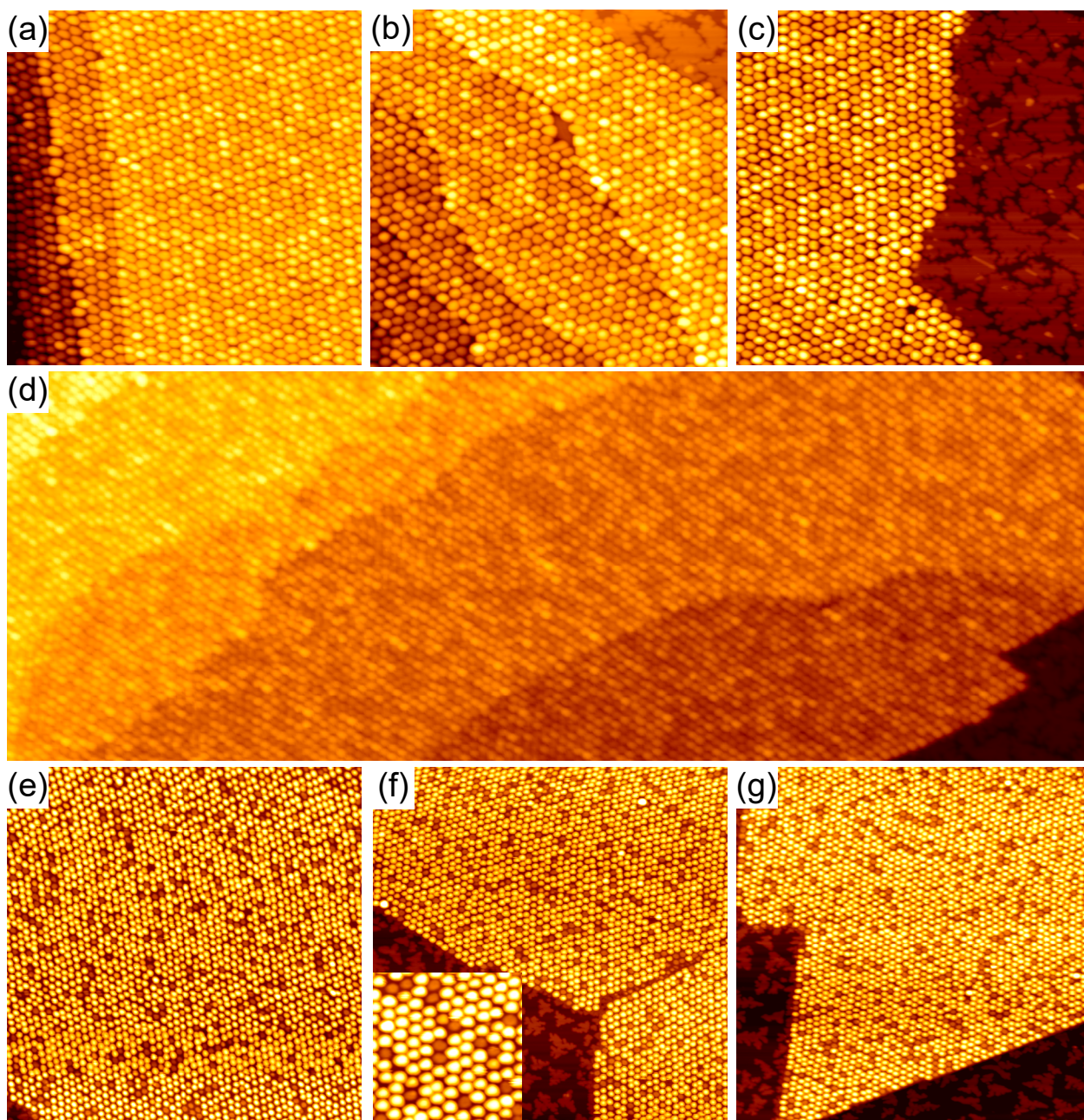
Figure S2: (a)-(d) STM topographs of 0.57 ML Ir deposited at 250 K and imaged at 300 K. (e)-(g) STM topographs of 0.34 ML Ir deposited at 350 K. The inset in (f) displays a magnified detail from the main image. Image sizes are (a)-(c) 80 nm × 80 nm, (d) 320 nm × 115 nm, (e)-(g) 133 nm × 133 nm, and for the inset in (f) 26 nm × 26 nm. Tunneling parameters are (a)-(c) $U_{bias} = -2.4$ V and $I_t = 58$ pA, (d) $U_{bias} = -2.7$ V and $I_t = 64$ pA, (e)-(g) $U_{bias} = -1.7$ V and $I_t = 59$ pA.
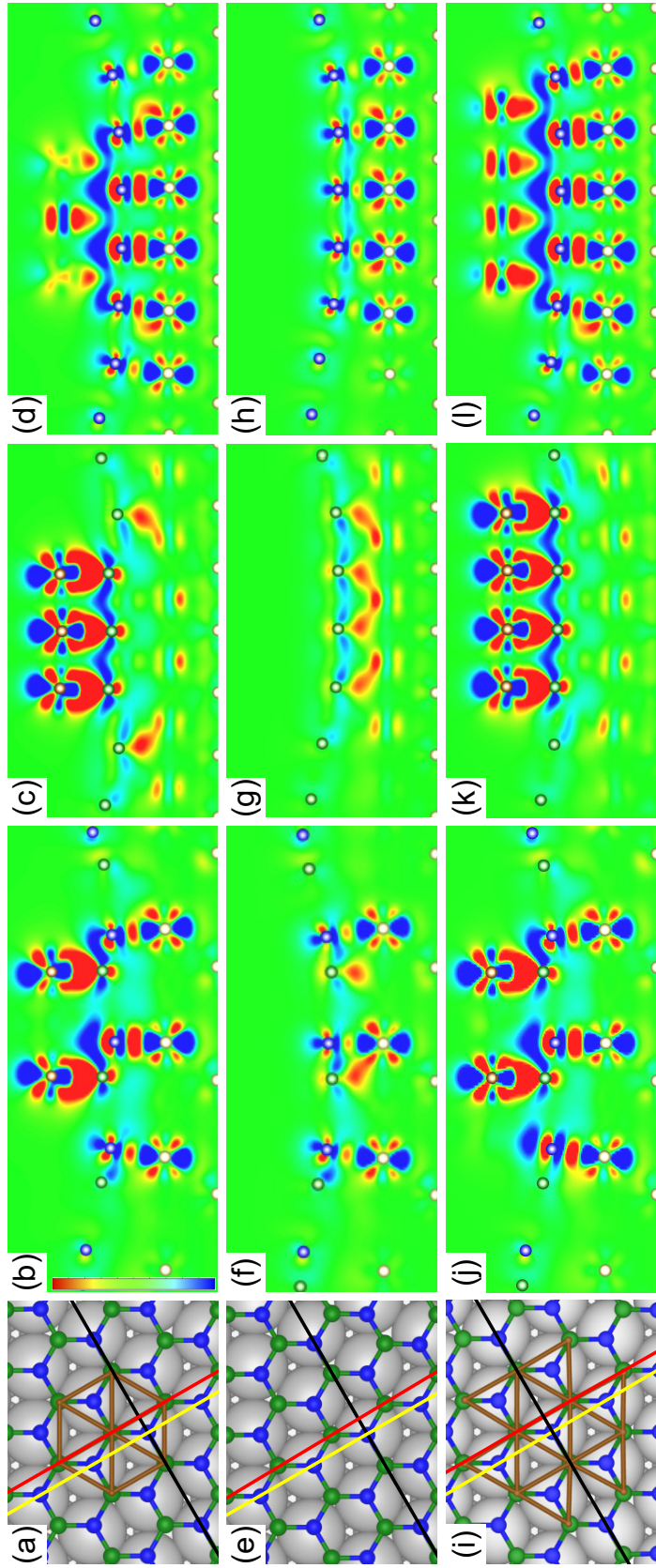
Figure S3: (a) Top view of a relaxed DFT geometry of an Ir heptamer (brown circles connected by sticks) adsorbed on h-BN on Ir(111). (b)-(d) Charge density difference between the relaxed system and subsystems of Ir cluster, h-BN and Ir substrate without changing atomic coordinates within each subsystem. The plot displayed in (b) is a cut along the black line in (a), (c) is along the red line, and (d) is along the yellow line. (e) Relaxed DFT geometry of the bare h-BN slab on Ir(111) without an adsorbed cluster. Correspondingly, (f) shows the charge density difference cut along the black line in (e), (g) along the red line and (h) along the yellow line. (i) Relaxed DFT geometry of an Ir dodecamer on h-BN on Ir(111). Again, (j) shows the charge density difference cut along the black line in (i), (k) along the red line, and (l) along the yellow line. In the geometries Ir substrate atoms are colored gray, B atoms green and N atoms blue. The color scale in the charge density difference plots ranges from a gain of $0.05\,e/A^3$ (red) to a loss of $0.05\,e/A^3$ (blue) in charge density.
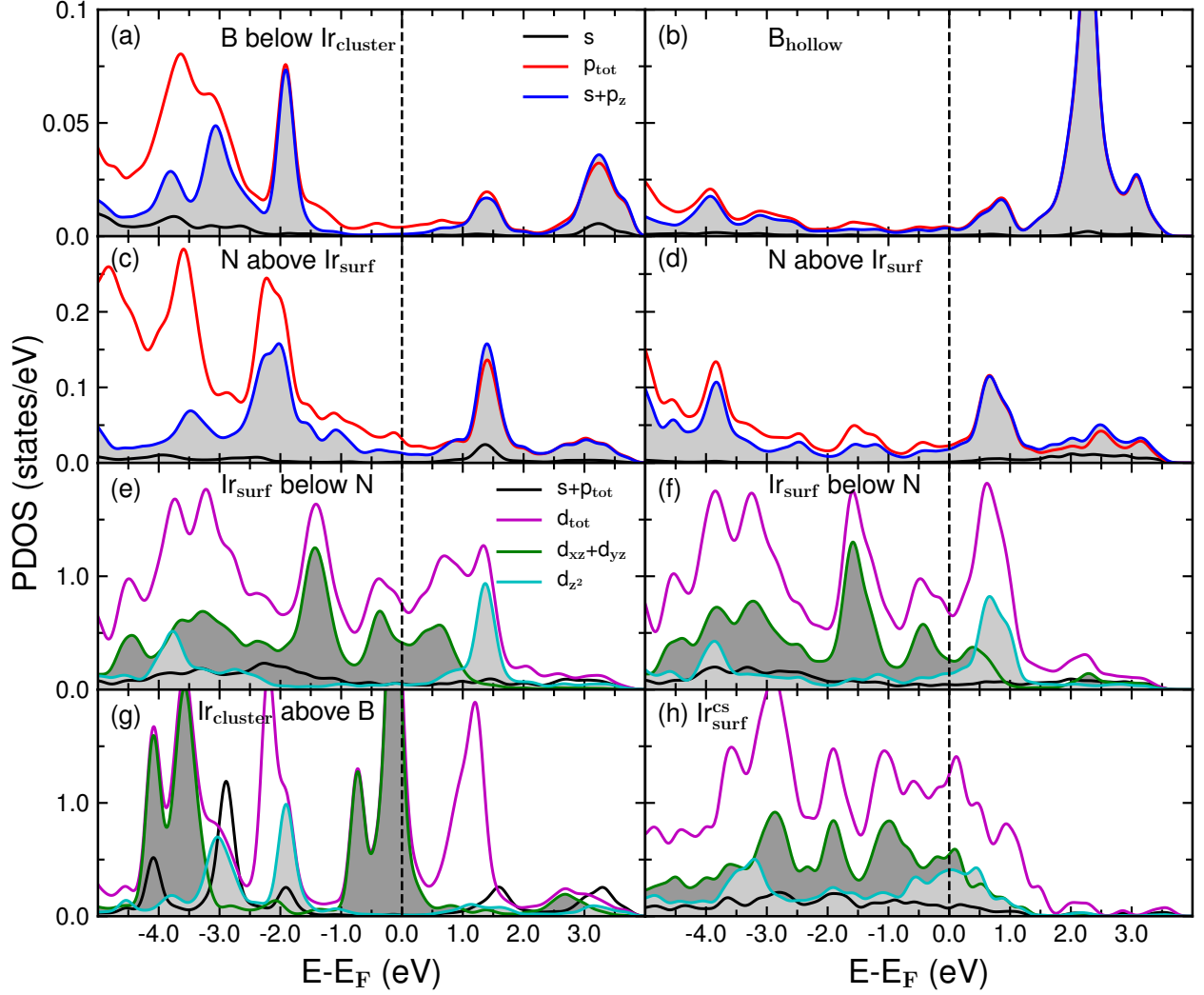
Figure S4: The projected density of states (PDOS) for (a) a B atom beneath an $Ir_{cluster}$ cluster atom, (b) the same B atom in a hollow site of the clean h-BN on Ir(111), (c) an N atom above an Ir_{surf} surface atom with adsorbed Ir cluster on top and (d) the same atom in the case of the pristine h-BN/Ir(111) system. Additionally, the PDOS of an Ir_{surf} atom below the N atom in the hybrid system (e) with and (f) without the Ir cluster as well as (g) that of an $Ir_{cluster}$ atom above the B atom are also shown. For comparison, in (h) the PDOS of the clean surface Ir_{surf}^{cs} atom with a substantial d_{z^2} contribution at E_F is depicted too. Then, as a key feature, note that at the Fermi energy E_F the electronic states of the h-BN on Ir(111) with and without the Ir cluster system are dominated by the out-of-plane $d_{xz} + d_{yz}$ states of the $Ir_{cluster}$ and Ir_{surf} atoms. On the other hand, the d_{z^2} orbitals of Ir_{surf} are split into bonding (below E_F) and anti-bonding (above E_F) states hybridized with the p_z ones of the N atoms located directly above them [see also Fig. 2(g) and (j) in the main text].

We note that the PDOS evaluated for a boron atom beneath an $Ir_{cluster}$ cluster one (see

Fig. S4a) exhibits a different peak structure as compared with the PDOS calculated for the same atom in a hollow site of the clean h-BN on Ir(111) (see Fig. S4b). This observation agrees well with a predominantly sp^3 hybridization of the h-BN in the valley region upon the adsorption of the Ir cluster while it is characterized by a sp^2 one in the case of the pristine h-BN/Ir(111) system.

Then, as discussed in the main text, the analysis of the PDOS for the Ir heptamer/h-BN/Ir(111) system revealed that at the h-BN/Ir(111) interface the surface Ir atoms form bonding and anti-bonding combinations with the p_z ones of the corresponding on-top N atoms (see Fig. S4c and e). A similar physical picture emerges for the clean h-BN on Ir(111) as depicted in Fig. S4d and f. However, the magnitude of this bonding-antibonding splitting of the Ir d_{z^2}- N p_z hybrid electronic states is significantly larger (by ≈ 0.8 eV) in the presence of the Ir cluster as compared to the clean h-BN/Ir(111) system, which clearly indicates a stronger local N-Ir interaction in the former case.
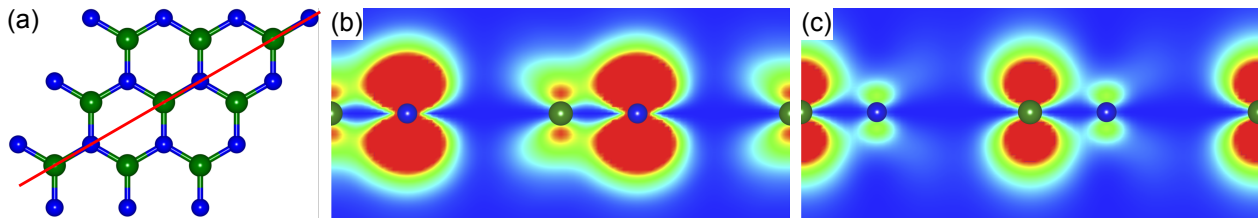
Figure S5: (a) Top view of a freestanding h-BN monolayer with a perpendicular plane crossing through the B-N bonds. (b) A charge density plot in the plane drawn in (a) for the highest occupied h-BN π-electronic states with a p_z character at the B and N atomic sites. Since N has a higher electronegativity as B, these π electronic states are mostly located at the N atoms with a large extension in space. (c) On the other hand, the lowest unoccupied π states of h-BN are predominantly located at the B atoms and exhibit also a substantial spatial extension.
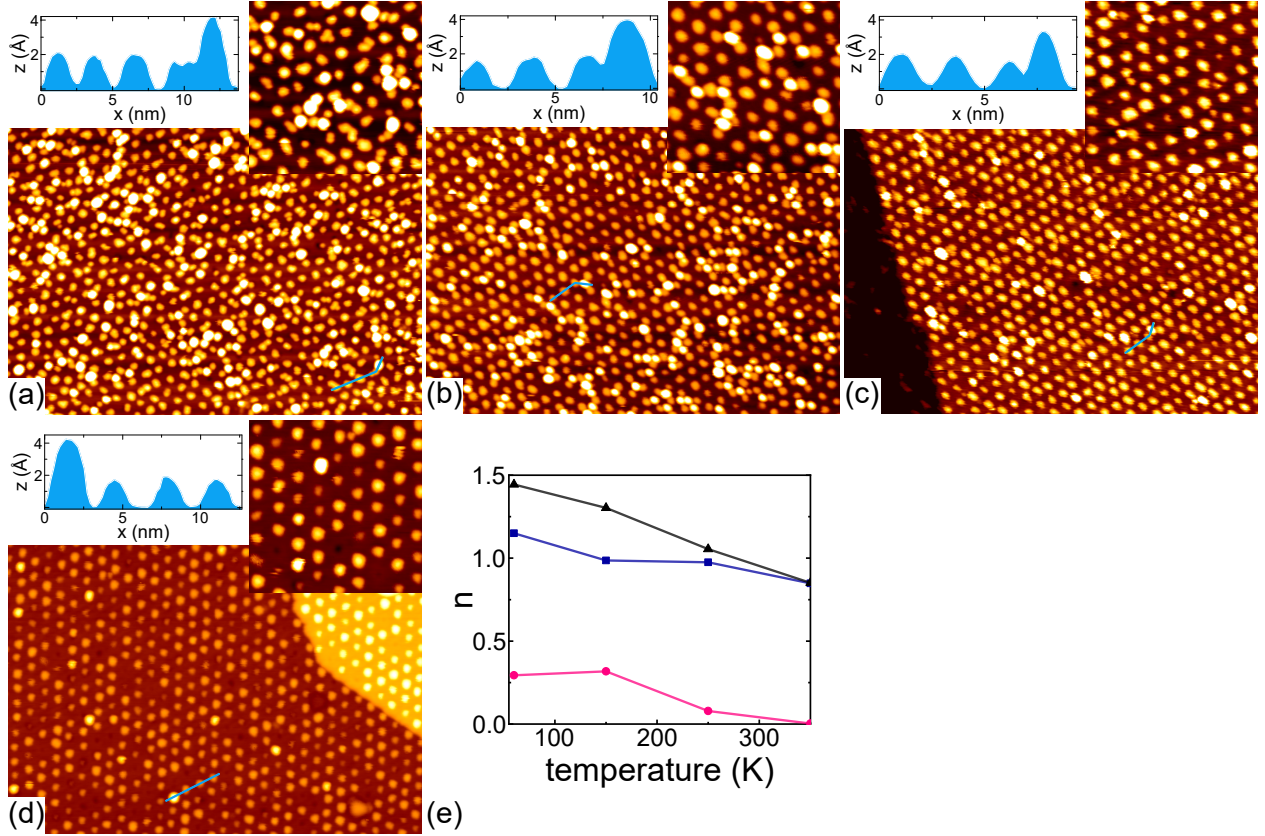
Figure S6: STM topographs of 0.05 ML Ir on h-BN/Ir(111), deposited at different temperatures. Deposition temperatures are: (a) 60 K, (b) 150 K, (c) 250 K, (d) 350 K. The image size is always 80 nm × 80 nm for the main images and 23 nm × 23 nm for the insets. All images were taken at temperatures lower than or equal to the indicated deposition temperature. (e) Cluster number density for the different deposition temperatures. Blue squares represent the number density of clusters in the valley n_{valley}, while pink dots are the cluster number density of center region clusters n_{center} (for the definition of the three regions in the moiré supercell, refer to Figure 2a in the main manuscript). Black triangles indicate the total cluster number density $n = n_{valley} + n_{center}$. Lines to guide the eye. Tunneling parameters are (a) $U_{bias} = -2.4$ V and $I_t = 84$ pA, (b) $U_{bias} = -2.4$ V and $I_t = 80$ pA, (c) $U_{bias} = -2.6$ V and $I_t = 50$ pA, (d) $U_{bias} = -2.9$ V and $I_t = 100$ pA.
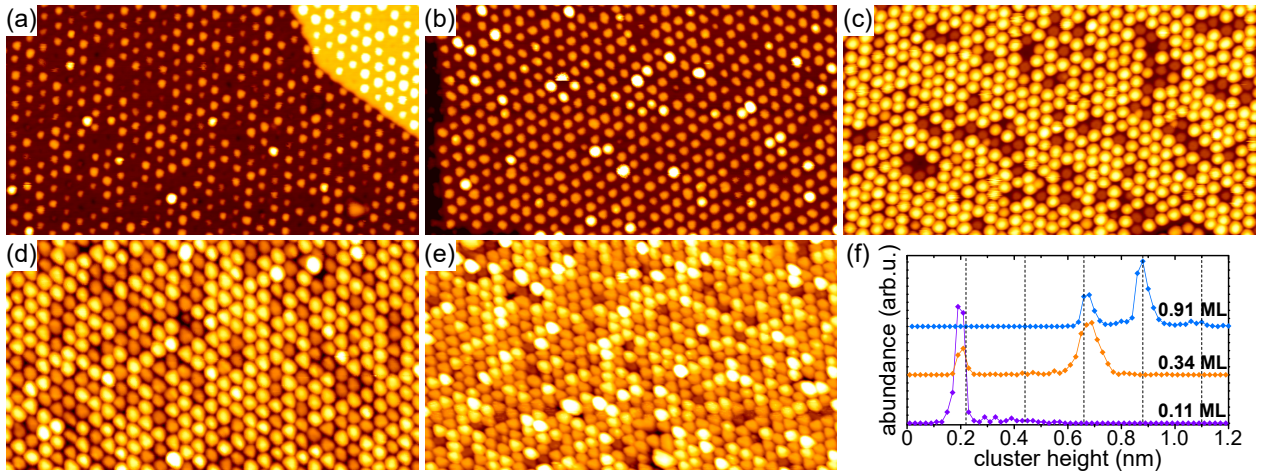
Figure S7: (a)–(e) STM topographs of h-BN/Ir(111) after deposition of an amount θ of Ir at 350 K. (a) $\theta = 0.05$ ML, average cluster size in atoms $s_{av} = 6$. (b) $\theta = 0.11$ ML, $s_{av} = 13$. (c) $\theta = 0.34$ ML, $s_{av} = 39$. (d) $\theta = 0.91$ ML, $s_{av} = 104$. (e) $\theta = 1.5$ ML, $s_{av} = 195$. The image size is always 80 nm $\times$ 45 nm. (f) Cluster height distribution for different coverages. Note that low cluster numbers are difficult to see in the distribution due to their fluctuating heights. This becomes apparent for two-layer clusters in the case of 0.11 ML and 0.34 ML Ir, or five-layer clusters for 0.91 ML Ir. Dashed lines indicate integer multiples of the Ir(111) inter-layer distance 0.22 nm. Tunneling parameters are (a) $U_{bias} = -2.9$ V and $I_t = 100$ pA, (b) $U_{bias} = -1.8$ V and $I_t = 65$ pA, (c) $U_{bias} = -1.7$ V and $I_t = 59$ pA, (d) $U_{bias} = -1.6$ V and $I_t = 64$ pA, (e) $U_{bias} = -1.7$ V and $I_t = 140$ pA.

Manuscript 2: Growth, Stability, and Electronic Decoupling of Pt Clusters on h-BN/Ir(111)

This chapter wholly consists of the above-named manuscript and its supplement.

The experiments were proposed by M. Will, P. Bampoulis, T. Hartl, J. Knudsen, and T. Michely. All STM and STS measurements were carried out by M. Will, T. Hartl, and P. Bampoulis at ATHENE. The STM data were analyzed by M. Will, while the STS data were analyzed by M. Will and P. Bampoulis. The work in Cologne was supervised by T. Michely. P. Lacovig and S. Lizzit set up the XPS experimental apparatus at ELETTRA with help from M. Will and P. Bampoulis. The XPS measurements were carried out by M. Will, T. Hartl, P. Bampoulis, V. Boix de la Cruz, and J. Knudsen. J. Knudsen and T. Michely supervised the XPS measurements. XPS data were analyzed by M. Will.

M. Will wrote the manuscript and finalized it in close collaboration with P. Bampoulis, T. Hartl, J. Knudsen, and T. Michely.

Growth, Stability and Electronic Decoupling of Pt Clusters on h-BN/Ir(111)

Moritz Will,[*,†] Tobias Hartl,[†] Virginia Boix de la Cruz,[‡] Paolo Lacovig,[¶] Silvano Lizzit,[¶] Jan Knudsen,[‡,§] Thomas Michely,[†] and Pantelis Bampoulis[†]

[†]II. Physikalisches Institut, Universität zu Köln, Cologne, D-50937, Germany

[‡]Division of Synchrotron Radiation Research, Lund University, Box 188, SE-22100 Lund, Sweden

[¶]Elettra-Sincrotrone Trieste S.C.p.A., Strada Statale 14 Km 163.5, I-34149 Trieste, Italy

[§]MAX IV Laboratory, Lund University, Box 118, SE-22100 Lund, Sweden

E-mail: will@ph2.uni-koeln.de

Phone: +49 (0)221 470-6876

1

Abstract

Motivated by the relevance of Pt clusters in heterogeneous catalysis, ordered Pt cluster superlattices are templated by the moiré of monolayer hexagonal boron nitride (h-BN) with Ir(111). Using X-ray photoelectron spectroscopy, scanning tunneling microscopy and scanning tunneling spectroscopy we provide a comprehensive picture for the mechanism of cluster binding, the thermal stability of clusters, cluster superlattice decay mechanisms, the morphological evolution of cluster shape with size, and finally for Pt cluster decoupling and internal electronic structure. It is found that the Pt cluster superlattices on h-BN on Ir(111) are thermally more stable than any other Pt cluster superlattice, are well decoupled from their substrate, and display a discrete cluster height-dependent electronic structure.

Introduction

To obtain an understanding of mechanisms in heterogeneous catalysis often model catalysts are used, *i.e.* simpler systems that can be controlled much better than industrial catalysts.[1] Examples include single crystal surfaces or size-selected metal clusters.[2,3] A new direction for such model systems are ordered cluster superlattices grown on a template, such as a thin Al_2O_3 layer on $Ni_3Al(111)$, or graphene (Gr) and hexagonal boron nitride (h-BN) moirés on single crystal surfaces.[4–8] These superlattices display an unparalleled high density of clusters with a narrow size distribution, each in the same well-defined and inert environment. Thereby the relation between the cluster structure and its catalytic activity becomes more direct and easier to interpret.

Pt clusters are of particular interest in surface chemistry due to their potential use as catalysts for many relevant reactions, *e.g.* CO oxidation, ethane hydrogenolysis, methane decomposition, water-gas shift, or in electrocatalysis.[9–15] Therefore, Pt cluster superlattices are of specific interest as model catalysts. Pt cluster superlattices have been grown on Gr/Ir(111),[16,17] Gr/Ru(0001)[18] and thin alumina films on $Ni_3Al(111)$.[19] Adsorption of O_2,

H_2, and CO on Pt cluster arrays were conducted and provide evidence for CO oxidation at room temperature.[20] The reaction of Pt clusters on Gr/Rh(111) with CO,[21] S,[22,23] and SO_2[24] as well as the system Pt/h-BN/Rh(111)[25] and its reaction with ethene[26,27] were investigated recently. However, one factor impeding the wide-spread use of such cluster arrays is their thermal decay through sintering already starting at 450 K.[17]

Ir cluster superlattices on h-BN/Ir(111) display excellent order and have been demonstrated to be thermally stable up 700 K,[28] *i.e.* to much higher temperatures than what has been reported up to now for other systems. This finding motivated the present study on structural evolution and thermal stability of Pt clusters on the same template. Besides the relevance of the system in view of potential applications in catalysis, the use of Pt as cluster metal - a metal distinct from the substrate one - allows us to experimentally study cluster binding by tracking the core level shifts of the involved elements using high resolution x-ray photoemission (XPS). To obtain a comprehensive picture, the chemical view of XPS is complemented by the structural perspective of scanning tunneling microscopy (STM). Lastly, scanning tunneling spectroscopy (STS) provides insight into the electronic decoupling of the clusters from the h-BN/Ir(111) substrate and resulting confinement effects.

In preparation of the data presented below, we briefly summarize the present knowledge on the h-BN/Ir(111) template. H-BN/Ir(111) forms a moiré superstructure with (11.7×11.7) h-BN unit cells matching (10.7×10.7) Ir surface unit cells, which results in a 29.1 Å repeat distance. The layer displays one chemisorbed and reactive valley in each moiré unit cell within an otherwise flat, physisorbed mesa.[29] In the valleys, defined by the locations in the moiré where N-atoms sit atop Ir substrate atoms, the sp^2 hybridized h-BN displays partial sp^3 character whereby bonds with the Ir substrate and a reactive spot towards the vacuum are formed.[29] Note that an sp^3 hybridized layer displays σ-bonds normal to the layer into both half-spaces. Upon deposition of Ir, clusters are formed in the reactive valleys, whereby the sp^3 binding motif is modified and strengthened.[28] This picture of cluster binding is up to now based only on density functional theory (DFT) calculations.
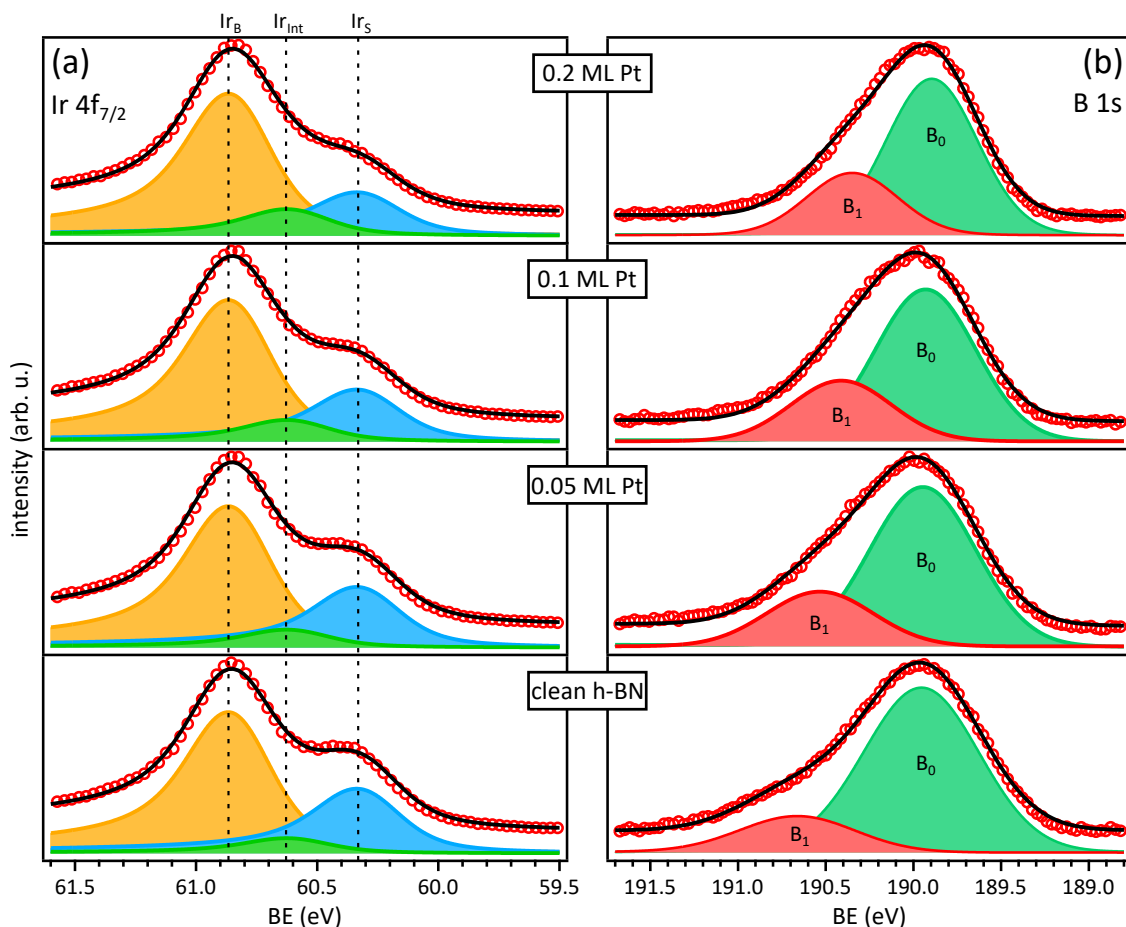
3

Results and discussion

Figure 1: (a) Ir $4f_{7/2}$ core level spectra measured at a photon energy of $h\nu = 390$ eV for clean h-BN/Ir(111) (bottom panel) and increasing amounts of Pt deposited on top. The three fitted components are denoted as Ir_B (orange bulk component), Ir_S (blue surface component), and Ir_{Int} (green interface component). (b) B 1s core level spectra measured at a photon energy of $h\nu = 390$ eV of the corresponding Pt coverages fitted with two components (see text). In both cases the data points are represented by red circles and the absolute fit by a solid black line.

Cluster binding: The Ir $4f_{7/2}$ core level measured on pristine h-BN/Ir(111) without Pt deposition is shown as a reference in the bottom panel of Figure 1a. The spectrum is fitted with three components which result from the different chemical environment of Ir atoms in the bulk (attributed to the Ir_B component at 60.86 eV, orange in Figure 1a), at the surface without bonds to adsorbates (Ir_S component at 60.34 eV, blue), and at the surface with chemical bonds to the valley of the h-BN moiré (Ir_{Int} component at 60.63 eV, green), in line

4

with refs. 29 and 30. Upon Pt deposition at 300 K a cluster superlattice forms with about one cluster per moiré unit cell growing almost linearly with deposited amount to about 23 atoms after 0.2 ML deposited (compare our STM data below). In consequence of deposition we observe a gradual redistribution of spectral weight from the surface component Ir_S to the interface component Ir_{Int}. This indicates an increasing amount of Ir surface atoms to which h-BN binds chemically.

The B 1s core level measured on pristine h-BN/Ir(111) without Pt deposited is shown in the bottom panel of Figure 1b for reference. The spectrum is fitted with two components which represent weakly bound B atoms B_0 at a BE of 189.95 eV (green) and strongly bound B atoms B_1 at a BE of 190.64 eV (red). These components are due to the two species of boron atoms in the mesa and the valley, respectively, consistent with the literature.[29] Upon Pt deposition we observe a redistribution of spectral weight from the B_0 component to the B_1 component of strongly interacting atoms (compare bottom two panels of Figure 1b). Moreover, a continuous downshift in the binding energy (BE) of the B_1 component with increasing coverage is observed.
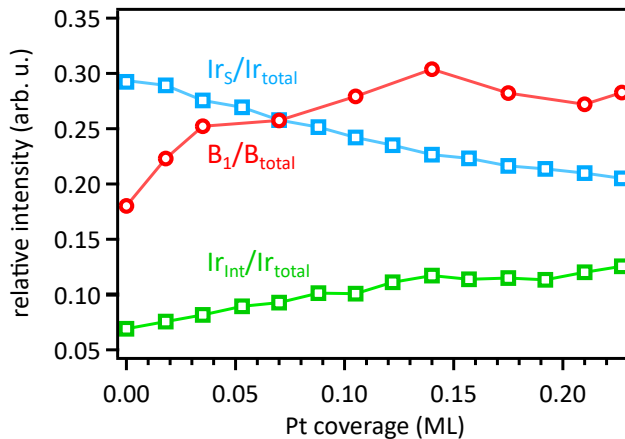

Figure 2: XPS analysis of the relative intensities of the B 1s and Ir $4f_{7/2}$ components as a function of Pt coverage. Blue squares: ratio of the intensities of the surface component Ir_S to the total intensity. Green squares: ratio of the intensities of the interface component Ir_{Int} to the total intensity. Red circles: ratio of the intensities of the B_1 to the total intensity of the B 1s core level. Lines to guide the eye.

A quantitative analysis of the spectral weight evolution of the Ir 4f and B 1s core level

components Ir_S, Ir_{Int}, and B_1 is provided in Figure 2. The components are normalized to the total intensity of the respective core level, and plotted as a function of the deposited Pt amount in green, blue, and red (color code according to color of component in Figure 1). The weight of the B_1 and Ir_{Int} components is increasing due to Pt deposition, while Ir_S is decreasing. The changes of Ir_S and Ir_{Int} evolve in parallel. Additionally, the rate of change is strongest for small coverages, in particular for the case of the B_1 component.

The interpretation of these changes is straightforward. Upon Pt deposition, clusters form in the valley regions of the moiré. Due to the growing footprint of the clusters with increasing Pt deposition, the valley region, *i.e.* the sp^3-hybridized area of h-BN, expands. In this area, strong bonds of B atoms to Pt cluster atoms are formed, giving rise to the growth of the B_1 component. The growth of the rehybridized h-BN area, also binding chemically to the Ir substrate, is directly reflected in the growth of the Ir_{Int} and decrease of the Ir_S component. These observations are firsthand experimental evidence for the involvement of the Ir substrate in cluster binding through the rehybridization mechanism, as predicted by DFT calculations.[28] These previous DFT calculations also indicate that it is the N atoms under the cluster being in chemical bond with the Ir, while the B atoms are in chemical bond to the Pt cluster. Binding through the rehybrization mechanism requires the N or B atoms to match with the top site of an Ir or Pt atom, repectively. As the lattice parameter of h-BN (2.48 Å[29]) differs substantially from the Ir (2.71 Å[31]) and Pt (2.77 Å[32]), at some extension the distance between N and Ir atoms increase. Consequently, further away from the center of the valley region rehybridization becomes energetically less favorable, thus slowing down the rate of decrease (increase) of the Ir_S (Ir_{Int}) component upon growing cluster footprint.

We interpret the downshift of the B_1 component in view of the results of the DFT calculations as well.[28] Prior to cluster adsorption, the B atoms in the valleys are only weakly interacting with the Ir surface. When a cluster is located in the valley, the B atoms move substantially upwards towards the cluster and strong bond formation to the cluster is observed. Thus, the chemical environment of the B atoms in the valley changes, explaining the
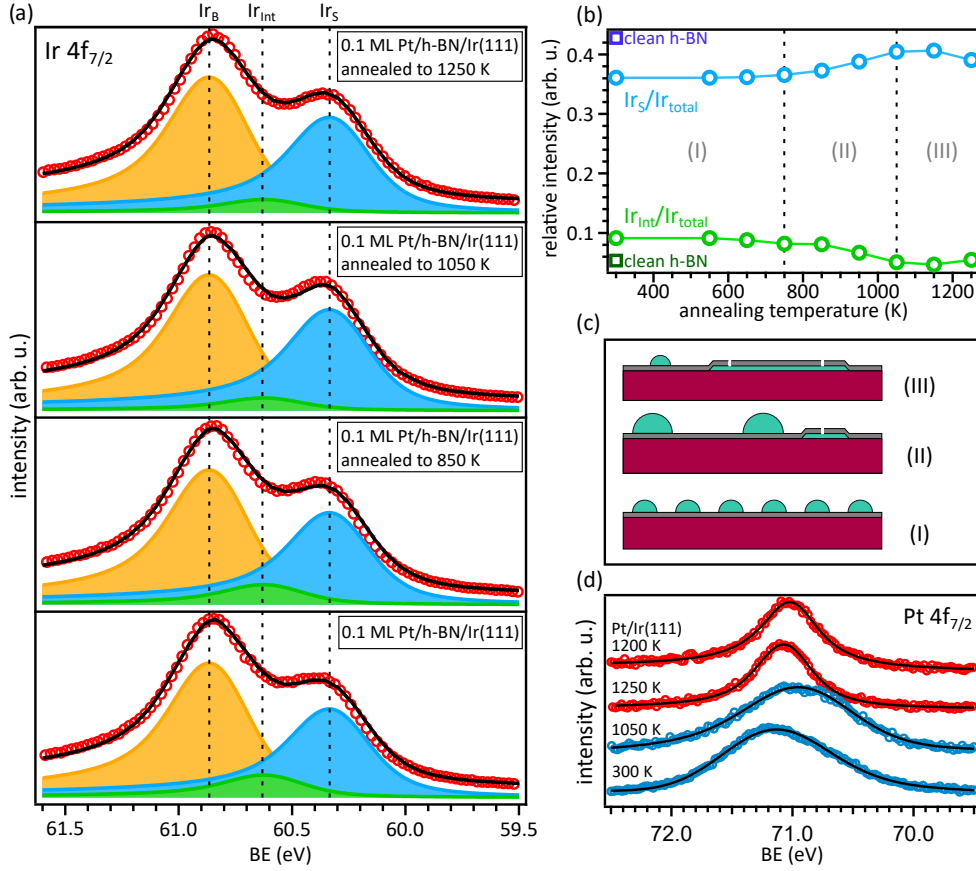
shift of the B_1 component.

Figure 3: (a) XP spectra of the Ir $4f_{7/2}$ core level measured at a photon energy of $h\nu = 140$ eV after deposition of 0.1 ML Pt on h-BN/Ir(111) at room temperature (bottom panel) and subsequent annealing steps up to 1250 K (intermediate and top panels). All spectra were taken at room temperature. (b) Change of weight of Ir_S and Ir_{Int} normalized to the total intensity of the Ir $4f_{7/2}$ core level as a function of annealing temperature for 0.1 ML Pt/h-BN/Ir(111) (circles). The values of clean h-BN/Ir(111) are given as squares for reference. Lines to guide the eye. Dashed lines separate the regimes I-III of cluster superlattice state and decay. See text. (c) Sketches depicting the regimes I-III of cluster superlattice state and decay. See text. Teal: deposited Pt metal; dark gray: h-BN; purple: Ir(111) substrate. (d) XP spectra of the Pt $4f_{7/2}$ core level after deposition of 0.1 ML Pt on h-BN/Ir(111) at room temperature (bottom, blue), after annealing at 1050 K (middle, blue), and 1250 K (middle, red). For comparison, the spectrum of 0.1 ML Pt deposited on bare Ir(111), after annealing at 1200 K is provided (top, red). Fits are represented by black lines.

Thermal stability – cluster sintering and intercalation: Figure 3a displays a sequence of XP spectra of the Ir $4f_{7/2}$ core level taken after deposition of 0.1 ML Pt at 300 K and subsequent annealing steps at 850 K, 1050 K, and 1250 K (bottom to top panels).

In between the annealing steps, the sample was cooled back to 300 K and the data was recorded. As in Figure 1a, the spectra are fitted by three components Ir_B, Ir_{Int}, and Ir_S. It is apparent that above 850 K the interface component Ir_{Int} gradually loses weight, while the surface component Ir_S gains weight. At 1250 K, the intensity of Ir_{Int} rises again, while Ir_S shrinks.

Figure 3b presents the evolution of Ir_{Int} and Ir_S with temperature quantitatively, with the intensity of the components normalized to the total intensity of the Ir 4f core level. Three regimes in the thermal evolution can be distinguished. (I) Until 750 K the relative weights of the components remain almost constant, as the cluster superlattice remains intact (bottom sketch in Figure 3c). (II) Above 750 K, the weight of Ir_S gradually increases while the one of Ir_{Int} gradually decreases. We attribute these changes to the decay of the cluster superlattice *via* sintering. Sintering clears moiré valleys which results in the recovery of the surface peak and reduction of the interface peak towards the values of bare h-BN, shown as squares in Figure 3b (compare middle panel of Figure 3c). (III) Beyond 1050 K we observe no further increase of the two components. Instead, Ir_{Int} rises again, while the Ir_S component drops. We attribute these changes to the intercalation of Pt clusters and the formation of intercalated islands at the interface between h-BN and Ir(111). Thereby the number of Ir surface atoms is reduced and thus Ir_S drops. Eventually, hardly any cluster remains on top of the h-BN (compare top panel of Figure 3c).

Additional evidence for intercalation of the Pt cluster material at high temperature is provided by the data displayed in Figure 3d. The Pt $4f_{7/2}$ core level after deposition at 300 K and after annealing to 1050 K are quite similar and rather broad. Upon annealing to 1250 K, the spectrum narrows considerably. It shifts to higher binding energies with a clear maximum at 71.06 eV and a FWHM of 0.55 eV. The spectrum is almost identical to a reference spectrum shown as well in Figure 3d. Here, Pt was deposited at 300 K on bare Ir(111) and subsequently annealed to 1200 K.

The similarity of the two spectra after deposition at 300 K on h-BN/Ir(111) and after

additional annealing to 1050 K (blue Figure 3d) and their difference from the two other spectra that are among themselves rather similar (red in Figure 3d) is interpreted as follows. The two blue spectra are characteristic for the multitude of different chemical environments of the Pt atoms in a cluster (surface atoms, edge atoms, corner atoms, atoms bound the h-BN, interior atoms), causing a multitude of different core level shifts that overlap. Although the clusters sinter upon annealing, the majority of Pt is present as clusters up to 1050 K and thus the spectra are similar. The narrower red spectra indicate a more homogeneous chemical environment, and as the reference spectrum is known to result form Pt directly adsorbed pseudomorphically to Ir(111), we infer that the same holds for the 1250 K spectrum, consistent with intercalation of the Pt cluster material. Further evidence for intercalation of cluster Pt by annealing is provided by the B 1s and N 1s core levels presented in Figure S2 of the supporting information.

A complementary view of cluster sintering and intercalation is provided by STM for larger clusters (average size 57 atoms, see below for size determination) grown by deposition of 0.5 ML Pt at 300 K. The STM topographs presented in Figure 4a-f show the sample directly after 0.5 ML Pt deposition and stepwise annealing at 650 K, 750 K, 850 K, 950 K, 1050 K, and 1250 K for 300 s. Imaging is always conducted at room temperature. No effect on the cluster number density n per moiré unit cell is observed up to 650 K (Figure 4a). After annealing at 750 K, depicted in Figure 4b, the cluster superlattice is still close to intact, but the onset of two decay processes is apparent. First, a flat island spreading over multiple moiré unit cells is visible (highlighted by a blue arrow). We attribute this to intercalated Pt at the interface of h-BN and Ir(111). Such an intercalation island forms by penetration of cluster material through the h-BN, driven by the energy gain of surface and interface energy when a cluster transforms to a flat island adsorbed to Ir(111).

Second, in Figure 4b and even more pronounced in Figure 4c also large clusters are observed next to empty moiré cells, while at the same time most clusters appear unchanged. This morphology is consistent with Smoluchowski ripening, *i. e.* the coalescence of clusters
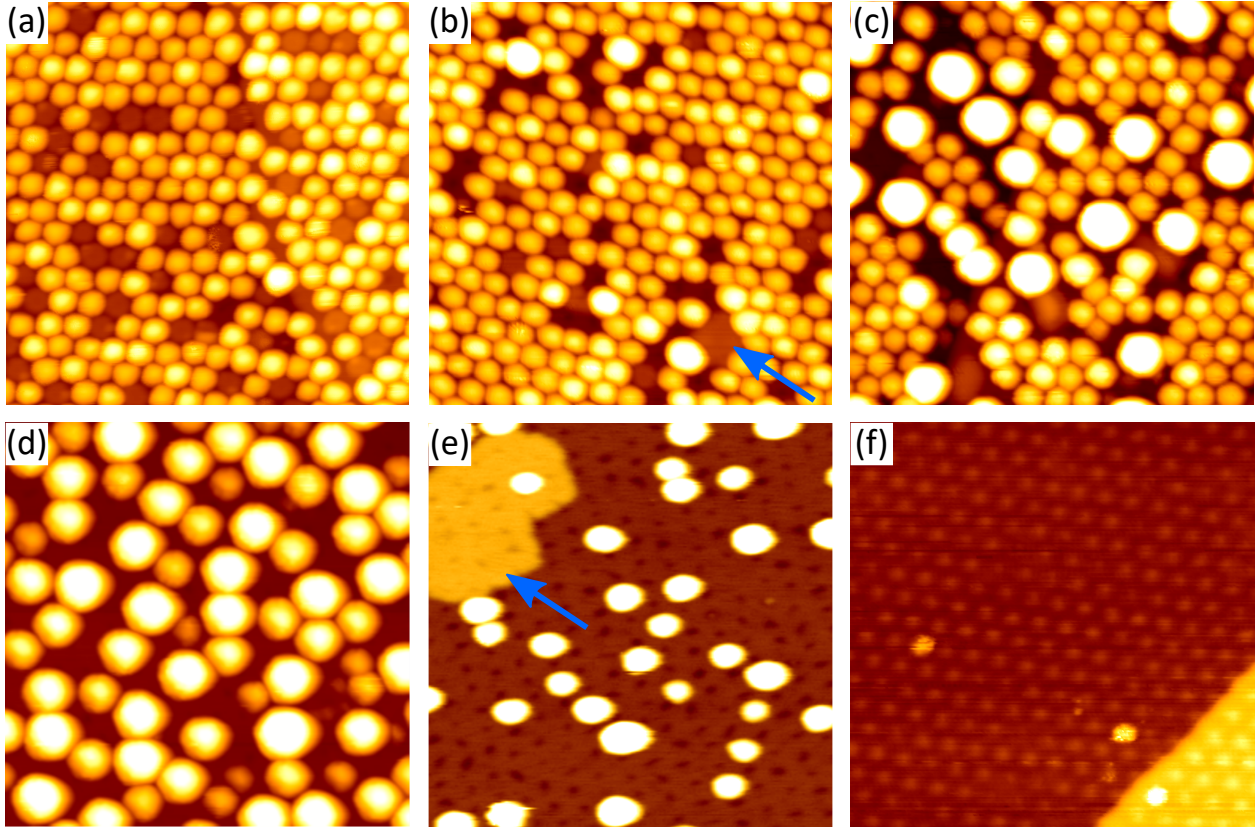
Figure 4: STM topographs after 0.5 ML Pt deposited at 300 K on h-BN/Ir(111) and annealed to (a) 650 K, (b) 750 K, (c) 850 K, (d) 950 K, (e) 1050 K, and (f) 1250 K prior to imaging at 300 K. Blue arrows in (b) and (e) highlight intercalation islands. See text. Image size in all cases is 45×45 nm^2.

upon encounter due to thermally excited fluctuations around their equilibrium position, in agreement with previous observations.[17,28] It is inconsistent with Ostwald ripening, *i. e.* the gradual shrinkage of smaller clusters at the expense of larger ones due to exchange of material driven by differences in chemical potential caused by different effective curvature and cluster size.

The STM findings are in line with our XPS results. Up to 950 K (Figure 4d) coalescence appears to be the dominant decay mechanism, while intercalation remains relatively sparse. Annealing to 1050 K (Figure 4e) then appears to reduce the cluster material significantly. At the same time large monolayer islands become apparent, where we detect moiré contrast on top of the islands (compare blue arrow in Figure 4e). This is unambiguous evidence for the islands being below the h-BN layer and support for our assumption of intercalation.

Finally, after annealing to 1250 K nearly all Pt clusters disappeared. The cluster material is intercalated underneath h-BN and has attached to preexisting steps, such that separate intercalation islands are no more visible.
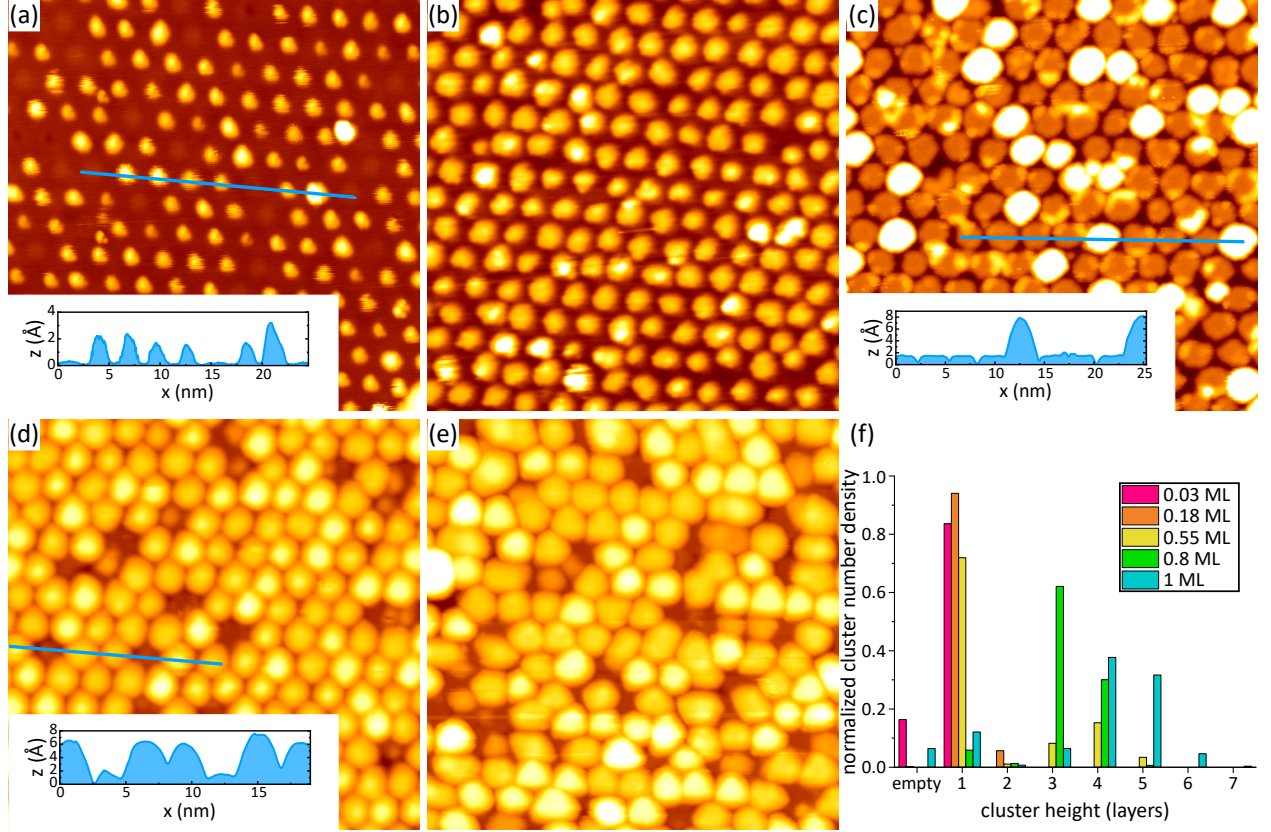

Figure 5: STM topographs of h-BN/Ir(111) after deposition of (a) $\theta = 0.03$ ML Pt, average cluster size in atoms $s_{av} = 3.4$ (see text); (b) $\theta = 0.18$ ML Pt, $s_{av} = 21$; (c) $\theta = 0.55$ ML Pt, $s_{av} = 63$; (d) $\Theta = 0.80$ ML Pt, $s_{av} = 92$; and (e) $\theta = 1.0$ ML, $s_{av} = 115$ at 300 K. Height profiles along the blue lines are shown below the respective STM topographs. Image size is 37×37 nm^2 in all cases. (f) Partial cluster number densities normalized to n and plotted as a function of cluster height and coverage θ.

Evolution of cluster superlattice with deposited amount and shape instability: The STM topgraphs of Figure 5 visualize the morphological evolution of the Pt cluster superlattice on h-BN/Ir(111) with increasing amounts of Pt deposited at 300 K. For all deposited Pt amounts θ visualized between 0.03 ML and 1 ML a cluster superlattice forms on the h-BN/Ir(111) template. For $\theta = 0.03$ ML (Figure 5a) some moiré unit cells remain empty. The cluster number density n per moiré unit cell is $n = 0.84$, but not $n = 1$

11

as for a perfect lattice. For aggregation of the randomly arriving adatoms within a unit cell and without intercell diffusion one expects a Poisson distribution of cluster sizes.[6] For $\theta = 0.03$ ML (average cluster size $s_{av} = 3.4$, see below) one would expect $n = 0.97$, i.e. only 3% of the cells should be empty. Considering that the Poisson distribution predicts that within 11% of the cells only a single adatom arrived, we conclude that at 300 K Pt monomers on h-BN/Ir(111) are subject to intercell diffusion on a time scale shorter than the deposition time of 15 s. We also note that imaging the bare h-BN layer at the location of the empty cells directly confirms the valley to be the binding site of the clusters, as expected from our previous results (compare Figure 1) and the literature.[28] For Pt coverages between 0.18 and 0.8 ML a perfect filling with $n = 1$ is found (compare Figure 5b to Figure 5d). For $\theta > 0.8$ ML coalescence of neighboring clusters leads to a reduced n. For $\theta = 1.0$ ML one obtains $n = 0.93$ as exemplified by Figure 5e. If θ, n, and the size of the moiré unit cell A_m given in iridium surface unit cells are given, the average cluster size can be calculated to be $s_{av} = \frac{A_m \theta}{n}$. For the presented data, it ranges from $s_{av} = 3.4$ atoms for $\theta = 0.03$ ML up to $s_{av} = 115$ atoms for $\theta = 1.0$ ML.

As apparent from the STM topographs and the corresponding line profiles, the cluster height increases stepwise, consistent with the Pt(111) step height of 2.2 Å. Figure 5f shows the height distribution of Pt clusters for different coverages. The partial cluster number density is normalized to n and plotted as function of cluster height and coverage θ. The most striking observation is that clusters of two layers height are nearly absent at all coverages investigated. This is most obvious for $\theta = 0.55$ ML, where the majority of clusters is still of monolayer height coexisting with a minority of clusters with three or more layers (yellow bars in Figure 5f; compare also Figure 5c). For larger deposited amounts the monolayer clusters diminish, the number of three or more layer clusters increases, but no two layer clusters come up. This implies that during growth clusters collapse from a flat monolayer directly to a trilayer or even four-layer height.

Additional insight into the cluster instability of large monolayer high clusters is provided

by an annealing experiment visualized in Figure 6. The amount of monolayer Pt clusters present after deposition of 0.55 ML at 300 K (Figure 6a) drops from 52 % to only 16 % after annealing to 730 K (Figure 6b). The drop is through transformation into three or four-layered clusters, while the cluster superlattice is barely disturbed. Evidently, an irreversible cluster reshaping takes place upon annealing, providing straightforward evidence for the metastability of large monolayer clusters at room temperature.

We speculate that the metastability is due to the mechanism of cluster binding to h-BN. As we have alluded before, owing to geometric reasons, the valley region cannot expand through the entire h-BN sheet. The growth of monolayer clusters first expands the rehybridized area in the valleys. However, this expansion eventually ceases because of the large distance of N atoms to Ir surface atoms far away from the center of the valley. Thus, the rim of extended clusters is only poorly bound to the substrate. This leads to a collapse of the cluster at a coverage of around 0.5 ML and causes their sudden reshaping from a flat to a more compact cluster with a smaller footprint, whereby metal-metal cohesion is gained without any significant loss of binding to the h-BN sheet.
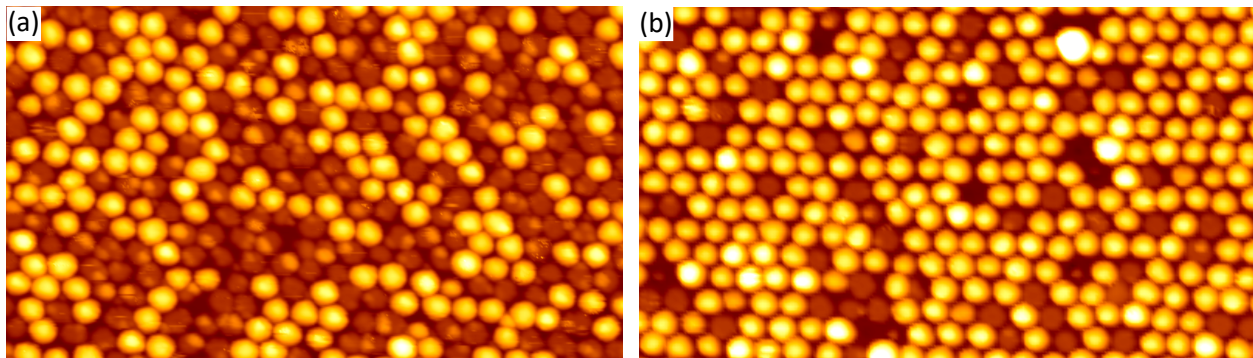

Figure 6: Shape transformation of Pt clusters on h-BN upon annealing. (a) STM topograph of 0.55 ML Pt/h-BN/Ir(111) after deposition at 300 K and (b) after additional annealing to 730 K for 60 s and imaged at 300 K. Image size is 70×40 nm^2.

Cluster decoupling and Coulomb staircase: Besides the enhanced thermal stability of the Pt clusters provided by the h-BN template, the large electronic band gap of h-BN is anticipated to electronically decouple the Pt clusters. We employed scanning tunneling spectroscopy to examine the differential conductance through the clusters as a function of
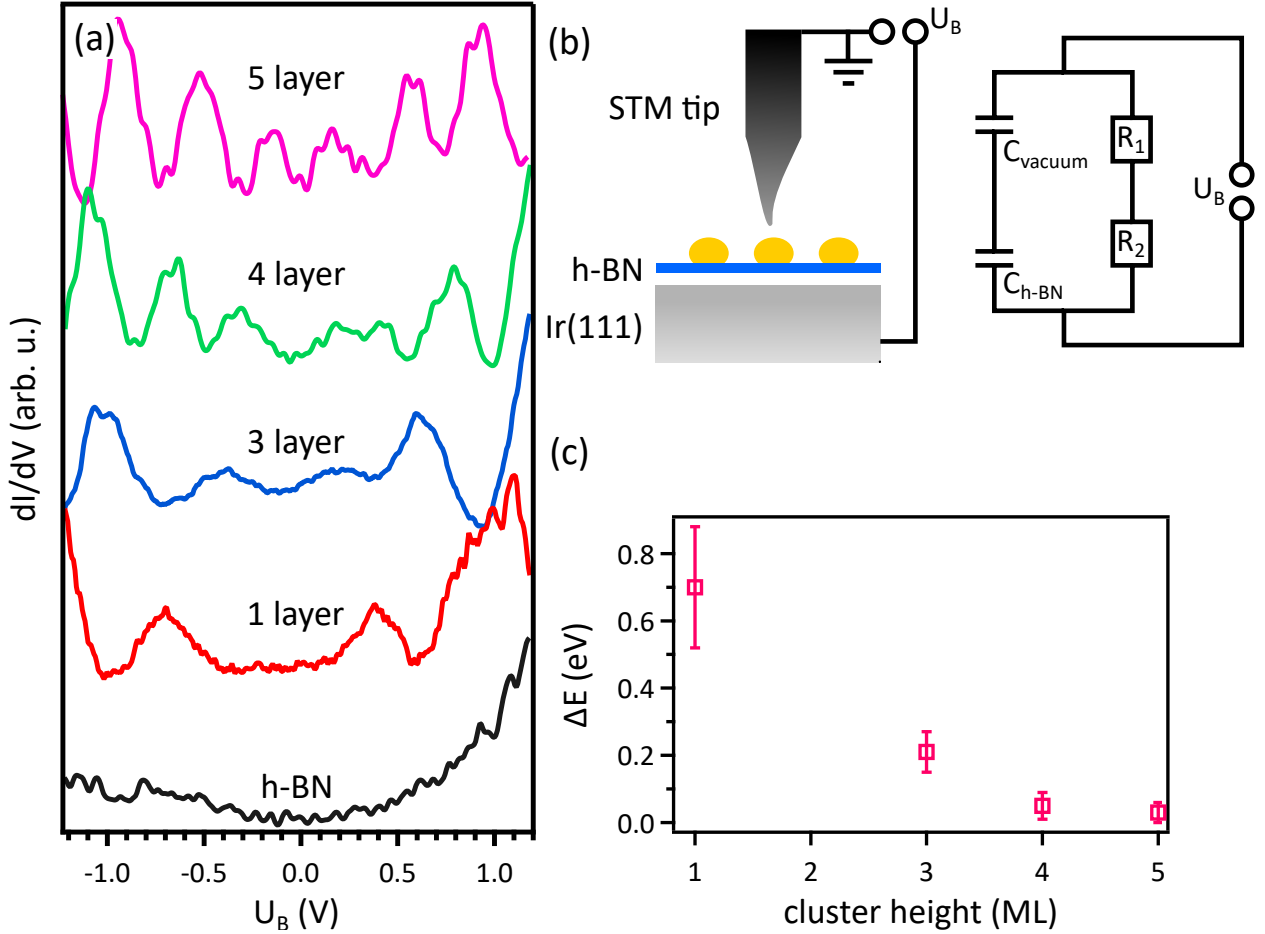
Figure 7: (a) Differential conductance dI/dV as a function of bias voltage U_B taken on pristine h-BN/Ir(111) (black), a one-layer Pt cluster (red), a three-layer Pt cluster (blue), a four-layer Pt cluster (green), and a five-layer Pt cluster (magenta) on h-BN/Ir(111). Spectra were taken on the center of a single cluster or of an h-BN valley. Set points: -1.5 V, 0.5 nA. (b) Schematic illustration of a double barrier tunneling junction formed by a cluster (yellow) between the STM tip and the h-BN/Ir(111) substrate (blue/light gray). The equivalent electrical circuit is depicted in the right panel. (c) Quantized energy spacing ΔE as a function of the cluster height in monolayers, averaged over at least 20 clusters.

the tunneling bias U_B. Figure 7a depicts characteristic examples of dI/dV spectra obtained by numerical differentiation of the $I(V)$ curves (averaged over 20 single point spectra, set points: -1.5 V, 0.5 nA). They are recorded at room temperature for h-BN (black line), for one (red), three (blue), four (green) and five (magenta) layer high clusters. While the dI/dV spectrum for h-BN on Ir(111) is featureless and similar to the one of Schulz *et al.* in ref. 33, the cluster spectra display height-dependent features in their dI/dV spectra. The one

14

layer Pt cluster has distinct peaks at -0.68 eV and 0.4 eV. We have compared several one layer high clusters and have extracted a peak-to-peak distance E_g around the Fermi level of 1.08 ± 0.18 eV. The three layer, four layer, and five layer high clusters display more regular peaks of decreasing spacing in energy. The peak-to-peak distances E_g for three layer, four layer, and five layer cluster are 0.59 ± 0.06 eV, 0.43 ± 0.04 eV and 0.41 ± 0.03 eV, respectively. We attribute these DOS features in the clusters to be the result of electronic decoupling from the Ir(111) substrate by the insulating h-BN monolayer.

As depicted in Figure 7b, the system can be considered as a double barrier tunnel junction, *i.e.*, one tunneling barrier between tip and cluster, and one between cluster and Ir(111). Both junctions can be approximated with a capacitance and a resistance, which gives rise to single electron tunneling effects. Therefore, the dI/dV spectra recorded on the Pt clusters are assigned to Coulomb staircase effects.[34] We note here that clusters of similar size display similar but not identical oscillations resulting in a distribution of oscillation periods. The measured small differences are the result of differences in the cluster atomic and electronic structure, varying tip apex, and variations in the cluster footprint area A, resulting thus in a change of the tip-cluster and cluster-substrate capacitors.

The period of the oscillations, E_g, is the sum of the quantized energy level spacing ΔE in the cluster, and the charging energy $E_c = e^2/C_\Sigma$.[35,36] $C_\Sigma = C_{h\text{-}BN} + C_{vacuum}$ is the cluster self-capacitance.[37] Deriving the cluster self capacitance assuming as a rough approximation plate capacitors yields $C_\Sigma = \epsilon_{h\text{-}BN}\epsilon_0 A/d_{h\text{-}BN} + \epsilon_0 A/d_{vac}$. Here $\epsilon_{h\text{-}BN} = 4$ is the dielectric constant of the h-BN film.[38–41] A is the cluster footprint area, which we assume for simplicity to remain constant due to the limited size of the valley. A reasonable estimate is a valley size able to support approximately 40 Pt atoms corresponding to an area of $\approx 2.6 \times 10^{-18}$ m^2. $d_{h\text{-}BN} = 0.25$ nm is the distance introduced by h-BN preventing the cluster and Ir(111) from contact.[28] $d_{vacuum} = 0.5$ nm is the tip-cluster separation, *i. e.* the distance the STM tip needs to move to come into contact with the cluster. With these numbers a charging energy E_c of ≈ 0.38 eV is estimated. Subtracting E_c from the measured E_g allows us to estimate the

spacing of the quantized energy levels, ΔE, in Pt clusters. In Figure 7c, ΔE is depicted as a function of the cluster size in layers. We find $\Delta E = 0.70 \pm 0.18$ eV for monolayer clusters, $\Delta E = 0.21 \pm 0.06$ eV for in three, $\Delta E = 0.05 \pm 0.04$ eV for four, and $\Delta E = 0.03 \pm 0.03$ eV for five layer high clusters. ΔE therefore decreases with increasing cluster size, as expected.

The insulating properties of h-BN provide an additional advantage over other cluster templates, since it electronically decouples the Pt nanoclusters. Decoupling enables us to resolve the intrinsic electronic properties of the clusters and to extract their cluster size-dependent quantized energy level spacing. Similar findings have been reported for isolated small gold clusters on ultrathin NaCl films[36] and colloidal nanoparticles supported on HOPG.[42] For the case of gold nanoclusters on NaCl, gap sizes in the order of 2 eV were reported that decrease with increasing particle size. For colloidal nanoparticles, as in the case of Thomas and co-workers, an increase of the charging energy with inverse nanoparticle diameter for ligand-stabilized Pd and Au clusters was reported, but the quantized level spacing ΔE could not be extracted.[43]

Conclusions

Up to now our inferences on the binding of noble metal cluster in the cluster superlattices templated by h-BN/Ir(111) were solely drawn from *ab initio* calculations.[28] Here we confirm through the analysis of XPS core levels that cluster binding involves chemical bond formation between the Ir substrate and h-BN and thereby provide strong evidence for the decisive role of the sp^3 binding motif in cluster binding. Shifts in the spectral weight of the Ir 4f$_{7/2}$ and B 1s core levels provide also direct evidence that the valley area subject to the sp^3 hybridization expands in response to cluster growth.

Pt cluster superlattices on h-BN/Ir(111) were found to be stable up to $650\,\mathrm{K}$ – a temperature at least $200\,\mathrm{K}$ higher than found for Pt cluster superlattices on other templates like Gr/Ir(111)[17] or h-BN/Rh(111).[44] Decay of the Pt cluster superlattice was followed through

16

XPS and STM annealing sequences and could be unambiguously identified to result from sintering *via* Smoluchowski ripening and intercalation similar to the case of Ir cluster super-lattices on h-BN/Ir(111).[28] Already after room temperature deposition of about three atoms per moiré unit cell a Pt cluster superlattice forms with nearly all cells occupied. Cluster coalescence and thereby decline of the superlattice only proceeds beyond average cluster sizes of 90 atoms. The Pt clusters grow first with monolayer thickness up to sizes of about 50 atoms, beyond which they collapse to three or more layer clusters. The origin of this metastability is traced back to the cluster footprint growing well beyond the maximum area of the binding valley, whereby the cluster rim is only poorly bound. Thermal or shape fluctuations then may trigger a massive cluster rearrangement to a lower energy configuration. Finally, the observation of cluster height dependent Coulomb oscillation in STS dI/dV spectra document not only cluster decoupling, but also allowed us to demonstrate a cluster height dependent quantization of their electronic structure. We are convinced that thermally rather stable Pt cluster superlattices on the h-BN/Ir(111) template provide with their tunable size and electronic structure a suitable testbed for systematic catalytic studies with Pt clusters.

Methods

STM and STS experiments were carried out in the ultrahigh vacuum system Athene in Cologne with a base pressure in the 10^{-11} mbar regime. Ir(111) was cleaned by cycles of 2 keV Xe^+ ion irradiation and flash annealing to 1550 K. An h-BN monolayer was grown at 1230 K by exposure to an ion gauge pressure of 5×10^{-9} mbar borazine ($B_3N_3H_6$) for 30 s. Exposure through a gas dosing tube gives rise to a pressure enhancement at the sample location by a factor of 80 compared to the one measured by the distant ion gauge. The resulting coverage of monolayer h-BN was 80 % consisting of well oriented islands with lateral extension of the order of 0.5 μm, as confirmed by low energy electron diffraction (LEED) and STM. The only partial coverage allowed to monitor the amount of Pt deposited

for each experiment by measuring the area of monolayer high pseudomorphic Pt islands grown on bare Ir(111) patches.

The XPS measurements were performed at the SuperESCA beamline of the Elettra synchrotron in Trieste. The borazine pressure was increased to 1×10^{-6} mbar (no gas dosing tube was used) and the exposure time to 600 s in order to ensure a monolayer h-BN sheet with 100 % coverage. The layer quality was checked with LEED and XPS. The absence of holes in the sheet was confirmed by the lack of an O 1s peak in the XP spectrum after exposure to 100 L CO. XP spectra were collected in normal emission with an overall energy resolution better than 50 meV. In order to simultaneously record the B 1s and Ir 4f core levels during deposition, the photon energy was tuned to $h\nu = 390$ eV (data shown in Figure 1), while high resolution data of the Ir 4f and Pt 4f core levels were measured at an energy of $h\nu = 140$ eV. After calibration of the binding energy to the Fermi edge, for the B 1s and N 1s core levels a polynomial background was subtracted prior to fitting. For Pt 4f and Ir 4f a linear background was used. Fits use asymmetric Doniach-Šunjić functions convoluted with a Gaussian for the case of Ir 4f. B 1s core levels were fitted with symmetrical Voigt functions.

Pt was deposited either by e-beam evaporation from Pt rods or by direct current heating of a Pt wire. For both methods the pressure during evaporation remained below 2×10^{-10} mbar. A typical deposition rate for e-beam evaporation was $\approx 10^{-2}$ ML/s while that for the current heated Pt wire was lower by a factor of 10. In Cologne, Pt deposition rates were calibrated by determining the fractional area of the sample covered with pseudomorphic Pt islands. The deposited amount is given in monolayers (ML) with respect to the surface atomic density of Ir(111). In Trieste, the e-beam evaporation rate was ≈ 10 times lower than in Cologne. It was re-calibrated by using the Ir 4f surface peak as a reference.

STM and STS were conducted at room temperature. Tunneling currents I were in the range of $I = 0.1 - 0.6$ nA and sample bias voltages U_B were in the range $U_B = \pm 2.0$ V. The STM data was processed with the WSxM[45] software.

Supporting Information Available

Figure S1 shows the evolution of the Pt 4f spectra of Pt clusters on h-BN/Ir(111) as a function of coverage. In Figure S2, the B 1s and N 1s spectra of Pt clusters on h-BN/Ir(111) are displayed after annealing steps up to 1250 K.

Acknowledgement

References

(1) Billinge, S. Materials Science: Nanoparticle Structures Served up on a Tray. *Nature* **2013**, *495*, 453–454.

(2) Goodman, D. Model Catalysts: from Imagining to Imaging a Working Surface. *J. Catal.* **2003**, *216*, 213–222.

(3) Heiz, U.; Schneider, W.-D. Nanoassembled Model Catalysts. *J. Phys. D Appl. Phys.* **2000**, *33*, R85.

(4) Henry, C. R. 2D-Arrays of Nanoparticles as Model Catalysts. *Catal. Lett.* **2015**, *145*, 731–749.

(5) Papp, C. From Flat Surfaces to Nanoparticles: *In Situ* Studies of the Reactivity of Model Catalysts. *Catal. Lett.* **2017**, *147*, 2–19.

(6) N'Diaye, A. T.; Bleikamp, S.; Feibelman, P. J.; Michely, T. Two-Dimensional Ir Cluster Lattice on a Graphene Moiré on Ir(111). *Phys. Rev. Lett.* **2006**, *97*, 215501.

(7) Degen, S.; Becker, C.; Wandelt, K. Thin Alumina Films on $Ni_3Al(111)$: A Template for Nanostructured Pd Cluster Growth. *Faraday Discuss.* **2004**, *125*, 343–356.

(8) Brihuega, I.; Michaelis, C. H.; Zhang, J.; Bose, S.; Sessi, V.; Honolka, J.; Schneider, M. A.; Enders, A.; Kern, K. Electronic Decoupling and Templating of Co Nanocluster Arrays on the Boron Nitride Nanomesh. *Surf. Sci.* **2008**, *602*, L95–L99.

(9) Ding, K.; Gulec, A.; Johnson, A. M.; Schweitzer, N. M.; Stucky, G. D.; Marks, L. D.; Stair, P. C. Identification of Active Sites in CO Oxidation and Water-Gas Shift over Supported Pt Catalysts. *Science* **2015**, *350*, 189–192.

(10) Fu, Q.; Saltsburg, H.; Flytzani-Stephanopoulos, M. Active Nonmetallic Au and Pt Species on Ceria-based Water-Gas Shift Catalysts. *Science* **2003**, *301*, 935–938.

(11) DeRita, L.; Dai, S.; Lopez-Zepeda, K.; Pham, N.; Graham, G. W.; Pan, X.; Christopher, P. Catalyst Architecture for Stable Single Atom Dispersion Enables Site-specific Spectroscopic and Reactivity Measurements of CO Adsorbed to Pt Atoms, Oxidized Pt Clusters, and Metallic Pt Clusters on TiO_2. *J. Am. Chem. Soc.* **2017**, *139*, 14150–14165.

(12) Wei, J.; Iglesia, E. Mechanism and Site Requirements for Activation and Chemical Conversion of Methane on Supported Pt Clusters and Turnover Rate Comparisons Among Noble Metals. *J. Phys. Chem. B* **2004**, *108*, 4094–4103.

(13) Shrestha, S.; Liu, Y.; Mustain, W. E. Electrocatalytic Activity and Stability of Pt Clusters on State-of-the-art Supports: a Review. *Catal. Rev.* **2011**, *53*, 256–336.

(14) Zhou, M.; Zhang, A.; Dai, Z.; Zhang, C.; Feng, Y. P. Greatly enhanced adsorption and catalytic activity of Au and Pt clusters on defective graphene. *J. Chem. Phys.* **2010**, *132*, 194704.

(15) Russell, J.; Zapol, P.; Král, P.; Curtiss, L. A. Methane Bond Activation by Pt and Pd Subnanometer Clusters Supported on Graphene and Carbon Nanotubes. *Chem. Phys. Lett.* **2012**, *536*, 9–13.

(16) Knudsen, J.; Feibelman, P. J.; Gerber, T.; Grånäs, E.; Schulte, K.; Stratmann, P.; Andersen, J. N.; Michely, T. Clusters binding to the graphene moiré on Ir(111): x-ray photoemission compared to density functional calculations. *Phys. Rev. B* **2012**, *85*, 035407.

(17) N'Diaye, A. T.; Gerber, T.; Busse, C.; Mysliveček, J.; Coraux, J.; Michely, T. A Versatile Fabrication Method for Cluster Superlattices. *New J. Phys.* **2009**, *11*, 103045.

(18) Donner, K.; Jakob, P. Structural Properties and Site Specific Interactions of Pt with the Graphene/Ru(0001) Moiré Overlayer. *J. Chem. Phys.* **2009**, *131*, 164701.

(19) Sitja, G.; Bailly, A.; De Santis, M.; Heresanu, V.; Henry, C. R. Regular Arrays of Pt Clusters on Alumina: A New Superstructure on $Al_2O_3/Ni_3Al(111)$. *J. Phys. Chem. C* **2019**, *123*, 24487–24494.

(20) Gerber, T.; Grånäs, E.; Schröder, U. A.; Stratmann, P.; Schulte, K.; Andersen, J. N.; Knudsen, J.; Michely, T. Stability and reactivity of graphene-templated nanoclusters. *J. Phys. Chem. C* **2016**, *120*, 26290–26299.

(21) Gotterbarm, K.; Späth, F.; Bauer, U.; Bronnbauer, C.; Steinrück, H.-P.; Papp, C. Reactivity of graphene-supported Pt nanocluster arrays. *ACS Catal.* **2015**, *5*, 2397–2403.

(22) Düll, F.; Schwaab, V.; Späth, F.; Bauer, U.; Bachmann, P.; Steinhauer, J.; Steinrück, H.-P.; Papp, C. Sulfur oxidation on graphene-supported platinum nanocluster arrays. *Chem. Phys. Lett.* **2018**, *708*, 165–169.

(23) DüİĹll, F.; Späth, F.; Bauer, U.; Bachmann, P.; Steinhauer, J.; Steinrück, H.-P.; Papp, C. Reactivity of CO on sulfur-passivated graphene-supported platinum nanocluster arrays. *J. Phys. Chem. C* **2018**, *122*, 16008–16015.

(24) Gotterbarm, K.; Späth, F.; Bauer, U.; Steinrück, H.-P.; Papp, C. Adsorption and reaction of SO_2 on graphene-supported Pt nanoclusters. *Top. Catal.* **2015**, *58*, 573–579.

(25) Düll, F.; Meusel, M.; Späth, F.; Schötz, S.; Bauer, U.; Bachmann, P.; Steinhauer, J.; Steinrück, H.-P.; Bayer, A.; Papp, C. Growth and stability of Pt nanoclusters from 1 to 50 atoms on h-BN/Rh(111). *Phys. Chem. Chem. Phys.* **2019**, *21*, 21287–21295.

(26) Düll, F.; Freiberger, E. M.; Bachmann, P.; Steinhauer, J.; Papp, C. Pt Nanoclusters Sandwiched between Hexagonal Boron Nitride and Nanographene as van der Waals Heterostructures for Optoelectronics. *ACS Appl. Nano Mater.* **2019**, *2*, 7019–7024.

(27) Düll, F.; Steinhauer, J.; Späth, F.; Bauer, U.; Bachmann, P.; Steinrück, H.-P.; Wickert, S.; Denecke, R.; Papp, C. Ethylene: Its adsorption, reaction, and coking on Pt/h-BN/Rh(111) nanocluster arrays. *J. Chem. Phys.* **2020**, *152*, 224710.

(28) Will, M.; Atodiresei, N.; Caciuc, V.; Valerius, P.; Herbig, C.; Michely, T. A Monolayer of Hexagonal Boron Nitride on Ir(111) as a Template for Cluster Superlattices. *ACS Nano* **2018**, *12*, 6871–6880.

(29) Farwick zum Hagen, F. H.; Zimmermann, D. M.; Silva, C. C.; Schlueter, C.; Atodiresei, N.; Jolie, W.; Martínez-Galera, A. J.; Dombrowski, D.; Schröder, U. A.; Will, M.; Lazić, P.; Caciuc, V.; Blügel, S.; Lee, T.-L.; Michely, T.; Busse, C. Structure and Growth of Hexagonal Boron Nitride on Ir(111). *ACS Nano* **2016**, *10*, 11012–11026.

(30) Orlando, F.; Larciprete, R.; Lacovig, P.; Boscarato, I.; Baraldi, A.; Lizzit, S. Epitaxial Growth of Hexagonal Boron Nitride on Ir(111). *J. Phys. Chem. C* **2012**, *116*, 157–164.

(31) Arblaster, J. W. Crystallographic Properties of Iridium. *Platinum Met. Rev.* **2010**, *54*, 93–102.

(32) Arblaster, J. Crystallographic Properties of Platinum. *Platinum Met. Rev.* **2006**, *50*, 118–119.

(33) Schulz, F.; Drost, R.; Hämäläinen, S. K.; Demonchaux, T.; Seitsonen, A. P.; Liljeroth, P. Epitaxial Hexagonal Boron Nitride on Ir(111): A Work Function Template. *Phys. Rev. B* **2014**, *89*, 235429.

(34) Likharev, K. K. Correlated Discrete Transfer of Single Electrons in Ultrasmall Tunnel Junctions. *IBM J. Res. Dev.* **1988**, *32*, 144–158.

(35) Beenakker, C. W. Theory of Coulomb-blockade oscillations in the conductance of a quantum dot. *Phys. Rev. B* **1991**, *44*, 1646.

(36) Li, Z.; Chen, H.-Y. T.; Schouteden, K.; Picot, T.; Liao, T.-W.; Seliverstov, A.; Van Haesendonck, C.; Pacchioni, G.; Janssens, E.; Lievens, P. Unraveling the atomic structure, ripening behavior, and electronic structure of supported Au_{20} clusters. *Sci. Adv.* **2020**, *6*, eaay4289.

(37) Heinzel, T.; Zozoulenko, I. *Mesoscopic Electronics in Solid State Nanostructures*; Wiley Online Library, 2003; Vol. 3.

(38) Jang, S. K.; Youn, J.; Song, Y. J.; Lee, S. Synthesis and characterization of hexagonal boron nitride as a gate dielectric. *Sci. Rep.* **2016**, *6*, 30449.

(39) Kim, S. M.; Hsu, A.; Park, M. H.; Chae, S. H.; Yun, S. J.; Lee, J. S.; Cho, D.-H.; Fang, W.; Lee, C.; Palacios, T.; Dresselhaus, M.; Kim, K. K.; Lee, Y. H.; Kong, J. Synthesis of large-area multilayer hexagonal boron nitride for high material performance. *Nat. Commun.* **2015**, *6*, 1–11.

(40) Kim, K. K.; Hsu, A.; Jia, X.; Kim, S. M.; Shi, Y.; Dresselhaus, M.; Palacios, T.; Kong, J. Synthesis and Characterization of Hexagonal Boron Nitride Film as a Dielectric Layer for Graphene Devices. *ACS Nano* **2012**, *6*, 8583–8590.

(41) Arya, S.; D'amico, A. Preparation, properties and applications of boron nitride thin films. *Thin Solid Films* **1988**, *157*, 267–282.

(42) Yang, P.; Arfaoui, I.; Cren, T.; Goubet, N.; Pileni, M.-P. Electronic Properties Probed by Scanning Tunneling Spectroscopy: From Isolated Gold Nanocrystal to Well-Defined Supracrystals. *Phys. Rev. B* **2012**, *86*, 075409.

(43) Thomas, P. J.; Kulkarni, G.; Rao, C. Effect of size on the Coulomb staircase phenomenon in metal nanocrystals. *Chem. Phys. Lett.* **2000**, *321*, 163–168.

(44) Düll, F.; Meusel, M.; Späth, F.; Schötz, S.; Bauer, U.; Bachmann, P.; Steinhauer, J.; Steinrück, H.-P.; Bayer, A.; Papp, C. Growth and stability of Pt nanoclusters from 1 to 50 atoms on h-BN/Rh(111). *Phys. Chem. Chem. Phys.* **2019**, *21*, 21287–21295.

(45) Horcas, I.; Fernández, R.; Gomez-Rodriguez, J.; Colchero, J.; Gómez-Herrero, J.; Baro, A. WSXM: a Software for Scanning Probe Microscopy and a Tool for Nanotechnology. *Rev. Sci. Instrum.* **2007**, *78*, 013705.

5.1 Manuscript 2: Supporting Information

Supporting Information:

Growth, Stability and Electronic Decoupling

of Pt Clusters on h-BN/Ir(111)

Moritz Will,*,[†] Pantelis Bampoulis,[†] Tobias Hartl,[†] Virginia Boix de la Cruz,[‡]

Paolo Lacovig,[¶] Silvano Lizzit,[¶] Jan Knudsen,[‡,§] and Thomas Michely[†]

[†]II. Physikalisches Institut, Universität zu Köln, Cologne, D-50937, Germany

[‡]Division of Synchrotron Radiation Research, Lund University, Box 188, SE-22100 Lund, Sweden

[¶]Elettra-Sincrotrone Trieste S.C.p.A., Strada Statale 14 Km 163.5, I-34149 Trieste, Italy

[§]MAX IV Laboratory, Lund University, Box 118, SE-22100 Lund, Sweden

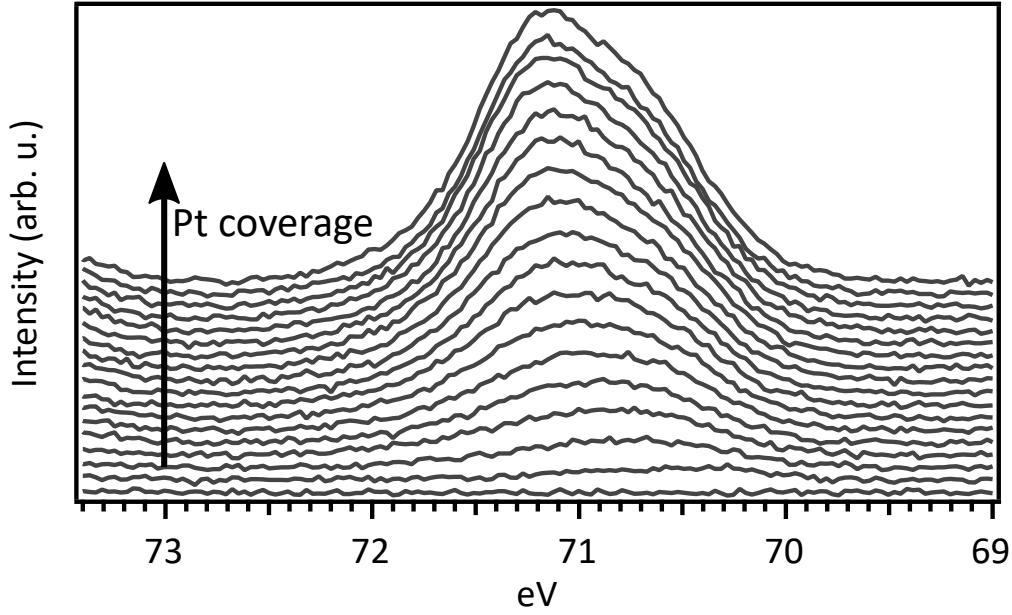E-mail: will@ph2.uni-koeln.de

Phone: +49 (0)221 470-6876

Figure S1: XPS analysis of the Pt $4f_{7/2}$ component measured at a photon energy of $h\nu = 140$ eV as a function of Pt coverage. The Pt coverage increases gradually from top to bottom. For the topmost spectrum it is $\theta = 0.22$ ML.

Figure S2a shows the B 1s and N 1s core levels when 0.1 ML Pt clusters on h-BN/Ir(111) are subject to annealing. As a first observation, the shoulder attributed to the h-BN valleys (see main text) at higher binding energies recovers when the clusters are annealed to 1250 K. Additionally, a gradual shift of the maximum of both of the spectra is observed from lower to higher annealing temperatures. These shifts are displayed distinctly in Figure S2b. The origin of the shift of the B 1s core level upon Pt adsorption is discussed in the main text. As visible in the plots, the shift upon annealing of the N 1s spectrum is rather gradual until 950 K, but a strong shift is observed from 950 K onwards. At the final data point recorded after annealing to 1250 K the BE of the B 1s and N 1s components are even lower than in the initial state of bare h-BN/Ir(111) (compare filled black data points and black spectra in Figure S2a).

We understand this in view of the interpretation given in the main text. At temperatures around 750 K, thermally induced coalescence and intercalation sets in which reduces the cluster number density n and recovers moiré valleys to their original state without a cluster.
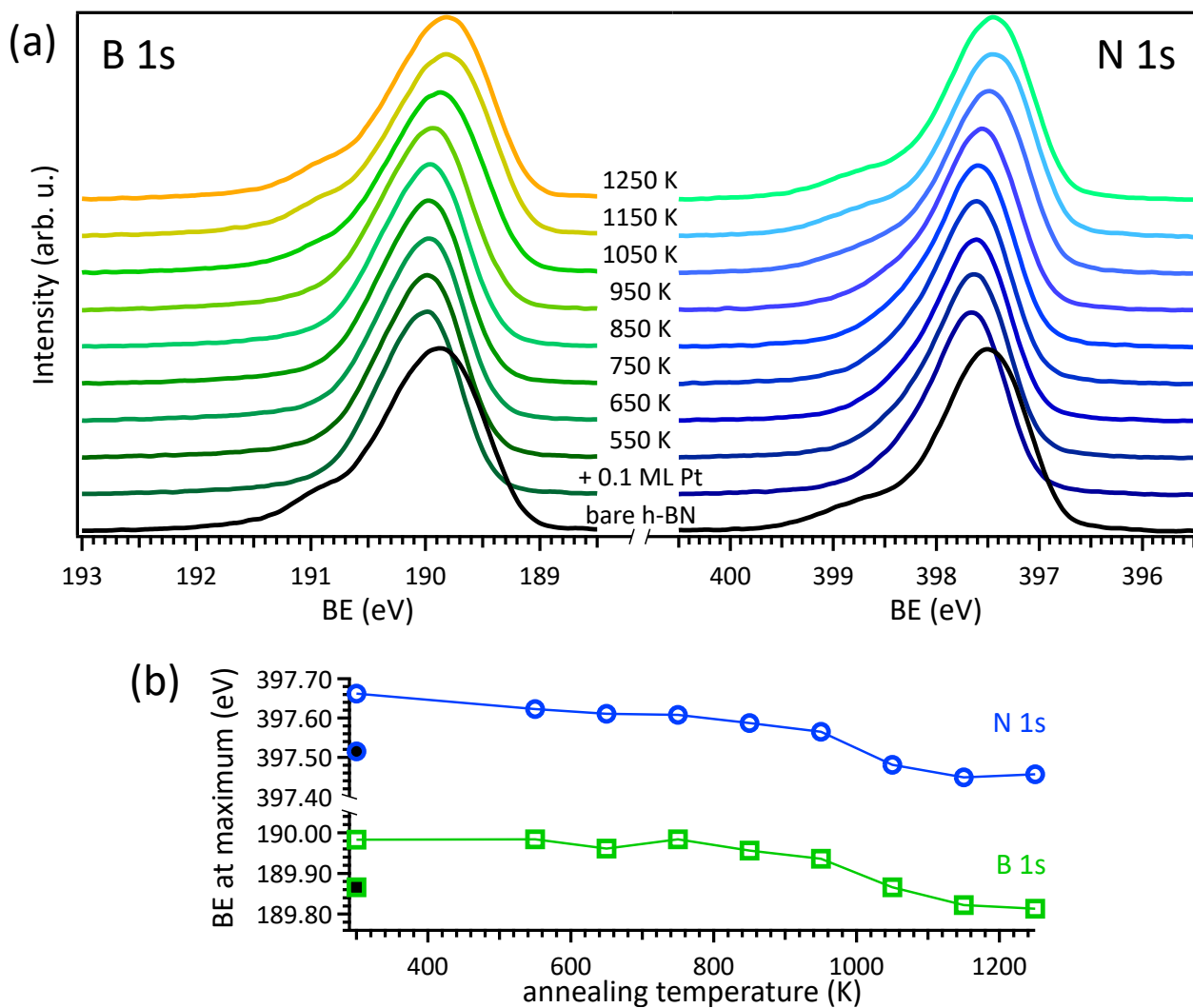
Figure S2: (a) XPS analysis of B 1s ($h\nu = 390$ eV) and N 1s ($h\nu = 500$ eV) components for 0.1 ML Pt clusters on h-BN at different annealing temperatures. The lowermost spectra in black were taken on clean h-BN/Ir(111) as a reference. All other spectra were taken after deposition of 0.1 ML Pt at 300 K and 30 s annealing at the indicated temperature. (b) Position of the maximal value of the B 1s (green) and N 1s (blue) core levels as a function of annealing temperature. The filled data points at 300 K were recorded on clean h-BN/Ir(111). Lines to guide the eye.

As a consequence, the B 1s and N 1s components associated with the strongly interacting B and N atoms in the valleys (see main text) recover, which leads to a shift of the absolute maximum. At 950 K the clusters have sintered, but many still remain on top of the h-BN. At 1050 K and higher, intercalation of those clusters takes over as the degradation mechanism of the superlattice, but some still remain on top. Finally, Pt islands are covering the Ir(111) surface and some h-BN binds to the Pt instead of the Ir(111) surface. As shown previously, both B 1s and N 1s spectra are shifted to lower binding energies for h-BN/Pt(111) compared to clean h-BN/Ir(111),[S1] explaining the slight reduction of the BE observed after annealing to 1250 K.

References

(S1) Preobrajenski, A.; Nesterov, M.; Ng, M. L.; Vinogradov, A.; Mårtensson, N. Monolayer h-BN on lattice-mismatched metal surfaces: On the formation of the nanomesh. *Chem. Phys. Lett.* **2007**, *446*, 119–123.

CHAPTER 6

Manuscript 3: Conformal Embedding of Cluster Superlattices with Carbon

This chapter wholly consists of the above-named manuscript and its supplement, published 7th October 2019 at ACS Applied Materials and Interfaces.

The experiments were proposed by M. Will, T. Hartl, P. Bampoulis, and T. Michely. Samples were grown and measured by M. Will, T. Hartl, and P. Bampoulis. All experiments were performed at ATHENE. The STM and STS data analysis was performed by M. Will, T. Hartl, and P. Bampoulis, who were the same to discuss and interpret the data together with T. Michely. All work was supervised by T. Michely.

M. Will wrote the manuscript, with advice and corrections from P. Bampoulis, T. Hartl, and T. Michely. It was finalized with P. Bampoulis and T. Michely.

Some of the results shown in this Chapter can be found in the Master's thesis of T. Hartl.

# Conformal Embedding of Cluster Superlattices with Carbon

Moritz Will,*[ID] Pantelis Bampoulis,[ID] Tobias Hartl, Philipp Valerius,[ID] and Thomas Michely

II. Physikalisches Institut, Universität zu Köln, Cologne D-50937, Germany

Ⓢ *Supporting Information*

ABSTRACT: Iridium cluster superlattices on the graphene moiré with Ir(111) are embedded with elemental carbon through vapor-phase deposition. Using scanning tunneling microscopy and spectroscopy, we find that carbon embedding is conformal and does not deteriorate the excellent order of the iridium clusters. The thermal and mechanical stability of the embedded clusters is greatly enhanced. Smoluchowski ripening as well as cluster pick-up by the scanning tunneling microscopy tip are both suppressed. The only cluster decay path left takes place at an elevated temperature of around 1050 K. The cluster material penetrates through the graphene sheet, whereby it becomes bound to the underlying metal. It is argued that conformal carbon embedding is an important step towards the formation of a new type of sintering-resistant cluster lattice material for nanocatalysis and nanomagnetism.

KEYWORDS: *clusters, graphene, Ir(111), cluster superlattice, scanning tunneling microscopy, sintering, catalysis, carbon embedding*
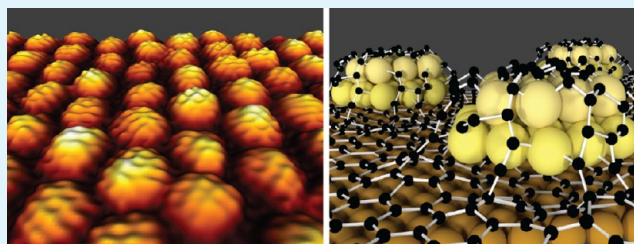
■ INTRODUCTION

Metal nanoclusters display size-dependent structural, electronic, optical, and magnetic properties.[1−3] The tunability of their electronic properties in combination with their unique surface-to-volume ratio makes noble metal clusters on an oxide- or carbon-based substrate the paradigmatic material in heterogeneous catalysis.[1,4−6] For instance, Pt and Pd nanoparticles embedded in carbon-based materials are the most efficient catalysts in methanol fuel cells.[7,8] Similarly, magnetic nanoclusters are decisive in pushing the limits of magnetic storage devices and their density forward.[9−11]

As the properties of nanoclusters are strongly size dependent, cluster beam deposition of mass-selected clusters on suitable substrates is a prime approach to understand their properties.[12,13] However, as their interaction in nanomagnetism and their action in nanocatalysis depend on their spacing, orientation, and their environment (e.g., through the reverse spillover effect[14]), the advantage of size control down to the atomic limit is partly counterbalanced by the random spacing in inhomogeneous environments caused by the randomness of the deposition process as well as postdeposition diffusion and coalescence.[15,16]

Templated cluster growth[17] is a viable alternative for fundamental investigations that eventually might become attractive also for applications. Placing a thin layer of a dissimilar material on a substrate creates a moiré. Within the large moiré supercell, the interaction of deposited atoms is inhomogeneous and may give rise to preferential binding at a specific site/area, and thereby to a two-dimensional (2D) cluster array or superlattice. The spacing of the clusters is then given by the size of the supercell, the size of the clusters is controlled by the deposited amount, and their size distribution is given by a Poisson distribution,[18] of which the standard deviation is the square root of the mean. A narrow size distribution, a uniform

spacing, identical environment, and an extremely high cluster density are attractive features of such templated superlattices. As pointed out by Billinge,[19] surface-sensitive X-ray diffraction of such cluster superlattices in operando would allow to follow the change of structure and shape of clusters as a function of reaction conditions. Examples of versatile templates for cluster superlattices are thin Al_2O_3 layers prepared on Ni$_3$Al(111),[14,17,20−22] graphene (Gr) on Ir(111)[11,18,23−26] or Rh(111),[27−31] and hexagonal boron nitride (h-BN) on Ir(111)[32] or Rh(111).[33−36]

One key problem in the application of the 2D cluster superlattices for model studies in catalysis is sintering. Degradation of clusters by sintering in harsh conditions encountered during catalytic reactions is often the cause of catalyst deactivation, especially in high-temperature applications, e.g., in the automotive industry and combustion processes.[37−39] For similar-sized and particularly small clusters in 2D arrays (average size from a few to 150 atoms), sintering takes place mainly through Smoluchowski ripening (thermally activated cluster motion and coalescence, see Supporting Information Figure S1a for an image of the process) under reaction conditions of elevated temperature and pressure.[23,24,32,40] The resulting decrease in cluster number leads to a loss of active surface area.[37,41] The related increase in size and shape affects the electronic properties of the cluster (e.g., through quantum effects) and all together to a loss of activity. These changes are irreversible and it is thus necessary to protect the nanocluster arrays against sintering.

Techniques to avoid sintering mainly involve increasing the binding to the substrate,[32] treatment with radical O or D,[42] particle encapsulation,[43−45] alloying with a reactive metal,[46,47]

and narrowing the size distribution to limit Ostwald ripening.[48] In these approaches, the onset for sintering is pushed to higher temperatures but is not completely prevented. Therefore, there is a strong need to find methods to prevent sintering and degradation of perfect cluster superlattices at application-relevant conditions.

Here, we report on the realization of an important step in a concept to develop a new type of cluster superlattice material that is able to withstand even harsh reaction conditions and that is not subject to sintering. As schematically sketched in Figure 1,
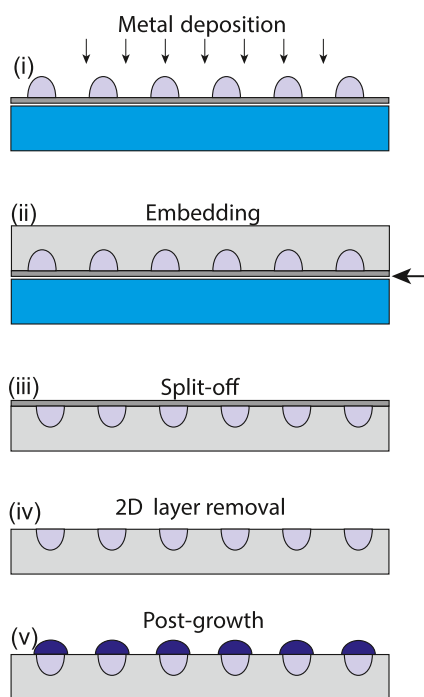
Figure 1. Concept for the fabrication of a sintering-resistant cluster superlattice membrane. (i) Formation of cluster superlattice by metal deposition onto a single-crystal 2D layer forming a moiré with the metal substrate, (ii) embedding of the cluster superlattice by C or oxide deposition, (iii) split-off from the metal substrate and the membrane turned upside down, (iv) removal of the 2D layer from the membrane, and (v) postgrowth of the metal nanoclusters. Arrow in (ii) points to the location of splitting. Medium blue: substrate metal, light blue: cluster metal, dark blue: postgrowth metal, dark gray: 2D layer, and light gray: embedding material.

after (i) the cluster superlattice growth on a single-crystal 2D layer forming a moiré with the metal substrate, (ii) conformal embedding into a matrix is conducted by the deposition of C or an oxide. Subsequently, (iii) the membrane formed by the 2D layer, the clusters, and the embedding matrix is removed from the metal substrate. (iv) When the membrane is freestanding by clamping or placed upside down on a new substrate, the 2D material cover layer can be removed. (v) Postgrowth can be conducted to enlarge the clusters. With step (iii), already a material for nanomagnetic studies is realized, which can be handled under ambient conditions as the encapsulated clusters are protected against degradation, e.g., by oxidation.[49] Also, new phases could be synthesized in the cavities that require high-temperature processing, e.g., L1$_0$ phase of FePt[11] without losing the regular cluster arrangement. For nanocatalytic studies, the clusters need to be reopened in step (iv), while step (v) is optional. Sintering is assumed to be suppressed for a reopened

cluster superlattice after step (iv), as coalescence would require the cluster to move out of its conformal shell onto the membrane. A process that would require a substantial reduction of the contact area between the cluster and the embedding shell, and thus a substantial activation energy to compensate for the reduced adhesion between the cluster and the membrane.

The crucial step in the sequence is the conformal embedding of the clusters into a matrix without the loss of the positional order. Moreover, the matrix has to adhere firmly to the clusters and the 2D layer, such that subsequent split-off from the metal substrate becomes possible through standard methods, e.g., through the hydrogen bubbling method.[50,51] Therefore, in the present article, we focus on the embedding process (i.e., step (ii) in Figure 1) and demonstrate the enhanced thermal and mechanical stability of the membrane. As a first system to be investigated, we pick the well characterized Ir superlattice on Gr/Ir(111)[18,23−25] and choose as embedding material elemental carbon.

■ RESULTS AND DISCUSSION

Figure 2 visualizes the key message of this article: embedding of a templated metal cluster array on Gr/Ir(111) with elemental C is conformal and stabilizes the clusters against sintering up to very high temperatures.

For reference, Figure 2a−c visualizes the decay of an Ir cluster array by thermal annealing. The cluster lattice in Figure 2a formed by θ = 0.4 ML of deposited Ir is templated by the well-known 9.32 × 9.32 Gr moiré superstructure with Ir(111), which causes a cluster spacing of 2.53 nm.[18] As each moiré unit cell has an area of A_m = 87 Ir substrate unit cells and the cluster number density n per moiré unit cell is n = 1, the average cluster size s_{av} is 35 Ir atoms (also denoted Ir$_{\overline{35}}$), according to

$$s_{av} = \frac{A_m \theta}{n} \tag{1}$$

The cluster array in Figure 2a extends over three substrate terraces. From the height profile in Figure 2a, it is apparent that the Ir clusters are one to three (111) layers high, consistent with their epitaxial growth.[18,23] Cluster templating is through preferred rehybridization of Gr to diamond-like sp^3 carbon in a specific area (hcp-area) of the moiré when the metal is deposited. Thereby, carbon atoms bind alternatively to Ir cluster atoms atop of them and to Ir substrate atoms underneath.[18,52]

After annealing to 850 K, n has decreased substantially, as seen in Figure 2b. The decrease of n is primarily by Smoluchowski ripening, see Figure S1a of the Supporting Information for an image of the process.[23] After annealing to 1350 K, the cluster material has largely disappeared and only very few clusters remain (compare Figure 2c). At high temperatures, a second mechanism of cluster decay takes over, namely penetration of the cluster material through the Gr sheet and attachment to the Ir substrate crystal; see Figure S1b of the Supporting Information for an image of the process. This intercalation process can be identified already at its onset in Figure 2b, where a small, one monolayer high Ir intercalation island is highlighted by an arrow. In Figure 2c, dark spots in the Gr sheet (indicated by the light blue arrow) are locations where Ir has probably etched its path to the substrate and the cluster material intercalated. Due to the high temperature, it forms no more islands but diffuses until it is incorporated into a preexisting Ir substrate step.

The thermal decay of the Ir cluster lattice is now contrasted to the thermal evolution of 1.6 ML carbon on Gr(111) visualized in
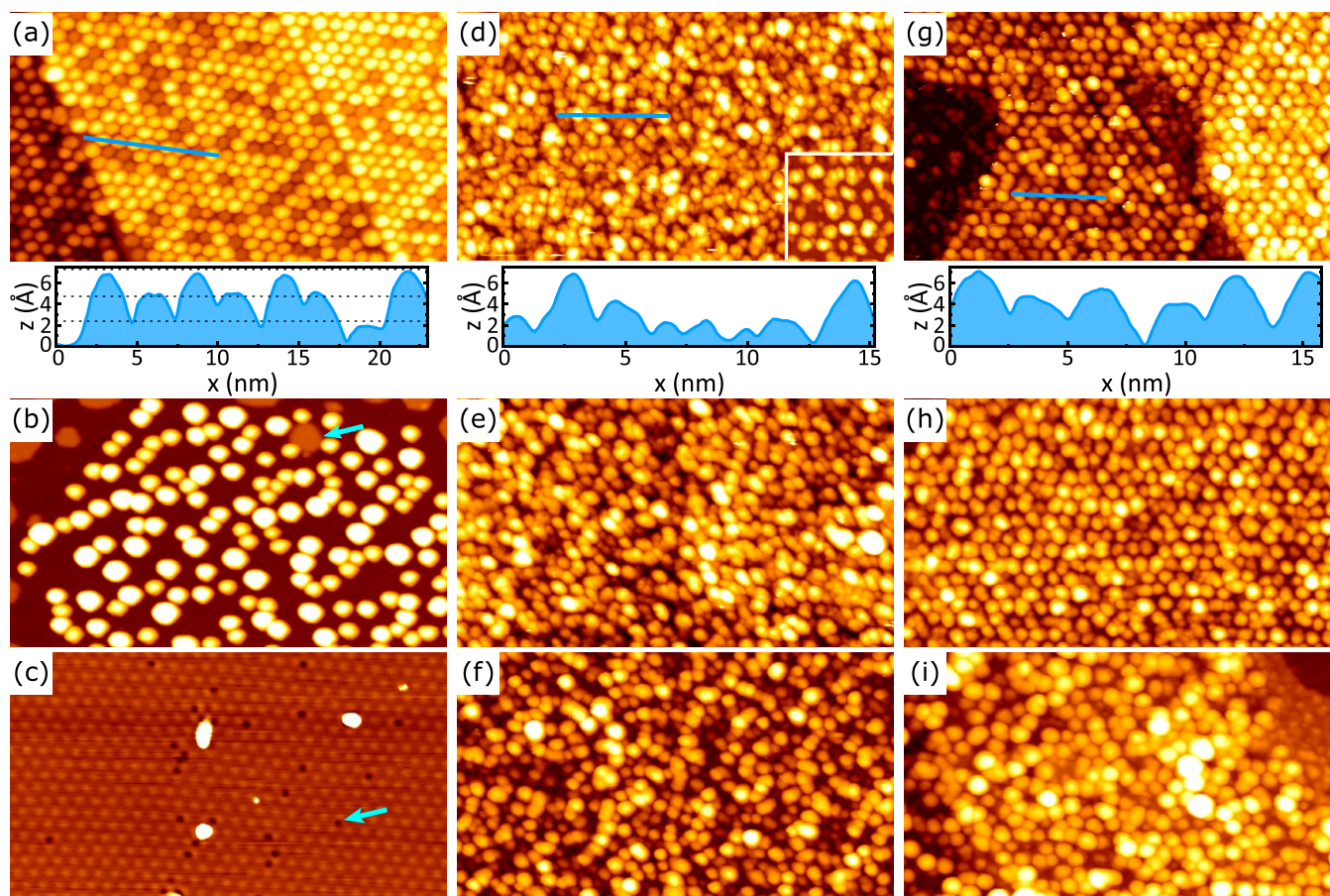
Figure 2. Thermal stability of cluster lattices on Gr/Ir(111). (a) Scanning tunneling microscopy (STM) topograph of Gr/Ir(111) after the deposition of 0.4 ML Ir at 300 K resulting in $Ir_{\overline{35}}$ clusters. (b, c) Topographs of the same sample as in (a), but after annealing intervals of 30 s at (b) 850 K and (c) 1350 K. The light blue arrow in (b) highlights intercalated Ir and in (c) holes on the graphene layer, see text. (d) STM topograph after the deposition of 1.6 ML C at 300 K. (e, f) Same as (d), but after annealing intervals of 30 s to (e) 850 K and (f) 1350 K. (g) STM topograph after the deposition of 0.4 ML Ir and the subsequent deposition of 1.6 ML C at 300 K resulting in C-embedded Ir clusters $Ir_{\overline{35}}C_{\overline{341}}$. (h, i) Same as (g), but after annealing intervals of 30 s to (h) 850 K and (i) 1350 K. Height profiles in (a), (d), and (g) are along blue lines in the STM topographs. Dotted horizontal lines in the height profile of (a) indicate the separation of Ir(111) planes. The inset in (d) shows an STM topograph after the deposition of 0.4 ML C on Gr/Ir(111). The image size is 70 nm × 40 nm in all cases.

Figure 2d−f (note that a 1.6 ML C corresponds to an average of 341 C atoms deposited per moiré unit cell. This results from eq 1 using $n = 1$ and taking into account that A_m has an area of 107 graphene unit cells each with a 2-atom basis). No ordered C cluster array evolves, although for smaller amounts, a reasonably ordered cluster array form (compare inset of Figure 2d and ref 26). These low-coverage C cluster arrays consist of fullerene-like caps of sp^2 hybridized C anchored to Gr with sp^3 bonds. Still, after 1.6 ML C was deposited, the characteristic length scale is set by the moiré, but apparently the initial C clusters connect and start to form an amorphous C matrix. The height profile of Figure 2d makes plain that no discrete height levels are present, as expected. Annealing of this sample to 850 [Figure 2e] and 1350 K [Figure 2f] does not result in major changes in the topography—just the smallest C features present at 300 K appear to have ripened away.

The extraordinary stability of C on Gr/Ir(111) motivates its use to stabilize the Ir cluster array against thermal decay. Figure 2g−i analyzes the case of $Ir_{\overline{35}}$ clusters embedded with 1.6 ML carbon. Figure 2g makes obvious that the ordered Ir cluster superlattice has survived the embedding process. The cluster number density remains close to unity and allows one to label these clusters as $Ir_{\overline{35}}C_{\overline{341}}$. Again, the height profile shown below

the STM topograph of Figure 2g displays no discrete height levels, which is not unexpected in view of the large amount of C deposited. Nevertheless, the regular spacing of the clusters is reflected in the profile. The STM topograph of Figure 2h after annealing to 850 K shows the same, if not an improved, order compared to the situation after growth in Figure 2g. Further annealing to 1350 K (Figure 2i) results in a moderate decay of the superlattice. The order is decreased, though still the moiré periodicity can be recognized. n is reduced to $n = 0.74$.

It is obvious from these experiments that deposited carbon conforms to a preexisting cluster superlattice (additional evidence is presented below) and that the Ir clusters with their carbon shell display a substantially enhanced stability against sintering by Smoluchowski ripening. Ir/C clusters therefore combine the two standout features of the single materials if deposited on Gr/Ir(111): the perfect ordering of the Ir clusters at room temperature and the high thermal stability of the C deposits.

A quantitative picture of thermal stability of embedded versus nonembedded clusters emerges from Figure 3. Here, the cluster number density n per moiré unit cell for Ir clusters embedded in 1.6 ML carbon (pink squares) is compared to same-sized bare Ir clusters (blue squares) as a function of temperature. It is obvious
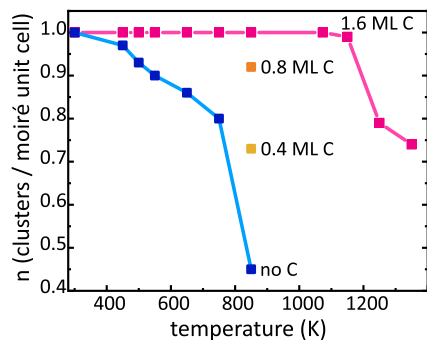
Figure 3. Cluster number density n as a function of annealing temperature T for cluster lattices on Gr/Ir(111). Blue squares: $n(T)$ for 0.45 ML Ir deposition. Annealing intervals were 300 s. Data from ref 23. Pink squares: $n(T)$ for 0.4 ML Ir and subsequent 1.6 ML C deposition. Annealing intervals were 30 s. Yellow and orange square: $n(T)$ for 0.4 ML Ir embedded with 0.4 ML (yellow) and 0.8 ML (orange) C with subsequent annealing to 850 K for 30 s. Corresponding STM topographs for 0.4 and 0.8 ML C embedding are provided in Figure S2 of the Supporting Information. Lines to guide the eye.

that cluster coalescence setting in already for bare Ir clusters at 450 K is dramatically suppressed by C embedding. Only above 1050 K, C-embedded cluster lattices visibly deteriorate. It is also apparent in Figure 3 that the stabilization effect of carbon embedding depends on the amount of C deposited. At 850 K, data points for 0.4 ML C embedding (yellow square) and 0.8 ML C embedding (orange square) are plotted. Comparing the four 850 K data points makes plain that the annealed cluster density is a monotonically increasing function of the embedding amount. The corresponding topographies for the 850 K data points are provided in Figure S2 of the Supporting Information.

To obtain insight into the mechanism of embedding, the room-temperature topography of $Ir_{\overline{35}}$ cluster arrays as a function of the embedding amount (0, 0.2, 0.4, 0.8, and 1.6 ML of C) is

presented in Figure 4a−e. Figure 4f serves as a reference with deposition of 0.4 ML carbon on bare Gr/Ir(111) without an Ir cluster array. It is apparent that the initial $Ir_{\overline{35}}$ lattice with $n = 1$ in Figure 4a is not perturbed upon adsorption of 0.2, 0.4, and 0.8 ML carbon as shown in Figure 4b−d. Although for 1.6 ML C [Figure 4e] the lattice is mostly conserved, the embedding carbon occasionally connects clusters, which then extend over several moiré unit cells. An example is marked by the light blue arrow.

Also after deposition of 0.4 ML C on bare Gr/Ir(111), a cluster array visible in Figure 4f forms but with an inferior order compared to an Ir cluster array. As mentioned above, the C clusters must be assumed to consist of fullerene-like caps that merge with Gr through strong sp³ bonds.[26] This in turns implies rehybridization of Gr to sp³, with the same local preference (for hcp areas) in the moiré, as if the metal would have been deposited. When comparing the high-resolution inset of C clusters in Figure 4f with the corresponding inset in Figure 4a for Ir clusters, a remarkable difference is apparent. While C clusters display a molecular orbital resolution, similar to what is observed when C_{60}[53] or the sp²-reconstructed surface of nanodiamond[54] is imaged, Ir clusters are featureless. This difference is in fact systematic and the molecular orbital resolution was taken as an indication for the formation of the fullerene-like sp²-hybridized carbon.[26] Similar molecular orbital resolution is present in all other insets of Figure 4 where C was deposited. The evident conclusion is that the deposited C adsorbs on the Ir clusters where it tends to form structures with sp²-hybridized character. The deposited C conforms to the preexisting Ir clusters. Also, apparent in Figure 4b−d is that the gaps between the clusters are not yet closed by C deposition. By picking up clusters after 0.4 ML C was deposited, larger areas of the Gr substrate become visible, which are flat. There is no indication that C adsorbed in the spaces between clusters. Compare also Figure S3 of the Supporting Information.
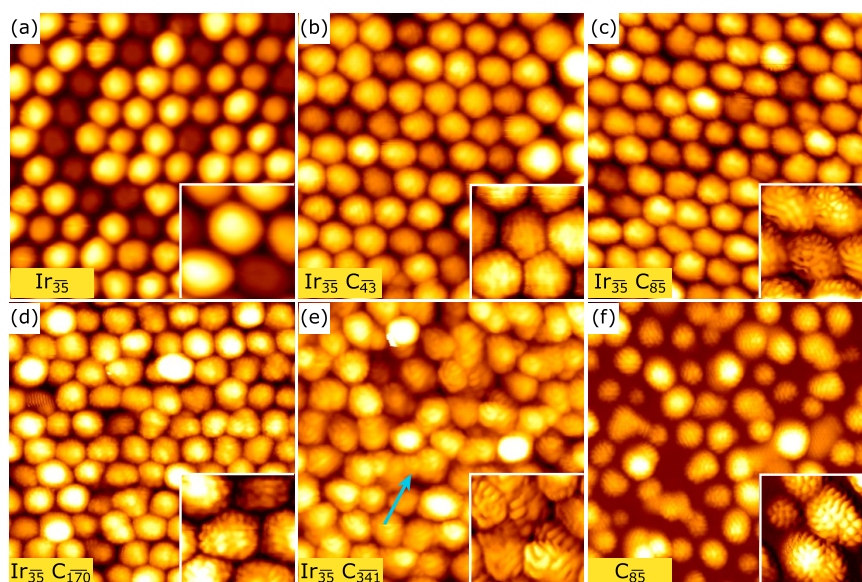
Figure 4. Sequence of STM topographs after the deposition of 0.4 ML Ir and subsequent embedding with increasing amounts of C at 300 K: (a) 0.0 ML (no carbon deposited), (b) 0.2 ML, (c) 0.4 ML, (d) 0.8 ML, and (e) 1.6 ML. (f) STM topograph after the deposition of 0.4 ML C at 300 K and annealing for 30 s to 850 K, but without prior deposition of Ir. Insets are zooms, filtered (see Methods) to enhance contrast. In the lower left corner of each topograph, the deposited material per moiré unit cell is given, which specifies in (a)−(e) the average cluster composition and size ($n = 1$). Light blue arrow in (e) indicates a cluster structure extending over more than one moiré unit cell. Topographs are 25 nm × 25 nm and insets are 6 nm × 6 nm. The average cluster sizes are calculated according to eq 1, see text.

Carbon vapor is composed predominantly of C-trimers with a small fraction of C-monomers,[55] which bind only weakly to Gr, even to Gr on Ir(111), but extremely strongly to Ir.[26,56] We therefore propose that the deposited C will adsorb directly on an Ir cluster, or if landed on Gr, diffuses until it reaches an Ir cluster edge, where it binds. Interacting C-monomers and C-trimers on the metal cluster will initiate the formation of a shell structure, predominantly with sp^2-binding motifs. Already during shell growth or no later than after its completion, the shell will develop strong sp^3-type bonds to Gr. This happens next to where the preexisting metal cluster had already introduced a rehybridization of Gr atoms to sp^3 carbon. This makes it easy for the shell to anchor strongly to the substrate. Once the shells are completed, subsequently arriving carbon will attach to the imperfectly bonded shells and an amorphous carbon network will develop that eventually will link all clusters. In this simple picture, the bonding preference of the arriving carbon to Ir rather than to Gr explains the conformal embedding of the Ir clusters, and the anchoring of the shell with sp^3 bonds to Gr explains the suppression of cluster coalescence by Smoluchowski ripening. The gradually increasing stability of the embedded cluster arrays as observed in Figure 3 is then a consequence of the gradually improving anchoring of the cluster shell to Gr.

Although our data convincingly demonstrate that cluster sintering is suppressed by C embedding, up to now no data for the effect of C embedding on cluster decay by intercalation are provided. When the metal escapes by intercalation to the substrate, an empty carbon shell would be left, which is not obvious to distinguish from a shell with a cluster inside. To this end, we conducted STS on clusters covered with different amounts of C. The resulting spectra are plotted in Figure 5 in the
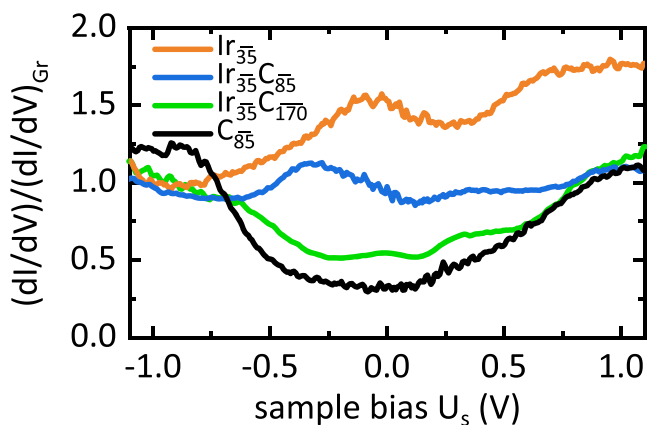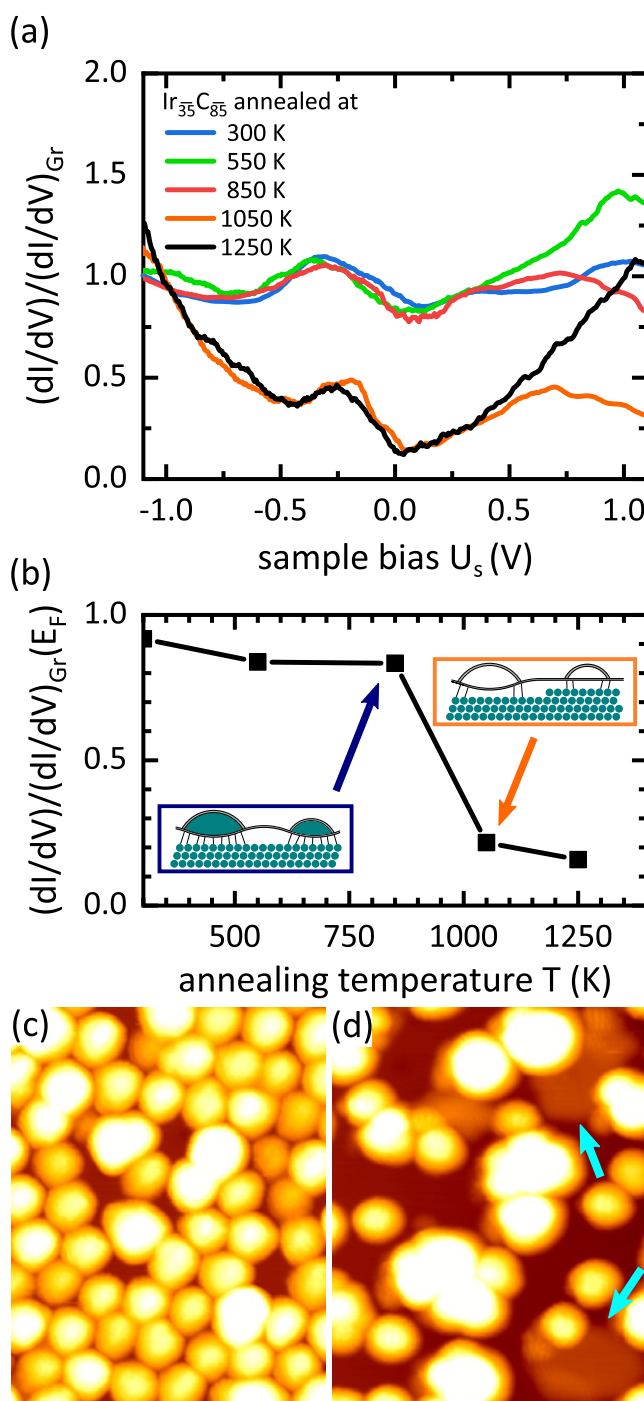

Figure 5. Differential conductance of clusters on Gr/Ir(111). Normalized tunneling conductance $(dI/dV)/(dI/dV_{Gr})$ as a function of bias voltage U_s for bare Ir clusters (0.4 ML Ir), bare C clusters (0.4 ML C), and Ir clusters embedded with C (0.4 ML Ir plus 0.4 or 0.8 ML C). The measured dI/dV cluster signal is normalized with the conductance dI/dV_{Gr} of bare Gr (see the Supporting Information).

range from −1 to +1 V. The spectra are averaged (see Methods) and normalized to the dI/dV signal of the bare Gr/Ir(111) surface (see the Supporting Information and Figure S4). The normalized cluster conductance is highest for bare Ir clusters and lowest for bare C clusters. It decreases gradually from the bare metallic to the bare C cluster signature for Ir clusters with an increasing amount of C embedding.

We use these signatures to obtain information on the internal structure of clusters formed by 0.4 ML Ir deposition with

subsequent 0.4 ML C embedding. Figure 6a displays the normalized and properly averaged dI/dV spectra for the initial $Ir_{\overline{35}}C_{\overline{85}}$ clusters as a function of the annealing temperature. It is


Figure 6. Dependence of the cluster conductance on the annealing temperature. (a) Normalized tunneling conductance $(dI/dV)/(dI/dV_{Gr})$ for $Ir_{\overline{35}}C_{\overline{85}}$ clusters (0.4 ML Ir and subsequently 0.4 ML C deposited) as a function of sample bias U_s for different annealing temperatures T. (b) Normalized tunneling conductance $(dI/dV)/(dI/dV_{Gr})$ for the same clusters at the Fermi energy E_F ($U_s = 0$ V) as a function of the annealing temperature. Insets: schematic sketches indicating the origin of conductance change with temperature. See text. (c, d) STM topographs for the same clusters after annealing to (c) 850 K and (d) 1050 K. Intercalation in (d) is highlighted by light blue arrows. The image size is 22 nm × 22 nm.

obvious that an abrupt decrease of conductivity takes place between 850 and 1050 K. This change is highlighted by plotting the conductance at the Fermi energy $E_F = 0$ eV as a function of the annealing temperature in Figure 6b. The clear change in conductivity suggests that for a temperature of 850 K the Ir within the embedding C shell is still present, while after annealing to 1050 K, it has escaped and intercalated underneath the Gr sheet (compare insets of Figure 6b). Our hypothesis is supported by the real space information provided in Figure 6c,d. In Figure 6d, after annealing to 1050 K, Ir intercalation islands are clearly visible and highlighted by arrows, while such islands are absent after annealing to 850 K in Figure 6c. For an embedding amount of 1.6 ML, STS is insensitive to the embedded Ir content due to the thick embedding layer. Nevertheless, in the light of the above experiments, it appears plausible that also for larger embedding amounts the Ir intercalates at 1050 K, while the C shell remains.

Our experiments presented up to now document the enhanced thermal stability of the embedded Ir cluster array on Gr/Ir(111). In the following, we explore changes in the mechanical stability of the cluster arrays as a consequence of embedding. Based on the work of Martinez-Galera et al.,[42] we employ a modified cluster pick-up procedure to investigate the effect of embedding on the mechanical stability of cluster arrays. The STM tip is positioned above a cluster, in all cases with a stabilization voltage $U_{stab} = -1.5$ V and current $I_{stab} = 0.5$ nA, the feedback loop is opened, an open-loop voltage U_{ol} is applied, and the tip is approached by a distance $z = 0.6$ nm to the sample. The combination of U_{stab}, I_{stab}, and z is chosen such that the tip and the cluster always come into contact, as obvious from $I(V)$ traces (compare Figure S5 of the Supporting Information).

The STM topograph in Figure 7a of bare Ir$_{\overline{35}}$ displays blue dots, where pick-up was tried with $U_{ol} = 1$ V. Figure 7b makes obvious, that the success rate for pick-up is close to 1. Pick-up with the same parameters, but for Ir$_{\overline{35}}$C$_{\overline{85}}$ clusters, fails nearly always; the pick-up probability is close to 0. Only increasing U_{ol} to 1.5 V again increases the success rate (compare Figure 7c and 7d), but it remains below the one of bare Ir clusters, irrespective of the magnitude of U_{ol}. Pick-up of clusters after embedding with 1.6 ML is impossible (compare Figure 7c), even when U_{ol} is increased to 2.5 V or z is increased to 1.2 nm. Figure 7f summarizes our results. We complemented these quantitative results by scratching experiments. By scanning an area with a low tunneling resistance, it is straightforward to clean the entire area from bare Ir clusters. However, we never succeeded in scratching away any embedded cluster after deposition with 1.6 ML C.

Cluster pick-up depends on the balance of (i) adhesion between the cluster and the tip, when a point-contact is formed and (ii) adhesion between the cluster and the substrate. For the pick-up of bare Ir clusters, the metal−metal contact adhesion between the cluster and the tip is obviously much larger than the cluster−Gr adhesion, enabling pick-up. The limited cluster−Gr adhesion is consistent with the Smoluchowski ripening of clusters at an elevated temperature. For a cluster embedded by a large amount of 1.6 ML carbon, the anchoring of the carbon shell to Gr through sp^3 bonds greatly enhances the adhesion of the entire cluster to Gr, consistent with the inability of cluster pick-up and lateral cluster manipulation by tip-scratching. The dependence of the fate of Ir$_{\overline{35}}$C$_{\overline{85}}$ clusters on U_{ol} provides additional insight into the point-contact cluster-tip adhesion. For these clusters, anchoring is not yet perfect (compare Figure 3, yellow data point). Increasing U_{ol} implies an increased power
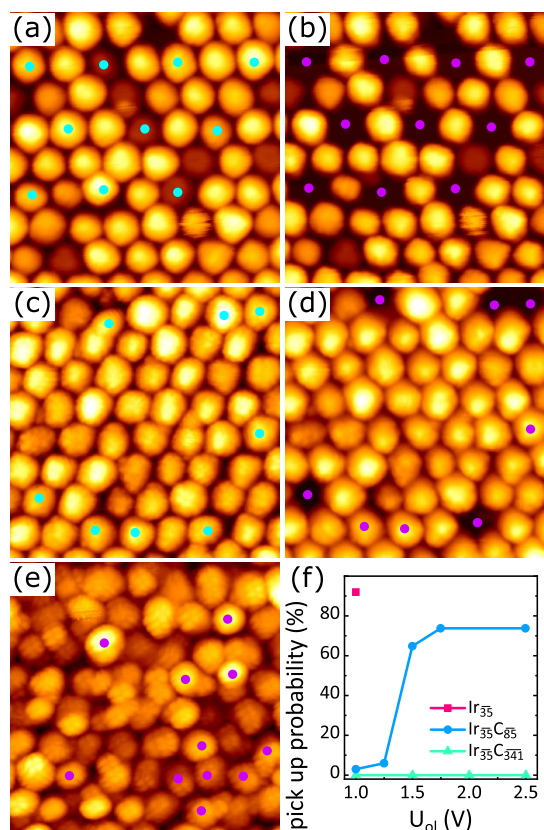
Figure 7. Cluster manipulation by STM tip. (a, b) Ir$_{\overline{35}}$ clusters after 0.4 ML deposition (a) before and (b) after manipulation attempt. Each attempt is performed by moving the tip to the location indicated by a blue dot, stabilizing the tip with $U_{stab} = -1.5$ V and $I_{stab} = 0.5$ nA, opening the feedback loop, applying an open-loop voltage $U_{ol} = 1$ V, and approaching by $z = 0.6$ nm. (c, d) Ir$_{\overline{35}}$C$_{\overline{85}}$ clusters [0.4 ML Ir and subsequently 0.4 ML C deposited] (c) before and (d) after manipulation attempt with the tip at the indicated position. Open-loop voltage increased to $U_{ol} = 1.5$ V, $z = 0.6$ nm. (e) Ir$_{\overline{35}}$C$_{\overline{341}}$ clusters (0.4 ML Ir and subsequently 1.6 ML C deposited) after manipulation attempt with the tip at the indicated locations. $U_{ol} = 1.5$ V, $z = 0.6$ nm. The topograph size is 19 nm × 19 nm in all images. (f) The pick-up probability as a function of open-loop voltage U_{ol}. Lines to guide the eye.

deposition into the cluster-tip point-contact. We speculate that the local heating will enhance the bond formation between the carbon shell and the tip. The larger the power deposited, the more bonds are formed in the "microwelding" process and thereby the pick-up probability increases with U_{ol}. In conclusion, carbon embedding increases the mechanical stability of the cluster in the array by the formation of anchoring bonds between the embedding shell and the Gr substrate.

■ CONCLUSIONS

We demonstrated conformal embedding of Ir cluster superlattices on Gr/Ir(111). Embedding preserves the initial order of the cluster superlattice. Through the embedding shell, the stability of the cluster superlattice is measured and Smoluchowski ripening is suppressed. Also, the mechanical stability of the 2D cluster array is dramatically enhanced, as proven by the inability to pick clusters up or to scratch them away with the STM tip. Careful spectroscopic measurements document that the dominant escape path of the cluster metal is through Gr toward the metal substrate, whereby the cluster intercalates.

This process sets in between 850 and 1050 K. In contrast to the cluster core, the carbon cluster shell remains stable to higher temperatures.

We anticipate that once the cluster membrane, consisting of Gr, the cluster array, and the embedding matrix is removed from the metallic substrate, the driving force for the escape of the cluster core metal (strong cluster metal−substrate metal bonding) will cease. This would make the 2D array thermally even more stable. Similar embedding processes will be possible also for other cluster sizes, other cluster superlattice materials, other 2D layer substrates (e.g., h-BN), and other embedding materials. Removing the membrane by the hydrogen bubbling method,[50,51] thickened to make it a mechanically stable object, and opened by 2D layer removal will provide an interesting new material for nanocatalysis and nanomagnetism.

METHODS

Sample preparation, growth, and in situ STM imaging were carried out in the ultrahigh vacuum system Athene with a base pressure in the 10^{-11} mbar regime. Ir(111) was cleaned by cycles of 2 keV Xe^+ sputtering and flash annealing to 1550 K. Gr was grown on Ir(111) by room-temperature adsorption of ethylene till saturation with subsequent thermal decomposition at 1300 K. This seeding growth step was followed by 180 s ethylene exposure at 1300 K and with a pressure of 1 × 10^{-8} mbar measured distant from a gas dosing tube. It gives rise to a local pressure enhancement by a factor of ≈80 at the sample location. The resulting Gr coverage was 80%, consisting of well-oriented islands with a lateral extension of the order of 1 μm, as checked with low-energy electron diffraction and STM.

Ir and C were e-beam-evaporated from high-purity rods with a deposition rate of ≈10^{-2} ML/s. During evaporation, the pressure remained below 5 × 10^{-10} mbar. Calibration of the deposited amount θ was conducted by the deposition of C or Ir on bare Ir(111) and subsequent annealing to 1470 K for C or 800 K for Ir to create compact Gr or Ir islands of monolayer thickness. The island coverage determination by STM together with the known deposition time interval enabled determination of the deposition flux. The deposited amount of Ir is specified in monolayers (ML) with respect to the surface atomic density of Ir(111), while the deposited amount of C is given in ML with respect to the atomic density in Gr.

STM and STS were conducted at room temperature. Tunneling currents I were in the range from $I = 0.1$ to 0.6 nA and sample bias voltages U_s were in the range $U_s = -(0.8-2.0)$ V. For tunneling spectroscopy and cluster manipulation, the tip was stabilized with a voltage $U_{stab} = -1.5$ V and at a tunneling current $I_{stab} = 0.5$ nA prior to loop opening. In a grid of typically 128×128 points, $I(U)$ spectra were taken and numerically differentiated to obtain dI/dV. The grid spectra taken on clusters, typically ≈5000 are averaged for representation. STM data were processed with WSxM.[57] Processing was limited to background subtraction and contrast adjustment, except for the insets of Figure 4. There, from the original, a Fourier space high-pass filtered image was subtracted to enhance orbital contrast.

ASSOCIATED CONTENT

ⓢ Supporting Information

The Supporting Information is available free of charge on the ACS Publications website at DOI: 10.1021/acsami.9b14616.

Images of cluster coalescence and metal cluster intercalation (Figure S1); morphology of cluster super-lattices after embedding with different amounts of carbon and annealing to 850 K (Figure S2); absence of C adsorption to Gr after deposition of 0.4 ML C on an Ir cluster superlattice (Figure S3); explanation of the nor-malization of STS spectra (Figure S4); and $I(V)$-trace taken during a cluster pick-up attempt (Figure S5) (PDF)

AUTHOR INFORMATION

Corresponding Author
*E-mail: will@ph2.uni-koeln.de. Phone: +49 (0)221 470-6876.

ORCID ⓞ
Moritz Will: 0000-0003-4822-9122
Pantelis Bampoulis: 0000-0002-2347-5223
Philipp Valerius: 0000-0002-2310-465X

Notes
The authors declare no competing financial interest.

REFERENCES

(1) Meiwes-Broer, K.-H. *Metal Clusters at Surfaces: Structure, Quantum Properties, Physical Chemistry*; Springer Science & Business Media, 2012.

(2) Khanna, S. N.; Castleman, A. W. *Quantum Phenomena in Clusters and Nanostructures*; Springer Science & Business Media, 2013.

(3) Kreibig, U.; Vollmer, M. *Optical Properties of Metal Clusters*; Springer Science & Business Media, 2013; Vol. 25.

(4) Gates, B. Supported Metal Clusters: Synthesis, Structure, and Catalysis. *Chem. Rev.* **1995**, *95*, 511−522.

(5) Heiz, U.; Landman, U. *Nanocatalysis*; Springer Science & Business Media, 2007.

(6) Lam, E.; Luong, J. H. Carbon Materials as Catalyst Supports and Catalysts in the Transformation of Biomass to Fuels and Chemicals. *ACS Catal.* **2014**, *4*, 3393−3410.

(7) Kundu, P.; Nethravathi, C.; Deshpande, P. A.; Rajamathi, M.; Madras, G.; Ravishankar, N. Ultrafast Microwave-Assisted Route to Surfactant-Free Ultrafine Pt Nanoparticles on Graphene: Synergistic CO-Reduction Mechanism and High Catalytic Activity. *Chem. Mater.* **2011**, *23*, 2772−2780.

(8) Liu, M.; Zhang, R.; Chen, W. Graphene-Supported Nano-electrocatalysts for Fuel Cells: Synthesis, Properties, and Applications. *Chem. Rev.* **2014**, *114*, 5117−5160.

(9) Weller, D.; Parker, G.; Mosendz, O.; Lyberatos, A.; Mitin, D.; Safonova, N. Y.; Albrecht, M. FePt Heat Assisted Magnetic Recording Media. *J. Vac. Sci. Technol., B: Nanotechnol. Microelectron.: Mater., Process., Meas., Phenom.* **2016**, *34*, No. 060801.

(10) Baltic, R.; Pivetta, M.; Donati, F.; Wäckerlin, C.; Singha, A.; Dreiser, J.; Rusponi, S.; Brune, H. Superlattice of Single Atom Magnets on Graphene. *Nano Lett.* **2016**, *16*, 7610−7615.

(11) Capiod, P.; Bardotti, L.; Tamion, A.; Boisron, O.; Albin, C.; Dupuis, V.; Renaud, G.; Ohresser, P.; Tournus, F. Elaboration of Nanomagnet Arrays: Organization and Magnetic Properties of Mass-Selected FePt Nanoparticles Deposited on Epitaxially Grown Graphene on Ir (111). *Phys. Rev. Lett.* **2019**, *122*, No. 106802.

(12) Wang, B.; Yoon, B.; König, M.; Fukamori, Y.; Esch, F.; Heiz, U.; Landman, U. Size-Selected Monodisperse Nanoclusters on Supported Graphene: Bonding, Isomerism, and Mobility. *Nano Lett.* **2012**, *12*, 5907−5912.

(13) Rondelli, M.; Zwaschka, G.; Krause, M.; Rötzer, M. D.; Hedhili, M. N.; Hötgerl, M. P.; D'Elia, V.; Schweinberger, F. F.; Basset, J.-M.; Heiz, U. Exploring the Potential of Different-Sized Supported Subnanometer Pt Clusters as Catalysts for Wet Chemical Applications. *ACS Catal.* **2017**, *7*, 4152−4162.

(14) Sitja, G.; Henry, C. R. Molecular Beam Study of the Oxidation of Carbon Monoxide on a Regular Array of Palladium Clusters on Alumina. *J. Phys. Chem. C* **2017**, *121*, 10706−10712.

(15) Mélinon, P.; Hannour, A.; Prevel, B.; Bardotti, L.; Bernstein, E.; Perez, A.; Gierak, J.; Bourhis, E.; Mailly, D. Functionalizing Surfaces with Arrays of Clusters: Role of the Defects. *J. Cryst. Growth* **2005**, *275*, 317−324.

(16) Palmer, R.; Pratontep, S.; Boyen, H.-G. Nanostructured Surfaces from Size-Selected Clusters. *Nat. Mater.* **2003**, *2*, 443.

(17) Becker, C.; Wandelt, K. *Templates in Chemistry III*; Springer, 2008; pp 45−86.

(18) N'Diaye, A. T.; Bleikamp, S.; Feibelman, P. J.; Michely, T. Two-Dimensional Ir Cluster Lattice on a Graphene Moiré on Ir(111). *Phys. Rev. Lett.* **2006**, *97*, No. 215501.

(19) Billinge, S. Materials Science: Nanoparticle Structures Served up on a Tray. *Nature* **2013**, *495*, 453−454.

(20) Degen, S.; Becker, C.; Wandelt, K. Thin Alumina Films on Ni$_3$Al(111): A Template for Nanostructured Pd Cluster Growth. *Faraday Discuss.* **2004**, *125*, 343−356.

(21) Sitja, G.; Moal, S. L.; Marsault, M.; Hamm, G.; Leroy, F.; Henry, C. R. Transition from Molecule to Solid State: Reactivity of Supported Metal Clusters. *Nano Lett.* **2013**, *13*, 1977−1982.

(22) Henry, C. R. 2D-Arrays of Nanoparticles as Model Catalysts. *Catal. Lett.* **2015**, *145*, 731−749.

(23) N'Diaye, A. T.; Gerber, T.; Busse, C.; Mysliveček, J.; Coraux, J.; Michely, T. A Versatile Fabrication Method for Cluster Superlattices. *New J. Phys.* **2009**, *11*, No. 103045.

(24) Gerber, T.; Knudsen, J.; Feibelman, P. J.; Granas, E.; Stratmann, P.; Schulte, K.; Andersen, J. N.; Michely, T. CO-induced Smoluchowski Ripening of Pt Cluster Arrays on the Graphene/Ir(111) Moiré. *ACS Nano* **2013**, *7*, 2020−2031.

(25) Franz, D.; Runte, S.; Busse, C.; Schumacher, S.; Gerber, T.; Michely, T.; Mantilla, M.; Kilic, V.; Zegenhagen, J.; Stierle, A. Atomic Structure and Crystalline Order of Graphene-Supported Ir Nanoparticle Lattices. *Phys. Rev. Lett.* **2013**, *110*, No. 065503.

(26) Herbig, C.; Knispel, T.; Simon, S.; Schröder, U. A.; Martínez-Galera, A. J.; Arman, M. A.; Teichert, C.; Knudsen, J.; Krasheninnikov, A. V.; Michely, T. From Permeation to Cluster Arrays: Graphene on Ir(111) Exposed to Carbon Vapor. *Nano Lett.* **2017**, *17*, 3105−3112.

(27) Papp, C. From Flat Surfaces to Nanoparticles: In Situ Studies of the Reactivity of Model Catalysts. *Catal. Lett.* **2017**, *147*, 2−19.

(28) Düll, F.; Bauer, U.; Späth, F.; Bachmann, P.; Steinhauer, J.; Steinrück, H.-P.; Papp, C. Bimetallic Pd−Pt Alloy Nanocluster Arrays on Graphene/Rh (111): Formation, Stability, and Dynamics. *Phys. Chem. Chem. Phys.* **2018**, *20*, 21294−21301.

(29) Düll, F.; Späth, F.; Bauer, U.; Bachmann, P.; Steinhauer, J.; Steinrück, H.-P.; Papp, C. Reactivity of CO on Sulfur-Passivated Graphene-Supported Platinum Nanocluster Arrays. *J. Phys. Chem. C* **2018**, *122*, 16008−16015.

(30) Gotterbarm, K.; Späth, F.; Bauer, U.; Bronnbauer, C.; Steinrück, H.-P.; Papp, C. Reactivity of Graphene-Supported Pt Nanocluster Arrays. *ACS Catal.* **2015**, *5*, 2397−2403.

(31) Gotterbarm, K.; Späth, F.; Bauer, U.; Steinrück, H.-P.; Papp, C. Adsorption and Reaction of SO$_2$ on Graphene-Supported Pt Nanoclusters. *Top. Catal.* **2015**, *58*, 573−579.

(32) Will, M.; Atodiresei, N.; Caciuc, V.; Valerius, P.; Herbig, C.; Michely, T. A Monolayer of Hexagonal Boron Nitride on Ir(111) as a Template for Cluster Superlattices. *ACS Nano* **2018**, *12*, 6871−6880.

(33) Brihuega, I.; Michaelis, C. H.; Zhang, J.; Bose, S.; Sessi, V.; Honolka, J.; Schneider, M. A.; Enders, A.; Kern, K. Electronic Decoupling and Templating of Co Nanocluster Arrays on the Boron Nitride Nanomesh. *Surf. Sci.* **2008**, *602*, L95−L99.

(34) McKee, W. C.; Patterson, M. C.; Huang, D.; Frick, J. R.; Kurtz, R. L.; Sprunger, P. T.; Liu, L.; Xu, Y. CO Adsorption on Au Nanoparticles Grown on Hexagonal Boron Nitride/Rh(111). *J. Phys. Chem. C* **2016**, *120*, 10909−10918.

(35) McKee, W. C.; Patterson, M. C.; Frick, J. R.; Sprunger, P. T.; Xu, Y. Adsorption of Transition Metal Adatoms on h-BN/Rh(111): Implications for Nanocluster Self-Assembly. *Catal. Today* **2017**, *280*, 220−231.

(36) Martínez-Galera, A. J.; Gómez-Rodríguez, J. M. Pseudo-Ordered Distribution of Ir Nanocrystals on h-BN. *Nanoscale* **2019**, *11*, 2317−2325.

(37) Bartholomew, C. H. Mechanisms of Catalyst Deactivation. *Appl. Catal., A* **2001**, *212*, 17−60.

(38) Benavidez, A. D.; Kovarik, L.; Genc, A.; Agrawal, N.; Larsson, E. M.; Hansen, T. W.; Karim, A. M.; Datye, A. K. Environmental Transmission Electron Microscopy Study of the Origins of Anomalous Particle Size Distributions in Supported Metal Catalysts. *ACS Catal.* **2012**, *2*, 2349−2356.

(39) Hansen, T. W.; DeLaRiva, A. T.; Challa, S. R.; Datye, A. K. Sintering of Catalytic Nanoparticles: Particle Migration or Ostwald Ripening? *Acc. Chem. Res.* **2013**, *46*, 1720−1730.

(40) Datye, A. K.; Xu, Q.; Kharas, K. C.; McCarty, J. M. Particle Size Distributions in Heterogeneous Catalysts: What Do They Tell Us about the Sintering Mechanism? *Catal. Today* **2006**, *111*, 59−67.

(41) Campbell, C. T.; Parker, S. C.; Starr, D. E. The Effect of Size-Dependent Nanoparticle Energetics on Catalyst Sintering. *Science* **2002**, *298*, 811−814.

(42) Martínez-Galera, A. J.; Brihuega, I.; Gutiérrez-Rubio, A.; Stauber, T.; Gómez-Rodríguez, J. M. Towards Scalable Nano-Engineering of Graphene. *Sci. Rep.* **2014**, *4*, No. 7314.

(43) Cao, A.; Veser, G. Exceptional High-Temperature Stability Through Distillation-Like Self-Stabilization in Bimetallic Nanoparticles. *Nat. Mater.* **2010**, *9*, 75.

(44) Lu, J.; Fu, B.; Kung, M. C.; Xiao, G.; Elam, J. W.; Kung, H. H.; Stair, P. C. Coking-and Sintering-Resistant Palladium Catalysts Achieved Through Atomic Layer Deposition. *Science* **2012**, *335*, 1205−1208.

(45) Tao, F. F.; Zhang, S.; Nguyen, L.; Zhang, X. Action of Bimetallic Nanocatalysts Under Reaction Conditions and During Catalysis: Evolution of Chemistry from High Vacuum Conditions to Reaction Conditions. *Chem. Soc. Rev.* **2012**, *41*, 7980−7993.

(46) Hejral, U.; Müller, P.; Balmes, O.; Pontoni, D.; Stierle, A. Tracking the Shape-Dependent Sintering of Platinum-Rhodium Model Catalysts Under Operando Conditions. *Nat. Commun.* **2016**, *7*, No. 10964.

(47) Niu, Y.; Schlexer, P.; Sebok, B.; Chorkendorff, I.; Pacchioni, G.; Palmer, R. E. Reduced Sintering of Mass-Selected Au Clusters on SiO2 by Alloying with Ti: An Aberration-Corrected STEM and Computational Study. *Nanoscale* **2018**, *10*, 2363−2370.

(48) Wettergren, K.; Schweinberger, F. F.; Deiana, D.; Ridge, C. J.; Crampton, A. S.; Rötzer, M. D.; Hansen, T. W.; Zhdanov, V. P.; Heiz, U.; Langhammer, C. High Sintering Resistance of Size-Selected Platinum Cluster Catalysts by Suppressed Ostwald Ripening. *Nano Lett.* **2014**, *14*, 5803−5809.

(49) Bunch, J.; Verbridge, S.; Alden, J.; Van Der Zande, A.; Parpia, J.; Craighead, H.; McEuen, P. Impermeable Atomic Membranes from Graphene Sheets. *Nano Lett.* **2008**, *8*, 2458−2462.

(50) Gao, L.; Ren, W.; Xu, H.; Jin, L.; Wang, Z.; Ma, T.; Ma, L.-P.; Zhang, Z.; Fu, Q.; Peng, L.-M.; Bao, X.; Chengothers, H.-M. Repeated Growth and Bubbling Transfer of Graphene with Millimetre-Size Single-Crystal Grains Using Platinum. *Nat. Commun.* **2012**, *3*, No. 699.

(51) Rakić, I. Š.; Čapeta, D.; Plodinec, M.; Kralj, M. Large-Scale Transfer and Characterization of Macroscopic Periodically Nano-Rippled Graphene. *Carbon* **2016**, *96*, 243−249.

(52) Feibelman, P. J. Pinning of Graphene to Ir (111) by Flat Ir Dots. *Phys. Rev. B* **2008**, *77*, No. 165419.

(53) Lakin, A. J.; Chiutu, C.; Sweetman, A. M.; Moriarty, P.; Dunn, J. L. Recovering Molecular Orientation from Convoluted Orbitals. *Phys. Rev. B* **2013**, *88*, No. 035447.

(54) Pawlak, R.; Glatzel, T.; Pichot, V.; Schmidlin, L.; Kawai, S.; Fremy, S.; Spitzer, D.; Meyer, E. Local Detection of Nitrogen-Vacancy Centers in a Nanodiamond Monolayer. *Nano Lett.* **2013**, *13*, 5803−5807.

(55) Zavitsanos, P.; Carlson, G. Experimental Study of the Sublimation of Graphite at High Temperatures. *J. Chem. Phys.* **1973**, *59*, 2966−2973.

(56) Herbig, C.; Åhlgren, E. H.; Jolie, W.; Busse, C.; Kotakoski, J.; Krasheninnikov, A. V.; Michely, T. Interfacial Carbon Nanoplatelet Formation by Ion Irradiation of Graphene on Iridium (111). *ACS Nano* **2014**, *8*, 12208−12218.

(57) Horcas, I.; Fernández, R.; Gomez-Rodriguez, J.; Colchero, J.; Gómez-Herrero, J.; Baro, A. WSXM: a Software for Scanning Probe

Microscopy and a Tool for Nanotechnology. *Rev. Sci. Instrum.* **2007**, *78*, No. 013705.

6.1 Manuscript 3: Supporting Information

Supporting Information:

Conformal Embedding of Cluster Superlattices

with Carbon

Moritz Will,* Pantelis Bampoulis, Tobias Hartl, Philipp Valerius, and Thomas

Michely

II. Physikalisches Institut, Universität zu Köln, Cologne, D-50937, Germany

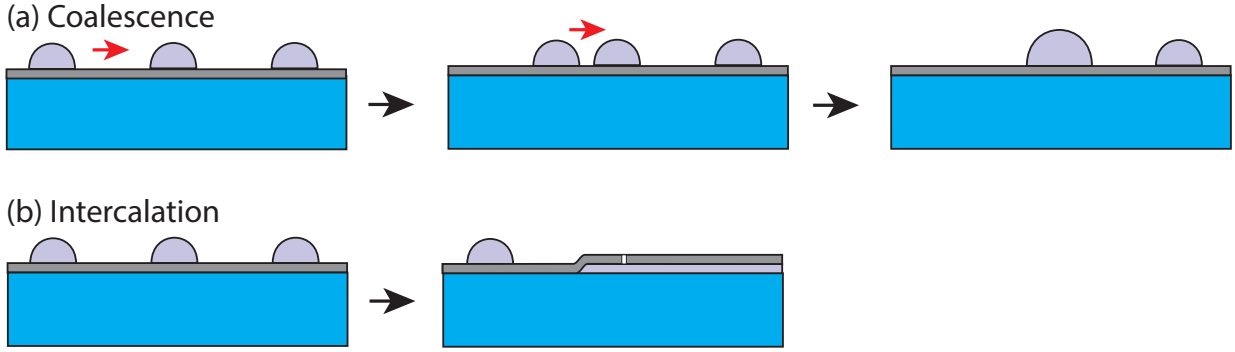E-mail: will@ph2.uni-koeln.de

Phone: +49 (0)221 470-6876

Figure S1: Schematic representation of the relevant degradation mechanisms of cluster super-lattices grown on Gr/Ir(111). (a) Thermally activated coalescence of two clusters, forming a single bigger cluster (Smoluchowski ripening) and (b) thermally activated intercalation of the cluster metal between the Gr sheet and the Ir(111) surface

The normalized differential conductance spectra of the C covered metal nanoclusters shown in the main manuscript were derived using the methodology described by Gomes et al.[S1] Using this method, numerically obtained dI/dV spectra averaged over several clusters were divided by the average spectrum obtained in pristine Gr. This procedure is used in order to eliminate contributions from the tip's and substrate's density of states.[S1–S3] Using graphene's spectrum as a reference point allowed us to compare spectra obtained on different samples, with different tips and after different thermal treatments. We note here, that regions of pristine graphene were obtained by picking up individual clusters as described in the main text. An example of this process is shown in Figure S4a, where dI/dV spectra obtained at 300 K on Gr and $Ir_{\overline{35}}C_{\overline{85}}$ clusters before normalization are displayed. The normalized differential conductance spectrum is shown in Figure S4b. Normalized dI/dV spectra obtained with different tips and at temperatures up to 850 K show very similar features to one another as shown in Figure 5 of the main text. This way contributions of the tip's DOS are canceled out allowing for a direct comparison between the measurements. Annealing to 1050 K and above leads to a substantial change of the clusters' differential conductance. Figure S4c displays dI/dV curves recorded on clusters and on Gr at 1250 K before normalization. Already here a substantial difference is observed between the clusters and the Gr signal. The normalized spectrum is illustrated in Figure S4d. As shown in the
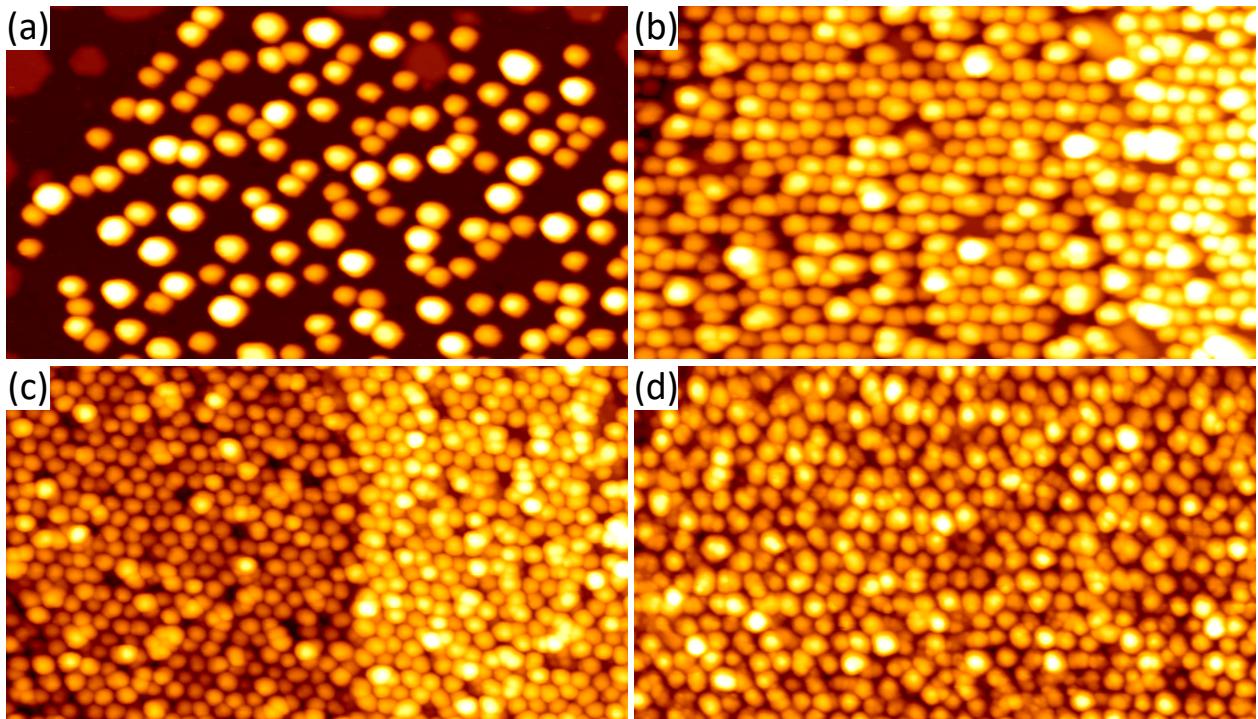
Figure S2: STM topographs of Ir clusters on Gr/Ir(111) embedded with different amounts of C and annealed to 850 K, representative of the data points in Figure 3 of the main manuscript. Annealing of clusters grown by deposition of 0.4 ML Ir on Gr/Ir(111) with subsequent deposition of (a) no additional C, (b) 0.4 ML C, (c) 0.8 ML C, and (d) 1.6 ML C. Image size is 70 nm × 40 nm in all topographs.
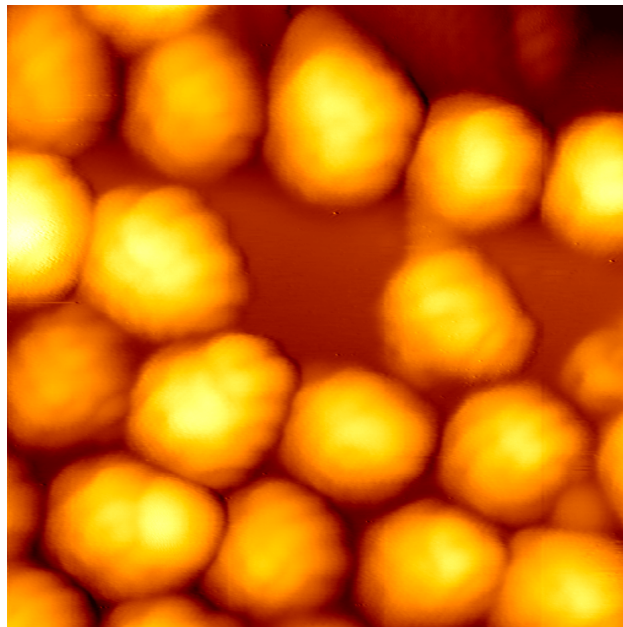

Figure S3: 11 nm × 11 nm STM topograph of Gr/Ir(111) after exposure to 0.4 ML Ir and subsequently to 0.4 ML C. A derived image has been added to the main image in order to highlight the cluster internal structure.
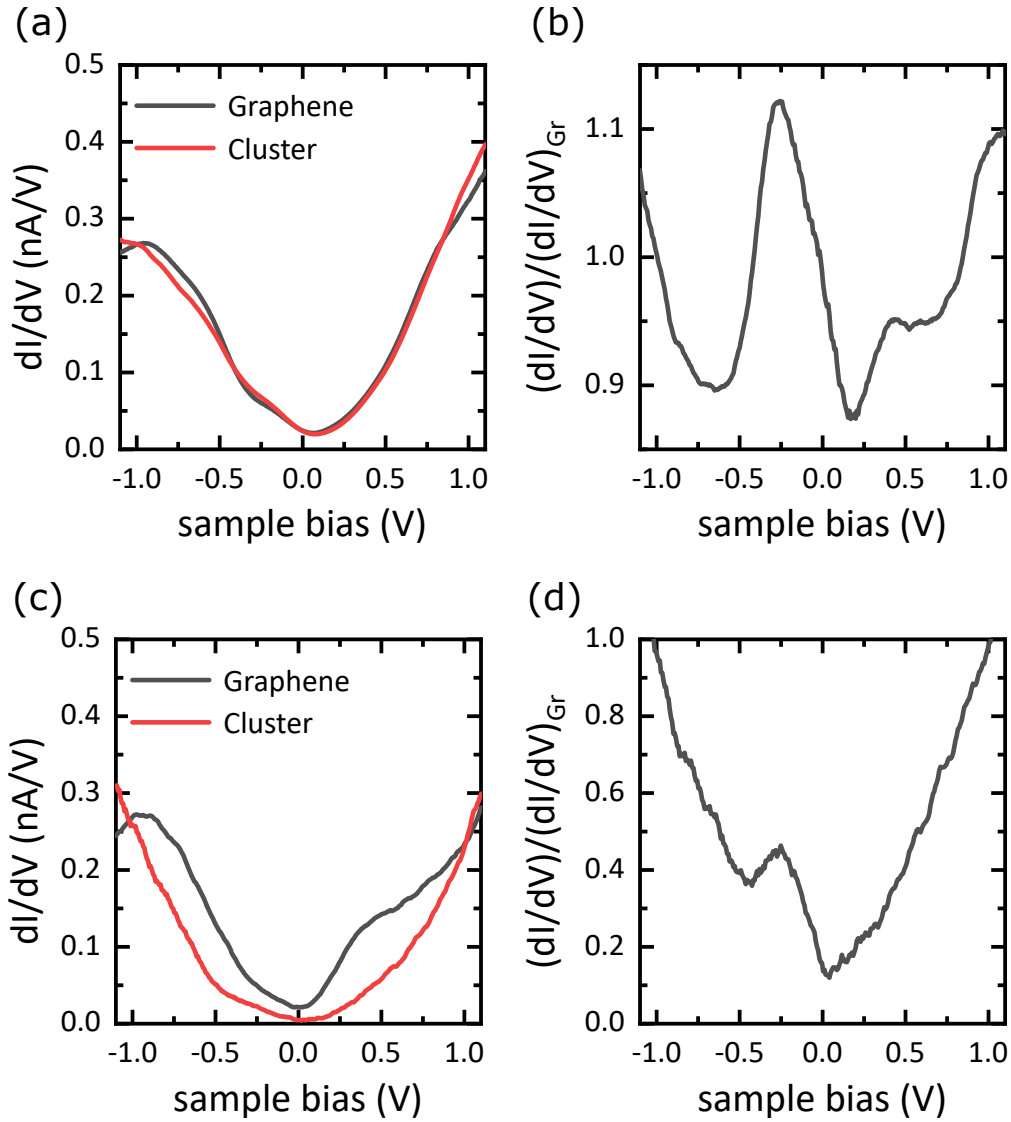
Figure S4: (a) Differential conductance spectra averaged over several $Ir_{\overline{35}}C_{\overline{85}}$ clusters (red) and pristine Gr regions (black) at 300 K. (b) Normalized differential conductance of $Ir_{\overline{35}}C_{\overline{85}}$ clusters at 300 K. c) Differential conductance spectra averaged over several clusters (red) and pristine graphene regions (black) after annealing to 1250 K. (d) Normalized differential conductance of $Ir_{\overline{35}}C_{\overline{85}}$ clusters after annealing to 1250 K.

main text, a similar curve is obtained also at 1050 K. Both spectra are significantly different from the ones obtained for samples annealed up to 850 K. The lower conductivity of the clusters above 1050 K indicates depletion of Ir from the C cage by intercalation to the Ir substrate. The differential conductance of the remaining cluster resembles that of the pure C clusters shown in Figure 4 of the main text.
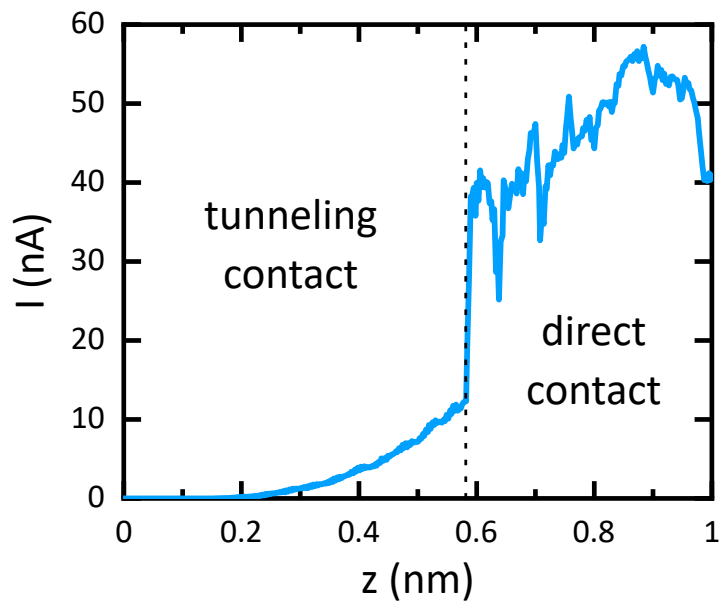

Figure S5: Typical I(z) spectrum of a cluster pick-up event with $U_{ol} = 1.5$ V and $z = 10$ Å, performed on Ir clusters embedded with 0.4 ML C. At a distance of 6 Å, the current jumps from an exponential increase into contact. Note that this spectrum only displays the tip approach, not the retract. Stabilization set points are $U = -1.5$ V and $I_t = 0.5$ nA.

References

(S1) Gomes, K. K.; Mar, W.; Ko, W.; Guinea, F.; Manoharan, H. C. Designer Dirac Fermions and Topological Phases in Molecular Graphene. *Nature* **2012**, *483*, 306.

(S2) Slot, M. R.; Gardenier, T. S.; Jacobse, P. H.; van Miert, G. C.; Kempkes, S. N.; Zevenhuizen, S. J.; Smith, C. M.; Vanmaekelbergh, D.; Swart, I. Experimental Realization and Characterization of an Electronic Lieb Lattice. *Nat. Phys.* **2017**, *13*, 672.

(S3) Kempkes, S.; Slot, M.; Freeney, S.; Zevenhuizen, S.; Vanmaekelbergh, D.; Swart, I.; Smith, C. M. Design and Characterization of Electrons in a Fractal Geometry. *Nat. Phys.* **2019**, *15*, 127.

PART III

Discussion

CHAPTER 7

Summary and Outlook

Here, we summarize the findings of each manuscript included in this thesis in more detail than what has been already provided in the publications. We attend to questions left open from the analysis, and give considerations which might have been beyond the scope of the manuscripts. Furthermore, we give an outlook and suggest possible, fruitful experiments for the future.

7.1 Chapter 5: Monolayer h-BN/Ir(111) as a Template for Cluster Superlattices

In chapter 4 we have demonstrated the use of a monolayer of h-BN/Ir(1 1 1) as a template for the growth of Ir, Au, and C cluster superlattices. For the case of Ir, deposition at 350 K leads to the formation of a cluster superlattice with a narrow size distribution. A perfect superlattice develops for average cluster sizes between $s_{av} = 4$ and 175 atoms, controlled by the deposited amount. We have confirmed the epitaxial growth of Ir clusters with respect to the substrate by a careful analysis of cluster envelopes and by measuring their layer-by-layer growth along the [1 1 1]-direction. The thermal stability of Ir clusters is the highest compared to any other cluster-substrate combination reported in the literature. Degradation of the superlattice only sets in at an annealing temperature of 700 K. It occurs *via* Smoluchowski ripening and intercalation below the h-BN. No evidence for Ostwald ripening of Ir clusters was found. Ir clusters (and also Au and C clusters) form mainly in the valley regions of the moiré. At low deposition temperatures and low coverages, a substantial amount of clusters are observed in the center region between three adjacent valleys. At these regions, point defects are present with varying concentration depending on the preparation procedure, which act as additional, albeit very small, binding sites for Ir species. At higher Ir coverages and thereby larger cluster sizes, the center region clusters are consumed by adjacent valley region clusters.

Using Ir as a paradigm, we unraveled the bonding mechanism of adsorbed Ir atoms on the h-BN/Ir(1 1 1) substrate by means of DFT calculations. An adsorbed Ir heptamer turns out to be most stable in the valley region of the moiré, when Ir atoms are on top of B atoms. All other configurations are energetically disfavored which is in line with the experimental results.

In clean h-BN/Ir(1 1 1) the N atoms hybridize with the d_{z^2} orbitals of the underlying Ir surface in the valley region, while the B atoms are located in the threefold-coordinated hollow sites. The reason for this lies in the electronegativity of nitrogen, which leads to a localization of the occupied states at the N atoms, which then hybridize with the Ir atoms below. When an Ir_7 cluster is adsorbed on top, the B atoms move upwards substantially and the unoccupied B states are filled with electrons from the Ir cluster d_{xz} and d_{yz} orbitals. This way an sp^3 configuration is reached, with bond angles around 111.5° and bond distances of 2.1 Å. The sp^3 nature of the bonds is confirmed by the calculated PDOS, which clearly shows the increased splitting of Ir d_{z^2} states at the Fermi energy into bonding and anti-bonding states and their overlap with the sp^2 orbitals of the N atom above.

Moreover, on h-BN/Ir(1 1 1) Au and C superlattices can be grown with a thermal stability that is much higher than on other templates. A gold superlattice with $n = 0.9$ is reported at a deposition temperature of 300 K, which could previously only be templated with a high number density at temperatures well below. C clusters are stable even after annealing to 1350 K. Carbon is fundamentally different from metal clusters in that it forms only directed, covalent bonds which is the cause for the enormous stability and different appearance of the clusters. They decay by penetration to the interface, where they form Gr flakes below the h-BN.

Outlook

In this work we have demonstrated that h-BN/Ir(1 1 1) is superior to all other known templates in many regards when it comes to synthesizing cluster superlattices under UHV conditions. When compared to another excellent template which is Gr/Ir(1 1 1), [198, 237] the single adsorption minimum of the moiré results in an increased order of the cluster lattices at low coverages. In addition, the extension of its unit cell enables cluster growth up to a larger size before coalescence sets in. The chemical selectivity provided by the bi-atomic composition of boron nitride suggests that other elements can be readily templated into regular arrays as well, which was indeed demonstrated in sections 5 and A.1. We mention here, that during the time of this thesis another beautiful example of highly ordered Ir cluster superlattices on h-BN/Rh(1 1 1) was reported in the literature, but their thermal stability is inferior to Ir/h-BN/Ir(1 1 1). [288] This is presumably due to the different binding mechanism of clusters to h-BN/Rh(1 1 1). We achieve the highest cluster density, best order and highest thermal stability for Ir, Au, and C, which pave the way for further experiments and applications in fields such as heterogeneous catalysis.

The simplest of such experiments might be a TPD/TPR experiment with which the adsorption and reaction of gases on metal clusters can be probed, similar to the work of Gerber *et al.* conducted on Pt and Au clusters on Gr/Ir(1 1 1). [246] Suitable reactions and cluster materials can be readily picked from the literature – Ir clusters are for example active for toluene and ethene hydrogenation. [344,345] No degradation of the Ir clusters is observed up to five minutes at

700 K, a temperature well above the working temperature of most conventionally used catalysts. Furthermore, the availability of a stable Au superlattice at 300 K opens the door to study catalysis over highly ordered Au clusters, for which important reactions such as CO oxidation [107] or selective alkene oxidation [110] have been reported at remarkably low temperatures.

At low deposition temperatures, even single Ir atoms can be efficiently templated on h-BN/Ir(1 1 1), making it attractive for the field of single atom catalysis. Single atom catalysts have become a hot topic in the last decade because they maximally increase the cost reduction and selectivity. [346–350] Systems such as Au_1/h-BN, [351] Au_2/h-BN, [352] and Fe_1/h-BN [353] have been studied theoretically by Gao, Zhao, and co-workers. Ir single-atom catalysts have been prepared on FeO_x and proved to be active for CO oxidation [354], as well as the water-gas-shift reaction [355]. However, the wet chemical method employed in these studies provides a much lower density of nanoparticles than templated growth on h-BN/Ir(1 1 1), which might increase the activity.

The ability to template small clusters with high precision down to the single atom limit is attractive not only for chemistry but also to the field of magnetism, as it offers the possibility to measure magnetic properties with integrating techniques such as x-ray magnetic circular dichroism. An impressive example is the array of Dy atoms on Gr/Ir(1 1 1), demonstrated by Baltic *et al.* [128], which act as single-atom magnets with a hysteresis loop. In the same work, the authors have investigated Dy atoms on h-BN/Ir(1 1 1), but find paramagnetic behavior with XMCD. Nevertheless, the templating properties of h-BN/Ir(1 1 1) might enable further studies in this field with materials such as Fe (section A.1.1), FePt [356], or Dy (section A.1).

Finally, the demonstration of highly stable C clusters on h-BN/Ir(1 1 1) proves that carbon forms similar structures as was found for Gr/Ir(1 1 1). [357] The C clusters are likely fullerene-like domes anchored to the h-BN by sp^3 hybridization. In view of the goal of this thesis, the embedding of cluster superlattices grown on h-BN/Ir(1 1 1) is promising with this in mind.

We also want to briefly address the weaknesses of h-BN/Ir(1 1 1) for templated cluster growth. While h-BN can be grown in large flakes extending over several hundred nm in size with high quality, inherently during the growth process small point defects are created, whose origin is so far unknown. As shown in chapter 4, they act as additional binding sites for cluster adsorption and they effectively pin very small clusters, likely not more than a few atoms large. This becomes more of a problem at low temperatures, where a substantial amount of such center clusters is observed. Apart from the fact that they derange the perfect order of the superlattice, their chemical environment is likely different than that of valley clusters, which is undesirable for most applications.

Another issue is the omnipresent inhomogeneity of h-BN/Ir(1 1 1). While large regions of the h-BN are homogeneously perfect, some areas extending over several tens of nm^2, exhibit substantially worse cluster ordering, earlier degradation of the superlattice at lower temperatures, and a different moiré appearance in STM when no clusters are present. [358] This indicates that

local conditions during growth play a critical role in the catalytic dehydrogenation of borazine on Ir(1 1 1) and influence the quality of the resulting h-BN layer. Both of these examples make plain, that optimizing the growth procedure of h-BN/Ir(1 1 1) and understanding the nature of the center region point defects is a potentially rewarding task for the future in view of improving the quality of grown cluster superlattices.

7.2 Chapter 6: Growth, Stability and Decoupling of Pt Clusters on h-BN/Ir(111)

In chapter 5 we comprehensively investigate Pt cluster superlattices grown on h-BN/Ir(1 1 1) by means of XPS and STM. The arrays display an exceptional degree of ordering and a high thermal stability, unmatched by Pt clusters on other substrates. We determine the binding site of the clusters as the valley region of the moiré and demonstrate the rehybridization of the h-BN upon cluster formation. A highly regular cluster array with $n = 1$ is formed for cluster sizes between $Pt_{\overline{21}}$ and $Pt_{\overline{92}}$. A lower cluster number density is observed for $Pt_{\overline{3.4}}$ clusters and $Pt_{\overline{115}}$ clusters. Monitoring the Ir 4f and B 1s core levels during Pt deposition allows us to follow the growth of Pt clusters in the valley areas of the h-BN as a function of size. Upon Pt deposition the weight of the B_1 component, representing the strongly interacting B atoms in the valleys, increases. This goes along with a decrease of the Ir 4f surface component Ir_S and an increase of the Ir 4f interface component Ir_{Int}. The Ir_S component is related to the Ir(111) surface atoms not interacting with h-BN, while the Ir_{Int} component is due to the surface atoms bonding to h-BN in the valleys. This directly evidences the growth of Pt clusters in the valley and the consequential expansion of the valley regions with increasing cluster footprint. Moreover, we have observed an energy shift of the B_1 component, which is caused by the chemical bonds to the Pt cluster atoms. The XPS measurements therefore provide the first direct evidence of the rehybridization mechanism of clusters on h-BN/Ir(1 1 1).

A stand-out feature of Pt clusters on h-BN/Ir(1 1 1) is the sparseness of two-layer clusters. Similar to Ir clusters on h-BN/Ir(1 1 1), Pt clusters grow layer-by-layer with heights of 2.2 Å, the Pt(1 1 1) step height. As observed by STM, for the case of 0.55 ML Pt deposition ($Pt_{\overline{63}}$), the majority of clusters are one-layer, with some occurrence of three- and four-layer clusters. $Pt_{\overline{92}}$ clusters are predominantly three- and four-layer. The largest amount of two-layer clusters is reported for $Pt_{\overline{21}}$ clusters, with an abundance of 6%. This suggests that clusters collapse directly from one to three layers during growth. Notably, annealing of $Pt_{\overline{63}}$ clusters at 730 K barely disturbs the lattice perfection, but transforms a substantial amount of one-layer to three-layer clusters. Two-layer Pt clusters are therefore unstable. Similar findings were reported for Ir clusters on h-BN/Ir(1 1 1), [298] but not on Gr/Ir(1 1 1), [198,237] suggesting the substrate as the cause of this metastability

Aside from the aforementioned re-structuring, the cluster lattice is perfectly stable up to

650 K. At 750 K, cluster sintering and intercalation sets in, with sintering being the predominant mechanism. At an annealing temperature of 1050 K, intercalation is the prevalent degradation mechanism. At 1250 K all Pt has penetrated to the h-BN/Ir(1 1 1) interface. These changes are evidenced both by direct STM imaging and by monitoring the evolution of the Ir 4f and Pt 4f core levels. The decrease of the Ir_{Int} component (and simultaneous increase of the Ir_S component) above 650 K is related to Smoluchowski ripening of clusters. When clusters coalesce, moiré valleys are restored to their original configuration. Consequentially, the Ir_{Int} and Ir_S components recover towards the values of clean h-BN/Ir(1 1 1). Above 1050 K, we again observe a decrease (increase) of the Ir_S (Ir_{Int}) component. This is due to intercalation of Pt taking over as the predominant decay mechanism. Intercalated Pt forms extended islands on the Ir(1 1 1) surface, thus reducing the Ir_S component. The intercalation mechanism is also evidenced by the changes of the Pt 4f core level. After deposition, the Pt 4f spectrum is broad, indicating many different species of atoms contributing to the signal. We attribute this to the different binding configurations of surface, edge, corner and center atoms in a Pt cluster. Annealing at 1250 K narrows down the Pt 4f spectrum, and induces an energy shift towards a BE of 71.06 eV. The resulting spectrum is similar to the one of Pt on bare Ir(1 1 1) annealed at 1200 K. From this we conclude that Pt forms flat islands on the Ir surface after annealing.

Moreover, we have demonstrated the electronic decoupling of Pt clusters on h-BN/Ir(1 1 1). Room-temperature STS on individual Pt clusters reveals peaks between -1.2 eV and 1.2 eV in the differential conductance spectra, while the signal of bare h-BN/Ir(1 1 1) is featureless. These peaks are attributed to Coulomb staircase effects caused by single-electron tunneling, as introduced in section 2.1. The observation of a Coulomb staircase necessitates strong insulation of the clusters from the substrate. The h-BN thereby acts as a tunneling barrier between cluster and Ir(1 1 1) surface and thus gives rise to a double-barrier tunneling junction. The peak-to-peak distance is found to decrease with increasing cluster size. This effect is attributed to the relation of the discrete level spacing ΔE of a cluster to its size and morphology. From the STS results, we were able to demonstrate that the quantized level spacing ΔE depends inversely on the Pt cluster height, as expected from previous considerations.

Outlook

Pt clusters are of paramount relevance for catalytic studies. To name a few, Pt clusters are commonly employed for CO oxidation in conventional car exhaust catalytic converters, [359] as catalysts for the water-gas shift reaction [360–362], alkane/alkene (de-)hydrogenation reactions, [322,363–365] or for hydrogen evolution. [366] The formation of stable cluster arrays of Pt is thus a promising prospect for model catalytic studies. By introducing h-BN/Ir(1 1 1) as a template for Pt cluster superlattices, we provide a new system for fundamental studies on catalysis, which surmounts other substrates with regards to structural perfection and thermal stability of the clusters. [14, 289] This would allow one for example to investigate the influence of cluster steps

and kinks on catalytic reactions, which is common practice done with single crystals already. [367] One possible route could be the comparison of predominantly two-dimensional $Pt_{\overline{21}}$ clusters to three-dimensional $Pt_{\overline{92}}$ clusters.

We provide the first experimental evidence of the binding of Pt clusters with h-BN/Ir(1 1 1) and thereby directly confirm the validity of the DFT results obtained in chapter 4 for Ir clusters. Moreover, the STS results demonstrate the electronic decoupling of Pt clusters caused by the h-BN sheet, which opens the way for applications in nano-electronics and nano-sensing. [60, 144, 368] Implementing a gate electrode would allow the use of Pt clusters as single-electron transistors.

7.3 Chapter 7: Conformal Embedding of Cluster Superlattices with Carbon

Chapter 6 contains a pivotal step in the formation of a stable, free-standing cluster superlattice membrane, namely the embedding in a host matrix consisting of amorphous carbon. Embedding is performed by deposition of elemental carbon from the gas phase onto an Ir cluster superlattice grown on Gr/Ir(1 1 1). STM imaging reveals that the thermal stability of Ir clusters after C deposition is significantly increased. Embedding with 1.6 ML C (resulting in $Ir_{\overline{35}}C_{\overline{341}}$) not only preserves the cluster superlattice order but also makes it substantially more resistant to sintering *via* Smoluchowski ripening. Even after annealing to 1350 K, the cluster number density remains at 0.74. As illustrated in chapter 6, the degree of stabilization of the superlattice against sintering is a function of the deposited amount of C. Without C, annealing of an $Ir_{\overline{35}}$ superlattice decreases the cluster number density to $n = 0.45$. Deposition of 0.4 ML C, resulting in $Ir_{\overline{35}}C_{\overline{85}}$, increases the cluster number density after annealing at 850 K from $n = 0.45$ (without C) to 0.74. At 0.8 ML C, we find $n = 0.93$ and at 1.6 ML the cluster superlattice is unperturbed with $n = 1$.

A key aspect of this work is to demonstrate that the C embedding of Ir clusters is conformal. The deposited C preferentially binds to the clusters rather than to the bare Gr regions in between adjacent clusters which does not degrade the initially formed superlattice. This is based on the following considerations: firstly, from energetic considerations, the C species bind much more strongly to Ir than to Gr/Ir(1 1 1). [369] Secondly, STM imaging reveals that clusters appear systematically different after C deposition. Bare Ir clusters are essentially featureless and round. In contrast to that, embedded clusters (even with little amounts of deposited C) show localized molecular orbitals reminiscent of fullerenes, [370–373] nanodiamonds, [374] or C clusters on Gr/Ir(1 1 1). [357] Thirdly, when individual clusters after C deposition are removed intentionally with the STM tip, bare Gr is found underneath and in close vicinity to the cluster. We envision C arriving on bare Gr to be mobile and migrate to the rims of a cluster where it forms sp^3-type

bonds with Gr, anchoring the cluster to the substrate. This gives rise to the enormous thermal stability of the embedded Ir clusters.

The anchoring of the Ir clusters by C is also supported by their increased mechanical stability. We have investigated the mechanical stability of Ir clusters embedded with C by systematically probing them with the STM tip. This is done in a controlled pick-up experiment. The tip is placed above a cluster with a specific set of stabilization parameters, the feedback loop is opened and the tip is brought into direct contact with the sample while an open-loop voltage U_{ol} is applied. We find that uncovered Ir clusters are always easily picked up by this procedure with a probability of 100%. In contrast to that, clusters covered with 0.4 ML C cannot be picked up below $U_{ol} < 1.5$ V. Above this voltage, the pick-up probability reaches 75 %, indicating a 'nano-welding' process, where the locally deposited power leads to bond formation between tip and cluster. Clusters embedded by 1.6 ML C could not be removed at all. Consequently, encapsulation in a matrix of C gradually stabilizes the clusters against pick-up.

Finally, we have addressed the question whether or not embedding with molecular C also protects the clusters against intercalation to the Gr-Ir(1 1 1) interface upon heating. To this end, STS measurements were conducted, utilizing the fingerprint of a pure C cluster on Gr/Ir(1 1 1), which is a low differential conductance around the Fermi level. In contrast to that, bare and embedded clusters display a higher dI/dV signal. Monitoring the differential conductance recorded on top of the embedded clusters after each annealing step, allowed us to determine the temperature where Ir intercalates below Gr. We find the transition to lie in the range between 850 and 1050 K, visible as a sharp drop in the normalized differential conductance. A quite similar temperature was determined by XPS measurements conducted on embedded Pt clusters on h-BN/Ir(1 1 1) by us. [375]

Outlook

Sintering of nanoparticles and intercalation underneath the supporting 2D layer hinder the use of cluster superlattices. In this work, we have essentially eliminated one of the two mechanisms completely using a protective C matrix. Underneath the amorphous carbon, the cluster superlattice remains completely intact and coalescence is fully suppressed. The demonstration of the conformal embedding of metal clusters with a host material like amorphous carbon is a crucial step towards creating a novel 2D material: a cluster superlattice membrane (compare section 3.3).

Of course this achievement comes with trade-offs. First of all, the clusters are no longer directly exposed to the environment which disables their surface chemistry. An idea to overcome this problem is to carefully etch away the a-C layer. Ideally, this would expose only the top of the clusters while most of the stabilizing matrix remains intact, enabling them to interact with adsorbants but still preventing coalescence. This concept is visualized schematically in Figure 7.1a. Embedded Ir clusters depicted in the leftmost sketch are subject to radical $O_1^{\bullet}$ exposure at room
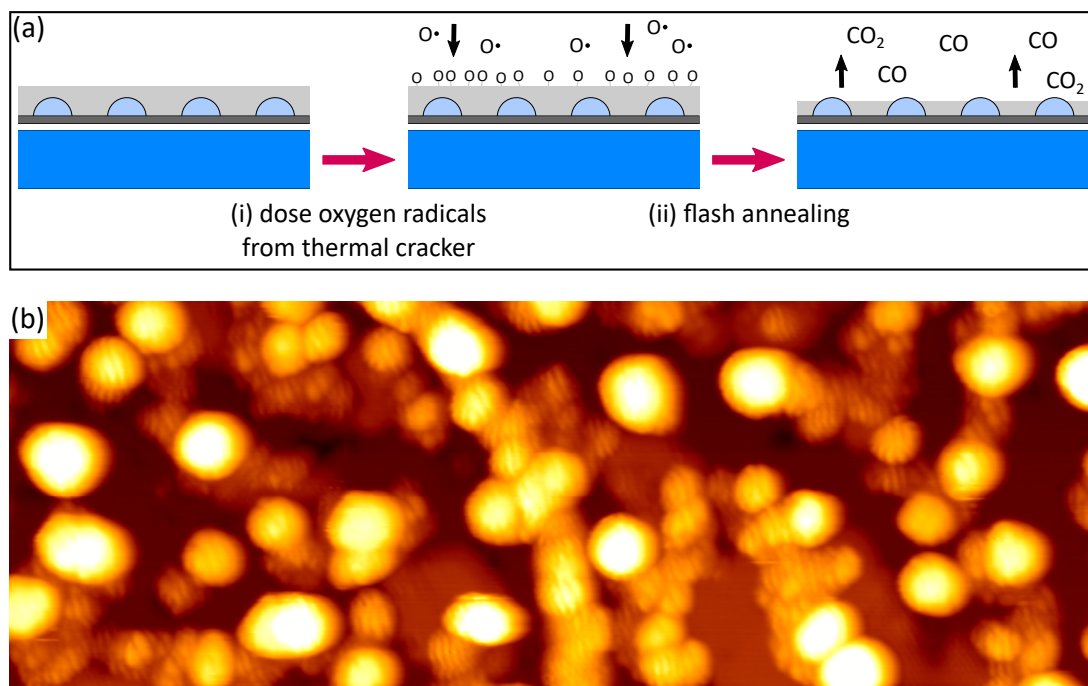
Figure 7.1: (a) Schematic drawing of the concept of embedded cluster etching showing a side view of embedded Ir clusters on Gr/Ir(1 1 1). (i) Oxygen radicals are supplied from a thermal gas cracker at room temperature. The radicals form bonds to the amorphous carbon layer. (ii) The sample is flash annealed, giving rise to etching of the a-C layer by CO and CO_2 formation. Dark blue: Ir(1 1 1) substrate; light blue: Ir clusters; dark gray: Gr; light gray: embedding a-C layer. (b) STM topograph of $Ir_{\overline{35}}C_{\overline{341}}$ clusters after two cycles of 2.5 L $O_1^\bullet$ dosing and flash annealing to 800 K. Image size is 50 nm × 18 nm.

temperature, which is supplied from a thermal gas cracker. Due to the enormous reactivity of the radicals, they attach to the outermost atoms of the a-C layer, visualized in the second sketch. Finally, after the radical dosing has been halted, the sample is flash annealed to a temperature, where adsorbed oxygen reacts to CO and CO_2 and desorbs from the sample. This process can then be repeated in cycles, while the degree of etching is controlled by the $O_1^\bullet$ dose and the annealing temperature. Figure 7.1b shows preliminary results of the etching process. It displays an STM topograph of $Ir_{\overline{35}}C_{\overline{341}}$ clusters, after two cycles of 2.5 L $O_1^\bullet$ dosing and flash annealing to 800 K. While the cluster superlattice is essentially destroyed, some cluster compounds remain on the surface with a clear molecular orbital contrast. Alongside those clusters, flat islands with a height of about 2 Å are present. No moiré contrast is visible in the entire topograph. We therefore assume, that the Gr has been etched away together with a large part of the embedding C. Some, presumably mostly sp^2-hybridized, carbon is remaining in the form of small and large clusters, identified by the molecular orbital resolution. The Ir clusters have escaped from the C shells, intercalated below the Gr layer on the Ir(1 1 1) surface, and formed flat islands. Some very large C clusters remain on the surface, suggesting that the etching efficiency varies locally. This presumably happens once bare Ir is exposed, since it locally catalyzes the chemical reaction

and accelerates the etching process. [376] Therefore, in order to etch away only the outermost a-C layer, further research is needed to enhance the control of the entire etching process.

The method presented in this study can be expanded to other substrate/cluster/embedding material combinations. The first material coming to mind is the usage of h-BN/Ir(1 1 1) as a substrate material. As we have shown in Chapter 4, it enables highly dense Au or Pt arrays to be templated, expanding the range of available materials. Indeed, successful embedding of Pt clusters on Gr/Ir(1 1 1) [377] and h-BN/Ir(1 1 1) [375] has been conducted by us. Furthermore, using an oxide as embedding material might be attractive in view of applications in heterogeneous catalysis and optics. Oxides play an important role in many catalytic reactions. Ceria (CeO_2) for example is well known as an oxygen storing support and is critical for many ecologically relevant reactions involving metal nanoparticles. [378–381] Silica (SiO_2) on the other hand has excellent insulating properties, which might electronically decouple the clusters from the environment and enhance optical and electronic features in the metal clusters. Additionally, oxides are more stable at elevated temperatures and ambient conditions. If one succeeds in removing a cluster superlattice embedded with silica, the Gr on the bottom could be easily etched away without harming the embedding matrix.
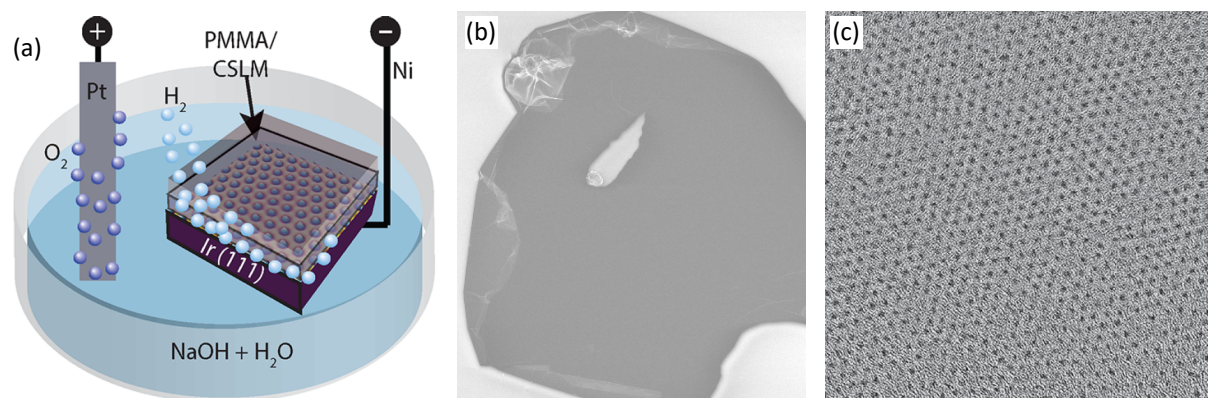
Figure 7.2: (a) Schematic picture showing the setup to electrochemically delaminate the membrane. Embedded Ir clusters on Gr/Ir(1 1 1) are covered with a PMMA support and immersed in NaOH solution. A voltage is applied between a Pt wire anode and the Ir(1 1 1) crystal cathode. (b) SEM image of a single membrane on the PMMA. The vertical field of view is 0.25 mm. (c) Bright field HRTEM image of the cluster superlattice membrane. Image size is 77 nm × 77 nm. Figures (a) and (c) adapted from ref. 377 and unpublished data thereof.

Finally, we want to address the immediate goal of the manuscript, illustrated already in Figure 1 of Chapter 6 and described in section 3.3 of the introduction: the synthesis of a free-standing cluster superlattice membrane. While step (I), cluster deposition has already been thoroughly investigated, the work presented in this Chapter has succeeded in completing step (II), embedding of the cluster superlattice. During the time of this thesis, we have managed to successfully transfer this membrane from the Ir(1 1 1) crystal, completing step (III) as well.

While the details of this process can be found in ref. 377, we provide a short overview of the results here.

Figure 7.2a presents a schematic of the delamination of a cluster superlattice membrane from the Ir(1 1 1) crystal. The sample has been prepared by growing $Ir_{\overline{35}}$ clusters and embedding them with 7 ML of C. To facilitate the removal, mild annealing at 850 K and Eu intercalation is conducted. Then, a PMMA film is placed on top of the sample to provide the necessary support. The sample is brought into an electrochemical cell filled with 2.5 M NaOH solution, depicted in Figure 7.2a. A Pt wire is used as an anode and a voltage slightly below the onset potential of hydrogen evolution is applied. H_2O intercalation below the Gr, as well as H_2 bubble formation at the Ir crystal induces delamination of the membrane at the interface of Gr and Ir(1 1 1). Figure 7.2b displays a SEM image after successful removal of an intact membrane patch, still resting on the PMMA. As a final step, this material is transferred onto another substrate, *e.g.* a TEM grid, and PMMA is dissolved by gentle acetone treatment. Figure 7.2c displays a HRTEM image of a free-standing membrane with the Ir clusters as dark spots arranged in a hexagonal lattice, confirming their presence and perfect ordering after even extensive *ex situ* treatment and transfer.

These membranes provide exciting new research possibilities, as the material is free-standing, inert, and stable. As it has been elaborated in Chapter 3.3, sintering *via* Smoluchowski ripening and Ostwald ripening is heavily suppressed, even when the 2D material cover is removed. Penetration of the cluster material through the Gr is improbable because the energy sink of the Ir(1 1 1) surface is not present anymore. Integrating cluster superlattices into devices therefore becomes easily possible, as well as studying cluster excitations inside their C shell with (magneto-)optical methods. If the 2D material can be removed, the clusters become directly exposed to the environment and could be envisioned as functioning (electro-)catalysts.

PART IV

Appendix

APPENDIX A

Scientific Appendix

*The scientific appendix contains contributions from M. Will, J. Hall, C. Speckmann, and T. Michely. A.1 For the Fe, Au, Mo, Dy, and Tm experiments, M. Will grew the samples, designed the experiments, carried out the measurements and analyzed the data. Fe, Au, and Mo samples were prepared at **ATHENE**. Au was evaporated from a Knudsen cell, while Fe and Mo were deposited from a high purity rod in an electron-beam evaporator. The Dy and Tm sample was grown and measured at **TuMA II**. Dy and Tm were evaporated from a low-temperature Knudsen cell.*
*For the Ta experiment, J. Hall grew the sample, designed the experiment, and carried out the measurements at **TuMA II**. The data were analyzed by M. Will. Ta was evaporated from a high-purity rod in an electron-beam evaporator.*
*For the Nb experiment, C. Speckmann grew the sample, designed the experiment, carried out the measurements at **TuMA II** and analyzed the data. Nb was evaporated from a high-purity rod in an electron-beam evaporator. The results can also be found in his Master's thesis.*
*A.2 For the CO experiments, M. Will grew the samples, designed the experiments, carried out the measurements and analyzed the data. The work was conducted at **ATHENE**.*
*All work was supervised by T. Michely.*

A.1 Other Materials on Gr and h-BN/Ir(111)

A.1.1 Au and Fe on h-BN/Ir(111)

Previously, in the introduction (chapter 2) and discussion (section 7.1), we have elaborated on the potential of metal clusters, especially when they are arranged in a periodic lattice. In chapter 4 we have demonstrated the ability of h-BN/Ir(1 1 1) to template regular arrays of Ir, C, and Au superlattices. In this section, we will investigate the versatility of the substrate by analyzing its interaction with other chemical elements. We have shown, that deposition of 0.4 ML Au at 300 K leads to a superlattice with $n = 0.7$. [298] Figure A.1a displays an STM topograph of h-BN/Ir(1 1 1) after deposition of 0.4 ML Au at 150 K. Because of the strong interaction of Au with the STM tip, the sample was additionally cooled to 40 K for imaging. The resulting superlattice is perfectly ordered with a cluster number density of $n = 1$.

Furthermore, we have studied Fe deposition on h-BN/Ir(1 1 1). Figure A.1b displays an STM topograph of 0.4 ML Fe/h-BN/Ir(1 1 1) at a deposition temperature of 150 K. An iron cluster superlattice has formed with $n = 0.88$. The ordering of the lattice is inferior to that of Ir or Au
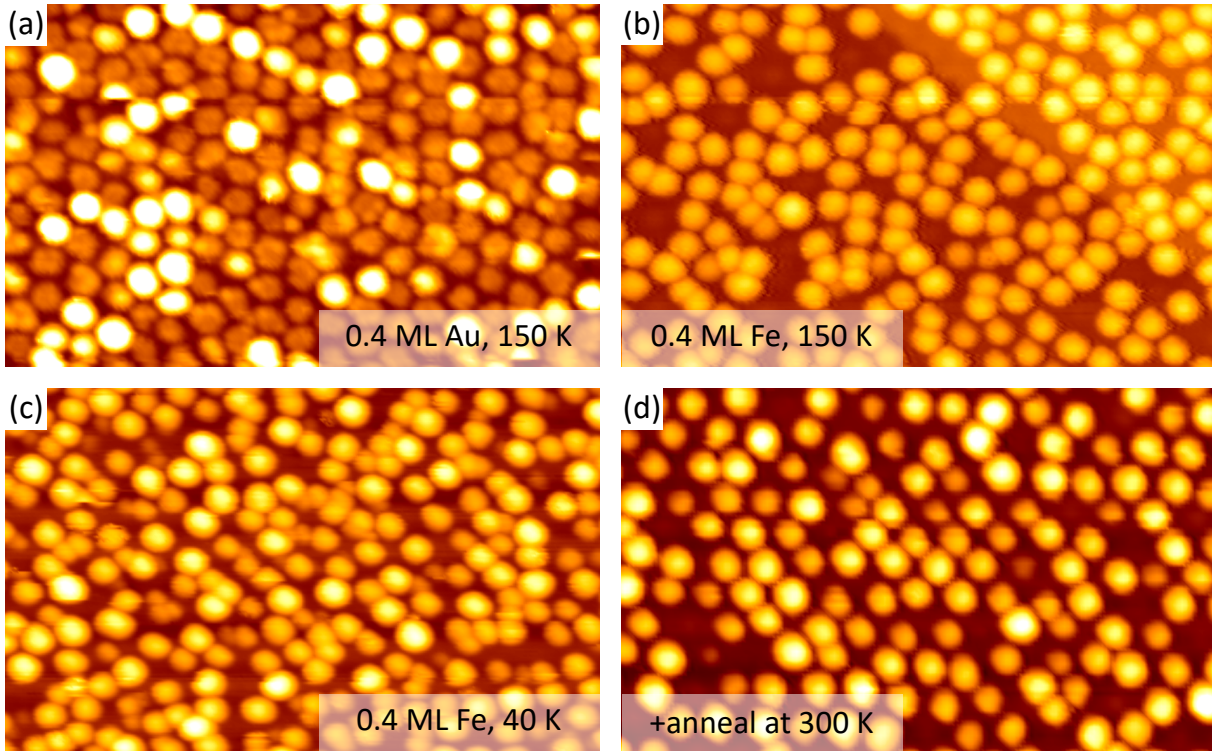
Figure A.1: STM topographs of Au and Fe clusters on h-BN/Ir(1 1 1). (a) 0.4 ML Au deposited on h-BN/Ir(1 1 1) at 150 K and imaged at 150 K. (b) 0.4 ML Fe/h-BN/Ir(1 1 1) deposited at 150 K and imaged at 40 K. (c) 0.4 ML Fe/h-BN/Ir(1 1 1) deposited and imaged at 40 K. (d) Same sample as in (c), but imaged at 300 K. Image size is in all cases 50 nm × 31 nm.

cluster on h-BN/Ir(1 1 1), indicating a weaker interaction between Fe and h-BN. Better ordering and filling is achieved, when Fe is deposited at 40 K (see Figure A.1c). Here, every moiré unit cell is occupied with at least one cluster. In addition, Fe clusters in the center regions in between three adjacent valleys are observed, similar to what was found for Ir deposition at low temperatures. [298] Annealing this sample at 300 K (depicted in Figure A.1d) leads to coalescence of some Fe clusters, resulting in a reduction of the cluster number density to $n = 0.9$. The center region clusters have disappeared.

In view of applications in catalysis and magnetism, obtaining a perfectly ordered cluster superlattice is beneficial. We have demonstrated, that h-BN/Ir(1 1 1) produces perfectly ordered lattices of Au clusters. Fe superlattices are promising for catalytic [382] and magnetic [4] studies. For the latter, a periodic arrangement is especially beneficial. [125] We have demonstrated, that Fe cluster superlattices with $n = 1$ can be obtained on h-BN/Ir(1 1 1) by Fe deposition at 40 K. These lattices barely degrade at 300 K, only reducing the cluster number density to $n = 0.9$. For practical reasons, superlattice stability at room temperature is vital, which is achieved with our templating method. In conclusion, Au and Fe cluster superlattices are templated with the best order and highest number density reported in the literature, [14] when compared *e.g.* to Au on h-BN/Rh(1 1 1), [295] Au on Gr/Ir(1 1 1) and Fe on Gr/Ir(1 1 1). [237]

A.1.2 Mo on h-BN/Ir(111)
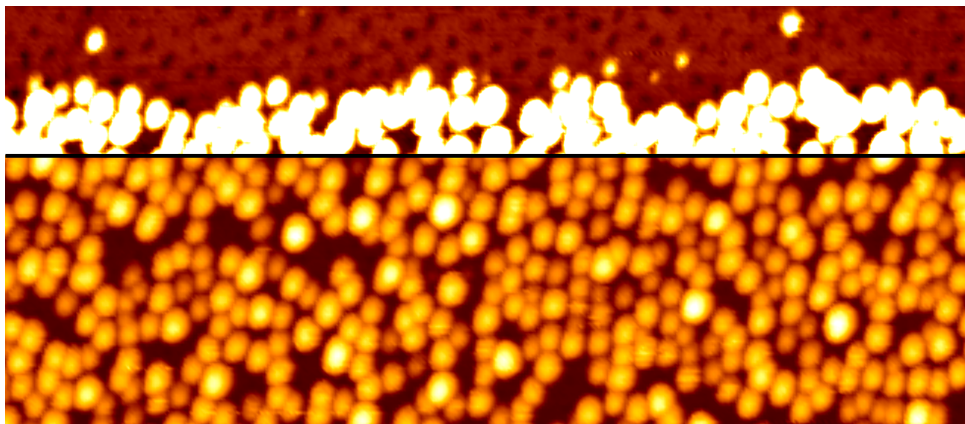
Figure A.2: STM topograph of Mo on h-BN/Ir(1 1 1). The deposited amount is unknown, but lies in the range of 0.8-1.5 ML, the deposition temperature was 40 K and the sample was annealed to 300 K for 60 s prior to imaging at 40 K. In the upper part of the topograph, clusters were intentionally removed with the tip prior to imaging. The contrast was additionally tuned to make the moiré visible. Image size is 125 nm × 55 nm.

Mo is an important material for commercial catalysts in petrochemistry, *e.g.* for the hydrodesulfurization of organic sulfur composites, [383] and was used as a sensitizer in dye-sensitized solar cells. [384] Figure A.2 shows Mo clusters grown on h-BN/Ir(1 1 1) at a deposition temperature of 40 K and annealing to 300 K for 60 s. Mo is only poorly templated by the substrate and the number density is well below unity. In the top part of the topograph, the h-BN moiré is imaged directly next to the cluster superlattice. From the position of the clusters with respect to the moiré, we conclude that Mo preferentially adsorbs in the valley regions. Note that the precise amount of Mo could not be reliably identified because of the 3D growth of Mo on Ir(1 1 1) and the lack of highly resolved STM topographs. We estimate the Mo coverage θ to be no less than 0.8 ML and no more than 1.5 ML.

A.1.3 Ta and Nb on Gr/Ir(111)

Ta and Nb deposition on Gr/Ir(1 1 1) was performed mainly in view of the growth of TaS_2 and NbS_2. Nevertheless, Ta clusters are interesting as calculations predict multiferroic behavior in the free-standing form. [385] Likewise, Nb clusters have gained significant attention, when their ferroelectricity was demonstrated in the free beam. [386] However, only few studies have reported Ta and Nb clusters supported on a substrate. Ta clusters were synthesized on alumina [387] and silica [388] and proved to be active for methane conversion to higher alkanes. [389] However, no reports for periodic arrays of small Ta and Nb clusters are available.

Figure A.3a shows the sample after deposition of 0.13 ML Ta on Gr/Ir(1 1 1). The substantial noise is due to the turbomolecular pumps being active during STM imaging. A periodic cluster
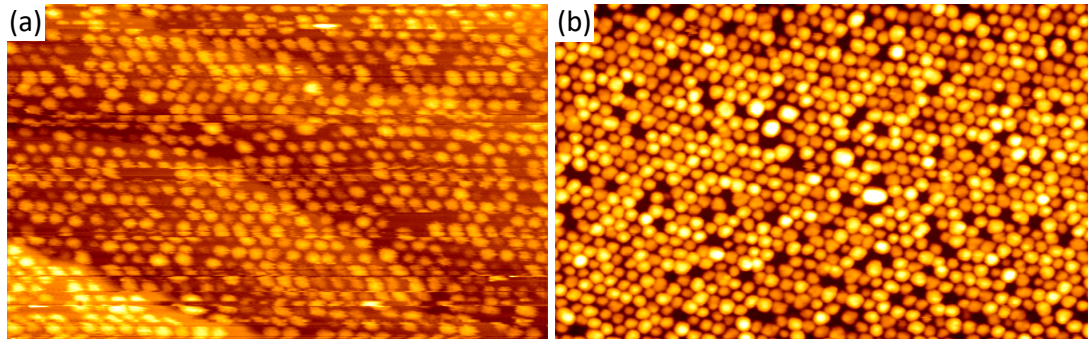
Figure A.3: STM topographs of Ta and Nb clusters on Gr/Ir(1 1 1). (a) 0.15 ML Ta deposited on Gr/Ir(1 1 1). STM imaging was conducted with running turbomolecular pumps (b) 0.43 ML Nb deposited on Gr/Ir(1 1 1). Image size is in (a) 81 nm × 50 nm and in (b) 100 nm × 62 nm.

superlattice of Ta has formed on the Gr surface. The presence of the noise and the unintentional cluster pick-up by the tip does not allow exact determination of the cluster number density. Nevertheless we expect $n > 0.9$. In Figure A.3b, Nb clusters have been grown by 0.43 ML Nb deposition on Gr/Ir(1 1 1) at 300 K. Some coalescence of Nb clusters is observed with $n = 0.9$. We speculate, that low-temperature deposition will lead to the emergence of a perfect cluster superlattice, as was reported for other metals on Gr/Ir(1 1 1). [237]
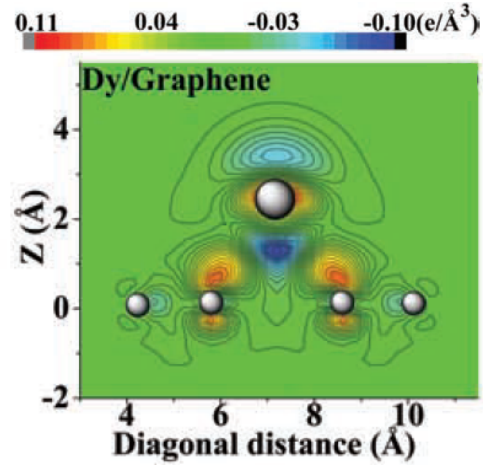
A.1.4 Dy and Tm on h-BN/Ir(111)
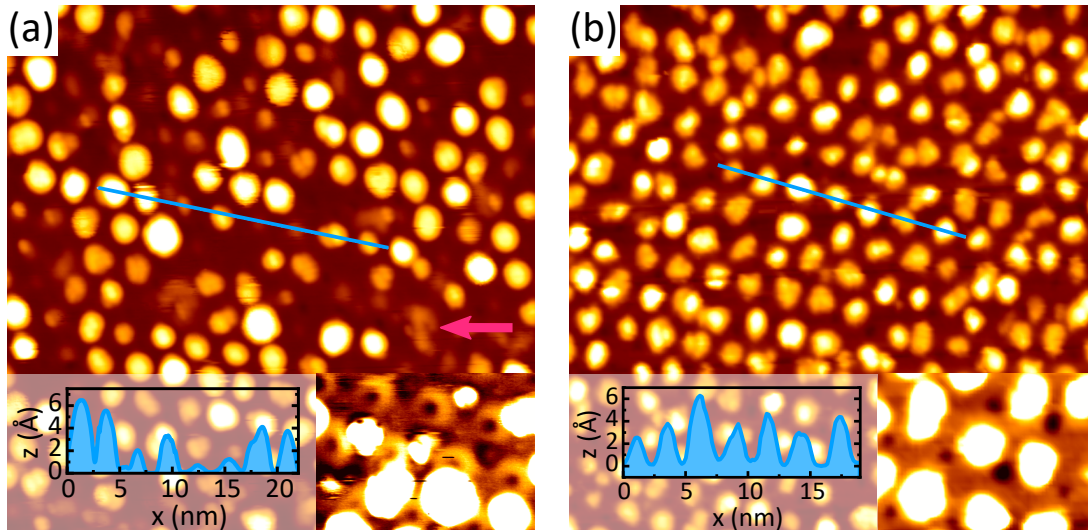
Figure A.4: STM topographs of Dy clusters on h-BN/Ir(1 1 1). (a) 0.3 ML Dy deposited on h-BN/Ir(1 1 1) at 300 K and imaged at 300 K. The inset shows a magnified image of a region where the moiré is visible together with Dy clusters. An arrow marks an irregular cluster. (b) 0.3 ML Dy/h-BN/Ir(1 1 1) deposited at 40 K, flash annealed to 300 K, and then imaged at 40 K. Inset shows a magnified image of a region where the moiré is visible together with Dy clusters. Line profiles along blue lines. Image size in the main images is 40 nm × 40 nm and in the insets 10 nm × 7 nm.

Rare-earth clusters are interesting in view of magnetic studies mainly because of their large magnetic moments. Dy in particular has one of the highest bulk magnetic moments of all lanthanides with $10.6\mu_B$. Size effects in rare-earth clusters have been studied in the free beam already during the 1990s. [390] Moreover, Dy deposition on Gr/SiC(0 0 0 1) was found to produce disordered islands on top of the Gr sheet. [203,391–393] Moreover, attempted growth of ordered Dy clusters on Gr/Ir(1 1 1) have proven unsuccessful. [394] An ordered superlattice of Dy would pave the way for magnetic studies on supported rare-earth clusters.

Figure A.4a shows an STM topograph of h-BN/Ir(1 1 1) after 0.3 ML Dy deposition at 300 K. An array of clusters has emerged on top of the h-BN substrate with a number density of $n \approx 0.7$. Most of them are regularly separated by the moiré lattice constant of 29.1 Å. Two different species are visible on the topograph: (1) large clusters which appear rather spherical and possess an apparent height between 3-7 Å. (2) Smaller, irregularly shaped clusters with an apparent height below 2 Å, one of them being marked by an arrow in Figure A.4a. In the inset of Figure A.4a, a magnified detail from the main topograph is displayed, in which the moiré contrast of h-BN/Ir(1 1 1) is visible. Clearly, the Dy clusters are adsorbing to the center sites in between three adjacent moiré valleys. From the topographs, we assume species (1)

Figure A.5: Charge density difference plot of a Dy adatom on free-standing Gr (cut through along the dense-packed row). It is obtained by substracting the charge density of the isolated atom and Gr layer from the optimized charge density. Adapted from ref. 393

to be Dy_{50} clusters on top of h-BN/Ir(1 1 1). The nature of species (2) cannot be unambiguously determined from the STM measurements. One possibility are Dy compounds intercalated to the h-BN/Ir(1 1 1) interface. Due to the prolonged shapes of the structures, it is implausible that they are simply small Dy clusters on top of h-BN, which are expected to be spherically shaped like other metal clusters. Another explanation might be contaminants from the evaporator which chemically interact with the h-BN.

As we have not reached a perfect filling of one cluster per moiré unit cell at 300 K, one approach is to reduce the sample temperature during deposition in order to reduce thermally activated diffusion and Smoluchowski ripening of small clusters during growth. Thus, we have deposited 0.3 ML Dy at 40 K. This procedure yields randomly adsorbed Dy clusters on the surface. Annealing to 300 K activates cluster diffusion to the most favorable adsorption site and significantly improves their order. Figure A.4b displays an STM topograph of the sample cooled back down to 40 K. It is apparent, that the cluster ordering and uniformity has substantially increased compared to Dy clusters deposited at 300 K. The cluster number density is $n = 1$. All clusters exhibit apparent heights of more than 2 Å. However, still some prolonged shapes are

observed occasionally. The inset once again displays a zoom, where the moiré valleys are visible adjacent to clusters, confirming their adsorption site to be the center region.

These results confirm that h-BN/Ir(1 1 1) can be used as a template for Dy cluster superlattice growth. In the following, we want to briefly discuss the binding of Dy clusters to h-BN/Ir(1 1 1). It appears to be quite different than that of Ir and Pt clusters, which adsorb in the valley region of the moiré. For Ir clusters, we have shown that rehybridization of the h-BN and bond formation between cluster d-orbitals and boron atoms is the cause of cluster formation on h-BN/Ir(1 1 1). This is likely different for the case of Dy clusters, because Dy does not have d-electrons available for bond formation, but rather $4f$ and $6s$ electrons. Figure A.5 displays a calculated charge density difference for an isolated Dy atom on free-standing Gr. [393] For Dy on Gr, the favored adsorption site is the hollow site, directly above the center of a carbon ring. As visible from the charge density difference plot, there is a significant charge redistribution in the charge cloud of the neighboring C atoms and the Dy atom. This indicates bond formation between those atoms. Similarly, Eu atoms, which are chemically close to Dy, are found to adsorb in the center of C rings on Gr/Ir(1 1 1). [395] It is reasonable to assume, that also for Dy adsorption on h-BN, the center of an h-BN ring might be preferred over the site on top of a B atom. Apparently, the valley region, where h-BN is already chemisorbed to Ir(1 1 1) does not provide favorable conditions for bond formation to Dy. Another cause for the occurrence of this adsorption site might lie in the center region defects, which we have mentioned already in chapter 4. It is possible that these defects in the h-BN provide binding sites for Dy clusters.
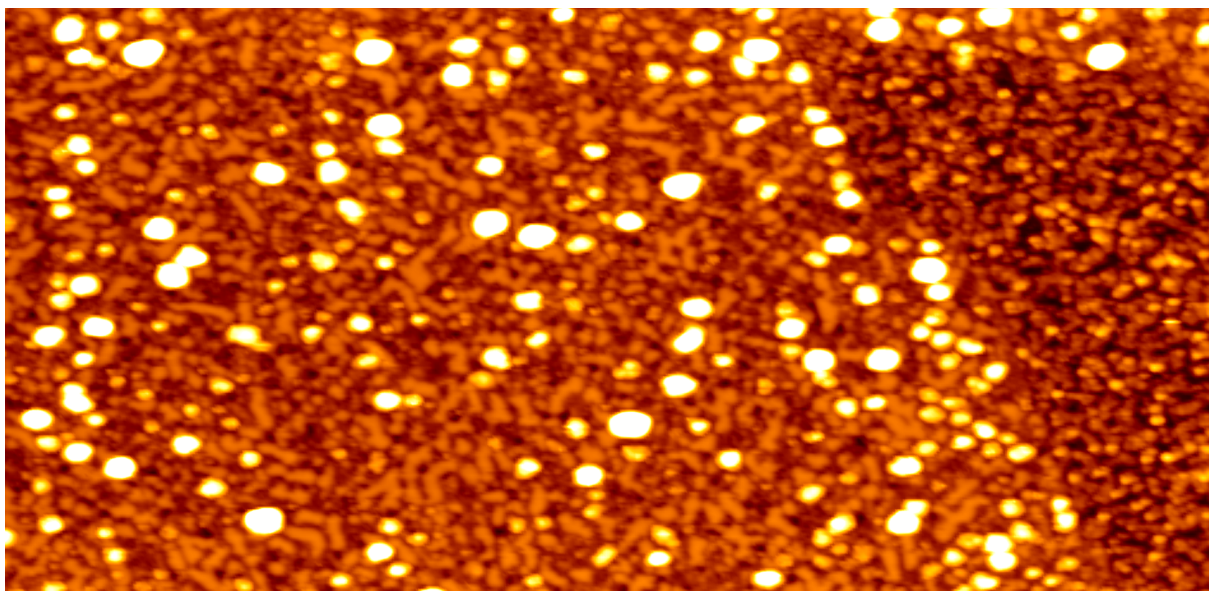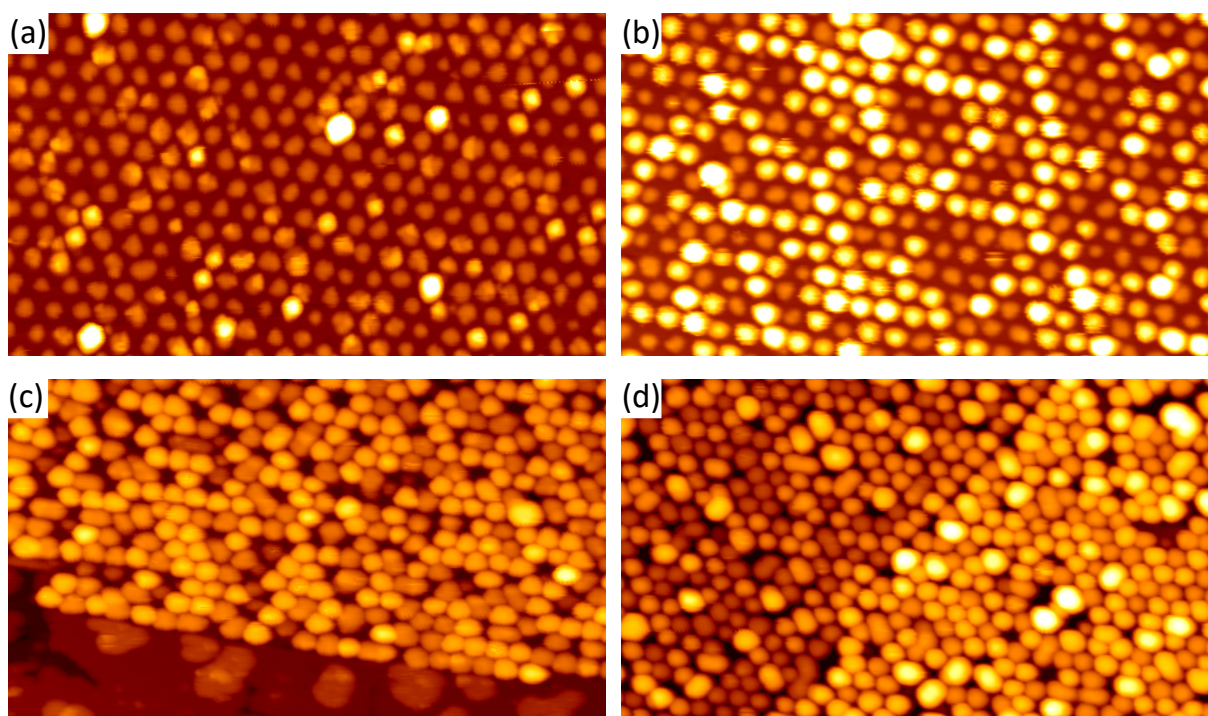

Figure A.6: STM topograph of Tm deposited on h-BN/Ir(1 1 1)at 300 K. Image size is 125 nm × 60 nm.

Tm deposition on h-BN/Ir(1 1 1) was also investigated in view of cluster formation. In Fig-

ure A.6, an unknown amount (between 0.7-1.5 ML) of Tm was deposited on h-BN/Ir(1 1 1) at 300 K. On the right side of the topograph, the rim of the h-BN flake is visible, where Tm was deposited onto the bare Ir(1 1 1). On the left, Tm/h-BN/Ir(1 1 1) is visible. Even though some clusters are observed , their sizes are irregular and no long-range order is observed. Together with the highly dispersed Tm clusters, flat, prolonged channels can be seen on the h-BN layer. These channels are reminiscent of intercalated Eu on Gr and h-BN/Ir(1 1 1), [396] indicating Tm intercalation below the h-BN sheet. It was found, that Tm readily intercalates below Gr/Ir(1 1 1) at 500 K, [397] indicating a strong driving force for Tm intercalation also for the case of h-BN/Ir(1 1 1). It remains to be seen if low-temperature deposition of Tm yields a periodic cluster superlattice.

A.2 The interaction of CO with Pt clusters on h-BN/Ir(1 1 1)

Figure A.7: Shape transformation upon CO adsorption. (a) STM topographs of 0.18 ML Pt deposited on h-BN/Ir(1 1 1) at 300 K and (b) after a dose of 100 L CO. (c) STM topographs of 1.15 ML Pt deposited on h-BN/Ir(1 1 1) at 300 K and (d) after a dose of 150 L CO. The z-contrast is identical in both image pairs. Image size is in (a) and (b) 70 nm × 40 nm, and in (c) and (d) 88 nm × 50 nm.

The interaction of CO with Pt surfaces is one of the most studied reactions in surface science. [398–404] Before scanning probe microscopy and other high resolution imaging techniques were
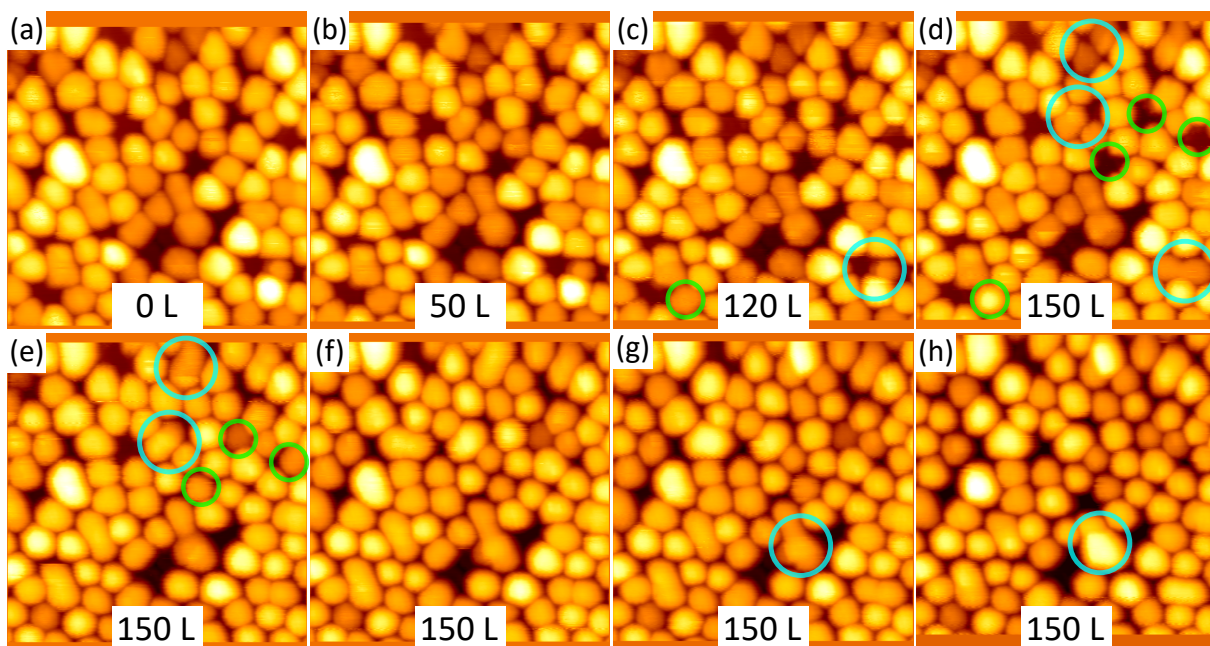
Figure A.8: Sequence of STM topographs showing the $Pt_{\overline{125}}$ cluster shape transformation upon CO dosing. Each image took 57 s to record. (a) STM topograph after deposition of 1.15 ML Pt deposition on h-BN/Ir(1 1 1). (b)-(c) STM topographs of the same location while CO is provided from the background pressure. The accumulated CO dose is given in the bottom of each topograph. (d) The CO valve was closed right before this topograph was recorded. Subsequent images were recorded (e) 1 min, (f) 2 min, (g) 3 min, and (h) 12 min after the closing of the valve. Individual sintering and reshaping events are marked by blue and green circles in consecutive images. The z-contrast is identical in all images. Image size is 30 nm × 30 nm in all cases.

available, CO chemisorption was an important method to access the properties of supported heterogeneous catalysts. [86,91] Because CO is present in significant concentrations even in the background pressure of a UHV system, understanding the interaction of CO with surfaces is often integral. Moreover, as an industrially essential reaction, CO oxidation to CO_2 over Pt was intensively studied in countless publications over the decades. [91, 100, 246, 268, 367, 405–409] As mentioned in section 2.3.2, the interaction of CO with Pt cluster superlattices on Gr/Ir(1 1 1) has been investigated in detail with STM and XPS. [243, 244] Here, we present results of CO dosing on Pt clusters grown on h-BN/Ir(1 1 1).

Figure A.7a shows an STM topograph of $Pt_{\overline{21}}$ clusters grown by 0.18 ML Pt deposition on h-BN/Ir(1 1 1) at 300 K. As visible in the topograph, most of the clusters are single layer. We find $n_1 = 0.94$ and $n_{\geq 3} = 0.06$. Figure A.7b depicts the same sample but after exposure to 100 L CO through a gas dosing tube. Dosing of CO does not impede the structural integrity of the cluster superlattice ($n = 1$). However, a substantial amount of clusters are now larger than two layers ($n_1 = 0.41$, $n_{\geq 3} = 0.59$). A similar effect is observed for larger clusters. Figure A.7c and d provide STM topographs of $Pt_{\overline{125}}$ clusters before (a) and after (b) exposure to 150 L CO. The cluster number density reduces from $n = 0.94$ to $n = 0.85$ upon CO exposure. We observe
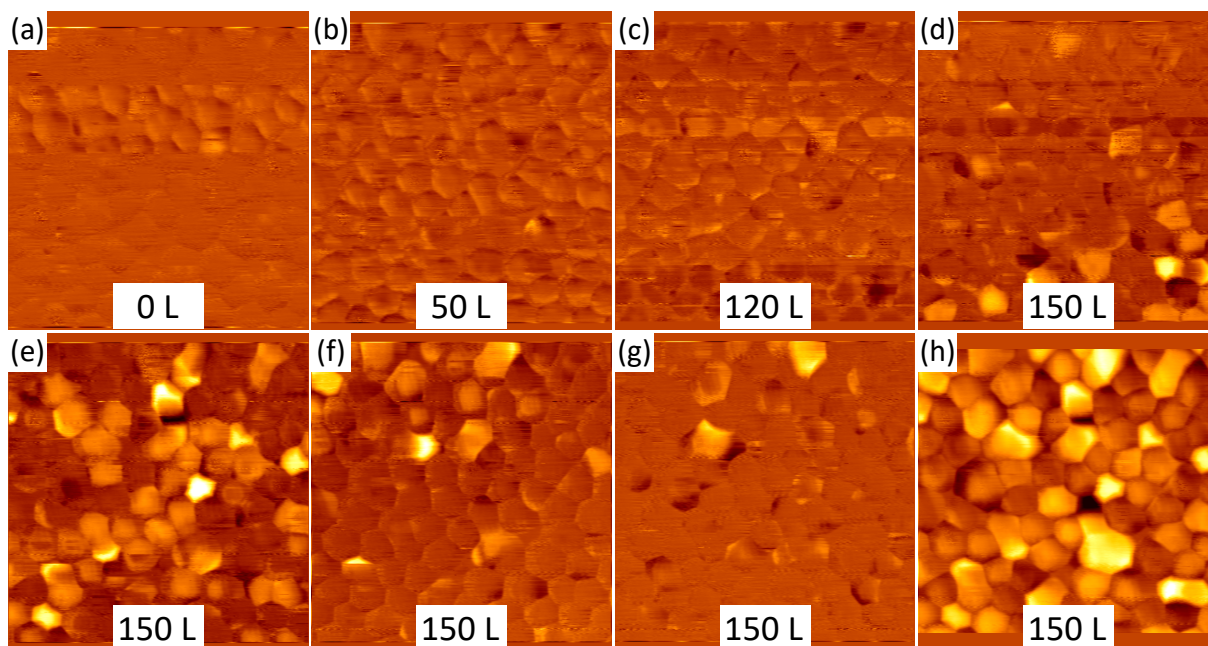
Figure A.9: (a)-(g) The same STM topographs as in Figure A.8, but plotted as the difference between the frame displayed in the figure and the previous frame of the movie. (h) Difference of the last and the first frame of Figure A.8.

an increased number of clusters spanning over multiple unit cells after CO dosing. Additionally, smaller clusters are found less frequently after the CO dosing, indicating cluster reshaping as well. From this data, we can clearly attribute the sintering of $Pt_{\overline{125}}$, and reshaping of $Pt_{\overline{21}}$ and $Pt_{\overline{125}}$ to the CO dosing.

To gain insight into the dynamics of CO adsorption and CO-induced reshaping, we conducted live STM imaging during gas exposure. Figure A.8 shows individual STM topographs recorded on the same spot of the sample, where each frame took 57 s to measure. The dose was increased stepwise during imaging. The total dose at the beginning of the frame is given in the center of the topographs and ranges from 0 to 150 L. Comparing the topographs of Figure A.8a-c, exposure to 120 L CO induces no significant changes. In the beginning of the frame shown in Figure A.8d, at an integrated amount of 150 L, the CO needle valve was closed. In the lower part of the image, changes to individual clusters are seen. A sintering event is encircled in light blue, while a cluster reshaping from a smaller to a larger height is marked by a green circle. Subsequently, many of such changes are observed when comparing Figures A.8d-f with some of them marked by circles. Finally, in Figure A.8g and h, an event of a large cluster reshaping is highlighted.

The changes seen in the STM movie are visualized instructively in Figures A.9a-h, which shows the difference between each frame depicted in Figure A.8 with respect to the previous one is shown. As mentioned before, essentially no change to the cluster superlattice is observed until the gas dosing tube is closed (compare Figures A.9a-c). Reshaping of clusters is only visible at

the bottom part of Figure A.9d. The reshaping process proceeds during the entire recording of the topograph of Figure A.9e (recorded 1 min after closing) and fades out approximately after half of Figure A.9f (recorded 2 min after closing). Individual events are still present 3 min after the valve was closed, as can be seen in Figure A.9g. Finally, Figure A.9h visualizes the total difference between the last frame and the cluster superlattice before CO dosing.

From the data obtained in the movies, we conclude, that CO-induced reshaping of $Pt_{\overline{125}}$ clusters on h-BN/Ir(1 1 1) occurs after the supply of CO has stopped. From the images in Figure A.9 we deduce the average time during which the restructuring occurs. Since one image takes about 60 s to record, we conclude that approximately 30 s after closing the CO valve the reshaping begins. It proceeds for about 120 s and ceases 150 s after the valve was shut.

APPENDIX B

List of Publications
(Liste der Teilpublikationen)

The results presented in this thesis can be found in the following publications:

Teile dieser Arbeit wurden als Bestandteil der folgenden Artikel in Fachzeitschriften bereits veröffentlicht:

[298] **M. Will**, N. Atodiresei, V. Caciuc, P. Valerius, C. Herbig, and T. Michely
A Monolayer of Hexagonal Boron Nitride on Ir(111) as a Template for Cluster Superlattices
ACS Nano, **12**, 7, (2018), 6871-6880

[410] **M. Will**, P. Bampoulis, T. Hartl, P. Valerius, and T. Michely
Conformal Embedding of Cluster Superlattices with Carbon
ACS Applied Materials & Interfaces, **11**, 43, (2019), 40524-40532

n/a **M. Will**, P. Bampoulis, T. Hartl, P. Valerius, V. Boix de la Cruz, P. Lacovig, S. Lizzit, J. Knudsen, and T. Michely.
Growth, Stability and Electronic Decoupling of Pt Clusters on Hexagonal Boron Nitride on Ir(111)
manuscript, in preparation

Further publications:

Weitere Publikationen:

n/a T. Hartl, P. Bampoulis, **M. Will**, V. Boix de la Cruz, P. Lacovig, S. Lizzit, J. Knudsen, and T. Michely
Embedding of Pt Clusters with Elemental Carbon
manuscript, in preparation

[377] T. Hartl, **M. Will**, D. Čapeta, R. Singh, D. Scheinecker, V. Boix de la Cruz, S. Dellmann, P. Lacovig, S. Lizzit, B. V. Senkovskiy, A. Grüneis, M. Kralj, J. Knudsen, J. Kotakoski, T. Michely, and P. Bampoulis
Cluster Superlattice Membranes
ACS Nano, **14** (2020), 13629-13637

[411] P. Valerius, C. Herbig, **M. Will**, M. A. Arman, J. Knudsen, V. Caciuc, N. Atodiresei, and T. Michely
Annealing of ion-irradiated hexagonal boron nitride on Ir(111)
Physical Review B, **96** (2017), 235410

[281] F. H. Farwick zum Hagen, D. M. Zimmermann, C. C. Silva, C. Schlueter, N. Atodiresei, W. Jolie, A. J. Martínez-Galera, D. Dombrowski, U. A. Schröder, **M. Will**, P. Lazić, V. Caciuc, S. Blügel, T.-L. Lee, T. Michely, and C. Busse
Structure and Growth of Hexagonal Boron Nitride on Ir(111)
ACS Nano, **10** (2016), 11012-11026

[412] M. Engler, F. Frost, S. Müller, S .Macko, **M. Will**, R. Feder, D Spemann, R. Hübner, S. Facsko, and T. Michely
Silicide induced ion beam patterning of Si(001)
Nanotechnology, **25** (2014), 115303

Conference contributions as presenting author:

Konferenzbeiträge als präsentierender Autor:

2017 DPG Spring Meeting, Dresden (DE), *A monolayer of hexagonal boron nitride on Ir(111) as a template for cluster growth.* Talk

2017 Carbonhagen, Copenhagen (DK), *A monolayer of hexagonal boron nitride on Ir(111) as a template for cluster growth.* Poster

2018 EWEG-2D (European Workshop on Epitaxial Graphene and 2D Materials), Salamanca (ES), *A monolayer of hexagonal boron nitride on Ir(111) as a template for cluster growth.* Talk

2018 ECOSS34 (European Conference on Surface Science), Århus (DK), *A monolayer of hexagonal boron nitride on Ir(111) as a template for cluster growth.* Talk

2019 DPG Spring Meeting, Regensburg (DE), *Lattice formation and binding of metal clusters to hexagonal boron nitride on Ir(111).* Poster

2020 DPG Spring Meeting, Dresden (DE) *Cluster superlattice membranes.* Talk, postponed due to COVID-19 pandemic.

2020 EWEG-2D (European Workshop on Epitaxial Graphene and 2D Materials), Sankt Moritz (CH), *Comprehensive STM and XPS study of Pt cluster lattices embedded with carbon.* Poster, postponed due to COVID-19 pandemic.

Bibliography

[1] D. J. Barber and I. C. Freestone, 'An Investigation of the Origin of the Colour of the Lycurgus Cup by Analytical Transmission Electron Microscopy', *Archaeometry* **32**, 33 (1990). Cited on page(s) 3

[2] H. W. Kroto, J. R. Heath, S. C. O'Brien, R. F. Curl and R. E. Smalley, 'C$_{60}$: Buckminsterfullerene', *Nature* **318**, 162 (1985). Cited on page(s) 3

[3] 'Market Report: Global Catalyst Market' (Acmite Market Intelligence, 2015), Vol. 3. Cited on page(s) 4 and 14

[4] J. Bansmann, S. Baker, C. Binns, J. Blackman, J.-P. Bucher, J. Dorantes-Dávila, V. Dupuis, L. Favre, D. Kechrakos, A. Kleibert, K.-H. Meiwes-Broer, G. M. Pastor, A. Perez, O. Toulemonde, K. N. Trohidou, J. Tuaillon and Y. Xie, 'Magnetic and structural properties of isolated and assembled clusters', *Surf. Sci. Rep.* **56**, 189 (2005). Cited on page(s) 4, 16, and 126

[5] D. Weller, G. Parker, O. Mosendz, A. Lyberatos, D. Mitin, N. Y. Safonova and M. Albrecht, 'FePt Heat Assisted Magnetic Recording Media', *J. Vac. Sci. Technol. B* **34**, 060801 (2016). Cited on page(s) 4

[6] P. V. Kamat, 'Photophysical, Photochemical and Photocatalytic Aspects of Metal Nanoparticles', *J. Phys. Chem. B* **106**, 7729 (2002). Cited on page(s) 4

[7] S. Lal, S. Link and N. J. Halas, 'Nano-Optics from Sensing to Waveguiding', *Nat. Photon.* **1**, 641 (2007). Cited on page(s) 4 and 11

[8] K. A. Willets and R. P. Van Duyne, 'Localized Surface Plasmon Resonance Spectroscopy and Sensing', *Annu. Rev. Phys. Chem.* **58**, 267 (2007). Cited on page(s) 4, 17, and 18

[9] U. Kreibig and M. Vollmer, 'Optical Properties of Metal Clusters', 'Springer Series in Materials Science' (Springer, 2013). Cited on page(s) 4 and 11

[10] M. Homberger and U. Simon, 'On the Application Potential of Gold Nanoparticles in Nanoelectronics and Biomedicine', *Philos. Trans. R. Soc. A* **368**, 1405 (2010). Cited on page(s) 4 and 11

[11] A. Mathew and T. Pradeep, 'Noble Metal Clusters: Applications in Energy, Environment, and Biology', *Part. Part. Syst. Charact.* **31**, 1017 (2014). Cited on page(s) 4

[12] A. Hierlemann, O. Brand, C. Hagleitner and H. Baltes, 'Microfabrication Techniques for Chemical/Biosensors', *Proc. IEEE* **91**, 839 (2003). Cited on page(s) 4

[13] S. Sun, C. B. Murray, D. Weller, L. Folks and A. Moser, 'Monodisperse FePt Nanoparticles and Ferromagnetic FePt Nanocrystal Superlattices', *Science* **287**, 1989 (2000). Cited on page(s) 5, 16, and 35

[14] C. R. Henry, '2D-Arrays of Nanoparticles as Model Catalysts', *Catal. Lett.* **145**, 731 (2015). Cited on page(s) 5, 14, 15, 17, 18, 21, 22, 117, and 126

[15] M. Boudart, 'Catalysis by Supported Metals', *Adv. Catal.* **20**, 153 (1969). Cited on page(s) 7 and 9

[16] C. Dong, Y. Li, D. Cheng, M. Zhang, J. Liu, Y.-G. Wang, D. Xiao and D. Ma, 'Supported Metal Clusters: Fabrication and Application in Heterogeneous Catalysis', *ACS Catal.* **10**, 11011 (2020). Cited on page(s) 8, 14, and 17

[17] A. Schmidt and V. Smirnov, 'Concept of "Magic" Number Clusters as a New Approach to the Interpretation of Unusual Kinetics of the Heck Reaction with Aryl Bromides', *Top. Catal.* **32**, 71 (2005). Cited on page(s) 9

Bibliography

[18] S. Ali, V. Myasnichenko and E. Neyts, 'Size-Dependent Strain and Surface Energies of Gold Nanoclusters', *Phys. Chem. Chem. Phys.* **18**, 792 (2016). Cited on page(s) 9

[19] G. C. Bond, 'The Origins of Particle Size Effects in Heterogeneous Catalysis', *Surf. Sci.* **156**, 966 (1985). Cited on page(s) 9

[20] A. Masson, B. Bellamy, Y. H. Romdhane, M. Che, H. Roulet and G. Dufour, 'Intrinsic Size Effect of Platinum Particles Supported on Plasma-Grown Amorphous Alumina in the Hydrogenation of Ethylene', *Surf. Sci.* **173**, 479 (1986). Cited on page(s) 9

[21] M. Che and C. O. Bennett, 'The Influence of Particle Size on the Catalytic Properties of Supported Metals', *Adv. Catal.* **36**, 55 (1989). Cited on page(s) 9

[22] H. Poppa, 'Nucleation, Growth, and TEM Analysis of Metal Particles and Clusters Deposited in UHV', *Catal. Rev.* **35**, 359 (1993). Cited on page(s) 9, 15, and 19

[23] M. Valden, X. Lai and D. W. Goodman, 'Onset of Catalytic Activity of Gold Clusters on Titania with the Appearance of Nonmetallic Properties', *Science* **281**, 1647 (1998). Cited on page(s) 9, 10, and 15

[24] V. Subramanian, E. E. Wolf and P. V. Kamat, 'Catalysis with TiO_2/Gold Nanocomposites. Effect of Metal Particle Size on the Fermi Level Equilibration', *J. Am. Chem. Soc.* **126**, 4943 (2004). Cited on page(s) 9

[25] J. Den Breejen, P. Radstake, G. Bezemer, J. Bitter, V. Frøseth, A. Holmen and K. de Jong, 'On the Origin of the Cobalt Particle Size Effects in Fischer-Tropsch Catalysis', *J. Am. Chem. Soc.* **131**, 7197 (2009). Cited on page(s) 9

[26] S. K. Shaikhutdinov, R. Meyer, M. Naschitzki, M. Bäumer and H.-J. Freund, 'Size and Support Effects for CO Adsorption on Gold Model Catalysts', *Catal. Lett.* **86**, 211 (2003). Cited on page(s) 9

[27] A. Wieckowski, E. Savinova and C. Vayenas, 'Catalysis and Electrocatalysis at Nanoparticle Surfaces' (CRC Press, 2003). Cited on page(s) 9

[28] C. R. Henry, 'Morphology of Supported Nanoparticles', *Prog. Surf. Sci.* **80**, 92 (2005). Cited on page(s) 9 and 15

[29] W. D. Williams, M. Shekhar, W.-S. Lee, V. Kispersky, W. N. Delgass, F. H. Ribeiro, S. M. Kim, E. A. Stach, J. T. Miller and L. F. Allard, 'Metallic Corner Atoms in Gold Clusters Supported on Rutile are the Dominant Active Site During Water-Gas Shift Catalysis', *J. Am. Chem. Soc.* **132**, 14018 (2010). Cited on page(s) 9 and 15

[30] A. S. Crampton, M. D. Rötzer, C. J. Ridge, F. F. Schweinberger, U. Heiz, B. Yoon and U. Landman, 'Structure Sensitivity in the Nonscalable Regime Explored via Catalysed Ethylene Hydrogenation on Supported Platinum Nanoclusters', *Nat. Commun.* **7**, 1 (2016). Cited on page(s) 9 and 15

[31] Z. Li, H.-Y. T. Chen, K. Schouteden, T. Picot, T.-W. Liao, A. Seliverstov, C. Van Haesendonck, G. Pacchioni, E. Janssens and P. Lievens, 'Unraveling the Atomic Structure, Ripening Behavior, and Electronic Structure of Supported Au_{20} Clusters', *Sci. Adv.* **6**, eaay4289 (2020). Cited on page(s) 9, 14, 15, and 30

[32] W. Knight, K. Clemenger, W. A. de Heer, W. A. Saunders, M. Chou and M. L. Cohen, 'Electronic Shell Structure and Abundances of Sodium Clusters', *Phys. Rev. Lett.* **52**, 2141 (1984). Cited on page(s) 9

[33] W. A. De Heer, 'The physics of simple metal clusters: experimental aspects and simple models', *Rev. Mod. Phys.* **65**, 611 (1993). Cited on page(s) 9 and 18

[34] W. A. de Heer, in 'Metal Clusters at Surfaces', edited by K.-H. Meiwes-Broer (Springer, 2000), Pages 1–35. Cited on page(s) 9

[35] H. Häkkinen and M. Manninen, 'How "Magic" is a Magic Metal Cluster?', *Phys. Rev. Lett.* **76**, 1599 (1996). Cited on page(s) 9

[36] G. Rosenfeld, A. F. Becker, B. Poelsema, L. K. Verheij and G. Comsa, 'Magic Clusters in Two Dimensions?', *Phys. Rev. Lett.* **69**, 917 (1992). Cited on page(s) 9

[37] Y. Wang and M. Lai, 'Formation of Surface Magic Clusters: a Pathway to Monodispersed Nanostructures on Surfaces', *J. Phys. Condens. Matter* **13**, R589 (2001). Cited on page(s) 9

[38] M. Lai and Y. Wang, 'Direct Observation of Two Dimensional Magic Clusters', *Phys. Rev. Lett.* **81**, 164 (1998). Cited on page(s) 9 and 20

[39] M. Lai and Y. Wang, 'Self-Organized Two-Dimensional Lattice of Magic Clusters', *Phys. Rev, B* **64**, 241404 (2001). Cited on page(s) 9

[40] H. Chang, M. Lai, J. Wei, C. Wei and Y. Wang, 'Structure Determination of Surface Magic Clusters', *Phys. Rev. Lett.* **92**, 066103 (2004). Cited on page(s) 9

[41] B. A. Lechner, F. Knoller, A. Bourgund, U. Heiz and F. Esch, 'A Microscopy Approach to Investigating the Energetics of Small Supported Metal Clusters', *J. Phys. Chem. C* **122**, 22569 (2018). Cited on page(s) 9

[42] H.-J. Freund, 'Clusters and Islands on Oxides: from Catalysis via Electronics and Magnetism to Optics', *Surf. Sci.* **500**, 271 (2002). Cited on page(s) 10, 11, 14, 15, 20, and 21

[43] M. Arenz, S. Gilb and U. Heiz, in 'Atomic Clusters: From Gas Phase to Deposited', Vol. 12 of 'The Chemical Physics of Solid Surfaces', edited by D. Woodruff (Elsevier, 2007), Pages 1 – 51. Cited on page(s) 11

[44] K. Taylor, C. Pettiette-Hall, O. Cheshnovsky and R. Smalley, 'Ultraviolet Photoelectron Spectra of Coinage Metal Clusters', *J. Chem. Phys.* **96**, 3319 (1992). Cited on page(s) 11

[45] C. Kuhrt and M. Harsdorff, 'Photoemission and Electron Microscopy of Small Supported Palladium Clusters', *Surf. Sci.* **245**, 173 (1991). Cited on page(s) 11

[46] G. K. Wertheim, in 'Small Particles and Inorganic Clusters', edited by C. Chapon, M. Gillet and C. Henry (Springer, 1989), Pages 319–326. Cited on page(s) 11

[47] S.-T. Lee, G. Apai, M. Mason, R. Benbow and Z. Hurych, 'Evolution of Band Structure in Gold Clusters as Studied by Photoemission', *Phys. Rev. B* **23**, 505 (1981). Cited on page(s) 11

[48] J. Alonso, 'Electronic and Atomic Structure, and Magnetism of Transition-Metal Clusters', *Chem. Rev.* **100**, 637 (2000). Cited on page(s) 11 and 16

[49] L. Novotny and B. Hecht, 'Principles of Nano-Optics' (Cambridge university press, 2012). Cited on page(s) 11

[50] K. L. Kelly, E. Coronado, L. L. Zhao and G. C. Schatz, 'The Optical Properties of Metal Nanoparticles: The Influence of Size, Shape, and Dielectric Environment', *J. Phys. Chem. B* **107**, 668 (2003). Cited on page(s) 11

[51] C. F. Landes, S. Link, M. B. Mohamed, B. Nikoobakht and M. A. El-Sayed, 'Some Properties of Spherical and Rod-Shaped Semiconductor and Metal Nanocrystals', *Pure Appl. Chem.* **74**, 1675 (2002). Cited on page(s) 11

[52] G. Bauer, F. Pittner and T. Schalkhammer, 'Metal Nano-Cluster Biosensors', *Microchim. Acta* **131**, 107 (1999). Cited on page(s) 11

[53] N. L. Rosi and C. A. Mirkin, 'Nanostructures in Biodiagnostics', *Chem. Rev.* **105**, 1547 (2005). Cited on page(s) 11

Bibliography

[54] B. Lamprecht, J. R. Krenn, G. Schider, H. Ditlbacher, M. Salerno, N. Félidj, A. Leitner, F. R. Aussenegg and J. Weeber, 'Surface Plasmon Propagation in Microscale Metal Stripes', *Appl. Phys. Lett.* **79**, 51 (2001). Cited on page(s) 11

[55] M. Furlan, T. Heinzel, B. Jeanneret, S. Lotkhov and K. Ensslin, 'Non-Gaussian Distribution of Nearest-neighbour Coulomb Peak Spacings in Metallic Single-electron Transistors', *Europhys. Lett.* **49**, 369 (2000). Cited on page(s) 12

[56] K. Seeger and R. E. Palmer, in 'Metal Clusters at Surfaces', edited by K.-H. Meiwes-Broer (Springer, 2000), Pages 275–301. Cited on page(s) 12

[57] A. N. Korotkov, R. H. Chen and K. K. Likharev, 'Possible Performance of Capacitively Coupled Single-Electron Transistors in Digital Circuits', *J. Appl. Phys.* **78**, 2520 (1995). Cited on page(s) 12

[58] Y. Selzer and D. L. Allara, 'Single-Molecule Electrical Junctions', *Annu. Rev. Phys. Chem.* **57**, 593 (2006). Cited on page(s) 12

[59] T. Heinzel and I. Zozoulenko, 'Mesoscopic Electronics in Solid State Nanostructures' (Wiley Online Library, 2003), Vol. 3. Cited on page(s) 12

[60] M. Kastner, 'The Single Electron Transistor and Artificial Atoms', *Ann. Phys.* **9**, 885 (2000). Cited on page(s) 12 and 118

[61] K. K. Likharev, 'Correlated Discrete Transfer of Single Electrons in Ultrasmall Tunnel Junctions', *IBM J. Res. Dev.* **32**, 144 (1988). Cited on page(s) 13 and 14

[62] A. Hanna and M. Tinkham, 'Variation of the Coulomb Staircase in a Two-Junction System by Fractional Electron Charge', *Phys. Rev. B* **44**, 5919 (1991). Cited on page(s) 13 and 14

[63] P. J. Thomas, G. Kulkarni and C. Rao, 'Effect of Size on the Coulomb Staircase Phenomenon in Metal Nanocrystals', *Chem. Phys. Lett.* **321**, 163 (2000). Cited on page(s) 13

[64] H. Grabert and M. Devoret, 'Single Charge Tunneling: Coulomb Blockade Phenomena In Nanostructures', 'Nato Science Series B' (Springer US, 2013). Cited on page(s) 14

[65] C. W. Beenakker, 'Theory of Coulomb-Blockade Oscillations in the Conductance of a Quantum Dot', *Phys. Rev. B* **44**, 1646 (1991). Cited on page(s) 14

[66] M. Amman, R. Wilkins, E. Ben-Jacob, P. Maker and R. Jaklevic, 'Analytic Solution for the Current-Voltage Characteristic of Two Mesoscopic Tunnel Junctions Coupled in Series', *Phys. Rev. B* **43**, 1146 (1991). Cited on page(s) 14

[67] J. Dubois, J. Gerritsen, S. Shafranjuk, E. Boon, G. Schmid and H. Van Kempen, 'Coulomb Staircases and Quantum Size Effects in Tunnelling Spectroscopy on Ligand-Stabilized Metal Clusters', *Europhys. Lett.* **33**, 279 (1996). Cited on page(s) 14

[68] M. Ancona, W. Kruppa, R. Rendell, A. Snow, D. Park and J. Boos, 'Coulomb Blockade in Single-Layer Au Nanocluster Films', *Phys. Rev. B* **64**, 033408 (2001). Cited on page(s) 14

[69] N. Oncel, A.-S. Hallback, H. J. Zandvliet, E. A. Speets, B. Jan Ravoo, D. N. Reinhoudt and B. Poelsema, 'Coulomb Blockade of Small Pd Clusters', *J. Chem. Phys.* **123**, 044703 (2005). Cited on page(s) 14

[70] P. Yang, I. Arfaoui, T. Cren, N. Goubet and M.-P. Pileni, 'Electronic Properties Probed by Scanning Tunneling Spectroscopy: From Isolated Gold Nanocrystal to Well-Defined Supracrystals', *Phys. Rev. B* **86**, 075409 (2012). Cited on page(s) 14

[71] M. T. Björk, C. Thelander, A. E. Hansen, L. E. Jensen, M. W. Larsson, L. R. Wallenberg and L. Samuelson, 'Few-electron Quantum Dots in Nanowires', *Nano Lett.* **4**, 1621 (2004). Cited on page(s) 14

[72] D. Tsoukalas, P. Normand, C. Aidinis, E. Kapetanakis and P. Argitis, 'Fabrication of Si Nanodevices by optical lithography and anisotropic etching', *Microelectron. Eng.* **41**, 523 (1998). Cited on page(s) 14

[73] R. Smith and H. Ahmed, 'Gate controlled Coulomb Blockade Effects in the Conduction of a Silicon Quantum Wire', *J. Appl. Phys.* **81**, 2699 (1997). Cited on page(s) 14

[74] D. Ralph, C. Black and M. Tinkham, 'Spectroscopic Measurements of Discrete Electronic States in Single Metal Particles', *Phys. Rev. Lett.* **74**, 3241 (1995). Cited on page(s) 14

[75] F. Godel, L. D. N. Mouafo, G. Froehlicher, B. Doudin, S. Berciaud, Y. Henry, J.-F. Dayen and D. Halley, 'Conductance Oscillations in a Graphene/Nanocluster Hybrid Material: Toward Large-Area Single-Electron Devices', *Adv. Mater.* **29**, 1604837 (2017). Cited on page(s) 14

[76] R. Andres, S. Datta, M. Dorogi, J. Gomez, J. Henderson, D. Janes, V. Kolagunta, C. Kubiak, W. Mahoney, R. Osifchin, R. Reifenberger, M. P. Samanta and W. Tian, 'Room Temperature Coulomb Blockade and Coulomb Staircase from Self-Assembled Nanostructures', *J. Vac. Sci. Technol. A* **14**, 1178 (1996). Cited on page(s) 14 and 17

[77] C. Schönenberger, H. Van Houten, H. Donkersloot, A. Van Der Putten and L. Fokkink, 'Single-Electron Tunneling up to Room Temperature', *Phys. Scr.* **1992**, 289 (1992). Cited on page(s) 14

[78] G. Lovat, B. Choi, D. W. Paley, M. L. Steigerwald, L. Venkataraman and X. Roy, 'Room-Temperature Current Blockade in Atomically Defined Single-Cluster Junctions', *Nat. Nanotechnol.* **12**, 1050 (2017). Cited on page(s) 14

[79] I. Brihuega, C. H. Michaelis, J. Zhang, S. Bose, V. Sessi, J. Honolka, M. A. Schneider, A. Enders and K. Kern, 'Electronic Decoupling and Templating of Co Nanocluster Arrays on the Boron Nitride Nanomesh', *Surf. Sci.* **602**, L95 (2008). Cited on page(s) 14 and 26

[80] D. Porath, Y. Levi, M. Tarabiah and O. Millo, 'Tunneling Spectroscopy of Isolated C_{60} Molecules in the Presence of Charging Effects', *Phys. Rev. B* **56**, 9829 (1997). Cited on page(s) 14

[81] J. M. Thijssen and H. S. Van der Zant, 'Charge Transport and Single-Electron Effects in Nanoscale Systems', *Phys. Stat. Sol. (b)* **245**, 1455 (2008). Cited on page(s) 14

[82] S. Willing, H. Lehmann, M. Volkmann and C. Klinke, 'Metal Nanoparticle Film-Based Room Temperature Coulomb Transistor', *Sci. Adv.* **3**, e1603191 (2017). Cited on page(s) 14

[83] G. Ertl, H. Knözinger, J. Weitkamp and F. Schüth, 'Handbook of Heterogeneous Catalysis' (John Wiley & Sons, Ltd, 1997). Cited on page(s) 14

[84] B. Gates, 'Supported Metal Clusters: Synthesis, Structure, and Catalysis', *Chem. Rev.* **95**, 511 (1995). Cited on page(s) 14 and 17

[85] J. Wilcoxon, in 'Metal Nanoparticles and Nanoalloys', Vol. 3 of 'Frontiers of Nanoscience', edited by R. L. Johnston and J. Wilcoxon (Elsevier, 2012), Pages 43 – 127. Cited on page(s) 14

[86] C. R. Henry, 'Surface Studies of Supported Model Catalysts', *Surf. Sci. Rep.* **31**, 231 (1998). Cited on page(s) 14, 15, and 132

[87] C. R. Henry, 'Catalytic Activity of Supported Nanometer-Sized Metal Clusters', *Appl. Surf. Sci.* **164**, 252 (2000). Cited on page(s) 14

[88] C. Papp, 'From Flat Surfaces to Nanoparticles: In Situ Studies of the Reactivity of Model Catalysts', *Catal. Lett.* **147**, 2 (2017). Cited on page(s) 14, 15, 20, 21, and 26

[89] D. W. Goodman, 'Catalysis: from Single Crystals to the "Real World"', *Surf. Sci.* **299**, 837 (1994). Cited on page(s) 14

[90] M. Boronat, A. Leyva-Pérez and A. Corma, 'Theoretical and Experimental Insights Into the Origin of the Catalytic Activity of Subnanometric Gold Clusters: Attempts to Predict Reactivity with Clusters and Nanoparticles of Gold', *Accounts Chem. Res.* **47**, 834 (2014). Cited on page(s) 15 and 16

[91] M. Boudart, 'Heterogeneous Catalysis by Metals', *J. Mol. Catal.* **30**, 27 (1985). Cited on page(s) 14 and 132

[92] P. L. Gunter, J. Niemantsverdriet, F. H. Ribeiro and G. A. Somorjai, 'Surface Science Approach to Modeling Supported Catalysts', *Catal. Rev.* **39**, 77 (1997). Cited on page(s) 14 and 18

[93] R. L. Johnston, in 'Metal Nanoparticles and Nanoalloys', Vol. 3 of 'Frontiers of Nanoscience', edited by R. L. Johnston and J. Wilcoxon (Elsevier, 2012), Pages 1 – 42. Cited on page(s) 14

[94] L. Liu and A. Corma, 'Metal Catalysts for Heterogeneous Catalysis: from Single Atoms to Nanoclusters and Nanoparticles', *Chem. Rev.* **118**, 4981 (2018). Cited on page(s) 14 and 30

[95] Z. Li, S. Ji, Y. Liu, X. Cao, S. Tian, Y. Chen, Z. Niu and Y. Li, 'Well-Defined Materials for Heterogeneous Catalysis: from Nanoparticles to Isolated Single-Atom Sites', *Chem. Rev.* **120**, 623 (2019). Cited on page(s) 14

[96] U. Heiz and W.-D. Schneider, 'Nanoassembled Model Catalysts', *J. Phys. D Appl. Phys.* **33**, R85 (2000). Cited on page(s) 14 and 18

[97] C. Binns, 'Nanoclusters Deposited on Surfaces', *Surf. Sci. Rep.* **44**, 1 (2001). Cited on page(s) 14 and 18

[98] U. Heiz and U. Landman, 'Nanocatalysis', 'NanoScience and Technology' (Springer, 2007). Cited on page(s) 14

[99] A. S. Crampton, M. D. Rötzer, C. J. Ridge, B. Yoon, F. F. Schweinberger, U. Landman and U. Heiz, 'Assessing the Concept of Structure Sensitivity or Insensitivity for Sub-Nanometer Catalyst Materials', *Surf. Sci.* **652**, 7 (2016). Cited on page(s) 14, 19, and 33

[100] U. Heiz, A. Sanchez, S. Abbet and W.-D. Schneider, 'Catalytic Oxidation of Carbon Monoxide on Monodispersed Platinum Clusters: Each Atom Counts', *J. Am. Chem. Soc.* **121**, 3214 (1999). Cited on page(s) 14, 19, and 132

[101] S. Abbet, A. Sanchez, U. Heiz, W.-D. Schneider, A. M. Ferrari, G. Pacchioni and N. Rösch, 'Acetylene cyclotrimerization on supported size-selected Pd n clusters ($1 \leq n \geq 30$): one atom is enough!', *J. Am. Chem. Soc.* **122**, 3453 (2000). Cited on page(s) 14

[102] K. Judai, S. Abbet, A. S. Wörz, U. Heiz and C. R. Henry, 'Low-Temperature Cluster Catalysis', *J. Am. Chem. Soc.* **126**, 2732 (2004). Cited on page(s) 15 and 19

[103] H. Tsunoyama, H. Sakurai, Y. Negishi and T. Tsukuda, 'Size-Specific Catalytic Activity of Polymer-Stabilized Gold Nanoclusters for Aerobic Alcohol Oxidation in Water', *J. Am. Chem. Soc.* **127**, 9374 (2005). Cited on page(s) 15

[104] E. T. Baxter, M.-A. Ha, A. C. Cass, A. N. Alexandrova and S. L. Anderson, 'Ethylene Dehydrogenation on $Pt_{4,7,8}$ Clusters on Al_2O_3: Strong Cluster Size Dependence Linked to Preferred Catalyst Morphologies', *ACS Catal.* **7**, 3322 (2017). Cited on page(s) 15

[105] M. Chen and D. Goodman, 'The Structure of Catalytically Active Gold on Titania', *Science* **306**, 252 (2004). Cited on page(s) 15

[106] W. Karim, C. Spreafico, A. Kleibert, J. Gobrecht, J. VandeVondele, Y. Ekinci and J. A. van Bokhoven, 'Catalyst Support Effects on Hydrogen Spillover', *Nature* **541**, 68 (2017). Cited on page(s) 15

[107] M. Haruta, T. Kobayashi, H. Sano and N. Yamada, 'Novel Gold Catalysts for the Oxidation of Carbon Monoxide at a Temperature far Below 0 °C', *Chem. Lett.* **16**, 405 (1987). Cited on page(s) 15 and 115

[108] M. Haruta, N. Yamada, T. Kobayashi and S. Iijima, 'Gold Catalysts Prepared by Coprecipitation for Low-Temperature Oxidation of Hydrogen and of Carbon Monoxide', *J. Catal.* **115**, 301 (1989). Cited on page(s) 15

[109] M. Haruta, 'Gold Rush', *Nature* **437**, 1098 (2005). Cited on page(s) 15 and 20

[110] M. D. Hughes, Y.-J. Xu, P. Jenkins, P. McMorn, P. Landon, D. I. Enache, A. F. Carley, G. A. Attard, G. J. Hutchings, F. King, E. H. Stitt, P. Johnston, K. Griffin and C. J. Kiely, 'Tunable gold catalysts for selective hydrocarbon oxidation under mild conditions', *Nature* **437**, 1132 (2005). Cited on page(s) 15 and 115

[111] J. Wang, G. Wang and J. Zhao, 'Density-Functional Study of Au$_n$ (n = 2-20) Clusters: Lowest-Energy Structures and Electronic Properties', *Phys. Rev. B* **66**, 035418 (2002). Cited on page(s) 15

[112] J. Bucher, 'Quantum Phenomena in Clusters and Nanostructures' (Springer, 2003), Pages 83–137. Cited on page(s) 16

[113] D. Weller and A. Moser, 'Thermal Effect Limits in Ultrahigh-Density Magnetic Recording', *IEEE Trans. Magn.* **35**, 4423 (1999). Cited on page(s) 16

[114] A. Cox, J. Louderback and L. Bloomfield, 'Experimental Observation of Magnetism in Rhodium Clusters', *Phys. Rev. Lett.* **71**, 923 (1993). Cited on page(s) 16

[115] A. Cox, J. Louderback, S. Apsel and L. Bloomfield, 'Magnetism in 4d-Transition Metal Clusters', *Phys. Rev. B* **49**, 12295 (1994). Cited on page(s) 16

[116] B. Reddy, S. Khanna and B. Dunlap, 'Giant Magnetic Moments in 4d Clusters', *Phys. Rev. Lett.* **70**, 3323 (1993). Cited on page(s) 16

[117] F. Liu, S. Khanna and P. Jena, 'Magnetism in Small Vanadium Clusters', *Phys. Rev. B* **43**, 8179 (1991). Cited on page(s) 16

[118] M. Moseler, H. Häkkinen, R. Barnett and U. Landman, 'Structure and Magnetism of Neutral and Anionic Palladium Clusters', *Phys. Rev. Lett.* **86**, 2545 (2001). Cited on page(s) 16

[119] S. Nayak and P. Jena, 'Anomalous Magnetism in Small Mn Clusters', *Chem. Phys. Lett.* **289**, 473 (1998). Cited on page(s) 16

[120] S. Nayak, M. Nooijen and P. Jena, 'Isomerism and Novel Magnetic Order in Mn$_{13}$ Cluster', *J. Phys. Chem. A* **103**, 9853 (1999). Cited on page(s) 16

[121] S. Khanna, B. Rao, P. Jena and M. Knickelbein, 'Ferrimagnetism in Mn$_7$ Cluster', *Chem. Phys. Lett.* **378**, 374 (2003). Cited on page(s) 16

[122] I. M. Billas, A. Châtelain and W. A. de Heer, 'Magnetism from the Atom to the Bulk in Iron, Cobalt, and Nickel Clusters', *Science* **265**, 1682 (1994). Cited on page(s) 16

[123] V. Sessi, K. Kuhnke, J. Zhang, J. Honolka, K. Kern, A. Enders, P. Bencok, S. Bornemann, J. Minár and H. Ebert, 'Cobalt Nanoclusters on Metal-Supported Xe Monolayers: Influence of the Substrate on Cluster Formation Kinetics and Magnetism', *Phys. Rev. B* **81**, 195403 (2010). Cited on page(s) 16

[124] N. Weiss, T. Cren, M. Epple, S. Rusponi, G. Baudot, S. Rohart, A. Tejeda, V. Repain, S. Rousset, P. Ohresser, F. Scheurer, P. Bencok and H. Brune, 'Uniform Magnetic Properties for an Ultrahigh-Density Lattice of Noninteracting Co Nanostructures', *Phys. Rev. Lett.* **95**, 157204 (2005). Cited on page(s) 16 and 19

[125] H. Brune, in 'Metal Clusters at Surfaces', edited by K.-H. Meiwes-Broer (Springer, 2000), Pages 67–105. Cited on page(s) 16, 19, and 126

[126] A. Cavallin, L. Fernández, M. Ilyn, A. Magaña, M. Ormaza, M. Matena, L. Vitali, J. Ortega, C. Grazioli, P. Ohresser, S. Rusponi, H. Brune and F. Schiller, 'Magnetism and Morphology of Co Nanocluster Superlattices on GdAu$_2$/Au(111)–(13 × 13)', *Phys. Rev. B* **90**, 235419 (2014). Cited on page(s) 16

[127] C. Vo-Van, S. Schumacher, J. Coraux, V. Sessi, O. Fruchart, N. B. Brookes, P. Ohresser and T. Michely, 'Magnetism of Cobalt Nanoclusters on Graphene on Iridium', *Appl. Phys. Lett.* **99**, 142504 (2011). Cited on page(s) 16 and 24

[128] R. Baltic, M. Pivetta, F. Donati, C. Wäckerlin, A. Singha, J. Dreiser, S. Rusponi and H. Brune, 'Superlattice of Single Atom Magnets on Graphene', *Nano Lett.* **16**, 7610 (2016). Cited on page(s) 16, 24, and 115

[129] M. Pauly, B. P. Pichon, P. Panissod, S. Fleutot, P. Rodriguez, M. Drillon and S. Begin-Colin, 'Size Dependent Dipolar Interactions in Iron Oxide Nanoparticle Monolayer and Multilayer Langmuir–Blodgett Films', *J. Mater. Chem.* **22**, 6343 (2012). Cited on page(s) 16

[130] R. Baltic, F. Donati, A. Singha, C. Wäckerlin, J. Dreiser, B. Delley, M. Pivetta, S. Rusponi and H. Brune, 'Magnetic Properties of Single Rare-Earth Atoms on Graphene/Ir(111)', *Phys. Rev. B* **98**, 024412 (2018). Cited on page(s) 16

[131] O. Ivanov, 'Determination of the Anisotropy Constant and Saturation Magnetization, and Magnetic Properties of Powders of an Iron-Platinum Alloy', *Phys. Met. Metallogr.* **35**, 81 (1973). Cited on page(s) 16

[132] J. Christodoulides, Y. Huang, Y. Zhang, G. Hadjipanayis, I. Panagiotopoulos and D. Niarchos, 'CoPt and FePt Thin Films for High Density Recording Media', *J. Appl. Phys.* **87**, 6938 (2000). Cited on page(s) 16

[133] S. Sun, 'Recent Advances in Chemical Synthesis, Self-Assembly, and Applications of FePt Nanoparticles', *Adv. Mater.* **18**, 393 (2006). Cited on page(s) 16

[134] Z. Dai, S. Sun and Z. Wang, 'Phase Transformation, Coalescence, and Twinning of Monodisperse FePt Nanocrystals', *Nano Lett.* **1**, 443 (2001). Cited on page(s) 16

[135] C.-B. Rong, N. Poudyal, G. S. Chaubey, V. Nandwana, R. Skomski, Y. Wu, M. J. Kramer and J. P. Liu, 'Structural Phase Transition and Ferromagnetism in Monodisperse 3 nm FePt Particles', *J. Appl. Phys.* **102**, 043913 (2007). Cited on page(s) 16

[136] J. Kim, C. Rong, J. P. Liu and S. Sun, 'Dispersible Ferromagnetic FePt Nanoparticles', *Adv. Mater.* **21**, 906 (2009). Cited on page(s) 16

[137] T. Klemmer, N. Shukla, C. Liu, X. Wu, E. Svedberg, O. Mryasov, R. Chantrell, D. Weller, M. Tanase and D. Laughlin, 'Structural Studies of L1$_0$ FePt Nanoparticles', *Appl. Phys. Lett.* **81**, 2220 (2002). Cited on page(s) 16

[138] C. Luo, S. H. Liou and D. J. Sellmyer, 'FePt:SiO$_2$ Granular Thin Film for High Density Magnetic Recording', *J. Appl. Phys.* **87**, 6941 (2000). Cited on page(s) 16

[139] B. Bian, D. E. Laughlin, K. Sato and Y. Hirotsu, 'Fabrication and Nanostructure of Oriented FePt Particles', *J. Appl. Phys.* **87**, 6962 (2000). Cited on page(s) 16 and 35

[140] P. Capiod, L. Bardotti, A. Tamion, O. Boisron, C. Albin, V. Dupuis, G. Renaud, P. Ohresser and F. Tournus, 'Elaboration of Nanomagnet Arrays: Organization and Magnetic Properties of Mass-Selected FePt Nanoparticles Deposited on Epitaxially Grown Graphene on Ir(111)', *Phys. Rev. Lett.* **122**, 106802 (2019). Cited on page(s) 16 and 35

[141] P. Munnik, P. E. de Jongh and K. P. de Jong, 'Recent Developments in the Synthesis of Supported Catalysts', *Chem. Rev.* **115**, 6687 (2015). Cited on page(s) 17

[142] M. Ichikawa, 'Metal Cluster Compounds as Molecular Precursors for Tailored Metal Catalysts', *Adv. Catal.* **38**, 283 (1992). Cited on page(s) 17

[143] J. Regalbuto, 'Catalyst Preparation: Science and Engineering' (CRC Press, 2016). Cited on page(s) 17

[144] H.-J. Freund, J. Libuda, M. Bäumer, T. Risse and A. Carlsson, 'Cluster, Facets, and Edges: Site-Dependent Selective Chemistry on Model Catalysts', *Chem. Rec.* **3**, 181 (2003). Cited on page(s) 17 and 118

[145] A. Kulkarni, R. J. Lobo-Lapidus and B. C. Gates, 'Metal Clusters on Supports: Synthesis, Structure, Reactivity, and Catalytic Properties', *Chem. Commun.* **46**, 5997 (2010). Cited on page(s) 17

[146] L. Jiao and J. R. Regalbuto, 'The Synthesis of Highly Dispersed Noble and Base Metals on Silica Via Strong Electrostatic Adsorption: I. Amorphous Silica', *J. Catal.* **260**, 329 (2008). Cited on page(s) 17

[147] A. Corma, P. Concepción, M. Boronat, M. J. Sabater, J. Navas, M. J. Yacaman, E. Larios, A. Posadas, M. A. López-Quintela, D. Buceta, E. Mendoza, G. Guilera and A. Mayoral, 'Exceptional Oxidation Activity with Size-Controlled Supported Gold Clusters of Low Atomicity', *Nat. Chem.* **5**, 775 (2013). Cited on page(s) 17

[148] Y. Shichibu and K. Konishi, 'HCl-Induced Nuclearity Convergence in Diphosphine-Protected Ultrasmall Gold Clusters: A Novel Synthetic Route to "Magic-Number" Au_{13} Clusters', *Small* **6**, 1216 (2010). Cited on page(s) 17

[149] M. Turner, V. B. Golovko, O. P. Vaughan, P. Abdulkin, A. Berenguer-Murcia, M. S. Tikhov, B. F. Johnson and R. M. Lambert, 'Selective Oxidation with Dioxygen by Gold Nanoparticle Catalysts Derived from 55-Atom Clusters', *Nature* **454**, 981 (2008). Cited on page(s) 17

[150] Z. L. Wang, 'Structural Analysis of Self-Assembling Nanocrystal Superlattices', *Adv. Mater.* **10**, 13 (1998). Cited on page(s) 17

[151] S. A. Claridge, A. Castleman Jr, S. N. Khanna, C. B. Murray, A. Sen and P. S. Weiss, 'Cluster-Assembled Materials', *ACS Nano* **3**, 244 (2009). Cited on page(s) 17 and 18

[152] M. Grzelczak, J. Vermant, E. M. Furst and L. M. Liz-Marzán, 'Directed Self-Assembly of Nanoparticles', *ACS Nano* **4**, 3591 (2010). Cited on page(s) 17

[153] M. A. Boles, M. Engel and D. V. Talapin, 'Self-Assembly of Colloidal Nanocrystals: from Intricate Structures to Functional Materials', *Chem. Rev* **116**, 11220 (2016). Cited on page(s) 17

[154] D. Vanmaekelbergh, 'Self-Assembly of Colloidal Nanocrystals as Route to Novel Classes of Nanostructured Materials', *Nano Today* **6**, 419 (2011). Cited on page(s) 17

[155] C. Murray, C. Kagan and M. Bawendi, 'Self-Organization of CdSe Nanocrystallites into Three-Dimensional Quantum Dot Superlattices', *Science* **270**, 1335 (1995). Cited on page(s) 17

[156] D. V. Talapin, E. V. Shevchenko, A. Kornowski, N. Gaponik, M. Haase, A. L. Rogach and H. Weller, 'A New Approach to Crystallization of CdSe Nanoparticles into Ordered Three-Dimensional Superlattices', *Adv. Mater.* **13**, 1868 (2001). Cited on page(s) 17

[157] A. Böker, J. He, T. Emrick and T. P. Russell, 'Self-Assembly of Nanoparticles at Interfaces', *Soft Matter* **3**, 1231 (2007). Cited on page(s) 17

[158] A. Dong, J. Chen, P. M. Vora, J. M. Kikkawa and C. B. Murray, 'Binary Nanocrystal Superlattice Membranes Self-Assembled at the Liquid–Air Interface', *Nature* **466**, 474 (2010). Cited on page(s) 17

[159] G. Singh, H. Chan, A. Baskin, E. Gelman, N. Repnin, P. Král and R. Klajn, 'Self-Assembly of Magnetite Nanocubes into Helical Superstructures', *Science* **345**, 1149 (2014). Cited on page(s) 17

[160] E. V. Shevchenko and D. V. Talapin, 'Semiconductor Nanocrystal Quantum Dots' (Springer, 2008), Pages 119–169. Cited on page(s) 17

[161] M. P. Boneschanscher, W. H. Evers, J. J. Geuchies, T. Altantzis, B. Goris, F. T. Rabouw, S. A. P. Van Rossum, H. S. J. Van Der Zant, L. D. A. Siebbeles, G. Van Tendeloo, I. Swart, J. Hilhorst, A. V. Petukhov, S. Bals and D. Vanmaekelbergh, 'Long-Range Orientation and Atomic Attachment of Nanocrystals in 2D Honeycomb Superlattices', *Science* **344**, 1377 (2014). Cited on page(s) 17

[162] V. Santhanam, J. Liu, R. Agarwal and R. P. Andres, 'Self-Assembly of Uniform Monolayer Arrays of Nanoparticles', *Langmuir* **19**, 7881 (2003). Cited on page(s) 17

[163] R. L. Whetten, J. T. Khoury, M. M. Alvarez, S. Murthy, I. Vezmar, Z. Wang, P. W. Stephens, C. L. Cleveland, W. Luedtke and U. Landman, 'Nanocrystal Gold Molecules', *Adv. Mater.* **8**, 428 (1996). Cited on page(s) 17

[164] R. P. Andres, J. D. Bielefeld, J. I. Henderson, D. B. Janes, V. R. Kolagunta, C. P. Kubiak, W. J. Mahoney and R. G. Osifchin, 'Self-Assembly of a Two-Dimensional Superlattice of Molecularly Linked Metal Clusters', *Science* **273**, 1690 (1996). Cited on page(s) 17

[165] K. Whitham, J. Yang, B. H. Savitzky, L. F. Kourkoutis, F. Wise and T. Hanrath, 'Charge Transport and Localization in Atomically Coherent Quantum Dot Solids', *Nat. Mater.* **15**, 557 (2016). Cited on page(s) 17

[166] K. An and G. A. Somorjai, 'Size and Shape Control of Metal Nanoparticles for Reaction Selectivity in Catalysis', *ChemCatChem* **4**, 1512 (2012). Cited on page(s) 17

[167] C. Pacholski, A. Kornowski and H. Weller, 'Self-Assembly of ZnO: from Nanodots to Nanorods', *Angew. Chem. Int. Ed.* **41**, 1188 (2002). Cited on page(s) 18

[168] J. A. Fan, C. Wu, K. Bao, J. Bao, R. Bardhan, N. J. Halas, V. N. Manoharan, P. Nordlander, G. Shvets and F. Capasso, 'Self-Assembled Plasmonic Nanoparticle Clusters', *Science* **328**, 1135 (2010). Cited on page(s) 18

[169] R. Abargues, J. Marqués-Hueso, J. Canet-Ferrer, E. Pedrueza, J. Valdés, E. Jiménez and J. Martínez-Pastor, 'High-resolution Electron-beam Patternable Nanocomposite Containing Metal Nanoparticles for Plasmonics', *Nanotechnology* **19**, 355308 (2008). Cited on page(s) 18

[170] T. Corrigan, S.-H. Guo, H. Szmacinski and R. Phaneuf, 'Systematic study of the Size and Spacing Dependence of Ag Nanoparticle Enhanced Fluorescence Using Electron-beam Lithography', *Appl. Phys. Lett.* **88**, 101112 (2006). Cited on page(s) 18

[171] M. K. Corbierre, J. Beerens and R. B. Lennox, 'Gold Nanoparticles Generated by Electron Beam Lithography of Gold(I)-thiolate Thin Films', *Chem. Mater.* **17**, 5774 (2005). Cited on page(s) 18

[172] J. Grunes, J. Zhu, E. A. Anderson and G. A. Somorjai, 'Ethylene Hydrogenation over Platinum Nanoparticle Array Model Catalysts Fabricated by Electron Beam Lithography: Determination of Active Metal Surface Area', *J. Phys. Chem. B* **106**, 11463 (2002). Cited on page(s) 18

[173] A. S. Eppler, J. Zhu, E. A. Anderson and G. A. Somorjai, 'Model Catalysts Fabricated by Electron Beam Lithography: AFM and TPD Surface Studies and Hydrogenation/Dehydrogenation of Cyclohexene + H_2 on a Pt Nanoparticle Array Supported by Silica', *Top. Catal.* **13**, 33 (2000). Cited on page(s) 18

[174] T. Atay, J.-H. Song and A. V. Nurmikko, 'Strongly Interacting Plasmon Nanoparticle Pairs: from Dipole-Dipole Interaction to Conductively Coupled Regime', *Nano Lett.* **4**, 1627 (2004). Cited on page(s) 18

[175] E. M. Hicks, S. Zou, G. C. Schatz, K. G. Spears, R. P. Van Duyne, L. Gunnarsson, T. Rindzevicius, B. Kasemo and M. Käll, 'Controlling Plasmon Line Shapes Through Diffractive Coupling in Linear Arrays of Cylindrical Nanoparticles Fabricated by Electron Beam Lithography', *Nano Lett.* **5**, 1065 (2005). Cited on page(s) 18

[176] B. Lamprecht, G. Schider, R. Lechner, H. Ditlbacher, J. R. Krenn, A. Leitner and F. R. Aussenegg, 'Metal Nanoparticle Gratings: Influence of Dipolar Particle Interaction on the Plasmon Resonance', *Phys. Rev. Lett.* **84**, 4721 (2000). Cited on page(s) 18

[177] F. Ribeiro and G. A. Somorjai, 'The Fabrication of "High-Technology" Catalysts', *Rec. Trav. Chim. Pays-Bas* **113**, 419 (1994). Cited on page(s) 18

[178] A. Broers, A. Hoole and J. Ryan, 'Electron Beam Lithography - Resolution Limits', *Microelectron. Eng.* **32**, 131 (1996). Cited on page(s) 18

[179] J. C. Hulteen and R. P. Van Duyne, 'Nanosphere Lithography: A Materials General Fabrication Process for Periodic Particle Array Surfaces', *J. Vac. Sci. Technol. A* **13**, 1553 (1995). Cited on page(s) 18

[180] C. L. Haynes and R. P. Van Duyne, 'Nanosphere Lithography: A Versatile Nanofabrication Tool for Studies of Size-Dependent Nanoparticle Optics', *J. Phys. Chem. B* **105**, 5599 (2001). Cited on page(s) 18

[181] G. H. Chan, J. Zhao, E. M. Hicks, G. C. Schatz and R. P. Van Duyne, 'Plasmonic Properties of Copper Nanoparticles Fabricated by Nanosphere Lithography', *Nano Lett.* **7**, 1947 (2007). Cited on page(s) 18

[182] T. R. Jensen, M. D. Malinsky, C. L. Haynes and R. P. Van Duyne, 'Nanosphere Lithography: Tunable Localized Surface Plasmon Resonance Spectra of Silver Nanoparticles', *J. Phys. Chem. B* **104**, 10549 (2000). Cited on page(s) 18

[183] U. Heiz and W.-D. Schneider, 'Size-Selected Clusters on Solid Surfaces', *Crit. Rev. Sol. State* **26**, 251 (2001). Cited on page(s) 18

[184] E. C. Tyo and S. Vajda, 'Catalysis by Clusters with Precise Numbers of Atoms', *Nat. Nanotechnol.* **10**, 577 (2015). Cited on page(s) 18 and 19

[185] C. L. Cleveland and U. Landman, 'Dynamics of Cluster-Surface Collisions', *Science* **257**, 355 (1992). Cited on page(s) 19

[186] A. Santra and D. Goodman, 'Oxide-Supported Metal Clusters: Models for Heterogeneous Catalysts', *J. Phys. Condens. Matter* **15**, R31 (2002). Cited on page(s) 19 and 20

[187] Y. Fukamori, M. König, B. Yoon, B. Wang, F. Esch, U. Heiz and U. Landman, 'Fundamental Insight into the Substrate-Dependent Ripening of Monodisperse Clusters', *ChemCatChem* **5**, 3330 (2013). Cited on page(s) 19, 30, and 31

[188] K. Wettergren, F. F. Schweinberger, D. Deiana, C. J. Ridge, A. S. Crampton, M. D. Rötzer, T. W. Hansen, V. P. Zhdanov, U. Heiz and C. Langhammer, 'High Sintering Resistance of Size-Selected Platinum Cluster Catalysts by Suppressed Ostwald Ripening', *Nano Lett.* **14**, 5803 (2014). Cited on page(s) 19, 31, and 34

[189] L. D. Socaciu, J. Hagen, T. M. Bernhardt, L. Wöste, U. Heiz, H. Häkkinen and U. Landman, 'Catalytic CO Oxidation by Free Au_2^-: Experiment and Theory', *J. Am. Chem. Soc.* **125**, 10437 (2003). Cited on page(s) 19

[190] A. Sanchez, S. Abbet, U. Heiz, W.-D. Schneider, H. Häkkinen, R. Barnett and U. Landman, 'When Gold is not Noble: Nanoscale Gold Catalysts', *J. Phys. Chem. A* **103**, 9573 (1999). Cited on page(s) 19

[191] B. Yoon, H. Häkkinen, U. Landman, A. S. Wörz, J.-M. Antonietti, S. Abbet, K. Judai and U. Heiz, 'Charging Effects on Bonding and Catalyzed Oxidation of CO on Au_8 Clusters on MgO', *Science* **307**, 403 (2005). Cited on page(s) 19

[192] H. Röder, E. Hahn, H. Brune, J.-P. Bucher and K. Kern, 'Building One- and Two-Dimensional Nanostructures by Diffusion-Controlled Aggregation at Surfaces', *Nature* **366**, 141 (1993). Cited on page(s) 19

Bibliography

[193] D. Chambliss, R. Wilson and S. Chiang, 'Nucleation of Ordered Ni Island Arrays on Au(111) by Surface-Lattice Dislocations', *Phys. Rev. Lett.* **66**, 1721 (1991). Cited on page(s) 19

[194] H. Brune, M. Giovannini, K. Bromann and K. Kern, 'Self-Organized Growth of Nanostructure Arrays on Strain-Relief Patterns', *Nature* **394**, 451 (1998). Cited on page(s) 19

[195] C. Goyhenex, C. Henry and J. Urban, '*In-Situ* Measurements of the Lattice Parameter of Supported Palladium Clusters', *Philos. Mag. A* **69**, 1073 (1994). Cited on page(s) 20

[196] H.-J. Freund, 'The Surface Science of Catalysis and More, Using Ultrathin Oxide Films as Templates: a Perspective', *J. Am. Chem. Soc* **138**, 8985 (2016). Cited on page(s) 20

[197] C. Becker and K. Wandelt, 'Templates in Chemistry III' (Springer, 2008), Pages 45–86. Cited on page(s) 20 and 21

[198] A. T. N'Diaye, S. Bleikamp, P. J. Feibelman and T. Michely, 'Two-Dimensional Ir Cluster Lattice on a Graphene Moiré on Ir(111)', *Phys. Rev. Lett.* **97**, 215501 (2006). Cited on page(s) 20, 23, 24, 25, 32, 114, and 116

[199] G. Sitja, R. O. Unac and C. Henry, 'Kinetic Monte Carlo Simulation of the Growth of Metal Clusters on Regular Array of Defects on Insulator', *Surf. Sci.* **604**, 404 (2010). Cited on page(s) 20

[200] C. Becker, K. Von Bergmann, A. Rosenhahn, J. Schneider and K. Wandelt, 'Preferential Cluster Nucleation on Long-range Superstructures on $Al_2O_3/Ni_3Al(111)$', *Surf. Sci.* **486**, L443 (2001). Cited on page(s) 20, 21, and 22

[201] M. Batzill, 'The Surface Science of Graphene: Metal Interfaces, CVD Synthesis, Nanoribbons, Chemical Modifications, and Defects', *Surf. Sci. Rep.* **67**, 83 (2012). Cited on page(s) 20 and 23

[202] E. Vesselli and M. Peressi, 'Studies in Surface Science and Catalysis' (Elsevier, 2017), Vol. 177, Pages 285–315. Cited on page(s) 21

[203] X. Liu, Y. Han, J. W. Evans, A. K. Engstfeld, R. J. Behm, M. C. Tringides, M. Hupalo, H.-Q. Lin, L. Huang, K.-M. Ho, D. Appy, P. Thiel and C.-Z. Wang, 'Growth Morphology and Properties of Metals on Graphene', *Prog. Surf. Sci.* **90**, 397 (2015). Cited on page(s) 21 and 129

[204] S. Degen, C. Becker and K. Wandelt, 'Thin Alumina Films on $Ni_3Al(111)$: A Template for Nanostructured Pd Cluster Growth', *Faraday Discuss.* **125**, 343 (2004). Cited on page(s) 21, 22, and 34

[205] G. Sitja and C. R. Henry, 'Molecular Beam Study of the Oxidation of Carbon Monoxide on a Regular Array of Palladium Clusters on Alumina', *J. Phys. Chem. C* **121**, 10706 (2017). Cited on page(s) 21 and 22

[206] G. Sitja, S. L. Moal, M. Marsault, G. Hamm, F. Leroy and C. R. Henry, 'Transition from Molecule to Solid State: Reactivity of Supported Metal Clusters', *Nano Lett.* **13**, 1977 (2013). Cited on page(s) 21 and 22

[207] S. Stempel, M. Bäumer and H.-J. Freund, 'STM Studies of Rhodium Deposits on an Ordered Alumina Film - Resolution and Tip Effects', *Surf. Sci.* **402**, 424 (1998). Cited on page(s) 21

[208] C. Becker, A. Rosenhahn, A. Wiltner, K. Von Bergmann, J. Schneider, P. Pervan, M. Milun, M. Kralj and K. Wandelt, 'Al_2O_3-Films on $Ni_3Al(111)$: a Template for Nanostructured Cluster Growth', *New J. Phys.* **4**, 75 (2002). Cited on page(s) 21 and 34

[209] A. Rosenhahn, J. Schneider, C. Becker and K. Wandelt, 'Oxidation of $Ni_3Al(111)$ at 600, 800, and 1050 K Investigated by Scanning Tunneling Microscopy', *J. Vac. Sci. Technol. A* **18**, 1923 (2000). Cited on page(s) 22

[210] M. Schmid, G. Kresse, A. Buchsbaum, E. Napetschnig, S. Gritschneder, M. Reichling and P. Varga, 'Nanotemplate with Holes: Ultrathin Alumina on $Ni_3Al(111)$', *Phys. Rev. Lett.* **99**, 196104 (2007). Cited on page(s) 22

[211] E. Vesselli, A. Baraldi, S. Lizzit and G. Comelli, 'Large Interlayer Relaxation at a Metal-Oxide Interface: the Case of a Supported Ultrathin Alumina Film', *Phys. Rev. Lett.* **105**, 046102 (2010). Cited on page(s) 22

[212] J. A. Olmos-Asar, E. Vesselli, A. Baldereschi and M. Peressi, 'Towards Optimal Seeding for the Synthesis of Ordered Nanoparticle Arrays on Alumina/Ni$_3$Al(111)', *Phys. Chem. Chem. Phys.* **17**, 28154 (2015). Cited on page(s) 22

[213] A. Lehnert, S. Rusponi, M. Etzkorn, S. Ouazi, P. Thakur and H. Brune, 'Magnetic Anisotropy of Fe and Co Adatoms and Fe Clusters Magnetically Decoupled from Ni$_3$Al(111) by an Alumina Bilayer', *Phys. Rev. B* **81**, 104430 (2010). Cited on page(s) 22

[214] A. Lehnert, A. Krupski, S. Degen, K. Franke, R. Decker, S. Rusponi, M. Kralj, C. Becker, H. Brune and K. Wandelt, 'Nucleation of ordered Fe islands on Al$_2$O$_3$/Ni$_3$Al(111)', *Surf. Sci.* **600**, 1804 (2006). Cited on page(s) 22

[215] S. Vlaic, L. Gragnaniello, S. Rusponi, A. Cavallin, F. Donati, Q. Dubout, C. Piamonteze, J. Dreiser, F. Nolting and H. Brune, 'Interlayer Exchange Coupling in Ordered Fe Nanocluster Arrays Grown on Al$_2$O$_3$/Ni$_3$Al(111)', *Phys. Rev. B* **89**, 245402 (2014). Cited on page(s) 22

[216] M. Marsault, G. Sitja and C. R. Henry, 'Regular Arrays of Pd and PdAu Clusters on Ultrathin Alumina Films for Reactivity Studies', *Phys. Chem. Chem. Phys.* **16**, 26458 (2014). Cited on page(s) 22 and 34

[217] N. Alyabyeva, A. Ouvrard, A.-M. Zakaria, F. Charra and B. Bourguignon, 'Transition from Disordered to Long-Range Ordered Nanoparticles on Al$_2$O$_3$/Ni$_3$Al(111)', *Appl. Surf. Sci.* **444**, 423 (2018). Cited on page(s) 22

[218] G. Sitja, A. Bailly, M. De Santis, V. Heresanu and C. R. Henry, 'Regular Arrays of Pt Clusters on Alumina: A New Superstructure on Al$_2$O$_3$/Ni$_3$Al(111)', *J. Phys. Chem. C* **123**, 24487 (2019). Cited on page(s) 22

[219] G. Hamm, C. Becker and C. Henry, 'Bimetallic Pd-Au Nanocluster Arrays Grown on Nanostructured Alumina Templates', *Nanotechnology* **17**, 1943 (2006). Cited on page(s) 22

[220] M. Marsault, G. H. A. Wörz, G. Sitja, C. Barth and C. Henry, 'Preparation of Regular Arrays of Bimetallic Clusters with Independent Control of Size and Chemical Composition', *Faraday Discuss.* **138**, 407 (2008). Cited on page(s) 22

[221] L. Gragnaniello, T. Ma, G. Barcaro, L. Sementa, F. R. Negreiros, A. Fortunelli, S. Surnev and F. P. Netzer, 'Ordered Arrays of Size-Selected Oxide Nanoparticles', *Phys. Rev. Lett.* **108**, 195507 (2012). Cited on page(s) 22

[222] A. Chaudhury, L. Gragnaniello, T. Ma, S. Surnev and F. Netzer, 'Alumina-Supported Array of Co Nanoparticles: Size-Dependent Oxidation Kinetics?', *J. Phys. Chem. C* **117**, 18112 (2013). Cited on page(s) 22

[223] A. Buchsbaum, M. De Santis, H. C. Tolentino, M. Schmid and P. Varga, 'Highly Ordered Pd, Fe, and Co Clusters on Alumina on Ni$_3$Al(111)', *Phys. Rev. B* **81**, 115420 (2010). Cited on page(s) 22

[224] T. Engel and G. Ertl, 'A Molecular Beam Investigation of the Catalytic Oxidation of CO on Pd(111)', *J. Chem. Phys.* **69**, 1267 (1978). Cited on page(s) 22

[225] C. Henry, C. Chapon and C. Duriez, 'Precursor State in the Chemisorption of CO on Supported Palladium Clusters', *J. Chem. Phys.* **95**, 700 (1991). Cited on page(s) 22

[226] C. Busse, P. Lazić, R. Djemour, J. Coraux, T. Gerber, N. Atodiresei, V. Caciuc, R. Brako, S. Blügel, J. Zegenhagen and T. Michely, 'Graphene on Ir(111): Physisorption with Chemical Modulation', *Phys. Rev. Lett.* **107**, 036101 (2011). Cited on page(s) 23

[227] J. Coraux, T. N. Plasa, C. Busse and T. Michely, 'Structure of Epitaxial Graphene on Ir(111)', *New J. Phys.* **10**, 043033 (2008). Cited on page(s) 23

Bibliography

[228] M. J. Allen, V. C. Tung and R. B. Kaner, 'Honeycomb Carbon: a Review of Graphene', *Chem. Rev.* **110**, 132 (2010). Cited on page(s) 23

[229] W. Choi, I. Lahiri, R. Seelaboyina and Y. S. Kang, 'Synthesis of Graphene and its Applications: A Review', *Crit. Rev. Solid State Mater. Sci.* **35**, 52 (2010). Cited on page(s) 23

[230] D. R. Cooper, B. D'Anjou, N. Ghattamaneni, B. Harack, M. Hilke, A. Horth, N. Majlis, M. Massicotte, L. Vandsburger, E. Whiteway and V. Yu, 'Experimental Review of Graphene', *Condens. Matter Phys.* **2012**, (2012). Cited on page(s) 23

[231] T. Land, T. Michely, R. Behm, J. Hemminger and G. Comsa, 'STM Investigation of Single Layer Graphite Structures Produced on Pt(111) by Hydrocarbon Decomposition', *Surf. Sci.* **264**, 261 (1992). Cited on page(s) 23

[232] A. Y. Tontegode, 'Carbon on Transition Metal Surfaces', *Prog. Surf. Sci.* **38**, 201 (1991). Cited on page(s) 23

[233] N. Gall, E. Rut'Kov and A. Y. Tontegode, 'Two Dimensional Graphite Films on Metals and Their Intercalation', *Int. J. Mod. Phys. B* **11**, 1865 (1997). Cited on page(s) 23

[234] A. Preobrajenski, M. L. Ng, A. Vinogradov and N. Mårtensson, 'Controlling Graphene Corrugation on Lattice-Mismatched Substrates', *Phys. Rev. B* **78**, 073401 (2008). Cited on page(s) 23, 25, and 26

[235] P. J. Feibelman, 'Pinning of Graphene to Ir(111) by Flat Ir Dots', *Phys. Rev. B* **77**, 165419 (2008). Cited on page(s) 24 and 25

[236] A. J. Martínez-Galera, I. Brihuega and J. M. Gomez-Rodriguez, 'Influence of the Rotational Domain in the Growth of Transition Metal Clusters on Graphene', *J. Phys. Chem. C* **119**, 3572 (2015). Cited on page(s) 24

[237] A. T. N'Diaye, T. Gerber, C. Busse, J. Mysliveček, J. Coraux and T. Michely, 'A Versatile Fabrication Method for Cluster Superlattices', *New J. Phys.* **11**, 103045 (2009). Cited on page(s) 24, 25, 30, 31, 34, 114, 116, 126, and 128

[238] D. Mousadakos, M. Pivetta, H. Brune and S. Rusponi, 'Sm Cluster Superlattice on Graphene/Ir(111)', *New J. Phys.* **19**, 123021 (2017). Cited on page(s) 24 and 25

[239] M. Pivetta, S. Rusponi and H. Brune, 'Direct Capture and Electrostatic Repulsion in the Self-Assembly of Rare-Earth Atom Superlattices on Graphene', *Phys. Rev. B* **98**, 115417 (2018). Cited on page(s) 24

[240] D. Franz, S. Runte, C. Busse, S. Schumacher, T. Gerber, T. Michely, M. Mantilla, V. Kilic, J. Zegenhagen and A. Stierle, 'Atomic Structure and Crystalline Order of Graphene-Supported Ir Nanoparticle Lattices', *Phys. Rev. Lett.* **110**, 065503 (2013). Cited on page(s) 24

[241] D. Franz, N. Blanc, J. Coraux, G. Renaud, S. Runte, T. Gerber, C. Busse, T. Michely, P. J. Feibelman, U. Hejral and A. Stierle, 'Atomic Structure of Pt Nanoclusters Supported by Graphene/Ir(111) and Reversible Transformation under CO Exposure', *Phys. Rev. B* **93**, 045426 (2016). Cited on page(s) 24

[242] S. Billinge, 'Materials Science: Nanoparticle Structures Served up on a Tray', *Nature* **495**, 453 (2013). Cited on page(s) 24

[243] T. Gerber, J. Knudsen, P. J. Feibelman, E. Granas, P. Stratmann, K. Schulte, J. N. Andersen and T. Michely, 'CO-induced Smoluchowski Ripening of Pt Cluster Arrays on the Graphene/Ir(111) Moiré', *ACS Nano* **7**, 2020 (2013). Cited on page(s) 24, 31, and 132

[244] N. Podda, M. Corva, F. Mohamed, Z. Feng, C. Dri, F. Dvorak, V. Matolin, G. Comelli, M. Peressi and E. Vesselli, 'Experimental and Theoretical Investigation of the Restructuring Process Induced by CO at Near Ambient Pressure: Pt Nanoclusters on Graphene/Ir(111)', *ACS Nano* **11**, 1041 (2017). Cited on page(s) 24, 32, and 132

[245] H. Noei, D. Franz, M. Creutzburg, P. Müller, K. Krausert, E. Grånäs, R. Taube, F. Mittendorfer and A. Stierle, 'Monitoring the Interaction of CO with Graphene Supported Ir Clusters by Vibrational Spectroscopy and Density Functional Theory Calculations', *J. Phys. Chem. C* **122**, 4281 (2018). Cited on page(s) 24

[246] T. Gerber, E. Grånäs, U. A. Schröder, P. Stratmann, K. Schulte, J. N. Andersen, J. Knudsen and T. Michely, 'Stability and reactivity of graphene-templated nanoclusters', *J. Phys. Chem. C* **120**, 26290 (2016). Cited on page(s) 24, 32, 114, and 132

[247] J. Knudsen, P. J. Feibelman, T. Gerber, E. Grånäs, K. Schulte, P. Stratmann, J. N. Andersen and T. Michely, 'Clusters Binding to the Graphene Moiré on Ir(111): X-Ray Photoemission Compared to Density Functional Calculations', *Phys. Rev. B* **85**, 035407 (2012). Cited on page(s) 25

[248] A. Cavallin, M. Pozzo, C. Africh, A. Baraldi, E. Vesselli, C. Dri, G. Comelli, R. Larciprete, P. Lacovig, S. Lizzit and D. Alfé, 'Local Electronic Structure and Density of Edge and Facet Atoms at Rh Nanoclusters Self-Assembled on a Graphene Template', *ACS Nano* **6**, 3034 (2012). Cited on page(s) 25

[249] A. J. Martínez-Galera, I. Brihuega, A. Gutiérrez-Rubio, T. Stauber and J. M. Gómez-Rodríguez, 'Towards Scalable Nano-Engineering of Graphene', *Sci. Rep.* **4**, 7314 (2014). Cited on page(s) 25

[250] K. Donner and P. Jakob, 'Structural Properties and Site Specific Interactions of Pt with the Graphene/Ru(0001) Moiré Overlayer', *J. Chem. Phys.* **131**, 164701 (2009). Cited on page(s) 25

[251] Y. Wang, A. Saranin, A. Zotov, M. Lai and H. Chang, 'Random and Ordered Arrays of Surface Magic Clusters', *Int. Rev. Phys. Chem.* **27**, 317 (2008). Cited on page(s) 25

[252] D.-e. Jiang, M.-H. Du and S. Dai, 'First Principles Study of the Graphene/Ru(0001) Interface', *J. Chem. Phys.* **130**, 074705 (2009). Cited on page(s) 25

[253] H. Zhang, Q. Fu, Y. Cui, D. Tan and X. Bao, 'Fabrication of Metal Nanoclusters on Graphene Grown on Ru(0001)', *Chinese Sci. Bull.* **54**, 2446 (2009). Cited on page(s) 25

[254] B. Wang, B. Yoon, M. König, Y. Fukamori, F. Esch, U. Heiz and U. Landman, 'Size-Selected Monodisperse Nanoclusters on Supported Graphene: Bonding, Isomerism, and Mobility', *Nano Lett.* **12**, 5907 (2012). Cited on page(s) 26

[255] Y. Han, A. K. Engstfeld, R. J. Behm and J. W. Evans, 'Atomistic Modeling of the Directed-Assembly of Bimetallic Pt-Ru Nanoclusters on Ru(0001)-Supported Monolayer Graphene', *J. Chem. Phys.* **138**, 134703 (2013). Cited on page(s) 26

[256] Y. Xu, L. Semidey-Flecha, L. Liu, Z. Zhou and D. W. Goodman, 'Exploring the Structure and Chemical Activity of 2-D Gold Islands on Graphene Moiré/Ru(0001)', *Faraday Discuss.* **152**, 267 (2011). Cited on page(s) 26

[257] R. Cortés, D. Acharya, C. Ciobanu, E. Sutter and P. Sutter, 'Graphene on Ru(0001) Moiré Corrugation Studied by Scanning Tunneling Microscopy on Au/Graphene/Ru(0001) Heterostructures', *J. Phys. Chem. C* **117**, 20675 (2013). Cited on page(s) 26

[258] Z. Zhou, F. Gao and D. W. Goodman, 'Deposition of Metal Clusters on Single-Layer Graphene/Ru(0001): Factors that Govern Cluster Growth', *Surf. Sci.* **604**, L31 (2010). Cited on page(s) 26 and 34

[259] Q. Liao, H. Zhang, K. Wu, H. Li, S. Bao and P. He, 'Nucleation and Growth of Monodispersed Cobalt Nanoclusters on Graphene Moiré on Ru(0001)', *Nanotechnology* **22**, 125303 (2011). Cited on page(s) 26

[260] E. Sutter, P. Albrecht, B. Wang, M.-L. Bocquet, L. Wu, Y. Zhu and P. Sutter, 'Arrays of Ru Nanoclusters with Narrow Size Distribution Templated by Monolayer Graphene on Ru', *Surf. Sci.* **605**, 1676 (2011). Cited on page(s) 26

[261] E. Sutter, B. Wang, P. Albrecht, J. Lahiri, M.-L. Bocquet and P. Sutter, 'Templating of Arrays of Ru Nanoclusters by Monolayer Graphene/Ru Moirés with Different Periodicities', *J. Phys. Condens. Matter* **24**, 314201 (2012). Cited on page(s) 26

[262] Z. Novotny, F. P. Netzer and Z. Dohnálek, 'Cerium Oxide Nanoclusters on Graphene/Ru(0001): Intercalation of Oxygen via Spillover', *ACS Nano* **9**, 8617 (2015). Cited on page(s) 26

[263] Z. Novotny, F. Netzer and Z. Dohnálek, 'Ceria Nanoclusters on Graphene/Ru(0001): A New Model Catalyst System', *Surf. Sci.* **652**, 230 (2016). Cited on page(s) 26

[264] R. T. Frederick, Z. Novotny, F. P. Netzer, G. S. Herman and Z. Dohnálek, 'Growth and Stability of Titanium Dioxide Nanoclusters on Graphene/Ru(0001)', *J. Phys. Chem. B* **122**, 640 (2018). Cited on page(s) 26

[265] E. N. Voloshina, Y. S. Dedkov, S. Torbrügge, A. Thissen and M. Fonin, 'Graphene on Rh(111): Scanning Tunneling and Atomic Force Microscopies Studies', *Appl. Phys. Lett.* **100**, 241606 (2012). Cited on page(s) 26

[266] M. Iannuzzi and J. Hutter, 'Comparative Study of the Nature of Chemical Bonding of Corrugated Graphene on Ru(0001) and Rh(111) by Electronic Structure Calculations', *Surf. Sci.* **605**, 1360 (2011). Cited on page(s) 26

[267] K. Gotterbarm, C. Bronnbauer, U. Bauer, C. Papp and H.-P. Steinrück, 'Graphene-supported Pd nanoclusters probed by carbon monoxide adsorption', *J. Phys. Chem. C* **118**, 25097 (2014). Cited on page(s) 26, 31, and 33

[268] K. Gotterbarm, F. Späth, U. Bauer, C. Bronnbauer, H.-P. Steinrück and C. Papp, 'Reactivity of Graphene-Supported Pt Nanocluster Arrays', *ACS Catal.* **5**, 2397 (2015). Cited on page(s) 26 and 132

[269] M. Sicot, S. Bouvron, O. Zander, U. Rüdiger, Y. S. Dedkov and M. Fonin, 'Nucleation and Growth of Nickel Nanoclusters on Graphene Moiré on Rh(111)', *Appl. Phys. Lett.* **96**, 093115 (2010). Cited on page(s) 26

[270] K. Gotterbarm, C. Bronnbauer, U. Bauer, C. Papp and H.-P. Steinrück, 'Graphene-Supported Pd nanoclusters Probed by Carbon Monoxide Adsorption', *J. Phys. Chem. C* **118**, 25097 (2014). Cited on page(s) 26

[271] K. Gotterbarm, F. Späth, U. Bauer, H.-P. Steinrück and C. Papp, 'Adsorption and Reaction of SO_2 on Graphene-Supported Pt Nanoclusters', *Top. Catal.* **58**, 573 (2015). Cited on page(s) 26

[272] F. Düll, V. Schwaab, F. Späth, U. Bauer, P. Bachmann, J. Steinhauer, H.-P. Steinrück and C. Papp, 'Sulfur oxidation on graphene-supported platinum nanocluster arrays', *Chem. Phys. Lett.* **708**, 165 (2018). Cited on page(s) 26

[273] F. Düll, U. Bauer, F. Späth, P. Bachmann, J. Steinhauer, H.-P. Steinrück and C. Papp, 'Bimetallic Pd–Pt Alloy Nanocluster Arrays on Graphene/Rh(111): Formation, Stability, and Dynamics', *Phys. Chem. Chem. Phys.* **20**, 21294 (2018). Cited on page(s) 26

[274] K. Watanabe, T. Taniguchi and H. Kanda, 'Direct-Bandgap Properties and Evidence for Ultraviolet Lasing of Hexagonal Boron Nitride Single Crystal', *Nat. Mater.* **3**, 404 (2004). Cited on page(s) 26

[275] A. Preobrajenski, A. Vinogradov and N. Mårtensson, 'Monolayer of h-BN Chemisorbed on Cu(111) and Ni(111): The Role of the Transition Metal 3d States', *Surf. Sci.* **582**, 21 (2005). Cited on page(s) 26

[276] S. Joshi, D. Ecija, R. Koitz, M. Iannuzzi, A. P. Seitsonen, J. Hutter, H. Sachdev, S. Vijayaraghavan, F. Bischoff, K. Seufert, J. V. Barth and W. Auwärter, 'Boron Nitride on Cu(111): an Electronically Corrugated Monolayer', *Nano Lett.* **12**, 5821 (2012). Cited on page(s) 26

[277] A. Preobrajenski, M. Nesterov, M. L. Ng, A. Vinogradov and N. Mårtensson, 'Monolayer h-BN on Lattice-Mismatched Metal Surfaces: On the Formation of the Nanomesh', *Chem. Phys. Lett.* **446**, 119 (2007). Cited on page(s) 26

[278] A. Nagashima, N. Tejima, Y. Gamou, T. Kawai and C. Oshima, 'Electronic Dispersion Relations of Monolayer Hexagonal Boron Nitride Formed on the Ni(111) Surface', *Phys. Rev. B* **51**, 4606 (1995). Cited on page(s) 26

[279] P. Bachmann, F. Düll, F. Späth, U. Bauer, H.-P. Steinrück and C. Papp, 'A HR-XPS Study of the Formation of h-BN on Ni(111) from the Two Precursors, Ammonia Borane and Borazine', *J. Chem. Phys.* **149**, 164709 (2018). Cited on page(s) 26

[280] F. Orlando, R. Larciprete, P. Lacovig, I. Boscarato, A. Baraldi and S. Lizzit, 'Epitaxial Growth of Hexagonal Boron Nitride on Ir(111)', *J. Phys. Chem. C* **116**, 157 (2012). Cited on page(s) 26

[281] F. H. Farwick zum Hagen, D. M. Zimmermann, C. C. Silva, C. Schlueter, N. Atodiresei, W. Jolie, A. J. Martínez-Galera, D. Dombrowski, U. A. Schröder, M. Will, P. Lazić, V. Caciuc, S. Blügel, T.-L. Lee, T. Michely and C. Busse, 'Structure and Growth of Hexagonal Boron Nitride on Ir(111)', *ACS Nano* **10**, 11012 (2016). Cited on page(s) 26 and 136

[282] M. Corso, W. Auwärter, M. Muntwiler, A. Tamai, T. Greber and J. Osterwalder, 'Boron Nitride Nanomesh', *Science* **303**, 217 (2004). Cited on page(s) 26

[283] A. Goriachko, Y. He, M. Knapp, H. Over, M. Corso, T. Brugger, S. Berner, J. Osterwalder and T. Greber, 'Self-Assembly of a Hexagonal Boron Nitride Nanomesh on Ru(0001)', *Langmuir* **23**, 2928 (2007). Cited on page(s) 26

[284] J. Gómez Díaz, Y. Ding, R. Koitz, A. P. Seitsonen, M. Iannuzzi and J. Hutter, 'Hexagonal Boron Nitride on Transition Metal Surfaces', *Theor. Chem. Acc.* **132**, 1350 (2013). Cited on page(s) 26

[285] W. Auwärter, 'Hexagonal Boron Nitride Monolayers on Metal Supports: Versatile Templates for Atoms, Molecules and Nanostructures', *Surf. Sci. Rep.* **74**, 1 (2019). Cited on page(s) 26

[286] J. Zhang, V. Sessi, C. H. Michaelis, I. Brihuega, J. Honolka, K. Kern, R. Skomski, X. Chen, G. Rojas and A. Enders, 'Ordered Layers of Co Clusters on BN Template Layers', *Phys. Rev. B* **78**, 165430 (2008). Cited on page(s) 26 and 27

[287] W. C. McKee, M. C. Patterson, J. R. Frick, P. T. Sprunger and Y. Xu, 'Adsorption of Transition Metal Adatoms on h-BN/Rh(111): Implications for Nanocluster Self-Assembly', *Catal. Today* **280**, 220 (2017). Cited on page(s) 27

[288] A. J. Martínez-Galera and J. M. Gómez-Rodríguez, 'Pseudo-Ordered Distribution of Ir Nanocrystals on h-BN', *Nanoscale* **11**, 2317 (2019). Cited on page(s) 27, 28, 34, and 114

[289] F. Düll, M. Meusel, F. Späth, S. Schötz, U. Bauer, P. Bachmann, J. Steinhauer, H.-P. Steinrück, A. Bayer and C. Papp, 'Growth and stability of Pt nanoclusters from 1 to 50 atoms on h-BN/Rh(111)', *Phys. Chem. Chem. Phys.* **21**, 21287 (2019). Cited on page(s) 27, 28, and 117

[290] Y. Zhang, Y. Zhang, D. Ma, Q. Ji, W. Fang, J. Shi, T. Gao, M. Liu, Y. Gao, Y. Chen, L. Xu and Z. Liu, 'Mn Atomic Layers under Inert Covers of Graphene and Hexagonal Boron Nitride Prepared on Rh(111)', *Nano Res.* **6**, 887 (2013). Cited on page(s) 27 and 33

[291] F. Wu, D. Huang, Y. Yue and L. Liu, 'Template Growth of Au, Ni and Ni-Au Nanoclusters on Hexagonal Boron Nitride/Rh(111): A Combined STM, TPD and AES study', *RSC Adv.* **7**, 44169 (2017). Cited on page(s) 27

[292] H. P. Koch, R. Laskowski, P. Blaha and K. Schwarz, 'Adsorption of Gold Atoms on the h-BN/Rh(111) Nanomesh', *Phys. Rev. B* **84**, 245410 (2011). Cited on page(s) 27

[293] H. P. Koch, R. Laskowski, P. Blaha and K. Schwarz, 'Adsorption of Small Gold Clusters on the h-BN/Rh(111) Nanomesh', *Phys. Rev. B* **86**, 155404 (2012). Cited on page(s) 27

Bibliography

[294] M. L. Ng, A. Preobrajenski, A. Vinogradov and N. Mårtensson, 'Formation and Temperature Evolution of Au Nanoparticles Supported on the h-BN Nanomesh', *Surf. Sci.* **602**, 1250 (2008). Cited on page(s) 27

[295] M. C. Patterson, B. F. Habenicht, R. L. Kurtz, L. Liu, Y. Xu and P. T. Sprunger, 'Formation and Stability of Dense Arrays of Au Nanoclusters on Hexagonal Boron Nitride/Rh(111)', *Phys. Rev. B* **89**, 205423 (2014). Cited on page(s) 27 and 126

[296] A. Goriachko, Y. B. He and H. Over, 'Complex Growth of NanoAu on BN Nanomeshes Supported by Ru(0001)', *J. Phys. Chem. C* **112**, 8147 (2008). Cited on page(s) 27

[297] W. C. McKee, M. C. Patterson, D. Huang, J. R. Frick, R. L. Kurtz, P. T. Sprunger, L. Liu and Y. Xu, 'CO Adsorption on Au Nanoparticles Grown on Hexagonal Boron Nitride/Rh(111)', *J. Phys. Chem. C* **120**, 10909 (2016). Cited on page(s) 27 and 31

[298] M. Will, N. Atodiresei, V. Caciuc, P. Valerius, C. Herbig and T. Michely, 'A Monolayer of Hexagonal Boron Nitride on Ir(111) as a Template for Cluster Superlattices', *ACS Nano* **12**, 6871 (2018). Cited on page(s) 28, 116, 125, 126, 135, and 167

[299] M. D. Argyle and C. H. Bartholomew, 'Heterogeneous Catalyst Deactivation and Regeneration: a Review', *Catalysts* **5**, 145 (2015). Cited on page(s) 29, 30, and 31

[300] M. v. Smoluchowski, 'Versuch einer mathematischen Theorie der Koagulationskinetik kolloider Lösungen', *Phys. Z.* **17**, 557 (1917). Cited on page(s) 30

[301] A. K. Datye, Q. Xu, K. C. Kharas and J. M. McCarty, 'Particle Size Distributions in Heterogeneous Catalysts: What Do They Tell Us about the Sintering Mechanism?', *Catal. Today* **111**, 59 (2006). Cited on page(s) 30 and 31

[302] C. Granqvist and R. Buhrman, 'Statistical Model for Coalescence of Islands in Discontinuous Films', *Appl. Phys. Lett.* **27**, 693 (1975). Cited on page(s) 30

[303] P. Wynblatt and N. Gjostein, 'Supported Metal Crystallites', *Prog. Solid State Chem.* **9**, 21 (1975). Cited on page(s) 30

[304] W. Ostwald, 'Über die vermeintliche Isomerie des roten und gelben Quecksilberoxyds und die Oberflächenspannung fester Körper', *Z. Phys. Chem.* **34**, 495 (1900). Cited on page(s) 30

[305] I. M. Lifshitz and V. V. Slyozov, 'The Kinetics of Precipitation from Supersaturated Solid Solutions', *J. Phys. Chem. Sol.* **19**, 35 (1961). Cited on page(s) 30

[306] C. Wagner, 'Theorie der Alterung von Niederschlägen durch Umlösen (Ostwald-Reifung)', *Z. Elektrochem.* **65**, 581 (1961). Cited on page(s) 30

[307] M. Kahlweit, 'Ostwald Ripening of Precipitates', *Adv. Colloid Interface Sci.* **5**, 1 (1975). Cited on page(s) 30

[308] R. Finsy, 'On the Critical Radius in Ostwald Ripening', *Langmuir* **20**, 2975 (2004). Cited on page(s) 30

[309] S. B. Simonsen, I. Chorkendorff, S. Dahl, M. Skoglundh, J. Sehested and S. Helveg, 'Direct Observations of Oxygen-Induced Platinum Nanoparticle Ripening Studied by *in situ* TEM', *J. Am. Chem. Soc.* **132**, 7968 (2010). Cited on page(s) 30

[310] S. B. Simonsen, I. Chorkendorff, S. Dahl, M. Skoglundh, J. Sehested and S. Helveg, 'Ostwald Ripening in a Pt/SiO₂ Model Catalyst Studied By *in situ* TEM', *J. Catal.* **281**, 147 (2011). Cited on page(s) 30

[311] A. T. DeLaRiva, T. W. Hansen, S. R. Challa and A. K. Datye, '*In situ* Transmission Electron Microscopy of Catalyst Sintering', *J. Catal.* **308**, 291 (2013). Cited on page(s) 30

[312] C. T. Campbell, S. C. Parker and D. E. Starr, 'The Effect of Size-Dependent Nanoparticle Energetics on Catalyst Sintering', *Science* **298**, 811 (2002). Cited on page(s) 31

[313] C. T. Campbell, 'The Energetics of Supported Metal Nnanoparticles: Relationships to Sintering Rates and Catalytic Activity', *Acc. Chem. Res.* **46**, 1712 (2013). Cited on page(s) 31

[314] K.-J. Hu, S. R. Plant, P. R. Ellis, C. M. Brown, P. T. Bishop and R. E. Palmer, 'Atomic Resolution Observation of a Size-dependent Change in the Ripening Modes of Mass-selected Au Nanoclusters Involved in CO Oxidation', *J. Am. Chem. Soc* **137**, 15161 (2015). Cited on page(s) 31

[315] E. Starodub, N. C. Bartelt and K. F. McCarty, 'Oxidation of Graphene on Metals', *J. Phys. Chem. C* **114**, 5134 (2010). Cited on page(s) 32

[316] E. Grånäs, J. Knudsen, U. A. Schröder, T. Gerber, C. Busse, M. A. Arman, K. Schulte, J. N. Andersen and T. Michely, 'Oxygen Intercalation under Graphene on Ir(111): Energetics, Kinetics, and the Role of Graphene Edges', *ACS Nano* **6**, 9951 (2012). Cited on page(s) 32

[317] E. Grånäs, M. Andersen, M. A. Arman, T. Gerber, B. Hammer, J. Schnadt, J. N. Andersen, T. Michely and J. Knudsen, 'CO Intercalation of Graphene on Ir(111) in the Millibar Regime', *J. Phys. Chem. C* **117**, 16438 (2013). Cited on page(s) 32

[318] E. Grånäs, T. Gerber, U. A. Schröder, K. Schulte, J. N. Andersen, T. Michely and J. Knudsen, 'Hydrogen Intercalation under Graphene on Ir(111)', *Surf. Sci.* **651**, 57 (2016). Cited on page(s) 32

[319] W. Auwärter, M. Muntwiler, T. Greber and J. Osterwalder, 'Co on h-BN/Ni(111): From Island to Island-chain Formation and Co Intercalation', *Surf. Sci.* **511**, 379 (2002). Cited on page(s) 33

[320] J. R. Rostrup-Nielsen, 'Industrial Relevance of Coking', *Catal. Today* **37**, 225 (1997). Cited on page(s) 33

[321] E. Wolf and F. Alfani, 'Catalysts Deactivation by Coking', *Catal. Rev.* **24**, 329 (1982). Cited on page(s) 33

[322] A. S. Crampton, M. D. Rötzer, F. F. Schweinberger, B. Yoon, U. Landman and U. Heiz, 'Ethylene Hydrogenation on Supported Ni, Pd and Pt Nanoparticles: Catalyst Activity, Deactivation and the d-band Model', *J. Catal.* **333**, 51 (2016). Cited on page(s) 33 and 117

[323] F. Düll, J. Steinhauer, F. Späth, U. Bauer, P. Bachmann, H.-P. Steinrück, S. Wickert, R. Denecke and C. Papp, 'Ethylene: Its Adsorption, Reaction, and Coking on Pt/h-BN/Rh(111) Nanocluster Arrays', *J. Chem. Phys.* **152**, 224710 (2020). Cited on page(s) 33

[324] H.-G. Boyen, G. Kästle, K. Zürn, T. Herzog, F. Weigl, P. Ziemann, O. Mayer, C. Jerome, M. Möller, J. P. Spatz, M. G. Garnier and P. Oelhafen, 'A Micellar Route to Ordered Arrays of Magnetic Nanoparticles: From Size-Selected Pure Cobalt Dots to Cobalt–Cobalt Oxide Core–Shell Systems', *Adv. Funct. Mater.* **13**, 359 (2003). Cited on page(s) 33

[325] A.-H. Lu, E. e. Salabas and F. Schüth, 'Magnetic Nanoparticles: synthesis, protection, functionalization, and application', *Angew. Chem. Int. Ed.* **46**, 1222 (2007). Cited on page(s) 33 and 35

[326] D. Peng, K. Sumiyama, T. Hihara, S. Yamamuro and T. Konno, 'Magnetic Properties of Monodispersed Co/CoO Clusters', *Phys. Rev. B* **61**, 3103 (2000). Cited on page(s) 33

[327] G. Haas, A. Menck, H. Brune, J. Barth, J. Venables and K. Kern, 'Nucleation and Growth of Supported Clusters at Defect Sites: Pd/MgO(001)', *Phys. Rev. B* **61**, 11105 (2000). Cited on page(s) 34

[328] J. Zhang and A. N. Alexandrova, 'Structure, Stability, and Mobility of Small Pd Clusters on the Stoichiometric and Defective TiO$_2$(110) Surfaces', *J. Chem. Phys.* **135**, 174702 (2011). Cited on page(s) 34

[329] M. Shekhar, J. Wang, W.-S. Lee, W. D. Williams, S. M. Kim, E. A. Stach, J. T. Miller, W. N. Delgass and F. H. Ribeiro, 'Size and Support Effects for the Water-Gas Shift Catalysis over Gold Nanoparticles Supported on Model Al$_2$O$_3$ and TiO$_2$', *J. Am. Chem. Soc.* **134**, 4700 (2012). Cited on page(s) 34

[330] W. Wallace, B. K. Min and D. Goodman, 'The Stabilization of Supported Gold Clusters by Surface Defects', *J. Mol. Catal. A Chem.* **228**, 3 (2005). Cited on page(s) 34

[331] A. J. Martínez-Galera, U. A. Schröder, C. Herbig, M. Arman, J. Knudsen and T. Michely, 'Preventing Sintering of Nanoclusters on Graphene by Radical Adsorption', *Nanoscale* **9**, 13618 (2017). Cited on page(s) 34

[332] J. Lu, B. Fu, M. C. Kung, G. Xiao, J. W. Elam, H. H. Kung and P. C. Stair, 'Coking-and Sintering-resistant Palladium Catalysts Achieved Through Atomic Layer Deposition', *Science* **335**, 1205 (2012). Cited on page(s) 34

[333] A. C. Reber and S. N. Khanna, 'Effect of Embedding Platinum Clusters in Alumina on Sintering, Coking, and Activity', *J. Phys. Chem. C* **121**, 21527 (2017). Cited on page(s) 35

[334] T. D. Gould, A. Izar, A. W. Weimer, J. L. Falconer and J. W. Medlin, 'Stabilizing Ni Catalysts by Molecular Layer Deposition for Harsh, Dry Reforming Conditions', *ACS Catal.* **4**, 2714 (2014). Cited on page(s) 35

[335] M. Cargnello, C. Gentilini, T. Montini, E. Fonda, S. Mehraeen, M. Chi, M. Herrera-Collado, N. D. Browning, S. Polizzi, L. Pasquato and P. Fornasiero, 'Active and Stable Embedded Au/CeO$_2$ Catalysts for Preferential Oxidation of CO', *Chem. Mater.* **22**, 4335 (2010). Cited on page(s) 35

[336] Z. Li, Z. Wang, B. Jiang and S. Kawi, 'Sintering Resistant Ni Nanoparticles Exclusively Confined within SiO$_2$ nanotubes for CH$_4$ Dry Reforming', *Catal. Sci. Technol.* **8**, 3363 (2018). Cited on page(s) 35

[337] F. Düll, E. M. Freiberger, P. Bachmann, J. Steinhauer and C. Papp, 'Pt Nanoclusters Sandwiched between Hexagonal Boron Nitride and Nanographene as van der Waals Heterostructures for Optoelectronics', *ACS Appl. Nano Mater.* **2**, 7019 (2019). Cited on page(s) 35

[338] Y. Ding, S. Majetich, J. Kim, K. Barmak, H. Rollins and P. Sides, 'Sintering Prevention and Phase Transformation of FePt Nanoparticles', *J. Magn. Magn. Matter.* **284**, 336 (2004). Cited on page(s) 35

[339] Y. Kobayashi, M. Horie, M. Konno, B. Rodríguez-González and L. M. Liz-Marzán, 'Preparation and Properties of Silica-coated Cobalt Nanoparticles', *J. Phys. Chem. B* **107**, 7420 (2003). Cited on page(s) 35

[340] A.-H. Lu, W.-C. Li, N. Matoussevitch, B. Spliethoff, H. Bönnemann and F. Schüth, 'Highly Stable Carbon-Protected Cobalt Nanoparticles and Graphite Shells', *Chem. Commun.* 98 (2005). Cited on page(s) 35

[341] N. O. Núñez, P. Tartaj, M. P. Morales, P. Bonville and C. J. Serna, 'Yttria-coated FeCo Magnetic Nanoneedles', *Chem. Mater.* **16**, 3119 (2004). Cited on page(s) 35

[342] C.-M. Seah, B. Vigolo, S.-P. Chai and A. R. Mohamed, 'Transfer of Wafer-scale Graphene onto Arbitrary Substrates: Steps Towards the Reuse and Recycling of the Catalyst', *2D Mater.* **5**, 042001 (2018). Cited on page(s) 36

[343] I. Š. Rakić, D. Čapeta, M. Plodinec and M. Kralj, 'Large-scale Transfer and Characterization of Macroscopic Periodically Nano-rippled Graphene', *Carbon* **96**, 243 (2016). Cited on page(s) 36

[344] O. Alexeev and B. Gates, 'Iridium Clusters Supported on γ-Al$_2$O$_3$: Structural Characterization and Catalysis of Toluene Hydrogenation', *J. Catal.* **176**, 310 (1998). Cited on page(s) 114

[345] F. Li and B. C. Gates, 'Size-Dependent Catalytic Activity of Zeolite-Supported Iridium Clusters', *J. Phys. Chem. C* **111**, 262 (2007). Cited on page(s) 114

[346] S. Liang, C. Hao and Y. Shi, 'The Power of Single-Atom Catalysis', *ChemCatChem* **7**, 2559 (2015). Cited on page(s) 115

[347] Y. Chen, Z. Huang, Z. Ma, J. Chen and X. Tang, 'Fabrication, Characterization, and Stability of Supported Single-Atom Catalysts', *Catal. Sci. Technol.* **7**, 4250 (2017). Cited on page(s) 115

[348] A. Beniya and S. Higashi, 'Towards Dense Single-Atom Catalysts for Future Automotive Applications', *Nat. Catal.* **2**, 590 (2019). Cited on page(s) 115

[349] H. Zhang, G. Liu, L. Shi and J. Ye, 'Single-Atom Catalysts: Emerging Multifunctional Materials in Heterogeneous Catalysis', *Adv. Energy Mater.* **8**, 1701343 (2018). Cited on page(s) 115

[350] A. Wang, J. Li and T. Zhang, 'Heterogeneous Single-Atom Catalysis', *Nat. Rev. Chem.* **2**, 65 (2018). Cited on page(s) 115

[351] M. Gao, A. Lyalin and T. Taketsugu, 'CO Oxidation on h-BN Supported Au Atom', *J. Chem. Phys.* **138**, 034701 (2013). Cited on page(s) 115

[352] M. Gao, A. Lyalin and T. Taketsugu, 'Catalytic Activity of Au and Au_2 on the h-BN Surface: Adsorption and Activation of O_2', *J. Phys. Chem. C* **116**, 9054 (2012). Cited on page(s) 115

[353] P. Zhao, Y. Su, Y. Zhang, S.-J. Li and G. Chen, 'CO Catalytic Oxidation on Iron-Embedded Hexagonal Boron Nitride Sheet', *Chem. Phys. Lett.* **515**, 159 (2011). Cited on page(s) 115

[354] J.-X. Liang, J. Lin, X.-F. Yang, A.-Q. Wang, B.-T. Qiao, J. Liu, T. Zhang and J. Li, 'Theoretical and Experimental Investigations on Single-Atom Catalysis: Ir_1/FeO_1 for CO Oxidation', *J. Phys. Chem. C* **118**, 21945 (2014). Cited on page(s) 115

[355] J. Lin, A. Wang, B. Qiao, X. Liu, X. Yang, X. Wang, J. Liang, J. Li, J. Liu and T. Zhang, 'Remarkable Performance of Ir_1/FeO_x Single-Atom Catalyst in Water Gas Shift Reaction', *J. Am. Chem. Soc.* **135**, 15314 (2013). Cited on page(s) 115

[356] T. Hartl, P. Bampoulis and T. Michely, private communication. Cited on page(s) 115

[357] C. Herbig, T. Knispel, S. Simon, U. A. Schröder, A. J. Martínez-Galera, M. A. Arman, C. Teichert, J. Knudsen, A. V. Krasheninnikov and T. Michely, 'From Permeation to Cluster Arrays: Graphene on Ir(111) Exposed to Carbon Vapor', *Nano Lett.* **17**, 3105 (2017). Cited on page(s) 115 and 118

[358] M. Will, 'Elemental Vapor Deposition on 2D Materials: Cluster Formation and Intercalation', Master's Thesis, Universität zu Köln, Germany. Cited on page(s) 115

[359] J. T. Kummer, 'Catalysts for Automobile Emission Control', *Prog. Energy Combust. Sci.* **6**, 177 (1980). Cited on page(s) 117

[360] Q. Fu, H. Saltsburg and M. Flytzani-Stephanopoulos, 'Active Nonmetallic Au and Pt Species on Ceria-based Water-Gas Shift Catalysts', *Science* **301**, 935 (2003). Cited on page(s) 117

[361] J. B. Park, J. Graciani, J. Evans, D. Stacchiola, S. D. Senanayake, L. Barrio, P. Liu, J. F. Sanz, J. Hrbek and J. A. Rodriguez, 'Gold, Copper, and Platinum Nanoparticles dispersed on $CeO_x/TiO_2(110)$ Surfaces: High Water-Gas Shift Activity and the Nature of the Mixed-metal Oxide at the Nanometer Level', *J. Am. Chem. Soc.* **132**, 356 (2010). Cited on page(s) 117

[362] I. González, R. Navarro, W. Wen, N. Marinkovic, J. Rodriguéz, F. Rosa and J. Fierro, 'A Comparative Study of the Water Gas Shift Reaction over Platinum Catalysts Supported on CeO_2, TiO_2 and Ce-modified TiO_2', *Catal. Today* **149**, 372 (2010). Cited on page(s) 117

[363] S. Vajda, M. J. Pellin, J. P. Greeley, C. L. Marshall, L. A. Curtiss, G. A. Ballentine, J. W. Elam, S. Catillon-Mucherie, P. C. Redfern, F. Mehmood and P. Zapol, 'Subnanometre Platinum Clusters as Highly Active and Selective Catalysts for the Oxidative Dehydrogenation of Propane', *Nat. Mater.* **8**, 213 (2009). Cited on page(s) 117

[364] J. Wei and E. Iglesia, 'Mechanism and Site Requirements for Activation and Chemical Conversion of Methane on Supported Pt Clusters and Turnover Rate Comparisons Among Noble Metals', *J. Phys. Chem. B* **108**, 4094 (2004). Cited on page(s) 117

[365] J. Russell, P. Zapol, P. Král and L. A. Curtiss, 'Methane Bond Activation by Pt and Pd Sub-nanometer Clusters Supported on Graphene and Carbon Nanotubes', *Chem. Phys. Lett.* **536**, 9 (2012). Cited on page(s) 117

[366] N. Cheng, S. Stambula, D. Wang, M. N. Banis, J. Liu, A. Riese, B. Xiao, R. Li, T.-K. Sham, L.-M. Liu, G. A. Botton and X. Sun, 'Platinum Single-atom and Cluster Catalysis of the Hydrogen Evolution Reaction', *Nat. Commun.* **7**, 1 (2016). Cited on page(s) 117

[367] J. Neugebohren, D. Borodin, H. W. Hahn, J. Altschäffel, A. Kandratsenka, D. J. Auerbach, C. T. Campbell, D. Schwarzer, D. J. Harding, A. M. Wodtke and T. N. Kitsopoulos, 'Velocity-resolved Kinetics of Site-specific Carbon Monoxide Oxidation on Platinum Surfaces', *Nature* **558**, 280 (2018). Cited on page(s) 118 and 132

[368] J. Park, A. N. Pasupathy, J. I. Goldsmith, C. Chang, Y. Yaish, J. R. Petta, M. Rinkoski, J. P. Sethna, H. D. Abruña, P. L. McEuen and D. C. Ralph, 'Coulomb Blockade and the Kondo Effect in Single-atom Transistors', *Nature* **417**, 722 (2002). Cited on page(s) 118

[369] C. Herbig, E. H. Åhlgren, W. Jolie, C. Busse, J. Kotakoski, A. V. Krasheninnikov and T. Michely, 'Interfacial Carbon Nanoplatelet Formation by Ion Irradiation of Graphene on Iridium (111)', *ACS Nano* **8**, 12208 (2014). Cited on page(s) 118

[370] J. Pascual, J. Gómez-Herrero, C. Rogero, A. Baró, D. Sánchez-Portal, E. Artacho, P. Ordejón and J. Soler, 'Seeing Molecular Orbitals', *Chem. Phys. Lett.* **321**, 78 (2000). Cited on page(s) 118

[371] X. Lu, M. Grobis, K. Khoo, S. G. Louie and M. Crommie, 'Charge Transfer and Screening in Individual C_{60} Molecules on Metal Substrates: A Scanning Tunneling Spectroscopy and Theoretical Study', *Phys. Rev. B* **70**, 115418 (2004). Cited on page(s) 118

[372] D. Leigh, C. Nörenberg, D. Cattaneo, J. Owen, K. Porfyrakis, A. Li Bassi, A. Ardavan and G. Briggs, 'Self-Assembly of Trimetallic Nitride Template Fullerenes on Surfaces Studied by STM', *Surf. Sci.* **601**, 2750 (2007). Cited on page(s) 118

[373] A. J. Lakin, C. Chiutu, A. M. Sweetman, P. Moriarty and J. L. Dunn, 'Recovering Molecular Orientation from Convoluted Orbitals', *Phys. Rev. B* **88**, 035447 (2013). Cited on page(s) 118

[374] R. Pawlak, T. Glatzel, V. Pichot, L. Schmidlin, S. Kawai, S. Fremy, D. Spitzer and E. Meyer, 'Local Detection of Nitrogen-Vacancy Centers in a Nanodiamond Monolayer', *Nano Lett.* **13**, 5803 (2013). Cited on page(s) 118

[375] T. Hartl, P. Bampoulis, M. Will, V. Boix de la Cruz, P. Lacovig, S. Lizzit, J. Knudsen and T. Michely, in preparation. Cited on page(s) 119 and 121

[376] U. A. Schröder, E. Grånäs, T. Gerber, M. A. Arman, A. J. Martínez-Galera, K. Schulte, J. N. Andersen, J. Knudsen and T. Michely, 'Etching of graphene on Ir(111) with molecular oxygen', *Carbon* **96**, 320 (2016). Cited on page(s) 121

[377] T. Hartl, M. Will, D. Čapeta, R. Singh, D. Scheinecker, V. Boix de la Cruz, S. Dellmann, P. Lacovig, S. Lizzit, B. V. Senkovskiy, A. Grüneis, M. Kralj, J. Knudsen, J. Kotakoski, T. Michely and P. Bampoulis, 'Cluster Superlattice Membranes', *ACS Nano* **14**, 13629 (2020). Cited on page(s) 121, 122, and 136

[378] A. Trovarelli, 'Catalytic Properties of Ceria and CeO_2-Containing Materials', *Catal. Rev.* **38**, 439 (1996). Cited on page(s) 121

[379] A. Trovarelli and P. Fornasiero, 'Catalysis by Ceria and Related Materials', Vol. 12 of 'Catalytic science series' (Imperial College Press, 2013). Cited on page(s) 121

[380] T. Montini, M. Melchionna, M. Monai and P. Fornasiero, 'Fundamentals and Catalytic Applications of CeO_2-Based Materials', *Chem. Rev.* **116**, 5987 (2016). Cited on page(s) 121

[381] L. Vivier and D. Duprez, 'Ceria-Based Solid Catalysts for Organic Chemistry', *ChemSusChem* **3**, 654 (2010). Cited on page(s) 121

[382] J. Berwanger, S. Polesya, S. Mankovsky, H. Ebert and F. J. Giessibl, 'Atomically Resolved Chemical Reactivity of Small Fe Clusters', *Phys. Rev. Lett.* **124**, 096001 (2020). Cited on page(s) 126

[383] A. N. Startsev, 'The Mechanism of HDS Catalysis', *Catal. Rev.* **37**, 353 (1995). Cited on page(s) 127

[384] A. Renaud, F. Grasset, B. Dierre, T. Uchikoshi, N. Ohashi, T. Takei, A. Planchat, L. Cario, S. Jobic, F. Odobel and S. Cordier, 'Inorganic Molybdenum Clusters as Light-Harvester in All Inorganic Solar Cells: a Proof of Concept', *ChemistrySelect* **1**, 2284 (2016). Cited on page(s) 127

[385] W. Fa, C. Luo and J. Dong, 'Coexistence of Ferroelectricity and Ferromagnetism in Tantalum Clusters', *J. Chem. Phys.* **125**, 114305 (2006). Cited on page(s) 127

[386] R. Moro, X. Xu, S. Yin and W. A. de Heer, 'Ferroelectricity in Free Niobium Clusters', *Science* **300**, 1265 (2003). Cited on page(s) 127

[387] S. Nepijko, M. Klimenkov, H. Kuhlenbeck, D. Zemlyanov, D. Herein, R. Schlögl and H.-J. Freund, 'TEM Study of Tantalum Clusters on Al_2O_3/NiAl(110)', *Surf. Sci.* **412**, 192 (1998). Cited on page(s) 127

[388] S. Nemana and B. C. Gates, 'Surface-Mediated Synthesis and Spectroscopic Characterization of Tantalum Clusters on Silica', *Langmuir* **22**, 8214 (2006). Cited on page(s) 127

[389] S. Nemana and B. C. Gates, 'Silica-Supported Tantalum Clusters: Catalysts for Conversion of Methane with n-Butane to Give Ethane,Propane, and Pentanes', *Catal. Lett.* **113**, 73 (2007). Cited on page(s) 127

[390] J. Bucher and L. Bloomfield, 'Magnetism of Free Transition Metal and Rare Earth Clusters', *Int. J. Mod. Phys. B* **7**, 1079 (1993). Cited on page(s) 129

[391] X. Liu, C.-Z. Wang, M. Hupalo, H.-Q. Lin, K.-M. Ho and M. C. Tringides, 'Metals on Graphene: Interactions, Growth Morphology, and Thermal Stability', *Crystals* **3**, 79 (2013). Cited on page(s) 129

[392] M. Hershberger, M. Hupalo, P. Thiel and M. Tringides, 'Growth of fcc(111) Dy Multi-height Islands on 6H-SiC(0001) Graphene', *J. Phys. Condens. Mat.* **25**, 225005 (2013). Cited on page(s) 129

[393] M. Hupalo, X. Liu, C.-Z. Wang, W.-C. Lu, Y.-X. Yao, K.-M. Ho and M. C. Tringides, 'Metal Nanostructure Formation on Graphene: Weak Versus Strong Bonding', *Adv. Mater.* **23**, 2082 (2011). Cited on page(s) 129 and 130

[394] D. Mousadakos, 'Rare Earth and Bimetallic Transition Metal Islands at Surfaces', Doctoral Thesis, École polytechnique fédérale de Lausanne, Lausanne, Switzerland, 2017. Cited on page(s) 129

[395] D. F. Förster, T. O. Wehling, S. Schumacher, A. Rosch and T. Michely, 'Phase Coexistence of Clusters and Islands: Europium on Graphene', *New J. Phys.* **14**, 023022 (2012). Cited on page(s) 130

[396] S. Schumacher, F. Huttmann, M. Petrović, C. Witt, D. F. Förster, C. Vo-Van, J. Coraux, A. J. Martínez-Galera, V. Sessi, I. Vergara, R. Rückamp, M. Grüninger, N. Schleheck, F. Meyer Zu Heringdorf, P. Ohresser, M. Kralj, T. O. Wehling and T. Michely, 'Europium Underneath Graphene on Ir(111): Intercalation Mechanism, Magnetism, and Band Structure', *Phys. Rev. B* **90**, 235437 (2014). Cited on page(s) 131

[397] S. Kraus and T. Michely, private communication. Cited on page(s) 131

[398] M. Trenary, S. Tang, R. Simonson and F. McFeely, 'An Angle-resolved Photoemission Study of CO Chemisorbed on the Pt(111) Surface', *Surf. Sci.* **124**, 555 (1983). Cited on page(s) 131

[399] A. Baró and H. Ibach, 'New Study of CO Adsorption at Low Temperature (90 K) on Pt(111) by EELS', *J. Chem. Phys.* **71**, 4812 (1979). Cited on page(s) 131

[400] H. Steininger, S. Lehwald and H. Ibach, 'On the Adsorption of CO on Pt(111)', *Surf. Sci.* **123**, 264 (1982). Cited on page(s) 131

[401] J. A. Stroscio and D. Eigler, 'Atomic and Molecular Manipulation with the Scanning Tunneling Microscope', *Science* **254**, 1319 (1991). Cited on page(s) 131

[402] M. Kinne, T. Fuhrmann, C. Whelan, J. Zhu, J. Pantförder, M. Probst, G. Held, R. Denecke and H.-P. Steinrück, 'Kinetic Parameters of CO Adsorbed on Pt(111) Studied by in situ High Resolution X-ray Photoelectron Spectroscopy', *J. Chem. Phys.* **117**, 10852 (2002). Cited on page(s) 131

[403] M. Kinne, T. Fuhrmann, J. Zhu, C. Whelan, R. Denecke and H.-P. Steinrück, 'Kinetics of the CO Oxidation Reaction on Pt(111) Studied by in situ High-resolution X-ray Photoelectron Spectroscopy', *J. Chem. Phys.* **120**, 7113 (2004). Cited on page(s) 131

[404] H. J. Yang, T. Minato, M. Kawai and Y. Kim, 'STM Investigation of CO ordering on Pt(111): From an isolated molecule to high-coverage superstructures', *J. Phys. Chem. C* **117**, 16429 (2013). Cited on page(s) 131

[405] R. L. Palmer and J. N. Smith Jr, 'Molecular Beam study of CO Oxidation on a (111) Platinum Surface', *J. Chem. Phys.* **60**, 1453 (1974). Cited on page(s) 132

[406] C. Campbell, G. Ertl, H. Kuipers and J. Segner, 'A Molecular Beam Study of the Catalytic Oxidation of CO on a Pt(111) Surface', *J. Chem.Phys.* **73**, 5862 (1980). Cited on page(s) 132

[407] A. Santra and D. Goodman, 'Catalytic Oxidation of CO by Platinum Group Metals: from Ultrahigh Vacuum to Elevated Pressures', *Electrochim. Acta* **47**, 3595 (2002). Cited on page(s) 132

[408] Y. Shi and K. M. Ervin, 'Catalytic Oxidation of Carbon Monoxide by Platinum Cluster Anions', *J. Chem. Phys.* **108**, 1757 (1998). Cited on page(s) 132

[409] F. Düll, F. Späth, U. Bauer, P. Bachmann, J. Steinhauer, H.-P. Steinrück and C. Papp, 'Reactivity of CO on Sulfur-passivated Graphene-supported Platinum Nanocluster Arrays', *J. Phys. Chem. C* **122**, 16008 (2018). Cited on page(s) 132

[410] M. Will, P. Bampoulis, T. Hartl, P. Valerius and T. Michely, 'Conformal Embedding of Cluster Superlattices with Carbon', *ACS Appl. Mater. Interfaces* **11**, 40524 (2019). Cited on page(s) 135 and 167

[411] P. Valerius, C. Herbig, M. Will, M. A. Arman, J. Knudsen, V. Caciuc, N. Atodiresei and T. Michely, 'Annealing of Ion-Irradiated Hexagonal Boron Nitride on Ir(111)', *Phys. Rev. B* **96**, 235410 (2017). Cited on page(s) 136

[412] M. Engler, F. Frost, S. Müller, S. Macko, M. Will, R. Feder, D. Spemann, R. Hübner, S. Facsko and T. Michely, 'Silicide Induced Ion Beam Patterning of Si(001)', *Nanotechnology* **25**, 115303 (2014). Cited on page(s) 136

Acknowledgements
(Danksagung)

Es folgt der schwierigste Teil des Verfassens einer Dissertation – die angemessene schriftliche Darstellung tiefempfundenen Dankes den unzählbar vielen Personen gegenüber, die durch ihren direkten oder indirekten Einfluss zu dieser wundervollen Zeit und dem vorliegenden Resultat beigetragen haben. Die mir dargebotenen Möglichkeiten und Erfahrungen weiß ich zutiefst zu schätzen und die vielen Personen, denen ich zum Dank verpflichtet bin, verdienen mehr als einen eigenen Paragraphen in diesem kurzen Kapitel.

Zunächst gilt mein Dank meinem Doktorvater Prof. **Thomas Michely**, der mir die Möglichkeit gab, meine Promotion in seiner Gruppe durchzuführen. Für seine direkte Betreuung, seine konstruktiven Ratschläge, die mich stets forderten, und die mir ermöglichten Besuche von internationalen Konferenzen und Arbeitsgruppen bin ich zutiefst dankbar; Auch für seine Motivation, die neun-Uhr-Plenarvorträge auf den DPG-Frühjahrstagungen wahrzunehmen, denn die waren meist höchst interessant.

Als nächstes danke ich Prof. **Alec Wodtke** für sein ehrliches Interesse an meinem Forschungsthema und die Übernahme der Korreferenz. Seine herzliche Art mich auf der ECOSS-Konferenz anzusprechen sowie seine Gastfreundschaft bei unserem unter besonderen Umständen entstandenen Besuch in Göttingen haben mich nachhaltig beeindruckt.

Prof. **Klas Lindfors**, der sich ohne Umschweife dazu bereit erklärt hat, den Vorsitz der Prüfungskommission dieser Arbeit zu übernehmen und uns wertvolle Anreize für optische Anwendungen von Clustern gab.

A whole-hearted thank you to astro-/cloud-photographer and coffee-addict **Pantelis Bampoulis**, who took the time off his telescope to be my thesis committee observer; who dedicated more time than he ever needed to support me, be it by measuring and discussing data together, motivating me, maintaining lady ATHENE, or proof-reading my thesis; who I spent a wonderful time with on a student-filled train through the alps, fantasizing about Coulomb blockade; who expounded the necessities of cold milk foam for a *Freddo Cappuccino*; and finally whom I am humbled to call my friend.

Ich danke **Stephan Jaschonek** und **Tobias Hartl**, die im Rahmen ihrer Bachelor- und

Erklärung zur Dissertation

gemäß der Promotionsordnung vom 12. März 2020

Hiermit versichere ich an Eides statt, dass ich die vorliegende Dissertation selbstständig und ohne die Benutzung anderer als der angegebenen Hilfsmittel und Literatur angefertigt habe. Alle Stellen, die wörtlich oder sinngemäß aus veröffentlichen und nicht veröffentlichen Werken dem Wortlaut oder dem Sinn nach entnommen wurden, sind als solche kenntlich gemacht. Ich versichere an Eides statt, dass diese Dissertation noch keiner anderen Fakultät oder Universität zur Prüfung vorgelegen hat; dass sie - abgesehen von unten angegebenen Teilpublikationen und eingebundenen Artikeln und Manuskripten - noch nicht veröffentlicht worden ist sowie, dass ich eine Veröffentlichung der Dissertation vor Abschluss der Promotion nicht ohne Genehmigung des Promotionsausschusses vornehmen werde. Die Bestimmungen dieser Ordnung sind mir bekannt. Darüber hinaus erkläre ich hiermit, dass ich die Ordnung zur Sicherung guter wissenschaftlicher Praxis und zum Umgang mit wissenschaftlichem Fehlverhalten der Universität zu Köln gelesen und sie bei der Durchführung der Dissertation zugrundeliegenden Arbeiten und der schriftlich verfassten Dissertation beachtet habe und verpflichte mich hiermit, die dort genannten Vorgaben bei allen wissenschaftlichen Tätigkeiten zu beachten und umzusetzen. Ich versichere, dass die eingereichte elektronische Fassung der eingereichten Druckfassung vollständig entspricht.

Teilpublikationen:

[298] M. Will, N. Atodiresei, V. Caciuc, P. Valerius, C. Herbig, and T. Michely, "A Monolayer of Hexagonal Boron Nitride on Ir(111) as a Template for Cluster Superlattices", *ACS Nano*, **12**, 7, (2018), 6871-6880

[410] M. Will, P. Bampoulis, T. Hartl, P. Valerius, and T. Michely, "Conformal Embedding of Cluster Superlattices with Carbon", *ACS Applied Materials & Interfaces*, **11**, 43, (2019), 40524-40532

n/a M. Will, P. Bampoulis, T. Hartl, V. Boix de la Cruz, P. Lacovig, S. Lizzit, J. Knudsen, and T. Michely. "Growth, Stability and Electronic Decoupling of Pt Clusters on Hexagonal Boron Nitride on Ir(111)", manuscript, in preparation

Köln, den 02.11.2020   Moritz Will   _____

Lebenslauf *(Curriculum Vitae)*

Persönliche Daten

Name	Will
Vorname	Moritz
Geburtstag	16.05.1991
Geburtsort	Bergisch Gladbach
Staatsangehörigkeit	Deutsch

Ausbildung

seit 04/2017	Promotionsstudium II. Physikalisches Institut, Universität zu Köln Arbeitsgruppe Michely
10/2015 – 03/2017	Master of Science in Physics Universität zu Köln Durchschnittsnote: 1,3 Masterarbeit "Elemental vapor deposition on 2D materials: Cluster formation and intercalation" (Note: sehr gut 1,0) II. Physikalisches Institut, Universität zu Köln Arbeitsgruppe Michely
10/2009 – 09/2015	Bachelor of Science in Physics Universität zu Köln Durchschnittsnote: 2,3 Bachelorarbeit "Ionenstrahlinduzierte Nanostrukturierung von Si$(0\,0\,1)$" (Note: sehr gut 1,0) II. Physikalisches Institut, Universität zu Köln Arbeitsgruppe Michely
06/2009	Allgemeine Hochschulreife, Dietrich-Bonhoeffer-Gymnasium Bergisch Gladbach, Durchschnittsnote: gut (2,0)